NANYANG TECHNOLOGICAL UNIVERSITY

NONLINEAR STANDING WAVES IN MINIATURE ACOUSTIC RESONATORS

NONLINEAR STANDING WAVES IN MINIATURE ACOUSTIC RESONATORS

LUO CHENG

LUO CHENG

SCHOOL OF MECHANICAL & AEROSPACE ENGINEERING

2007

2007

Nonlinear Standing Waves in Miniature Acoustic Resonators

Luo Cheng

School of Mechanical & Aerospace Engineering

A thesis submitted to the Nanyang Technological University
in fulfilment of the requirement for the degree of
Doctor of Philosophy

2007

ABSTRACT

The research on both fundamental mechanisms and applications in nonlinear acoustic resonances has recently become active. By using shaped resonators, the acoustic saturations occurred in straight cylindrical resonators have been removed and large amplitude pressure oscillations have been obtained. Acoustic compressors have been developed following this technology. It is of interests to investigate if the nonlinear resonance can be used to produce high pressure gas oscillations in miniature/micro scales, which would be useful in microfluidics and bio-engineering applications. In order to have nonlinear resonances in small resonators, some issues, such as viscosity effects, resonator configurations and actuating methods, need to be studied.

This thesis presents a study on nonlinear resonance oscillations in shaped resonators. The main objective of the study is to investigate acoustic characteristics of nonlinear standing waves in small-size and miniature resonators. This is achieved by studying the effect of resonator geometry and driving methods on the resonance pressures theoretically and experimentally. At the end of the study, a novel design for miniature resonators is demonstrated.

The theoretical study in this dissertation mainly comprises three aspects. Firstly, resonance pressures in shaped resonators driven by a shaking force are studied. The resonators are of two types of configurations: one is axisymmetric with cross sectional area being exponentially expanded; another is of a low-aspect-ratio rectangular cross section whose width is exponentially expanded. One-dimensional nonlinear wave equations are obtained by modifying equations developed by Ilinskii *et al.* (1998), taking into account of shear viscosity and bulk viscosity terms which are derived from

general dissipation terms and linear momentum equations for both resonators. The governing equations, describing finite amplitude gas oscillations generated by harmonically shaking the entire resonator, are solved by the Galerkin's method. Nonlinear resonance phenomena, such as shock-free high amplitude pressure waveforms and frequency shift, are obtained and discussed for different resonator configurations. Especially, the effect of resonator size reduction on nonlinear standing waves is examined.

Secondly, the resonances generated by a piston are investigated. The piston is located at the big end of an exponentially expanded resonator while the other end is closed. The boundary conditions in this case are non-homogenous. A function, which satisfies the non-homogenous boundary conditions, is introduced in the solution procedure to remove the non-homogeneous boundary conditions, and the Galerkin's method is applied to solve the nonlinear equation for the velocity potential. The nonlinear resonance characteristics obtained from the piston are compared with that obtained through shaking. The study on the case of piston driving is to provide reference data for extending the piston driving method to a more generalized boundary driving in miniature resonators.

Thirdly, the energy loss in the nonlinear resonance is discussed based on dissipations in boundary layers and quality factors. The energy is mainly dissipated within boundary layers where shear viscosity and thermal diffusion convert dynamic energy into heat. The shear viscous effect and thermal diffusion effect are combined together in a dimensionless parameter in the governing equations, and the energy dissipation is studied in terms of total dissipation, dissipation density and its spatial distribution in

the resonators. The energy loss is also evaluated by quality factors. The quality factor is computed in two ways. One is based on decay factors for linear systems, and another is directly based on the dissipated energy and total stored energy during the nonlinear resonance, so that the nonlinear effect is included. The quality factors are calculated for resonators with various dimensions and configurations, and the results confirm that the quality factors are lower and dissipations are higher for smaller resonators.

The experiments have been carried out partially to verify some of the simulation results obtained for axisymmetric resonators, and mainly to investigate the possibility of achieving useful dynamic pressures in small-size or miniature resonators. The small-size and miniature resonators in the study are of various configurations and driving methods, which cannot be simulated by the modeling technique used for the axisymmetric resonators. Four resonators were fabricated and tested, including an axisymmetric resonator and three low-aspect-ratio rectangular (LARR) resonators. The axisymmetric resonator was exponentially expanded with the flare constant α = 5.6, and was driven by a loudspeaker (functioning as a piston) at the big end. The measured results from the axisymmetric resonator, in terms of resonance pressure amplitudes, resonance frequency and ratio of pressures at the two ends of the resonator, were compared with the simulated results. The three LARR resonators consisted of resonance cavities linked by contracting ducts to small ends. Two of them had 5 mm cavity depths and were driven by a 3 inch speaker from side walls. The third one had a 3 mm cavity depth and was driven by a 50 mm diameter piezoelectric disk which formed one side wall of the resonator cavity. The test results show that these low-aspect-ratio resonators are of similar resonance characteristics as

those observed in the axisymmetric resonators, which lead to the conclusion that LARR resonators could be developed further as miniature acoustic resonators.

ACKNOWLEDGEMENT

The author would like to firstly express his deep appreciation to his supervisor, A/P Huang Xiaoyang and co-supervisor, A/P Nguyen Nam-Trung for their invaluable guidance and support throughout this project.

Furthermore, the author would like to also express his thanks to A/P Zhao Yong, Dr. Su Xiaohui and Lv Xin for all the assistance and encouragement that they had rendered. Thanks to Center for Mechanics of Micro-System and Computational Numerical Center for their helpful assistance to the experiment. The author is grateful to friends for all things that he would have taken for granted.

Last but not least, the author would like to thank his families, their morale and consistent supports have always inspired him to improve himself.

NOMENCLATURE

Symbols

A, a	Non-dimensional and dimensional acceleration of oscillation (-, m/s^2)
B, b	Non-dimensional and dimensional width of LARR resonator (-, m)
c_0	Speed of sound (m/s)
C_p	Specific heat at constant pressure (J/(kg·K))
C_v	Specific heat at constant volume (J/(kg·K))
D, e_{dis}	Non-dimensional and dimensional dissipation (-, W)
E, e	Non-dimensional and dimensional total energy (-, J)
f	Frequency (Hz)
F	Mass flux (kg/s)
H, h	Non-dimensional and dimensional height of LARR resonator (-, m)
j	Unit imaginary number
k_n	Natural acoustic wave numbers
K	Thermal conductivity (W/(m·K))
L, l	Non-dimensional and dimensional length of resonator (-, m)
M	Mass per unit length (kg/m)
P, p	Non-dimensional and dimensional pressure (-, Pa)
Pr	Prandtl number
Q	Quality factor
Q_B	Quality factor due to dissipation associated with the volume change
Q_S	Quality factor due to dissipation associated with the shear motion
R, r	Non-dimensional and dimensional radius (-, m)

R_{const}	Universal gas constant (J/(mol·K))
S, s	Non-dimensional and dimensional across-sectional area (-, m^2)
T, t	Non-dimensional and dimensional time (-, s)
T_k	Absolute temperature (K)
u	Particle velocity in the x-direction (m/s)
v	Particle velocity in the y-direction (m/s)
W_n	Weighting functions
X, x	Non-dimensional and dimensional coordinate along the resonator (-, m)
Y, y	Non-dimensional and dimensional transverse coordinate (-, m)

Greek Symbols

α^{BL}	Absorption coefficient for the boundary layer
κ	Decay factor (s^{-1})
η	Dynamic viscosity coefficient (Pa·s)
α	Flare constant
ω_0	Fundamental frequency of a cylindrical resonator (s^{-1})
ρ	Gas density (kg/m^3)
ν	Kinematic viscosity coefficient (m^2/s)
σ	Non-dimensional decay factor
γ	Ratio of specific heats
ζ	The second viscosity coefficient (Pa·s)
θ_{therm}^{BL}	Thickness of thermal boundary layer (m)
θ_{visc}^{BL}	Thickness of viscous boundary layer (m)

Ψ_n	Trial function
δ	Viscosity parameter (m/s)
Ω , ω	Non-dimensional and dimensional driving frequency (-, s^{-1})
Φ , φ	Non-dimensional and dimensional velocity potential (-, m^2/s)

Subscripts

0	Ambient value
acc	Accumulative value
x	Component in x-direction
y	Component in y-direction

Superscript

$\overline{(\ )}$	Average
$\widetilde{(\ )}$	Amplitude
$\widehat{(\ )}$	Per unit volume
BL	Boundary layer

TABLE OF CONTENTS

TABLE OF FIGURES

LIST OF TABLES

PUBLICATIONS ARISING FROM THIS THESIS

Journal paper:

Luo C., Huang X. Y. and Nguyen N. T., *Generation of shock free pressure waves in shaped resonators by boundary driving*, The Journal of the Acoustical Society of America, Vol. 121, No. 5, pp. 2515-2521 (2007).

Luo C., Huang X. Y. and Nguyen N. T., *Effect of resonator dimensions on nonlinear standing waves*, The Journal of the Acoustical Society of America, Vol. 117, No. 1, pp 96 - 107 (2005).

Conference paper:

Huang X. Y., **Luo C.** and Nguyen N. T., *Acoustic pressures in miniature resonators*,19th International Congress on Acoustics, MADRID, September 2007.

Huang X. Y., **Luo C.** and Nguyen N. T., *Acoustic pressure generated in shaped resonators for potential application in micro energy system*, International Conference on Micro Energy System, Sanya, China, September 2005.

CHAPTER 1

INTRODUCTION

1.1.BACKGROUND

Finite-amplitude acoustic phenomena in resonant cavities have been of practical interest since the 1930s, when German researchers studied acoustic resonance in connection with the development of mufflers for tanks. It was found that there was an intrinsic limit for sound waves in gases (in closed half-wavelength resonator cavities) that would never allow high-energy levels and acoustic pressures to exist. Experimental work had shown that sound waves in a resonator would build up energy only to a certain level when shock waves started to form. Once a shock wave exists, any energy added to the wave is wasted as heat without any increase in the dynamic pressures. The phenomenon is commonly observed in a cylindrical tube whose two ends are sealed and is under a sinusoidal shaking along its axial direction, shown in Figure 1.1. Dynamic pressures will be generated in the gas inside the tube, in response to the shaking.

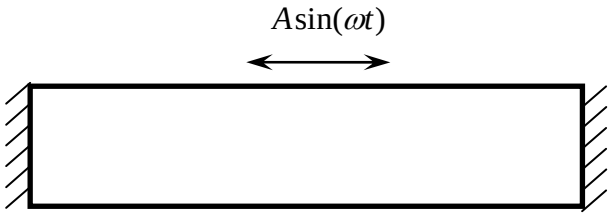

Figure 1.1 A cylindrical duct under sinusoidal shaking along its axis.

When the driving frequency is close to the resonance frequency, at which the pressure wavelength is equal to double of the tube length, the pressure oscillation amplitude reaches to the maximum, and will increase following the increase of driving strength

until the shock wave forms. These are illustrated in Figure 1.2. Shock wave has higher acoustic modes (f_3, f_5), as shown in Figure 1.2. Since pressure waves only reflect at two ends of cylindrical tube, f_3 and f_5 are multiples of fundamental frequency. Those higher acoustic modes can dissipate additional driving energy so that pressure amplitude can not be very high even though stronger driving is applied. The change from sinusoidal waves to shock waves is a typical nonlinear characteristic of gas dynamics.

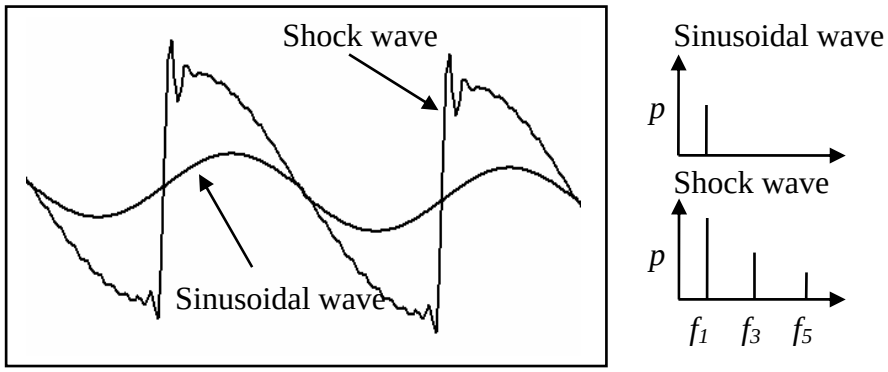

Figure 1.2 Pressure waveform and spectrum of sinusoidal wave and shock wave.

The shock waves and pressure amplitude limits have recently been removed. Lucas (1999) devised a new technique by which standing sound waves resonating in a specially shaped closed tube can be loaded with thousands of times more energy than was previously possible. The technology developed by Lucas is known as Resonant Macrosonic Synthesis (RMS). Lucas discovered that for resonant sound waves, the geometry of the resonator cavity through which the sound waves travel was the most important factor in determining the waveform. For a resonator whose cross section area expands along the axial direction, higher acoustic modes are no longer multiples of fundamental frequency and they are difficult to build up. Therefore, the RMS allows the synthesis of non-shocked waveforms, which in turn allows large amounts of energy to be added to the wave, leading to very high dynamic pressures. At the

same time it may also produce high density ratio because of reduction of dissipation. This is important in inertial confinement fusion, for example.

Since RMS can transfer a large amount of energy into a sound wave, a wide range of physical effects becomes possible. One example shows that the dynamic (oscillating) pressures exceeding 500psi in gases is possible (Lawrenson *et al*. 1998). The fluid power industry can benefit through RMS's ability to compress gas. This will remove the need for moving parts, lubrication oil, so that to eliminate the risk of fluid contamination. Industries that may benefit from this include: chemicals, pharmaceuticals, semiconductor manufacture, natural and commercial gas handling, refrigeration, air conditioning and air compression. One of the first areas to take advantage of the technology is acoustical compressors, which use sound energy to compress the gas and promise higher energy efficiency. Figure 1.3 illustrates the operation principle of the acoustic compressor designed by Lucas *et al*. (1999).

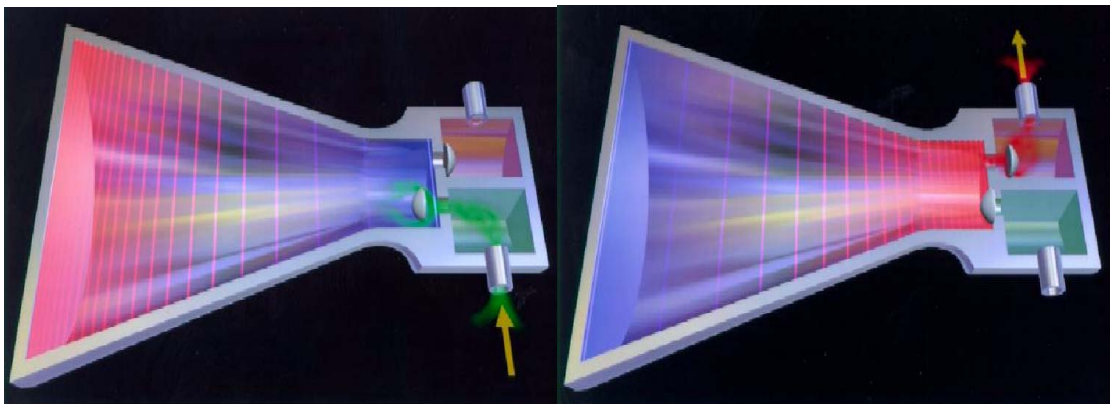

(a) Gas is sucked in (b) Gas is compressed out

Figure 1.3 Acoustic compressor design taken from Lucas.

In this device, the sound waves are created and sustained in a closed, horn-shaped resonator. The sound waves can convert low-pressure gas from the suction chamber on the lower right [Figure 1.3(a)] into high-pressure gas exiting the discharge chamber

on the upper right [Figure 1.3(b)]. During a single "acoustic cycle" (which lasts 0.002 second in the process shown above), the sound wave oscillates between high and low pressures in certain regions of the main chamber. In the part of the cycle depicted above, the right end of the main chamber is a low-pressure region for the sound wave; consequently, the suction valve is pulled open and the low-pressure gas is induced into the main chamber. A thousandth of a second later, the right end of the main chamber becomes a high-pressure region, which opens the discharge valve and allows the gas to exit.

The RMS technology may be further developed in several aspects, such as to have different driving methods other than shaking and to have miniature or even micro scale resonators. The miniaturization of RMS technology is especially important to the development of microfuidic devices.

Microfluidics, as a new research area (Gad-et-hak, 1999), has recently become very active, driven by its applications in biomedical engineering and life science. Microflduidic devices integrate together small pumps, valves, sensors and actuators, etc. to handle small amount of liquid and gas. Micro pumps have been successfully developed and widely used to move liquid in micro systems (Nguyen, 2000). Workable micro compressors, however, have not been reported, probably because of the difficulties in increasing gas pressure in miniature/micro scales. It is of interest to know if the large amplitude pressures can be generated in miniature resonators and it is therefore meaningful to study if RMS technology can be applied to develop miniature/micro scale compressors, which motivates the research presented in this thesis.

1.2 OBJECTIVES AND SCOPE

The objectives of this study are:

- To investigate the effect of size reduction in resonators on the resonance characteristics, including resonance pressure amplitudes, resonance frequencies and waveforms, etc.
- To study shaped resonator with various configuration under boundary driving, which may be more suitable to miniature resonators.

The scope of this study encompasses the following aspects:

1. To conduct analytical study, taking into account of viscosity of air, to investigate effect of resonator dimensions and geometry on nonlinear pressure waves.
2. To conduct analytical study on nonlinear standing waves generated by a piston in expanded resonators.
3. To investigate the energy dissipations in resonators.
4. To conduct an experimental study to validate the mathematical model and test boundary driving for miniature resonators.

1.3 LAYOUT OF THESIS

There are seven chapters in this thesis. Chapter 1 gives a brief introduction to Resonant Macrosonic Synthesis (RMS) and a description of the objectives and scope of this project. In Chapter 2 a literature review which focuses on the nonlinear standing waves in acoustical resonator and its applications.

In Chapter 3, the acoustical waves in various resonators are studied and the effect of size reduction in resonators on nonlinear standing waves is discussed. The velocity profile in axisymmetric and rectangular duct is discussed and one-dimensional shear viscous and bulk viscous terms are derived from general 3-D dissipation form. Mathematical models for several kinds of shaped resonator under entirely shaking force are developed and solved by the Galerkin's method.

In Chapter 4, wave equations for resonators driven by a piston are derived from the mathematical model in Chapter 3 by handling the piston driving boundary condition. The nonlinear standing waves in shaped resonator obtained by a piston are investigated, and the results are compared with the shaking condition. Analysis of the two kinds of driving forces is also carried out.

Energy dissipation in acoustical resonator is discussed in Chapter 5. The effect of the viscous boundary layer is to exert a shear force on the side of the control volume. Similarly, the effect of the thermal boundary layer is to transfer heat to the control volume through the side surface. The effect of thermal dissipation on acoustical pressure waves is studied. The stored energy and dissipation in shaped resonator are estimated analytically, and the quality factors are discussed.

In Chapter 6, acoustical waves in several shaped resonators are studied experimentally. A comparison of experimental and simulation results is performed to validate the numerical model developed in Chapter 3. Finally a novel miniature resonator and boundary driving method is proposed and examined in experiment.

Chapter 7 gives the main conclusions drawn from this study and recommendations for future work.

CHAPTER 2

LITERATURE REVIEW

2.1 FUNDAMENTALS OF SOUND WAVES AND RESONANCES

2.1.1 SOUND WAVES

Sound is a disturbance of mechanical energy that propagates through matters as a wave. Sound waves are characterized by frequency, wavelength, period, amplitude and velocity, etc. These physical properties may change with ambient conditions. For example, the speed of sound in air and other gases depends on temperature. In air, the speed of sound is approximately 343 m/s, in water 1500 m/s and in a bar of steel 5000 m/s.

Sound pressure is the pressure deviation from the local ambient pressure caused by a sound wave. Sound pressure can be measured using a microphone in air and a hydrophone in water. The SI unit for sound pressure is pascal (Pa). The effective sound pressure amplitude used in the measurement is the root-mean-square of the instantaneous sound pressure over a given interval of time. In a sound wave, the complementary variable to sound pressure is the acoustic particle velocity. For small amplitudes, sound pressure and particle velocity are linearly related and their ratio is the acoustic impedance. The acoustic impedance depends on characteristics of the wave and medium.

As the human ear can detect sounds with a very wide range of amplitudes, sound pressure is often measured as a level on a logarithmic decibel scale. The sound pressure level (SPL) is defined as

$$SPL = 10\log_{10}\left(\frac{p^2}{p_0{}^2}\right) = 20\log_{10}\left(\frac{p}{p_0}\right) \quad \text{dB}, \tag{2.1}$$

where p is the root-mean-square sound pressure and p_0 is a reference sound pressure. Commonly used reference sound pressures, defined in the standard ANSI S1.1-1994, are 20 μPa in air and 1 μPa in water. Table 2.1 shows some examples of sound pressure and sound pressure levels.

Table 2.1 Examples of sound pressure and sound pressure levels

Source of sound	Sound pressure (pascal)	Sound pressure level (dB)
threshold of pain	100	134
hearing damage of short term effect	20	approx. 120
jet, 100m distant	6 - 200	110 - 140
jack hammer, 1 m distant / discotheque	2	approx. 100
hearing damage of long-term effect	6×10^{-1}	approx. 90
major road, 10 m distant	2×10^{-1} - 6×10^{-1}	80 - 90
passenger car, 10 m distant	2×10^{-2} - 2×10^{-1}	60 - 80
TV set at home level, 1 m distant	2×10^{-2}	ca. 60
normal talking, 1 m distant	2×10^{-3} - 2×10^{-2}	40 - 60
very calm room	2×10^{-4} - 6×10^{-4}	20 - 30
leaves noise, calm breathing	6×10^{-5}	10
auditory threshold at 2 kHz	2×10^{-5}	0

The propagation of sound waves in air can be modeled by conservation of mass and conservation of momentum,

$$\frac{\partial \rho}{\partial t} + \nabla \bullet (\rho \mathbf{v}) = 0\,, \tag{2.2}$$

$$\rho\left(\frac{\partial \mathbf{v}}{\partial t} + (\mathbf{v}\bullet\nabla)\mathbf{v}\right) = -\nabla p + \mu\left(\nabla^2 \mathbf{v} + \frac{1}{3}\nabla(\mathbf{v}\bullet\nabla)\right), \tag{2.3}$$

where ρ is mass density, p is pressure, and $\mathbf{v}$ is acoustic fluid velocity vector. Since sound waves are generally weak disturbances, nonlinear equations(2.2) and (2.3) can be linearized. For weak disturbance, one-dimensional linear momentum equation is given as

$$\rho \frac{du}{dt} + \frac{\partial p}{\partial x} = 0\,. \tag{2.4}$$

From the linearized one-dimensional continuity equation, the linearized one-dimensional momentum equation and the equation of state, the one-dimensional wave equation can be obtained as,

$$\frac{\partial^2 p}{\partial x^2} - \frac{1}{{c_0}^2}\frac{\partial^2 p}{\partial t^2} = 0\,, \tag{2.5}$$

where c_0 is the speed of sound.

2.1.2 RESONANCE AND STANDING WAVES

Standing waves are of waves pattern created within a medium when the reflected waves from one end of the medium interfere with incident waves from the source. Figure 2.1 shows the standing waves in an air column. As illustrated in the figure, a

node for air particle displacement is always an antinode for pressure, and vice versa. When the air is constrained to a node, the air motion will be alternately squeezing toward that point and expanding away from it, causing the pressure variation to be at a maximum.

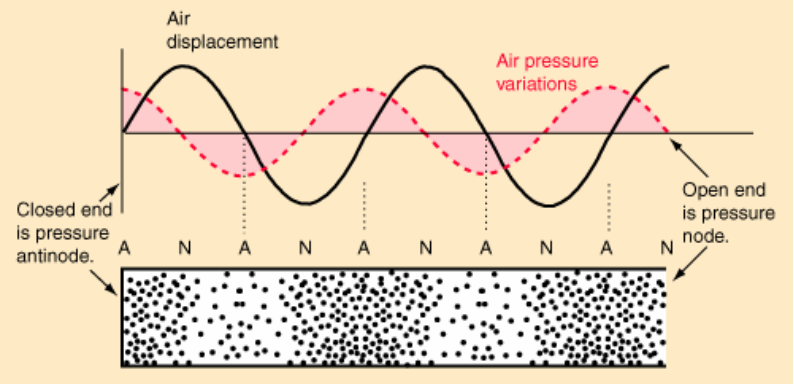

Figure 2.1 Standing waves in air column.

Acoustic resonance is the tendency of an acoustic system to have maximum response to the external driving and absorb more energy when the driving frequency of its oscillations matches the system's natural frequency of vibration (its resonant frequency) than it does at other frequencies. A resonant system may have multiple resonance frequencies.

The standing waves and acoustic resonance can happen in a cylindrical tube with both ends closed. At the resonance, the air column inside the tube will vibrate in a fundamental mode such that the tube length is one half the wavelength of the sound wave, as shown in Figure 2.2. Each end of the column must be an antinode for the acoustical pressure since the ends are closed and are node for the air motion. For the fundamental mode, there is one node at the center. The resonance frequencies in this case are

$$f_n = \frac{nc_0}{2L}, \quad n = 1, 2, 3, \cdots, \tag{2.6}$$

where c_0 is speed of sound and L is the length of tube. The driving in this case is by shaking the tube. The resonance may also be obtained by a piston oscillating at on end.

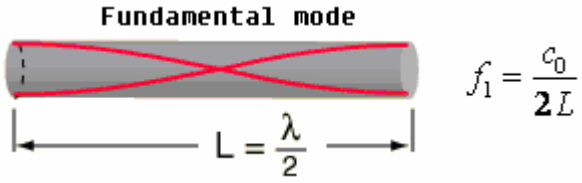

Figure 2.2 Cylindrical air column in a closed tube.

2.2 NONLINEAR STANDING WAVES IN CYLINDRICAL RESONATOR

2.2.1 SHOCK WAVES IN CYLINDRICAL RESONATOR

Sound pressure waves will be of sinusoidal waveforms at the resonance in a cylindrical resonator under weak excitation. Distortion and shock waves in resonators may occur if the driving is strong, due to the nonlinear characteristics of fluids. Figure 2.3 shows the waveforms predicted by Chun and Kim (2000) at one end of a cylindrical resonator. Gas in the cylindrical resonator is excited by an external oscillation force. At the weak excitation, the resonance pressure waves will be sine waves. But for a stronger driving acceleration ($10m/s^2$), the pressure waveform is distorted. When the driving becomes stronger ($100m/s^2$), the pressure waveforms are evolved into saw-tooth forms, i.e., shocks. When the shock waves are formed in the resonator, most of the dynamic energy at the fundamental driving frequency will loss to the viscous dissipation at the shock fronts where the pressure and velocity change abruptly. As a consequence, the pressure amplitude will no longer increase following the driving strength. This is called acoustic saturation. It is therefore called finite amplitude standing waves.

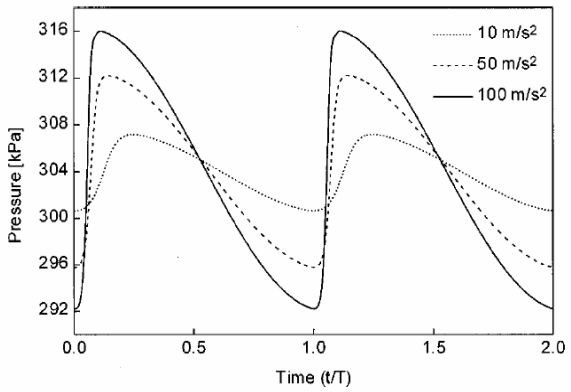

Figure 2.3 Shock waves at one end of a cylindrical resonator driven by external acceleration force.

The propagation of the shock wave in the cylindrical resonator is shown in Figure 2.4. At the half cycle, the shock propagates in the opposite direction.

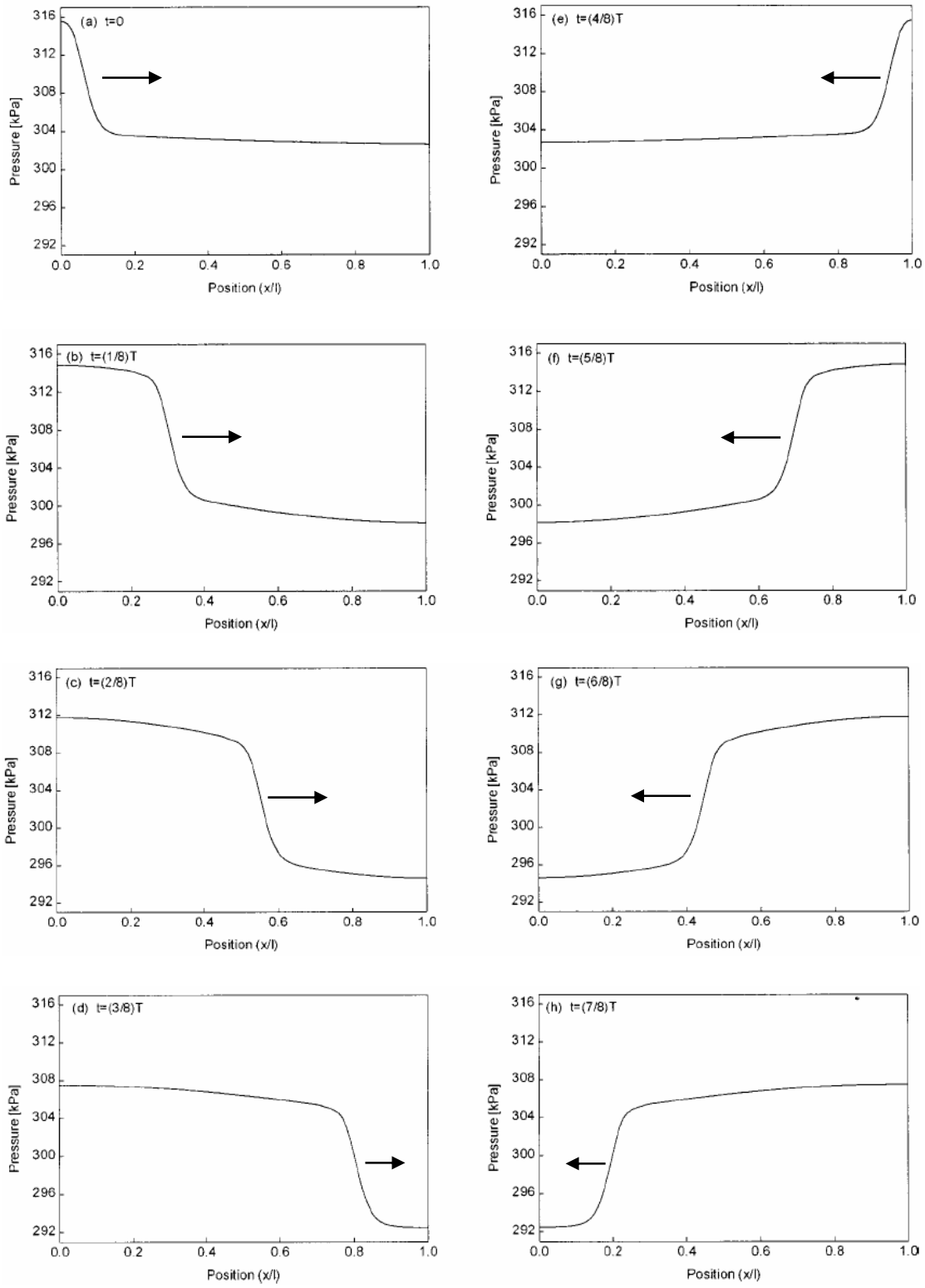

Figure 2.4 Propagation of shock wave in cylindrical resonator (Chun and Kim, 2000).

2.2.2 RESEARCH WORKS ON SHOCK WAVES IN CYLINDRICAL RESONATORS

The nonlinear phenomenon of acoustical waves in cylindrical resonators has been extensively investigated by both theoretical modeling and experimental measurements. Most reported studies are limited to finite-amplitude standing waves in resonators of constant cross section with a piston excitation at one end and a rigid cap at the other end.

Betchov (1958) introduced a simple theoretical analysis on the inviscid gas dynamics, based on discontinuous linearized solutions and secular equations. Saenger and Hudson (1960) also developed a theory to understand the motion of the gas in a tube, which included the dissipative effects of wall friction and heat conduction to the tube wall. They tried to describe shock waves under an assumption that the solution consisted of a continuous and discontinuous components. Later, Weiner (1966) and Temkin (1969) used the same assumption in their analysis, in which the wavefront was consisted of a discontinuous shock front connected by a continuous section.

Chester (1964) introduced a second order theoretical analysis that included the effects of boundary layer and volume absorption, and the results explained the nonlinear phenomena at near-resonant frequencies. Cruikshank (1972) compared experimental results in a resonator with Chester's predictions and found qualitative agreement between them.

Coppens and Sanders (1968) presented a perturbation expansion for a one-dimensional second order nonlinear wave equation, which was extended later to a

three-dimensional model for lossy cavities (Coppens and Sanders, 1975). A single nonlinear equation was used to describe the finite amplitude standing waves in a cavity. Linear resonance frequencies and quality factors were used to predict amplitudes of higher harmonics of the finite-amplitude wave.

Gaitan and Atchley (1993) used the perturbation model developed by Coppens and Sanders (1968) to study finite-amplitude standing waves in harmonic and inharmonic resonators. The harmonic resonator was a uniform cylinder (Figure 2.5 (a)), while the inharmonic resonator consisted of a cylindrical tube with a midsection that had an expansion or a contraction (Figure 2.5 (b)). The measurements showed good agreement with the model. It was also found that the variable cross section significantly reduced transfer of energy from the fundamental resonance frequency to higher harmonics.

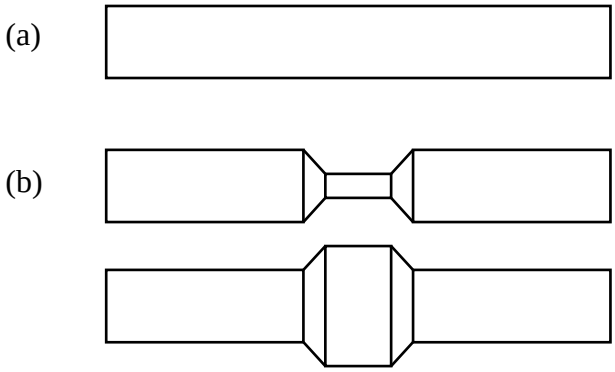

Figure 2.5 (a) Harmonic resonator (b) Inharmonic resonators with an expanded or a contracted midsection.

Other than the piston driving, Lee and Wang (1992) numerically analyzed the nonlinear resonance of a closed rigid tube, in which the gas was assumed to be excited by an external body force. The nonlinear resonance of an air-filled acoustic resonator with rigid walls was studied numerically using the fully nonlinear Lagrangian wave

equation. The effects of bulk viscous dissipation were included. The results were found very similar to those obtained in a piston-driven resonant tube.

2.3 NONLINEAR STANDING WAVES IN SHAPED RESONATOR

2.3.1 ANALYTICAL STUDY

In contrast to the cylindrical resonators, the shaped resonators refer to the resonators whose cross sections are not uniform, such as horns. The development of theoretical models of acoustic horn was started with a paper published in 1919 by Webster (Webster, 1919). Webster derived an equation for modeling one-dimensional plane-wave propagation in horns, often called the Webster horn equation. Webster's equation models the propagation of pressure waves in a horn assuming that no transverse modes exist. Under this assumption any point within the horn falls on some isophase surface which spans the cross section of the horn, over which the pressure is constant, as shown in Figure 2.6.

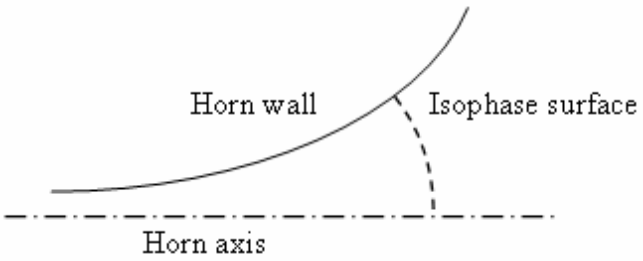

Figure 2.6 Flared horn.

Goldstein and McLachlan (1935) studied nonlinear wave propagation in horns and developed a simple formula for estimating the nonlinear distortion of purely progressive waves in an exponential horn. Post and Hixson (1994) conducted a review on waves in horns and concluded that only minor improvements to Webster's horn model had been made in the past 80 years. A more sophisticated mathematical model was not practicable because of the corresponding increase in difficulty of solution. The useful contributions that various researchers had made to Webster's original model equation were (i) choosing the appropriate size of mouth for the one-

dimensional horn representation, and (ii) defining the rate of wavefront area expansion more accurately than by means of the plane-wave model (Holland *et al.*, 1991). Moreover, the assumption had always been that the amplitude of the disturbance was small and the sound propagation was linear. Eisner (1967) gave a complete solution of the Webster horn equation.

Chester (1994) investigated the disturbances produced in a gas-filled resonator of varying cross section by oscillations of a piston at one end. The resonator was rigidly terminated at the other end and the piston was oscillated at near resonance frequencies. The main purpose of his investigation was to examine the influence of area variation on the basic solution obtained earlier (Chester, 1964) from a resonator of uniform cross section. Within a band of excitation frequencies around each resonance frequency, shock waves appeared in the solution; outside this frequency band the pressure waveforms were found continuous, but not purely sinusoidal.

Ilinskii *et al*. (1998) developed a one-dimensional model to analyze nonlinear standing waves of high amplitude in an acoustical resonator. They converted gas dynamic equations into a single nonlinear equation, shown in Eq. (2.7), to describe the nonlinear standing waves in an axisymmetric resonator with arbitrary cross sectional shape. The cross section shape was given by a function $r = r(x)$. An external harmonic force shook the entire resonator in the axial direction to excite the gas inside the resonator. The oscillation of entire resonator was characterized by the acceleration $a(t)$. In their study, the energy dissipation in the volume was taken into account. The energy losses in the boundary layer were taken into account by an effective absorption coefficient whose value was greater than the volume dissipation.

$$\frac{c_0^2}{r^2}\frac{\partial}{\partial x}\left(r^2\frac{\partial\varphi}{\partial x}\right)-\frac{\partial^2\varphi}{\partial t^2}+\frac{\delta}{r^2}\frac{\partial^2}{\partial t\partial x}\left(r^2\frac{\partial\varphi}{\partial x}\right)=\frac{da}{dt}x+a(t)\frac{\partial\varphi}{\partial x}$$
$$+\frac{\gamma-1}{r^2}a(t)x\frac{\partial}{\partial x}\left(r^2\frac{\partial\varphi}{\partial x}\right)+2\frac{\partial^2\varphi}{\partial x\partial t}\frac{\partial\varphi}{\partial x}+\frac{\gamma-1}{r^2}\frac{\partial\varphi}{\partial t}\frac{\partial}{\partial x}\left(r^2\frac{\partial\varphi}{\partial x}\right) \quad (2.7)$$
$$+\frac{1}{3}\frac{\partial}{\partial x}\left(\frac{\partial\varphi}{\partial x}\right)^3+\frac{\gamma-1}{2r^2}\left(\frac{\partial\varphi}{\partial x}\right)^2\frac{\partial}{\partial x}\left(r^2\frac{\partial\varphi}{\partial x}\right).$$

In Eq. (2.7), φ is velocity potential and δ is a parameter related to viscosity. Eq. (2.7) was non-dimensionalized and then transformed to the frequency domain. The equations for the complex amplitudes of spectral components were integrated numerically using the fifth-order Runge–Kutta formulas with adaptive stepsize control. Results for three resonators: a cylinder, a cone and a bulb were presented. Theoretical predictions for the amplitude related resonance frequency shift, hysteretic effects, and waveform distortions were presented. The results for waveforms agreed well with measurements by Lawrenson *et al*. (1998), shown in Figure 2.7. The model provided insight into the physics of nonlinear standing waves in resonators of different shape and gave a tool to design resonators that had characteristics suitable for specific applications.

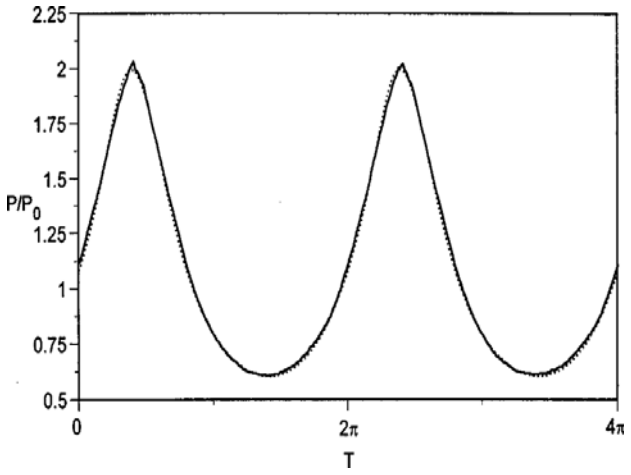

Figure 2.7 The nonlinear standing wave in conical resonator compared with the measurement (the solid line) by Lawrenson *et al*. (1998).

Later, Ilinskii *et al*. (2001) modified their one-dimensional model by including energy losses in the boundary layer along the resonator wall. The influence of the boundary layer on the acoustical field was taken into account by introducing an additional term into the continuity equation that described the mass flow from the boundary layer to the volume, so that the energy dissipation in the boundary layer was estimated. A simple eddy viscosity model was applied to include the losses associated with the turbulence. The new model was solved numerically for three types of resonators, a cylinder, a horn cone and a bulb resonator.

Erickon and Zinn (2003) used the Galerkin method to solve the wave equation developed by Ilinskii *et al*. (1998). They assumed that the velocity potential could be expressed by an infinite series expansion as following:

$$\Phi(X,T) = \sum_{n=1}^{\infty} \eta_n(T)\Psi_n(X), \tag{2.8}$$

where $\Psi_n(X)$ are the trial functions, describing the spatial dependence of the natural acoustic mode shape of a given duct geometry, and $\eta_n(T)$ are time-dependent amplitudes of these acoustic modes. The objective of using the Galerkin method is to derive a set of equations for the time-dependent amplitudes, $\eta_n(T)$, that will minimize the residual in obtaining the solutions. It was demonstrated by Erickon and Zinn (2003) that the results obtained by the Galerkin method were in excellent agreement with the results obtained with other numerical solution techniques. They further investigated the forced response of an exponentially expanded duct, and it was shown that for a given forcing amplitude, there existed a nonmonotonic increase in compression ratio as the duct's flare constant was increased.

2.3.2 EXPERIMENTAL STUDY

Lucas (1994) applied a patent for acoustical compressors based on high amplitude standing waves in shaped resonator. A conventional reciprocating electro-mechanical actuator was used to oscillate the resonator. This driving method made virtually all of the interior surface area of the resonator available for driving the working fluid. The experimental testing results on the shaped resonators by this driving technique were reported by Lawrenson *et al*. (1998).

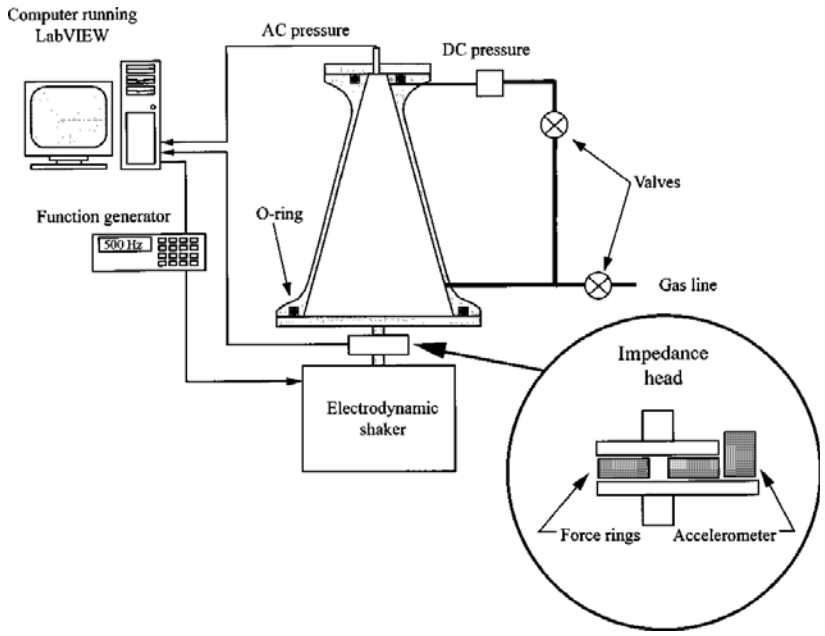

Figure 2.8 Experimental apparatus by Lawrenson *et al*. (1998).

Lawrenson *et al.* (1998) showed measured macrosonic standing waves in gases in oscillating shaped resonators. The experimental setup is shown in Figure 2.8. The power was delivered to the resonator by oscillating it with a linear actuator (entire resonator drive). The strong dependence of the pressure waveform upon the cavity shape was demonstrated. This dependence was exploited to provide control of harmonic phase and amplitude, thus avoided shocks and enabled resonant waveforms to reach macrosonic pressures. Standing wave overpressures in excess of 340% of ambient pressure were demonstrated in these resonators, compared to maximum

overpressures of 17% observed in cylindrical ones. Ratios of maximum to minimum pressures of 27 were observed compared to 1.3 for cylinders. Measurements were conducted on four axisymmetric resonators: cylinder, cone, horn-cone hybrid, and bulb (Figure 2.9). These resonators were filled with nitrogen, propane, or refrigerant R-134a. Some effects, including nonlinearly generated dc pressures of 40% of ambient pressure and hardening/softening resonance behaviors, were observed. Lawrenson *et al.*, (1998) claimed that the shaped resonators, together with the entire resonator drive, provided high-power transduction of energy through resonant sound waves and opened a wide range of new commercial applications for macrosonic waves.

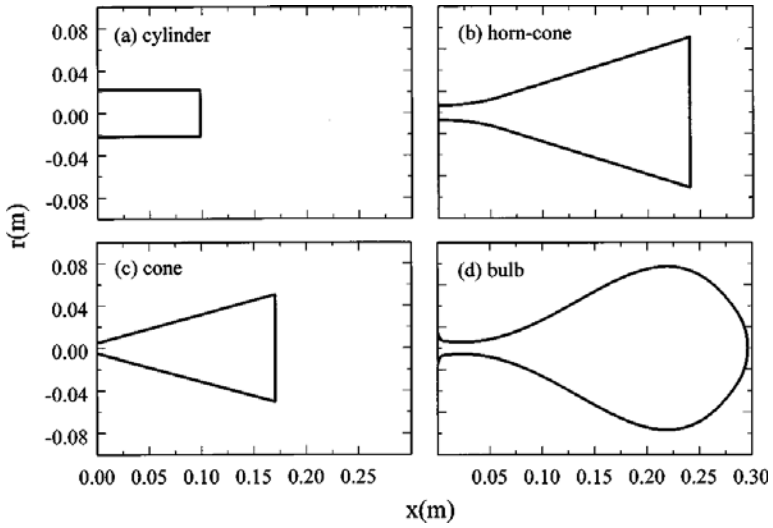

Figure 2.9 Interior geometry of resonators by Lawrenson *et al*. (1998): (a) cylinder, (b) horn-cone, (c) cone and (d) bulb.

2.3.3 NUMERICAL STUDY

Chun and Kim (2000) presented a numerical investigation on nonlinear oscillations of gas in an axisymmetric tube. One-dimensional nonlinear governing equations, which explicitly included attenuation terms related to viscosity, were derived. The equations were solved numerically by using a higher-order finite difference scheme, which

consisted of a spatial differentiation part and a time evolution part respectively. In order to get an accurate numerical solution, they developed a numerical code with a fourth-order compact scheme for spatial differentiation and a fourth-order Adams method for time evolution. The Adams' method is a numerical method for solving linear first-order ordinary differential equations of the form

$$\frac{dy}{dx} = f(x, y). \tag{2.9}$$

By applying the Maclaurin series to y,

$$y_{n+1} = y_n + \left(\frac{dy}{dx}\right)_n (x - x_n) + \frac{1}{2}\left(\frac{d^2y}{dx^2}\right)_n (x - x_n)^2 + \ldots, \tag{2.10}$$

and

$$\left(\frac{dy}{dx}\right)_{n+1} = \left(\frac{dy}{dx}\right)_n + \left(\frac{d^2y}{dx^2}\right)_n (x - x_n)^2 + \ldots, \tag{2.11}$$

the fourth order interpolation is obtained as

$$y_{n+1} - y_n = h(q_n + \tfrac{1}{2}\nabla q_{n-1} + \tfrac{5}{12}\nabla^2 q_{n-2} + \tfrac{3}{8}\nabla^3 q_{n-3} + \tfrac{251}{720}\nabla^4 q_{n-4}) \tag{2.12}$$

where q_n is $\left(\frac{dy}{dx}\right)_n$, $\nabla q_n \equiv \left(\frac{d^2y}{dx^2}\right)_n$, $\nabla^2 q_n \equiv \left(\frac{d^3y}{dx^3}\right)_n$, and $h = x_{n+1} - x_n$.

The numerical simulations were finally accomplished by Chun and Kim (2000) to study the effect of the tube shape on the maximum pressure. The tubes of cylindrical, conical, and cosine shape with the same volume and length were investigated. The results showed that the resonance frequency and patterns of pressure waves strongly

depend not only on the tube shape but also the amplitude of driving acceleration. It was found that the 1/2 cosine-shape tube was more suitable to induce high compression ratio than other shapes.

Vanhille and Campos-Pozuelo (2000) presented a numerical formulation for modeling standing acoustic waves of finite but moderate amplitudes. A thermoviscous fluid in a one-dimensional tube with rigid walls was studied. The fluid was initially at rest and was excited by an oscillating piston. A second-order wave equation for viscous and homogeneous fluids was used and perturbation method was employed. The numerical simulation was carried out by a multi-time-step, implicit, six-point finite-difference scheme of high order in the time domain. The procedure of computational code is shown in Figure 2.10. The particle displacement, pressure waveforms and pressure distributions were obtained.

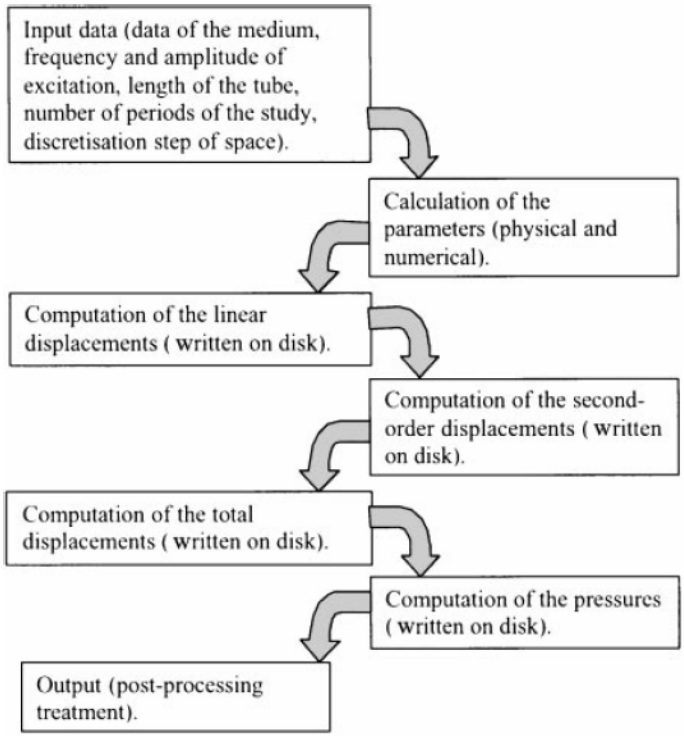

Figure 2.10 Procedure of computational code by Vanhille and Campos-Pozuelo (2000).

2.4 FEATURES OF RESONANCE IN SHAPED RESONATORS

The major features of nonlinear resonance in shaped resonators are reviewed in this section, including shock free pressure waveforms, high amplitude pressures, and frequency shift, etc.

2.4.1 SHOCK FREE PRESSURE WAVES

Figure 2.11 shows four axisymmetric resonators investigated by Chun and Kim (2000). For these tubes, the patterns of area change along the axis may be classified as follows:

(a) reference tube: uniform area, Figure 2.11(a);

(b) tube I: area increases only, Figure 2.11(b);

(c) tube II: area increases and converges, Figure 2.11(c);

(d) tube III: area increases, converges, and decreases, Figure 2.11(d).

The performance of each tube was evaluated under identical conditions. For this purpose, all tubes had the same length of 0.2m and volume of $4.765\times10^{-4}\,\mathrm{m}^3$. In addition, except the reference tube, the radius at $x=0$ was 0.005m for shaped resonator. These resonators are driven by an external oscillation force.

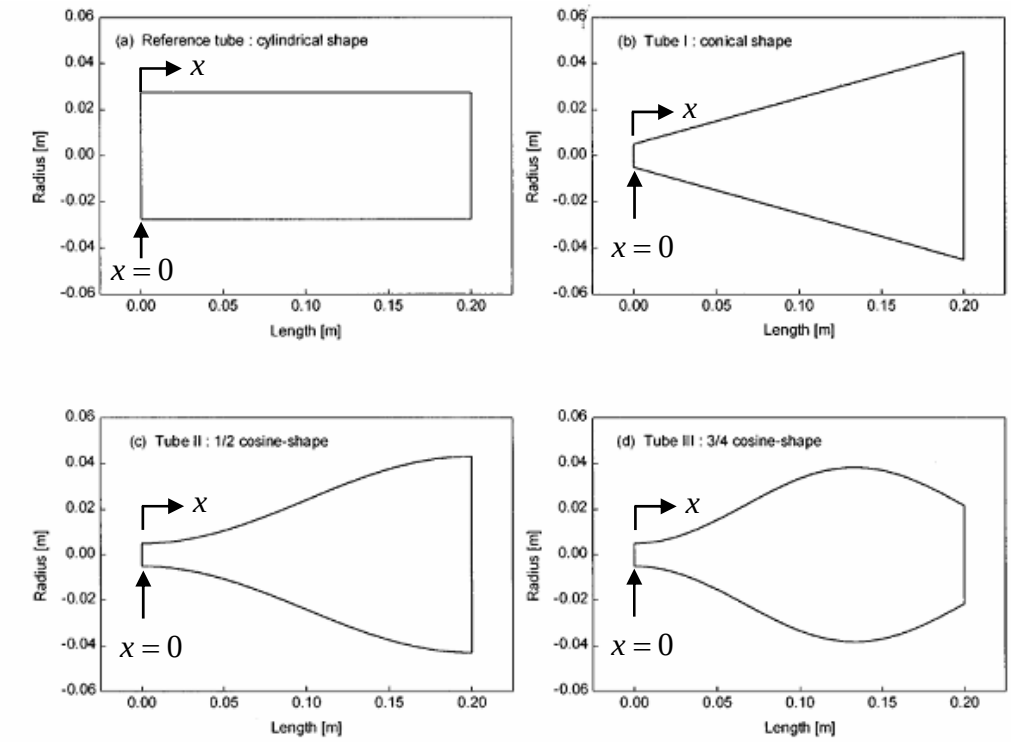

Figure 2.11 Interior geometry of resonators tested by Chun and Kim (2000): (a) reference tube (cylindrical shape), (b) tube I (conical shape), (c) tube II (1/2 cosine shape), and (d) tube III (3/4 cosine shape).

Figure 2.12 shows the pressure waves obtained at $x = 0$ of four resonators obtained by Chun and Kim (2000). For the cylindrical reference resonator, shock waves were obtained at acceleration amplitude of 100 m/s^2, as shown in Figure 2.12(a). In this case, the compression ratio, which is defined by the ratio of maximum pressure (point A) to minimum pressure (point B), was 1.081. In contrast to the cylindrical tube, the shaped resonators (tube I, II, III) can generate shock free pressure waves at even stronger driving with acceleration amplitude up to 300 m/s^2. Pressure waves at the small end ($x = 0$) of the conical shape tube are shown in Figure 2.12(b). The compression ratio for tube II is 3.1 at acceleration of 300 m/s^2. Pressure waves at the small end ($x = 0$) of the ½ cosine shape tube are shown in Figure 2.12(c). As the acceleration increases, waveforms show a broader peak and lower trough than the

results of tube I. Small ripples appear in the peak when acceleration is 300 m/s^2. Figure 2.12(d) shows the waveforms obtained at the small end ($x = 0$) of the ¾ cosine shape tube. It can be seen from Figure 2.12 that shock wave can be eliminated in shaped resonators at strong driving.

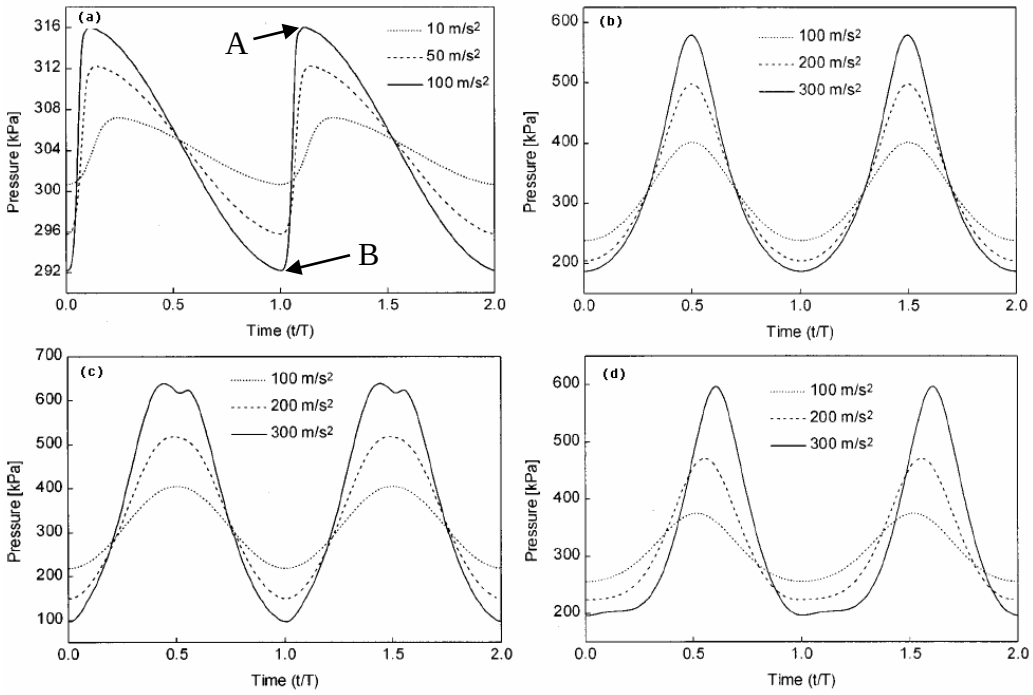

Figure 2.12 Pressure waves obtained at *x*=0 of four tube resonators tested by Chun and Kim (2000). (a) reference tube (cylindrical shape), (b) tube I (conical shape), (c) tube II (1/2 cosine shape), and (d) tube III (3/4 cosine shape).

2.4.2 HIGH AMPLITUDE PRESSURE WAVES

Since the shock waves are suppressed in the shaped resonators, the amplitude limit is removed, therefore the pressure amplitudes can be increased. Figure 2.13 shows high amplitude pressure waves measured at the small end of a horn-cone resonator by Lawrenson *et al.* (1998). The waveform is of quite high amplitude, and has multiple micro-shocks in the higher pressure regions. The peak pressure $p_{\max}$ is 1446 kPa and the minimum pressure $p_{\min}$ is 53.1 kPa in this case, so that the peak-to-peak

amplitude of the waveform is 1390 kPa. The pressure ratio in this case is $p_{\max} / p_{\min} = 27$.

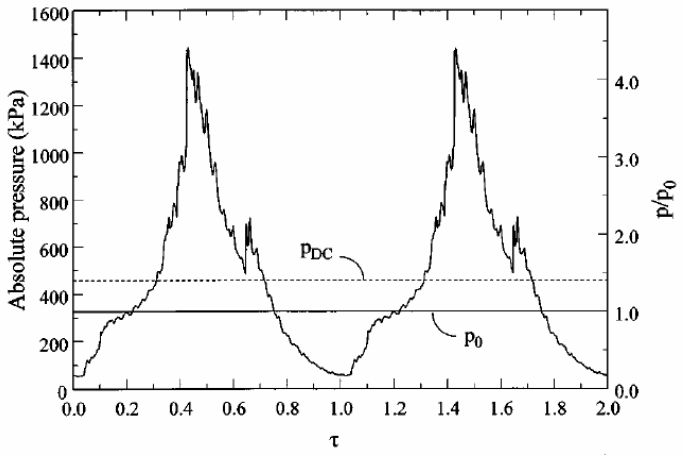

Figure 2.13 High amplitude pressure waves measured at small end of horn-cone resonator charged with R-134a (Lawrenson *et al.*, 1998).

The waveform measured at the small end of the horn-cone resonator was compared to a waveform measured at one end of the cylindrical resonator in Figure 2.14(a). The enlarged waveforms at one end of the cylindrical resonator are shown in Figure 2.14(b). The waveforms were measured for a power input of 41.7 W, and the static pressure p_0 inside the resonator was 311 kPa for the cylinder and 306 kPa for the horn-cone. It's clearly illustrated in Figure 2.14(a) that horn-cone resonator can generate much higher pressure waves than in the cylinder. A comparison of the total pressure amplitudes in these two resonators is shown in Table 2.2. The resonance frequencies were 808.3 Hz for the cylinder and 463.6 Hz for the horn-cone. The comparison of the waveforms for the cylinder and the horn-cone resonator shows changes that can be made in the resonance pressures by changing resonator geometry. For the same ''cost'' measured in watts, the horn-cone resonator gives much higher ''return'' in pressure amplitudes.

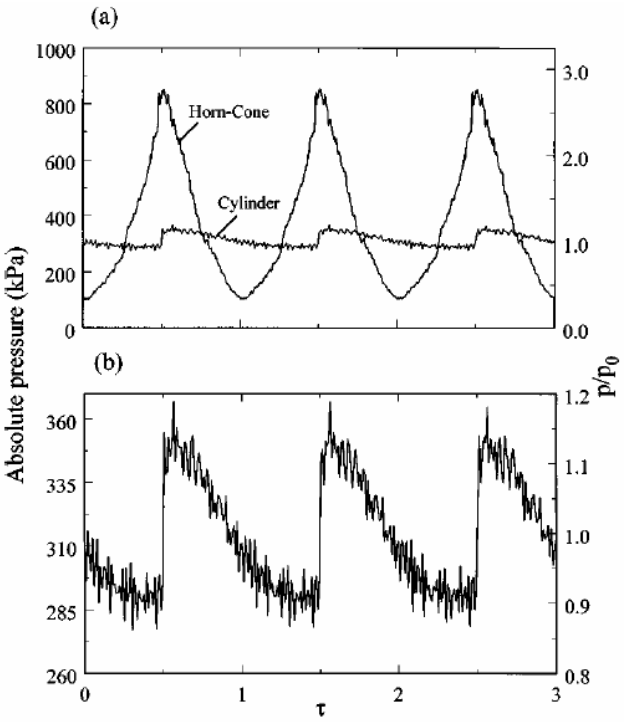

Figure 2.14 Waveforms at one end of cylinder and small end of horn-cone for 41.7 W of power input. Resonators were filled with R-134a (ambient pressure p_0=311 kPa for cylinder and 306 kPa for horn-cone. Lawrenson *et al.*, 1998).

Table 2.2 Comparison of performance for cylinder and horn-cone with 41.7W power delivery. Resonators were filled with R-134a.

Resonator	Power (W)	p_{max} (kPa)	p_{min} (kPa)	Pk-pk pressure (kPa)	$\frac{p_{max}}{p_{min}}$	p_0 (kPa)
Cylinder	41.7	360	264	95.2	1.36	311
Horn-cone	41.7	833	104	729	8.03	306

The peak-to-peak pressure amplitude is 95.2 kPa for the cylinder's waveform shown in Figure 2.14(b), and the pressure ratio is 1.36. For the same power input (41.7 W), the horn-cone resonator achieved a peak-to-peak pressure amplitude of 729 kPa, and the resulting pressure ratio was 8.03. Unlike the cylinder, the horn-cone resonator is well suited for use in compressor and pumping applications, because usefully high

pressures can be obtained for a reasonable amount of input power (Lawrenson *et al.*, 1998)

2.4.3 FREQUENCY SHIFT, HARDENING AND SOFTENING BEHAVIOUS

The fundamental resonance frequency of a shaped resonator is different from that of a cylindrical resonator with uniform cross sections, either higher or lower, depending on the geometric configuration and the driving strength.

Hamilton *et al.* (2001) investigated the frequency response of a nonlinear acoustical resonator analytically and numerically. They considered a resonator with a cross-sectional area S that may be expressed in the form

$$S(x) = S_0 + \delta S(x), \tag{2.13}$$

and

$$\frac{\delta S}{S_0} = \sum_{n=1}^{\infty} \left[a_n \cos(2n\pi x / l) + b_n \sin(2n\pi x / l) \right], \tag{2.14}$$

where x is the axial coordinate, l is resonator length, S_0 is a reference area, and δS is a small perturbation that varies slowly with x. Eq. (2.14) is the expansion of the shape perturbation in harmonics of the lowest spatial frequency component of the resonator, $2\pi / l$. The natural frequency of the uniform cylindrical resonator is given by

$$\omega_{0n} = n\pi c_0 / l, \qquad n = 1, 2, 3, \cdots. \tag{2.15}$$

By using perturbation theory, the natural frequency shift as a function of resonator shape was obtained

$$\frac{\delta\omega_n}{\omega_{0n}} = -\frac{a_n}{2}. \tag{2.16}$$

The study showed that each natural frequency can be shifted independently via appropriate spatial modulation of the resonator wall. The *n*th natural frequency of the resonator was affected only by the *n*th spatial frequency of the shape perturbation. Only the even (cosine) terms in the expansion of the shape perturbation would affect the natural frequencies. Odd spatial modulations (sine terms) had no effect on the natural frequencies.

The amplitude-frequency response curve and nonlinear resonance frequency shift for the fundamental mode at different driving strength are shown in Figure 2.15. Figure 2.15(a) and (b) demonstrate the hardening behaviors for resonator with cross-sectional area of $S = S_0 \exp[0.2\cos(2\pi x/l)]$ as the resonance frequencies are increased with the driving strength, while Figure 2.15(c) and (d) show the softening behavior for resonator with cross-sectional area of $S = S_0 \exp[-0.2\cos(2\pi x/l)]$, as the resonance frequencies are decreased with the driving. For a resonator driven at its lowest natural frequency, it was found that whether hardening or softening behavior occurred depended primarily on whether the nonlinearly generated second-harmonic frequency was greater or less than the second natural frequency of the resonator.

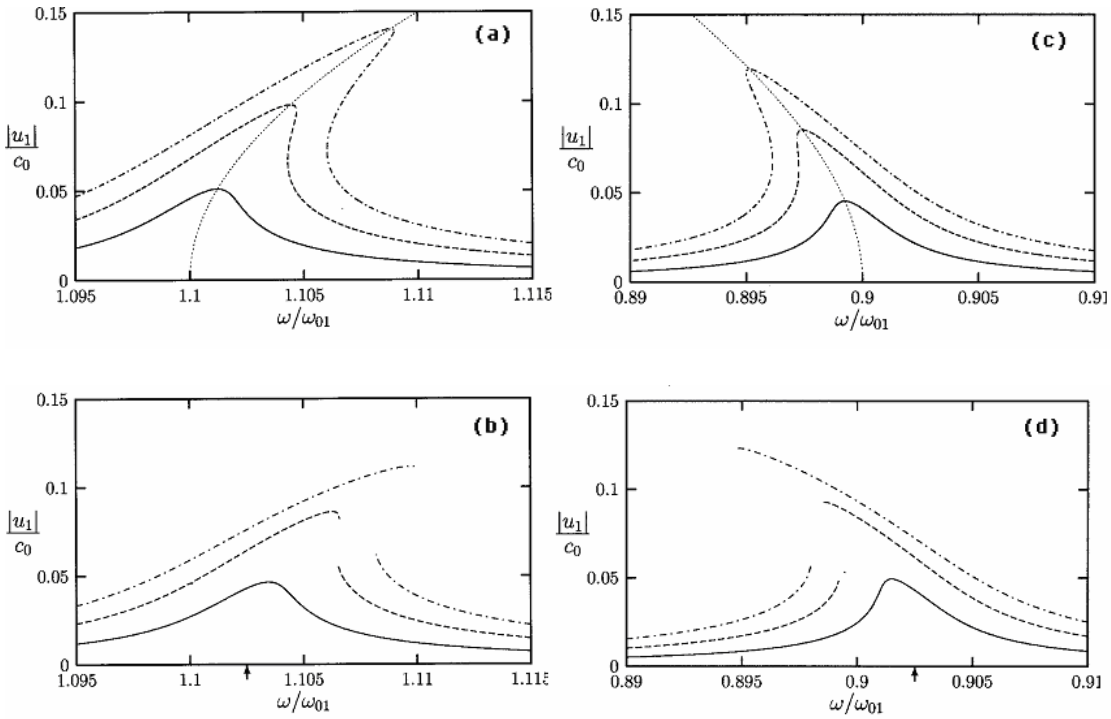

Figure 2.15 Analytical (a) (c) and numerical (b) (d) results for amplitude-frequency response curves by Hamilton (2001). (a) and (b) show a hardening behavior; (c) and (d) show a softening behavior. For the hardening behavior (a) and (b) the driving strength is 0.3×10^{-4} (solid lines), 0.6×10^{-4} (dashed lines) and 0.9×10^{-4} (dot-dash lines). For the softening behavior (c) and (d) the driving strength is 0.5×10^{-4} (solid lines), 1.0×10^{-4} (dashed lines) and 1.5×10^{-4} (dot-dash lines).

2.5 ACOUSTICAL QUALITY FACTOR

The quality factor or Q factor is a measure of the rate at which a vibration system dissipates its energy. A higher Q factor indicates a lower rate of energy dissipation. For example, a pendulum suspended from a high-quality bearing, oscillating in air, would have a high Q factor, while the same pendulum immersed in oil would have a low one. For very strong damping, Q factor < 1, the system is so strongly damped that it could not complete a single cycle of oscillation. The system resonance behavior depends strongly on Q factor.

There can be different ways to define the Q factor. For example, the Q factor may be defined as the number of oscillations required for a freely oscillating system's energy to fall off to $1/e^{2\pi}$, or about 1/535, of its original energy. The quality factor may also be calculated as 2π times the ratio of the energy stored divided by the energy lost per cycle. When a system is under excitation, the relationship of Q factor to the width of the resonance frenquency is given by

$$Q = \frac{f_0}{\Delta f}, \tag{2.17}$$

where f_0 is the resonance frequency, and $\Delta f = f_2 - f_1$ stands for the bandwidth, as shown in Figure 2.16.

For a single damped mass-spring system, the Q factor represents the effect of mechanical resistance, i.e.,

$$Q = \frac{\sqrt{MK}}{R}, \tag{2.18}$$

where M is the mass, K is the spring constant, and R is the mechanical resistance.

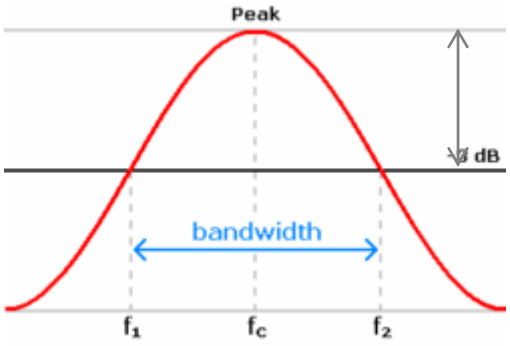

Figure 2.16 Definition of Q factor.

Moloney and Hatten (2001) measured the acoustical Q-factor for a set of cylindrical pipes having the same resonant frequency, but different diameters. The formula used by Moloney and Hatten to evaluate Q factor is given here,

$$Q = 2\pi \frac{\text{stored energy}}{\text{energy lost per cylce}} \tag{2.19}$$

The quality factor of a damped oscillator equals 2π times the ratio of stored energy to the energy dissipated per cycle. This makes Q-factor a sensitive probe of energy losses. The variation of Q-factor against diameter was well fitted with two parameters, one corresponded to energy loss via radiation from the ends of the pipe, and the other to thermal and viscous losses very close to the pipe wall. The wall loss parameter was quite constant no matter where the pipes were located, but the radiative loss parameter varied significantly with location inside a room, suggesting that room reflections affected the sound radiated from the pipe.

Biwa *et al*. (2005) measured the Q factor of a cylindrical acoustic resonator externally driven at the fundamental resonance frequency. The experimental apparatus is schematically shown in Figure 2.17. The acoustic resonator was made of a Pyrex glass cylinder with length $L = 1020mm$ and inner radius $r_0 = 10.5mm$. The working fluid was atmospheric air. One end of the resonator was closed by a rigid plate, and the other was connected to a compression driver. The constant-voltage signal from a synthesizer was sent through a power amplifier to the driver in the frequency range 135–165 Hz. The acoustic energy stored in the resonator and the power dissipated per unit time were evaluated through the simultaneous measurements of acoustic pressure and velocity, in order to determine the Q value of the resonator. The resulting Q value was 36. However, the Q value determined from a frequency response curve known as a conventional technique turned out to be 25, which was 30% less than that obtained by the energy loss method.

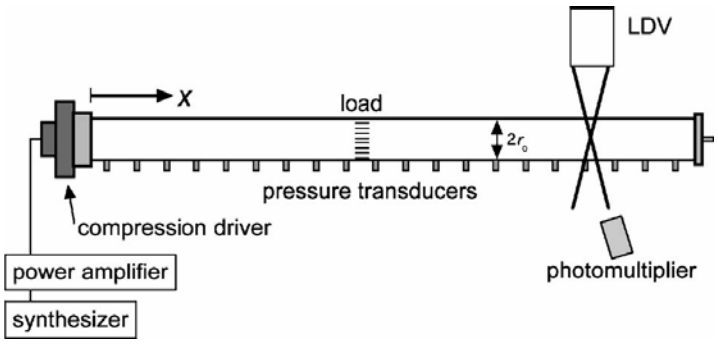

Figure 2.17 Schematic illustration of acoustic resonator (Biwa *et al*. 2005).

Ilinskii *et al*. (2001) studied the dependence of the energy loss and the quality factor respectively for cylindrical resonator, horn-cone, and bulb-type resonators. Figure 2.18(a) and (b) show the energy losses and the quality factor of the cylindrical resonator respectively for different acceleration amplitudes. The energy loss curves show the energy losses reach their maximum value at the resonance. The energy loss

increases with increasing levels of acceleration. The quality factor shows a similar but opposite behavior. It reaches a minimum value close to the resonance frequency. The quality factor decreases with increasing level of acceleration.

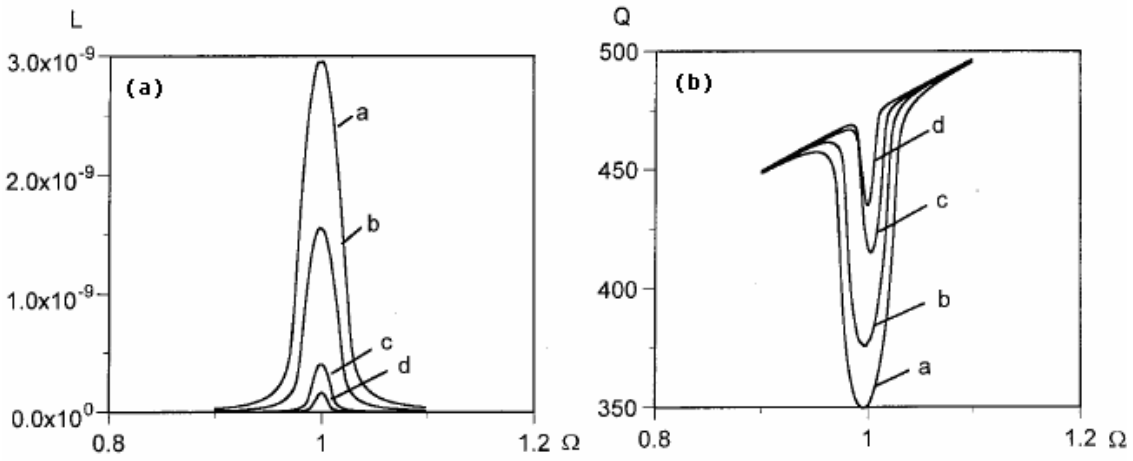

Figure 2.18 Dependence of energy losses (a) and the quality factor (b) on the frequency in the cylindrical resonator for different acceleration amplitudes: A=5×10^{-4} (curves a), A=3×10^{-4} (curves b), A=1×10^{-4} (curves c), A=0.5×10^{-4} (curves d), (Ilinskii *et al.*, 2001).

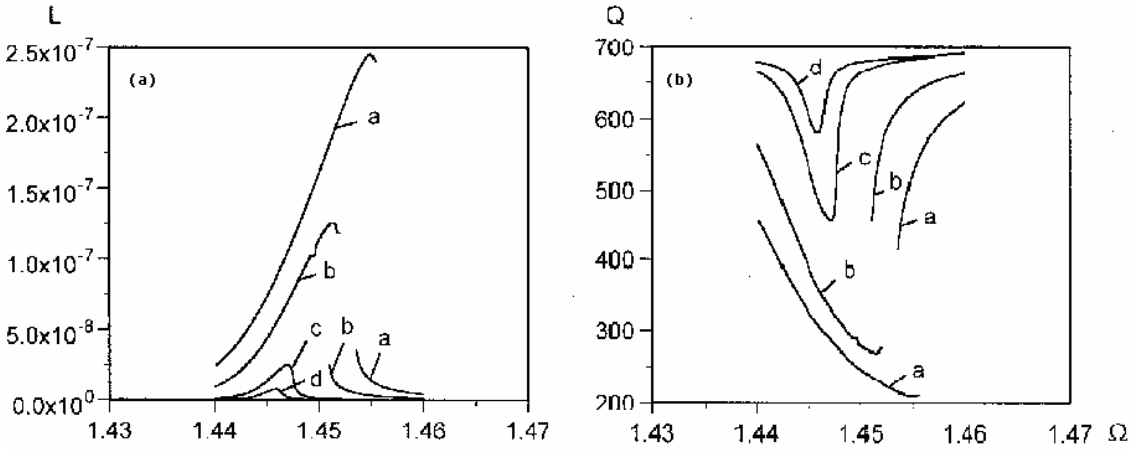

Figure 2.19 Dependence of energy losses (a) and the quality factor (b) on the frequency in the horn cone for different acceleration amplitudes: A=5×10^{-4} (curves a), A=3×10^{-4} (curves b), A=1×10^{-4} (curves c), A=0.5×10^{-4} (curves d), (Ilinskii *et al.*, 2001).

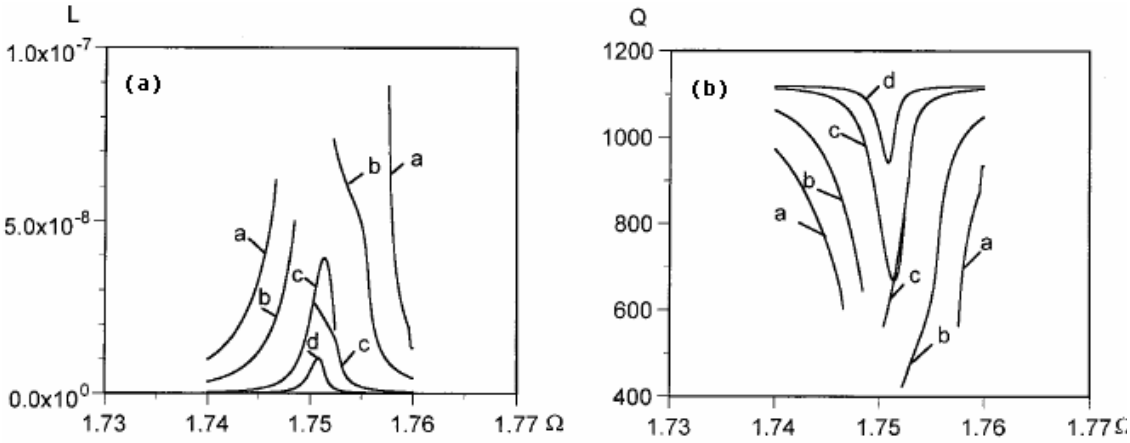

Figure 2.20 Dependence of energy losses (a) and the quality factor (b) on the frequency in the bulb-type resonator for different acceleration amplitudes: $A=5\times10^{-4}$ (curves a), $A=3\times10^{-4}$ (curves b), $A=1\times10^{-4}$ (curves c), $A=0.4\times10^{-4}$ (curves d), (Ilinskii *et al.*, 2001).

The energy losses and the quality factors for horn-cone and bulb-type resonators are shown in Figure 2.19 and Figure 2.20 respectively. In these cases, the energy losses increase with increasing levels of acceleration and shift to higher frequencies. The quality factors show a similar but opposite behavior. They decrease with increasing level of acceleration and shift to higher frequencies.

In additional, Breidenthal (2003 and 2006) studied dissipation caused by turbulence. It's found that exponential and super-exponential forcing of turbulent flow has a strong effect on the dissipation rate. It appears that for all canonical laboratory flows except Rayleigh-Taylor, acceleration reduces the turbulent dissipation in a self-similar way.

2.6 APPLICATION OF ACOUSTIC RESONATORS

2.6.1 ACOUSTICAL COMPRESSORS

Acoustic resonators have been used as gas compressors. Three types of acoustical compressors have been reported: (a) acoustical compressor designed by Lucas *et al.* (1999), (b) Boship's compressor (2000) and (c) piezoelectric acoustic compressor by Baz (2000). A simple representation of Lucas' compressor (Lucas *et al.*, 1999) is shown in Figure 2.21 (more details are given in section 2.3.2). A conventional reciprocating electro-mechanical actuator is used to oscillate a specially shaped chamber.

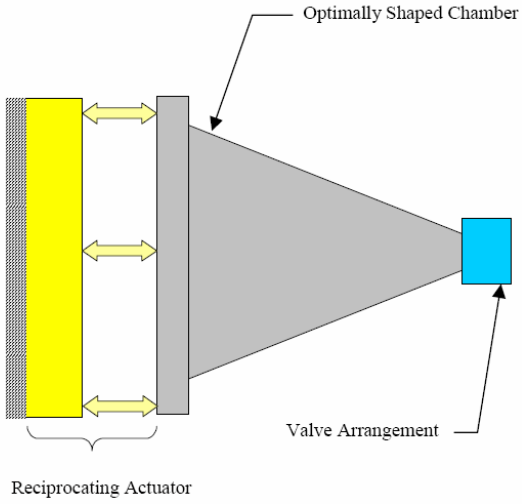

Figure 2.21 Acoustic compressor by Lucas *et al.* (1999).

Bishop (2000) filed a patent for acoustic compressors based on generating standing waves in a resonator. In Bishop's compressor which is sketched in Figure 2.22, a piezoelectric actuator was used to generate standing pressure waves in a cylindrical resonator. The standing waves generated by the actuator created negative and positive pressure during each acoustic cycle. The valves allowed the working fluid to be drawn into the resonator during the negative pressure portion of the cycle and delivered to the system during the positive pressure portion. The pressure developed in the

cylindrical resonator of Bishop's compressor was considerably less than the pressure that could be generated in a shaped resonator.

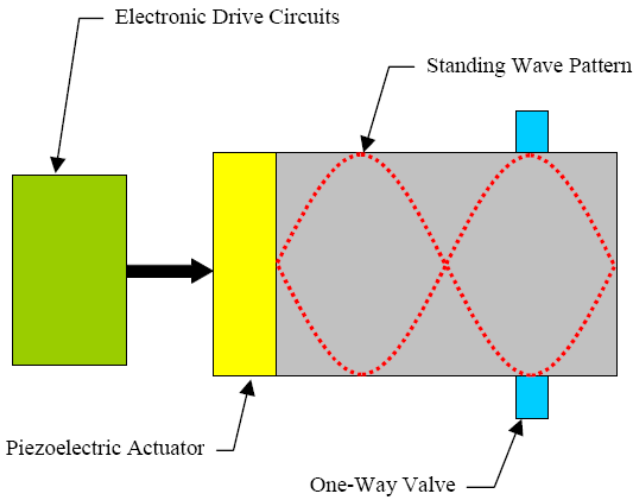

Figure 2.22 Standing wave compressor of Bishop (2000).

Baz (2000) created a new type of acoustical compressor consisting of a specially shaped resonator with the fluid driven directly by a piezoelectric actuator. Baz and Sabbagh (2006) presented a coupled nonlinear model for the piezoelectric resonators created by Baz (2000). The model was to describe the nonlinear interaction between the dynamics of the gas inside the resonator and the piezoelectric diaphragm, as shown in Figure 2.23 (a). A coupled-field model was used to predict the pressure profiles which were generated inside the resonator geometries shown in Figure 2.23 (b) ~ (e). This model was validated by both exact solutions for simple cavity configurations and published experimental results. It was found that the model could give accurate predictions over a broad range of excitation amplitudes and frequencies. This accuracy would allow the proposed model to be used as an effective design tool of piezoelectric acoustic resonators for a wide range of applications.

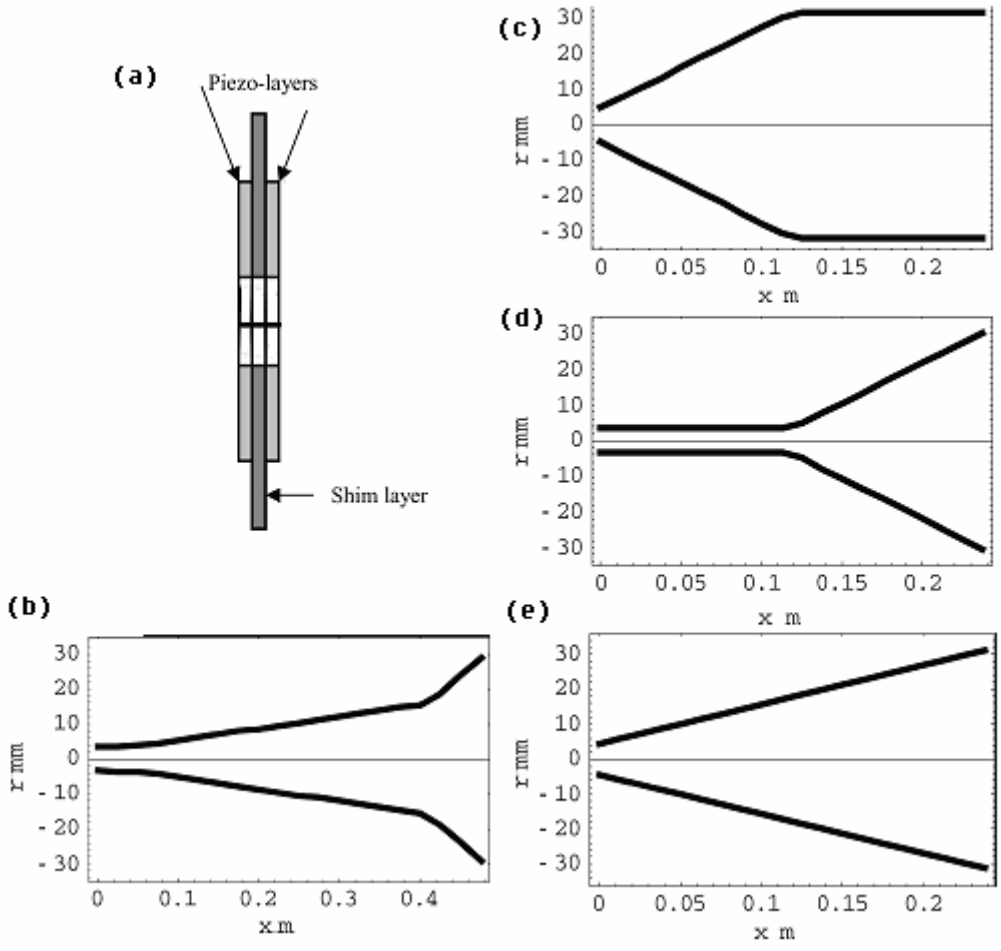

Figure 2.23 (a) Geometry of piezoelectric bimorph and (b) ~ (e) axisymmetric resonator profiles by Sabbagh and Baz (2006).

Dickens (2004) developed a one-dimensional, axisymmetric, linear finite element model describing a fluid interacting with a piezoelectric actuator. This system was used to generate finite amplitude standing waves in an acoustic resonator with rigid walls. His model included the effects of viscous and thermal damping of the fluid at the boundary of the resonator, and material damping in the piezoelectric actuator. Two types of piezoelectric actuators were considered, a stacked layer actuator, and a bending bimorph actuator. The resulting finite element equations were used to determine the optimum shape for the acoustic resonator that resulted in the maximum

pressures for the least input power. The optimal resonators (Figure 2.24) could generate ±19 psi at 1700 Hz for 50 watts of power using air as a working fluid and ±70 psi at 950 Hz for 42 watts of power using R-134A as a working fluid. The optimization results were verified against the commercial finite element code ANSYS and published experimental data.

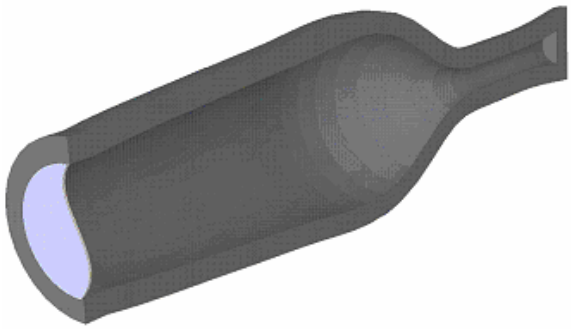

Figure 2.24 Cross section of optimized shape of a resonator in a linear model by Dicken (2004).

2.6.2 OTHER APPLICATIONS

Bash *et al*. (2002) introduced a unique thermal management architecture that employed vapor-compression refrigeration to cool multiple independently operating microprocessors in a small volume. The refrigeration system was driven by an acoustic compressor technology that had the virtues of, among other things, being highly variable, oil-less, and orientation independent, and thus was able to operate under significant variations in loading and deployment of electronics. The complete acoustic compressor (Figure 2.25) had three major components, 1) a resonator and valve hardware, 2) a motor and suspension hardware, and 3) a controller. A testbed was built to demonstrate the use of the technology to cool a prototype 5U server heat source temperature. Compressor efficiencies were found to be high at a loading equal

to or greater than 40% of the maximum capacity, while functionality was demonstrated down to 20% of maximum capacity.

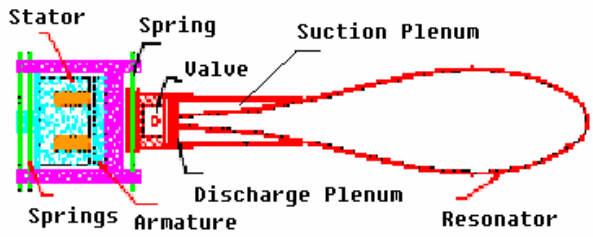

Figure 2.25 Acoustical compressor used for thermal management (Bash *et al.*, 2002).

Application of acoustic resonators even may be extended to nuclear engineering. Taleyarkhan and Lahey (2002) announced that they had produced thermonuclear fusion by imploding tiny deuterium-rich gas bubbles with sound waves and neutrons. Later, they presented detailed experiments and their planed to turn tabletop apparatus into a full-scale electricity-generating device (Taleyarkhan and Lahey, 2005). Thermonuclear fusion had held out the promise of cheap, clean, and virtually limitless energy.

2.7 OTHER METHODS IN NONLINEAR RESONANCE

2.7.1 DISPERSIVE RESONATORS

Instead of generating high amplitude pressures by changing the cross-section of a tube, Sugimoto *et al*. (2003) worked on another approach. They developed a weakly nonlinear theory for the air column in a tube with an array of Helmholz resonators. Later, Masuda *et al*. (2005) conducted an experiment to demonstrate the annihilation of shocks and generation of high-amplitude oscillations. The experimental setup is illustrated in Figure 2.26. The tube and resonators were designed to avoid higher harmonic resonances. One end of the tube was closed by a flat plate while the other end was connected to the drive unit. A rubber diaphragm sandwiched by a couple of circular plates was stretched to cover the whole cross section of the tube and clamped at its edge. Two stainless-steel plates were bolted together at the center to the axis of the linear motor. The bottom plate was driven by a linear motor whose motion was controlled by power supply.

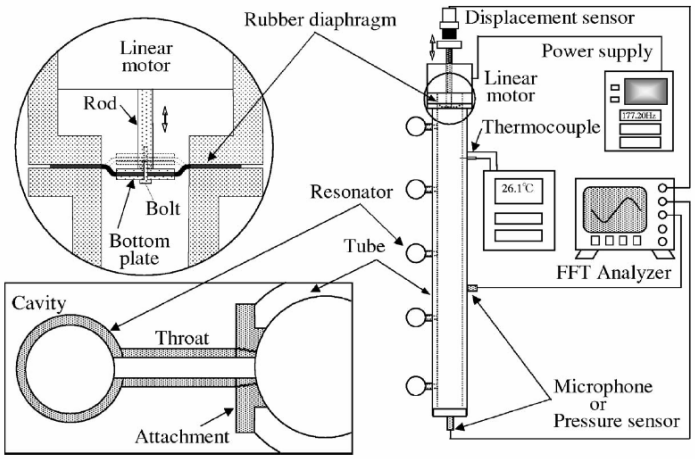

Figure 2.26 Experimental apparatus by Masuda *et al*. (2005).

Figure 2.27 shows the shock free pressure waves obtained in the tube with an array of Helmholz resonators. $\tilde{p}'$ denotes the excess pressure and p_0 is the equilibrium

pressure. The solid and broken lines represent the measured and analytical results, respectively. Higher harmonics were suppressed significantly. As a consequence, the pressure profile appeared to be nearly sinusoidal. The experimental results showed good agreement with the weakly nonlinear theory.

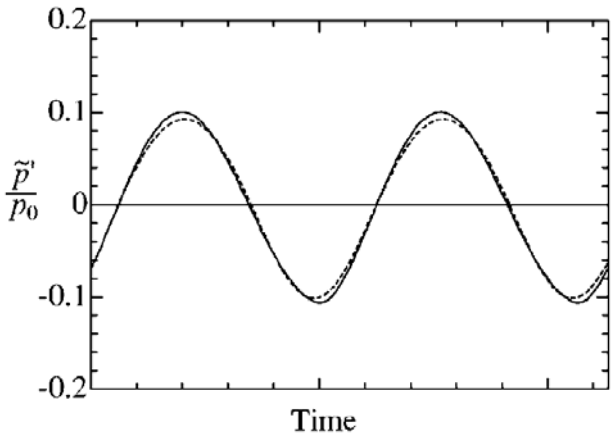

Figure 2.27 Shock free pressure waves at one end of the tube. $\tilde{p}'$ denotes the excess pressure and p_0 is the equilibrium pressure. The solid and broken lines represent the measured and analytical results, respectively (Masuda *et al.*, 2005).

2.7.2 ACTIVE CONTROL TECHNIQUE

Another approach to generate high amplitude pressure waves was proposed by Huang and Brisson (1997). They developed an active control approach to observe and control nonlinear effects for high-amplitude acoustic waves in a resonator. Figure 2.28 shows the schematic diagram for the control loop. The computer generated a multi-frequency control signal to the shaker system. Based on this input, the shaker physically shook the air-filled cavity to induce acoustic oscillations. A pressure gauge, mounted on the top of the acoustic cavity, measured the acoustic pressure oscillations inside the cavity. The output of this gauge was, in turn, fed to a lock-in amplifier and back to the

computer. An accelerometer was used to directly measure the accelerations imposed on the cavity by the shaker.

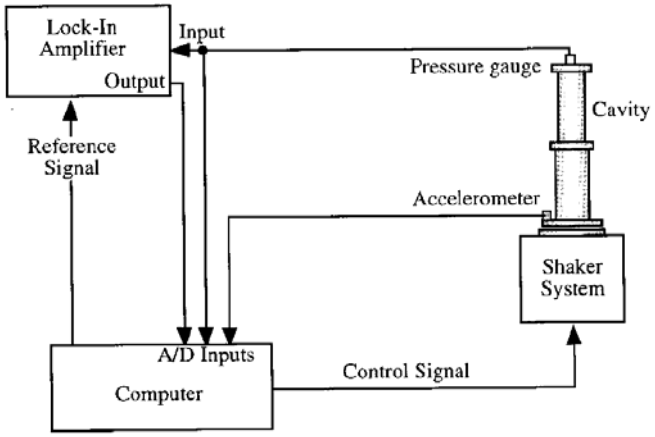

Figure 2.28 Experimental apparatus by Huang and Brisson (1997).

By suppressing nonlinear interactions between the fundamental and other modes, Huang and Brisson (1997) demonstrated the generation of high amplitude waves with minimal distortion (Figure 2.29). The overall pressure response to a single tone drive, shown in Figure 2.29(a) was clearly distorted. When a second drive tone was introduced to suppress the second mode response of the resonator, the pressure response of the resonator looked much more harmonic (Figure 2.29(c)). By further suppressing the third harmonics, response was nearly harmonic. Figure 2.29 (b), (d) and (e) show the spectrums of the pressure responses. It can be seen that the introduction of second and third drive tones effectively suppressed the energy transfer from the fundamental mode to the fourth and higher modes of the resonator. With the improvement of waveforms, the pressure amplitude of the fundamental mode also increased with the presence of the canceling drive tones.

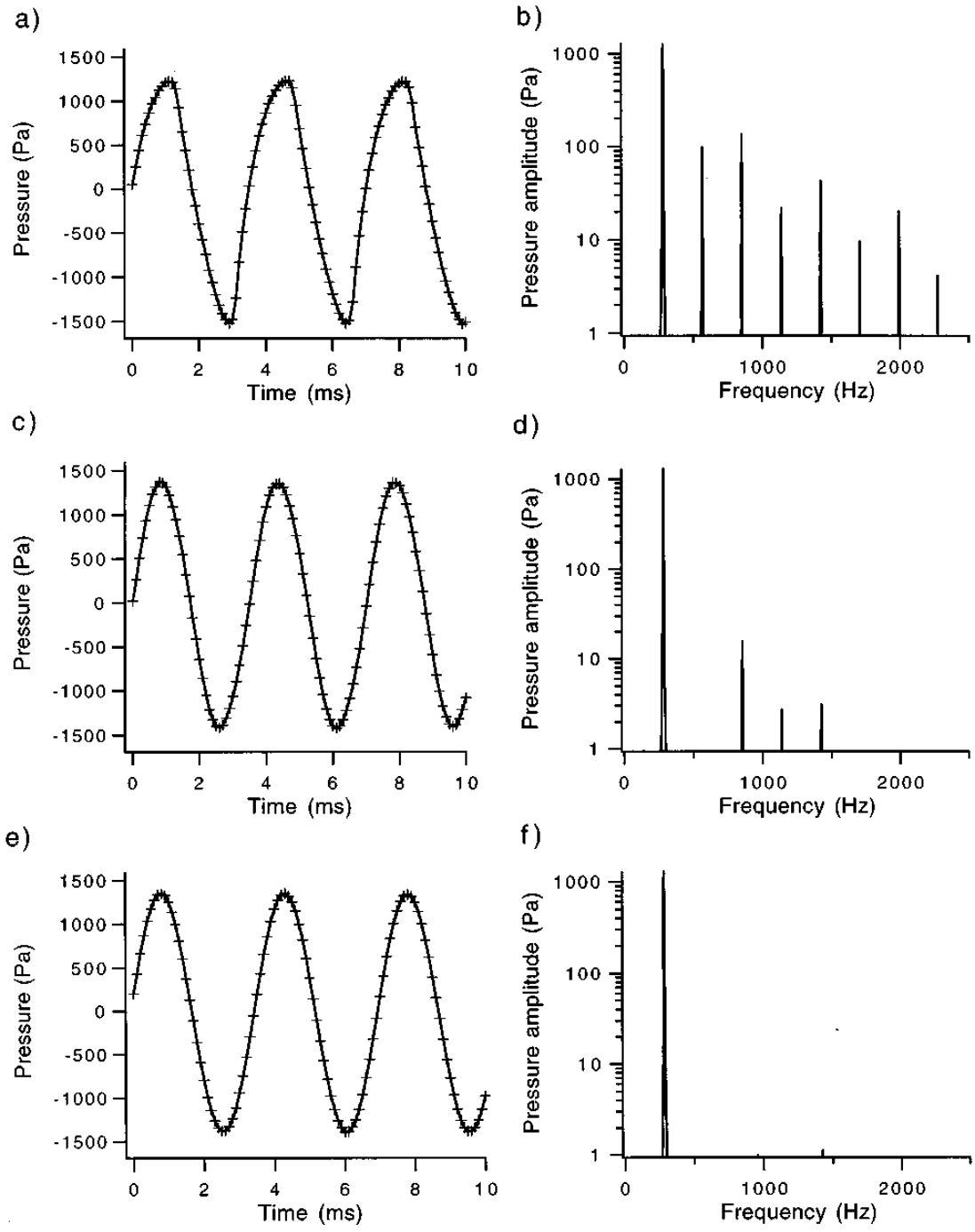

Figure 2.29 Nonlinear pressure response of active control (a) the experimental pressure versus time and (b) the amplitude spectrum at resonance with a single-frequency drive; (c) the experimental pressure versus time and (d) the amplitude spectrum at resonance with second harmonic suppressed; (e) the experimental pressure versus time and (f) the amplitude spectrum at resonance with both the second and third harmonics suppressed (Huang and Brisson, 1997).

2.8 SUMMARY

Fundamentals of acoustics in resonators with uniform and non-uniform cross section area have been reviewed. It can be seen that the pressure amplitudes in uniform resonators are much lower than that in non-uniform resonators. In order to create high amplitude pressure waves, resonators with non-uniform across sectional area are attracting more and more attentions by researchers. Many experimental and analytical works have been done in this area, including measurement of high amplitude acoustical waves, modeling of gas motion, study of frequency shifting, and investigation of energy losses *etc*. However, there are some other issues have not been discussed deeply yet. With the fast development of micro devices, resonators in small scales may have useful applications in microfluidic devices and issues associated with the size reduction need to be investigated, such as, the effect of reduction of resonator size on the nonlinear standing waves, energy losses in shaped resonators, and driving method suitable for miniature resonators, *etc*. These are discussed and presented in the following chapters.

CHAPTER 3

EFFECT OF RESONATOR DIMENSIONS ON NONLINEAR STANDING WAVES

3.1 INTRODUCTION

This chapter presents a study to evaluate effect of resonator size on resonance characteristics. This is achieved by including the dissipation associated with shear viscosity in the dynamic equations. The study has been conducted on two types of resonators, one is an axisymmetric resonator whose cross section area is exponentially expanded from one end to another. Another is a low aspect ratio rectangular duct whose transverse dimension is also exponentially expanded. Both resonators are sealed at their ends and shaken by an external force along their axial directions.

The one-dimensional model developed by Ilinskii *et al*. (1998) is used in the present study, with modification to take into account the shear viscous terms which were ignored previously. The dynamics equations for dimensionless velocity potentials are solved by the Galerkin's method, and the resonance pressures are computed. The effect of the resonator sizes are evaluated by calculating pressure waves forms, compression ratios and resonance frequency shift for resonators with various dimensions.

3.2 DISSIPATION TERMS

Viscosity is a fluid's internal resistance to flow and may be considered as a measure of fluid friction. All fluids, i.e., all liquids and gases, exhibit viscosity to some degrees. As shown in Figure 3.1, layers in the flow move at different velocities and the fluid viscosity arises from the shear stress between the layers.

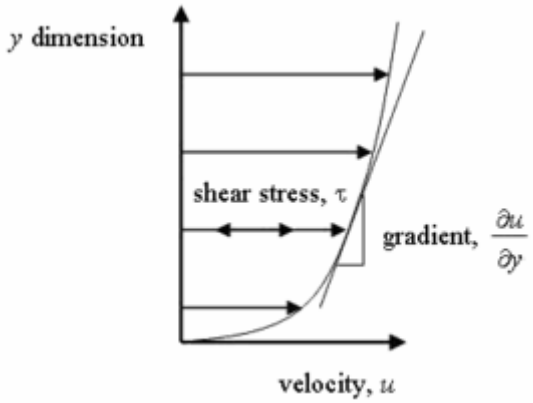

Figure 3.1 Viscosity in fluid.

It has been postulated that, for a straight, parallel and uniform flow, the shear stress, τ, between layers is proportional to the velocity gradient, $\partial u / \partial y$, in the direction perpendicular to the layers. The shear stress τ may be calculated by

$$\tau = \eta \frac{\partial u}{\partial y}. \tag{3.1}$$

Here, u is flow velocity, η is the coefficient of shear viscosity, or the dynamic viscosity. Most gases satisfy Newton's criterion and are known as Newtonian fluids. In general, the dissipation terms in the momentum equations for a velocity component, denoted by i, can be presented in a form (Landau and Lishitz, 1987),

$$\eta\frac{\partial^2 u_i}{\partial x_k \partial x_k}+\left(\zeta+\frac{1}{3}\eta\right)\frac{\partial^2 u_k}{\partial x_i \partial x_k}=\eta\left(\nabla^2\mathbf{u}\right)_i+\left(\zeta+\frac{1}{3}\eta\right)\left[\nabla\left(\nabla\cdot\mathbf{u}\right)\right]_i$$
$$=\eta\left\{\left(\nabla^2\mathbf{u}\right)_i-\left[\nabla\left(\nabla\cdot\mathbf{u}\right)\right]_i\right\}+\left(\zeta+\frac{4}{3}\eta\right)\left[\nabla\left(\nabla\cdot\mathbf{u}\right)\right]_i, \tag{3.2}$$

where $\mathbf{u}$ is velocity vector and ζ is coefficient of bulk viscosity or the second viscosity coefficient. The first term on the right hand side of Eq. (3.2) is the dissipation associated with the shear viscosity, and the second term is associated with the bulk viscosity.

3.2.1 DISSIPATION IN CYLINDRICAL TUBES

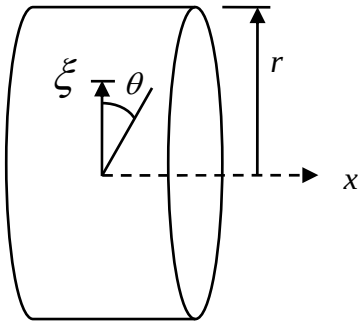

Figure 3.2 Tube with cylindrical coordinates.

Figure 3.2 shows a tube with a circular cross section of radius r. The cylindrical coordinate in the axial direction is denoted by x and the coordinate in the radius direction is denoted by ξ. For the x velocity component, u, the first term on the right hand side of Eq. (3.2) becomes

$$\eta\left\{\left(\nabla^2\mathbf{u}\right)_i-\left[\nabla\left(\nabla\cdot\mathbf{u}\right)\right]_i\right\}=\eta\frac{1}{\xi}\frac{\partial}{\partial\xi}\left(\xi\frac{\partial u}{\partial\xi}\right). \tag{3.3}$$

Eq. (3.3) is induced by the shear motion of the velocity and is referred to as the shear viscosity term. Since the flow velocity in the one-dimensional model by Ilinskii *et al*. (1998) is the average velocity over the cross section of the resonator, the following calculation is to derive the shear viscosity term in terms of the average velocity in the axial direction.

We consider a tube with a circular cross section of radius r, shown in Figure 3.2, the linear momentum equation including the shear viscosity is

$$\rho\frac{\partial u}{\partial t}=-\frac{\partial p}{\partial x}+\eta\frac{1}{\xi}\frac{\partial}{\partial\xi}\left(\xi\frac{\partial u}{\partial\xi}\right), \tag{3.4}$$

where $u=u(x,\xi,t)$ is axial velocity, $p=p(x,t)$ is acoustic pressure. By setting $u=v(x,\xi)e^{i\omega t}$, $\partial p/\partial x=p_x e^{i\omega t}$ (the real part will be taken from the results) and substituting them into equation (3.4), one obtains

$$\frac{\partial^2 v}{\partial\xi^2}+\frac{1}{\xi}\frac{\partial v}{\partial\xi}+\beta^2 v=\frac{p_x}{\eta}, \tag{3.5}$$

where $\beta^2=-\dfrac{i\rho\omega}{\eta}$, and $\beta=(1-i)\sqrt{\dfrac{\rho\omega}{2\eta}}$. The solution of equation (3.5) for $v(x,\xi)$, subject to boundary condition $v\big|_{\xi=r}=0$ and v being finite at $\xi=0$, is

$$v=\frac{p_x}{\eta\beta^2}\left[1-\frac{J_0(\beta\xi)}{J_0(\beta r)}\right],\quad \text{or,}\quad u=ve^{i\omega t}=U(x,t)\left[1-\frac{J_0(\beta\xi)}{J_0(\beta r)}\right], \tag{3.6}$$

where, $U(x,t)=p_x e^{i\omega t}/\eta\beta^2$, J_0 is the Bessel function of zeroth order. The average of u over the cross section of the tube is

$$\bar{u} = \frac{U(x,t)}{\pi r^2}\int_0^r 2\pi\xi\left[1-\frac{J_0(\beta\xi)}{J_0(\beta r)}\right]d\xi = U(x,t)\left[1-\frac{2J_1(\beta r)}{\beta r J_0(\beta r)}\right], \tag{3.7}$$

where J_1 is the Bessel function of the first order. Using the velocity profile (3.6), the shear viscosity term in the momentum equation can be evaluated as

$$\eta\frac{1}{\xi}\frac{\partial}{\partial\xi}\left(\xi\frac{\partial u}{\partial\xi}\right) = U(x,t)\frac{\eta\beta^2}{J_0(\beta r)}J_0(\beta\xi)\,. \tag{3.8}$$

The average of the shear viscosity term (3.8) over the tube cross section is

$$\begin{aligned}\overline{\eta\frac{1}{\xi}\frac{\partial}{\partial r}\left(\xi\frac{\partial u}{\partial\xi}\right)} &= U(x,t)\frac{\eta\beta^2}{J_0(\beta r)}\frac{1}{\pi r^2}\int_0^r 2\pi\xi J_0(\beta\xi)d\xi \\ &= U(x,t)\frac{2\eta\beta}{r}\frac{J_1(\beta r)}{J_0(\beta r)} = \frac{2\eta\beta}{r}\frac{J_1(\beta r)}{J_0(\beta r)}\left[1-\frac{2J_1(\beta r)}{(\beta r)J_0(\beta r)}\right]^{-1}\bar{u}\,,\end{aligned} \tag{3.9}$$

in which, Eq. (3.7) has been used to eliminate $U(x,t)$ and $\bar{u}$ is average velocity.

The value $|\beta r|$ in Eq. (3.9) can be estimated by taking η in order of 10^{-5} for air, ω in order of 10^3 (assuming the oscillation frequency to be 500Hz), so that

$$|\beta r| \sim r\sqrt{\rho\omega/\eta} \sim r\times 10^4\,. \tag{3.10}$$

Since the radius r is always larger than 10^{-3} m in the present study, therefore we have,

$$|\beta r| \gg 1\,. \tag{3.11}$$

It can be shown (Abramowitz and Stegun, 1972) that for $|\beta r| \gg 1$, $J_1(\beta r)/J_0(\beta r) \to -i$, so that,

$$\overline{\eta \frac{1}{\xi}\frac{\partial}{\partial r}\left(\xi \frac{\partial u}{\partial \xi}\right)} \xrightarrow{|\beta r|\gg 1} \frac{2\eta\beta}{r}(-i)\left[1+\frac{2i}{(\beta r)}\right]^{-1}\bar{u} \simeq (-1-i)\frac{\sqrt{2\eta\rho\omega}}{r}\bar{u}. \tag{3.12}$$

By taking the real part in Eq. (3.12), we have

$$\overline{\eta \frac{1}{\xi}\frac{\partial}{\partial r}\left(\xi \frac{\partial u}{\partial \xi}\right)} \xrightarrow{|\beta r|\gg 1} -\frac{\sqrt{2\eta\rho\omega}}{r}\bar{u}. \tag{3.13}$$

This is the shear viscous term for one-dimensional acoustic waves in a tube with circular cross section. It can be seen from Eq. (3.13) that the shear viscosity term takes into account the effect of frequency ω and tube radius r. The dissipation increases as ω increases and r decreases.

Let i in Eq. (3.2) be the x component of the velocity vector $\mathbf{u}$, the second term on the right hand side becomes

$$\left(\zeta+\frac{4}{3}\eta\right)\left[\nabla(\nabla\cdot\mathbf{u})\right]_i = \left(\zeta+\frac{4}{3}\eta\right)\frac{\partial}{\partial x}(\nabla\cdot\mathbf{u}). \tag{3.14}$$

By taking average velocity in an axisymmetric tube for $\nabla\cdot\mathbf{u}$, one obtains the dissipation term associated with the volume expansion of the gas, which was derived by Ilinskii *et al.* (1998),

$$(\zeta + 4\eta/3)\frac{\partial}{\partial x}\left(\frac{1}{r^2}\frac{\partial}{\partial x}(r^2\bar{u})\right). \tag{3.15}$$

This is named bulk viscosity in the present study.

3.2.2 DISSIPATION IN A LOW ASPECT RATIO RECTANGULAR DUCT

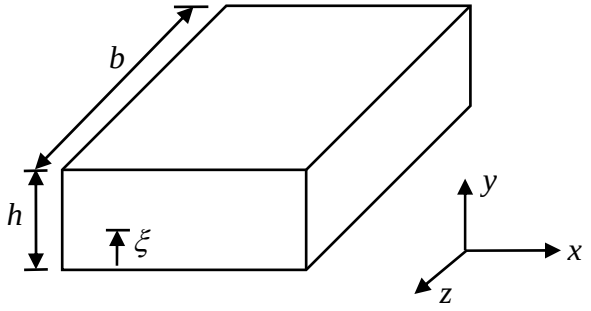

Figure 3.3 Rectangular duct with Cartesian coordinates.

Figure 3.3 show a duct with a low aspect ratio rectangular cross-section. The duct height is h and the width is b ($h \ll b$). For this duct, Eqs. (3.3), (3.4) and (3.5) become

$$\eta\left\{\left(\nabla^2\mathbf{u}\right)_i - \left[\nabla\left(\nabla\cdot\mathbf{u}\right)\right]_i\right\} = \eta\frac{\partial^2 u}{\partial\xi^2}, \tag{3.16}$$

$$\rho\frac{\partial u}{\partial t} = -\frac{\partial p}{\partial x} + \eta\frac{\partial^2 u}{\partial\xi^2}, \tag{3.17}$$

$$\frac{\partial^2 v}{\partial\xi^2} - \beta^2 v = \frac{p_x}{\eta}, \tag{3.18}$$

where, $\beta^2 = \frac{i\rho\omega}{\eta}$ and $\beta = (1+i)\sqrt{\frac{\rho\omega}{2\eta}}$. The velocity u obtained from the solution of equation (3.18), subject to boundary condition $v|_{\xi=h} = v|_{\xi=0} = 0$, is

$$u = ve^{i\omega t} = U(x,t)\left\{\cosh(\beta y) - 1 - \frac{\cosh(\beta h) - 1}{\sinh(\beta h)}\sinh(\beta y)\right\}, \tag{3.19}$$

where, $U(x,t) = p_x e^{i\omega t} \big/ \eta\beta^2$. The average of u over the duct height is

$$\bar{u} = \frac{U(x,t)}{\beta h}\left\{\sinh(\beta h) - \beta h - \frac{\left[\cosh(\beta h) - 1\right]^2}{\sinh(\beta h)}\right\}. \tag{3.20}$$

The average of shear stress $\eta\overline{\partial^2 u / \partial\xi^2}$ can be worked out based on Eq. (3.19). By following the same procedure for the tube with circular cross section, it gives

$$\overline{\eta\frac{\partial^2 u}{\partial\xi^2}} \xrightarrow{|\beta h| \gg 1} -\frac{\sqrt{2\eta\rho\omega}}{h}\bar{u}. \tag{3.21}$$

By taking average velocity in a low aspect ratio rectangular tube for $\nabla\cdot\mathbf{u}$, the bulk viscosity is

$$(\zeta + 4\eta/3)\frac{\partial}{\partial x}\left(\frac{1}{b}\frac{\partial}{\partial x}(b\bar{u})\right). \tag{3.22}$$

Equations (3.13), (3.15), (3.21) and (3.22) are included in the one-dimensional momentum equations, which are presented in next section.

3.3 GOVERNING EQUATIONS

The governing equations derived in this chapter are based on the model developed by Ilinskii *et al*. (1998). The difference between the present model and Ilinskii's is the way handling dissipation terms in the momentum equation. In the present model, the shear viscosity is considered which is shown later to be the major mechanism of energy loss. Another difference is that real gas properties are used in the present study to calculate the viscosity coefficients instead of a calibration value with experimental results (Ilinskii *et al*., 1998). The governing equation for gas motion in a closed resonator is derived from three basic equations: (1) equation of state, which relates the internal forces of the fluid to the deformation of the fluid, (2) equation of mass conservation, and (3) equation of momentum conservation. By defining a velocity potential, Ilinskii *et al*. (1998) derived the momentum equation in terms of velocity potential. With integration and differentiation preformed on the momentum equation, the pressure and density variables were eliminated using the state equation and mass conservation equation. Finally, a nonlinear equation in terms of velocity potential was obtained to describe the nonlinear standing waves in axisymmetric resonators.

The present study includes both axisymmetric and low aspect ratio rectangular resonators.

3.3.1 EQUATION FOR AXISYMMETRIC RESONATORS

The one-dimensional acoustic wave field in a resonator of arbitrary axisymmetric shape is considered here. The resonator is closed at both ends and oscillating along its axis, which is driven by a shaker.

Equation of state

The equation of state for a perfect gas is

$$p = \rho R_{const} T \,, \tag{3.23}$$

where p is the total pressure in Pascal, ρ is the density (kg/m^3) and T is the absolute temperature in Kelvin. The quantity R_{const} is a constant whose value depends on the particular gas involved.

It is found experimentally that acoustic processes are nearly adiabatic (Morse, 1968), and exchange of thermal energy from one particle of fluid to another is insignificant. The heat conduction during a cycle of the acoustic disturbance becomes negligible under these conditions, the entropy (and not the temperature) of the fluid remains nearly constant. The behavior of perfect gas is described by the adiabatic equation of state,

$$p = \left(\frac{\rho}{\rho_0} \right)^{\gamma} p_0 \,, \tag{3.24}$$

where $\gamma = \dfrac{C_p}{C_v}$ is the ratio of specific heats. This means that the thermal conductivity of the fluid and the temperature gradients of the disturbance must be so small that no significant thermal flux occurs during the time of disturbance.

Equation of mass conservation for axisymmetric resonator

Figure 3.4 shows the axisymmetric resonator whose cross-section area is expanded in x-direction. The radius r is a function of x. The axial velocity along the x-direction

is $u = u(x, \xi, t)$, depending on x, t, and the radial location ξ. The velocity is not uniform over the cross section of the resonator, especially $u(x, \xi, t) = 0$ on the wall of the resonator.

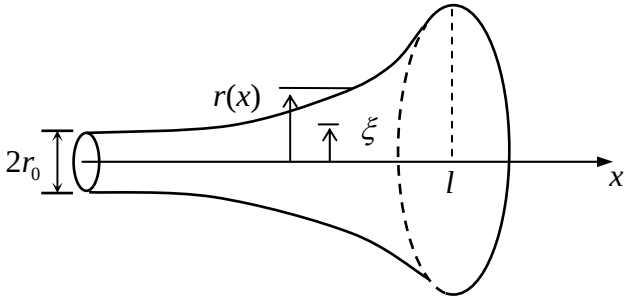

Figure 3.4 Axisymmetric resonator, exponentially expanded.

The average velocity of u over the cross section can be calculated by

$$\bar{u}(x,t) = \frac{1}{\pi r^2} \int_0^r 2\pi u(x,\xi,t)\xi d\xi \,, \tag{3.25}$$

and the mass flux through the cross section is

$$F = \int_0^r 2\pi\rho u(x,\xi,t)\xi d\xi = \rho\bar{u}\pi r^2 \,. \tag{3.26}$$

With the hypothesis of continuous medium, the net influx must equal the rate of increase, so that,

$$\frac{\partial M}{\partial t} + \frac{\partial F}{\partial x} = 0 \,. \tag{3.27}$$

Here, notation M is introduced as the mass per unit length,

$$M = \rho \pi r^2 \,. \tag{3.28}$$

By substituting Eqs. (3.26) and (3.28) into Eq. (3.27), the mass conservation equation for the gas in the axisymmetric resonator is obtained as:

$$\frac{\partial \rho}{\partial t}+\frac{1}{r^2}\frac{\partial}{\partial x}\left(r^2\rho\bar{u}\right)=0\,. \tag{3.29}$$

Equation of momentum conservation for axisymmetric resonator

Using the shear viscous term of Eq. (3.13) and bulk viscous term of Eq. (3.15) obtained previously, the one-dimensional momentum equation is written as

$$\frac{\partial \bar{u}}{\partial t}+\bar{u}\frac{\partial \bar{u}}{\partial x}=-\frac{1}{\rho}\frac{\partial p}{\partial x}-a(t)+\frac{(\zeta+4\eta/3)}{\rho}\frac{\partial}{\partial x}\left(\frac{1}{r^2}\frac{\partial}{\partial x}(r^2\bar{u})\right)-\frac{\sqrt{2\rho_0\eta\omega}}{r\rho}\cdot\bar{u}\,. \tag{3.30}$$

Here, p is the pressure, $a(t)$ is the acceleration of the resonator, and ζ and η are coefficients of viscosity. Above equations are all written in the coordinate system moving with the resonator body, so that the shaking of the resonator is converted to an external force applied on the fluid inside the resonator.

By introducing the velocity potential φ,

$$\bar{u}=\frac{\partial \varphi}{\partial x}\,, \tag{3.31}$$

Equation (3.30) written in terms of the velocity potential φ takes the form

$$\frac{\partial^2 \varphi}{\partial t \partial x} + \frac{1}{2}\frac{\partial}{\partial x}\left(\frac{\partial \varphi}{\partial x}\right)^2 = -\frac{1}{\rho}\frac{\partial p}{\partial x} - a(t) + \frac{(\zeta + 4\eta/3)}{\rho}\frac{\partial}{\partial x}\left(\frac{1}{r^2}\frac{\partial}{\partial x}(r^2 \frac{\partial \varphi}{\partial x})\right) - \sqrt{\frac{2\eta\omega}{r^2\rho}}\frac{\partial \varphi}{\partial x}. \tag{3.32}$$

After substituting p from Eq. (3.24) into Eq. (3.32) and integrating with respect to x, one obtains

$$\frac{\partial \varphi}{\partial t} + \frac{1}{2}\left(\frac{\partial \varphi}{\partial x}\right)^2 = -\frac{\gamma p_0}{(\gamma - 1)\rho_0^{\gamma}}\rho^{(\gamma-1)} - a(t)x + \frac{\delta}{r^2}\frac{\partial}{\partial x}\left(r^2 \frac{\partial \varphi}{\partial x}\right) - \sqrt{\frac{2\eta\omega}{r^2\rho}}\varphi + \phi(t), \tag{3.33}$$

where

$$\delta = \frac{(\zeta + 4\eta/3)}{\rho_0}. \tag{3.34}$$

The replacement of ρ by ρ_0 in the dissipative term means that the nonlinear terms associated with dissipation are ignored.

In equation (3.33), $\phi(t)$ is an arbitrary function of time and Ilinskii *et al.* (1998) suggested $\phi(t)$ to have a following form

$$\phi(t) = \frac{c_0^{\,2}}{\gamma - 1}, \tag{3.35}$$

where c_0 is the small signal propagation speed. The sound propagation speed c is of the form

$$c^2 = \frac{dp}{d\rho} = \frac{\gamma p_0}{\rho_0^{\gamma}} \rho^{(\gamma-1)} = \frac{\gamma p_0}{\rho_0} \left(\frac{\rho}{\rho_0} \right)^{\gamma-1} = c_0^{\,2} \left(\frac{\rho}{\rho_0} \right)^{\gamma-1}. \tag{3.36}$$

Equation (3.33) then takes the form

$$\frac{\partial \varphi}{\partial t} + \frac{1}{2} \left(\frac{\partial \varphi}{\partial x} \right)^2 = -\frac{c^2 - c_0^{\,2}}{\gamma - 1} - a(t)x + \frac{\delta}{r^2} \frac{\partial}{\partial x} \left(r^2 \frac{\partial \varphi}{\partial x} \right) - \sqrt{\frac{2\eta\omega}{r^2 \rho}} \varphi . \tag{3.37}$$

Differentiation of Eq. (3.37) with respect to t gives

$$\begin{aligned} \frac{\partial^2 \varphi}{\partial t^2} + \frac{1}{2} \frac{\partial}{\partial t} \left(\frac{\partial \varphi}{\partial x} \right)^2 &= -\frac{\gamma p_0}{\rho_0^{\gamma}} \rho^{(\gamma-2)} \frac{\partial \rho}{\partial t} \\ &\quad - \frac{da}{dt} x + \frac{\delta}{r^2} \frac{\partial^2}{\partial t \partial x} \left(r^2 \frac{\partial \varphi}{\partial x} \right) - \sqrt{\frac{2\eta\omega}{r^2 \rho}} \frac{\partial \varphi}{\partial t}. \end{aligned} \tag{3.38}$$

The derivative of $\partial\rho/\partial t$ can be eliminated from Eq. (3.38) by using Eq. (3.29) in the form

$$\frac{\partial \rho}{\partial t} = -\frac{1}{r^2} \frac{\partial}{\partial x} \left(r^2 \rho \frac{\partial \varphi}{\partial x} \right) = -\frac{\partial \rho}{\partial x} \frac{\partial \varphi}{\partial x} - \frac{\rho}{r^2} \frac{\partial}{\partial x} \left(r^2 \frac{\partial \varphi}{\partial x} \right). \tag{3.39}$$

Substitution of $\partial\rho/\partial t$ in Eq. (3.39) into Eq. (3.38) yields

$$\begin{aligned} \frac{\partial^2 \varphi}{\partial t^2} + \frac{1}{2} \frac{\partial}{\partial t} \left(\frac{\partial \varphi}{\partial x} \right)^2 &= \frac{\gamma p_0}{\rho_0^{\gamma}} \rho^{(\gamma-2)} \left[\frac{\partial \rho}{\partial x} \frac{\partial \varphi}{\partial x} + \frac{\rho}{r^2} \frac{\partial}{\partial x} \left(r^2 \frac{\partial \varphi}{\partial x} \right) \right] \\ &\quad - \frac{da}{dt} x + \frac{\delta}{r^2} \frac{\partial^2}{\partial t \partial x} \left(r^2 \frac{\partial \varphi}{\partial x} \right) - \sqrt{\frac{2\eta\omega}{r^2 \rho}} \frac{\partial \varphi}{\partial t}. \end{aligned} \tag{3.40}$$

The derivative of $\partial\rho/\partial x$ is eliminated from Eq. (3.40) by differentiation of Eq. (3.33) with respect to x

$$\frac{\partial^2\varphi}{\partial x\partial t}+\frac{1}{2}\frac{\partial}{\partial x}\left(\frac{\partial\varphi}{\partial x}\right)^2=-\frac{\gamma\, p_0}{\rho_0{}^{\gamma}}\rho^{(\gamma-2)}\frac{\partial\rho}{\partial x}-a(t)\,. \tag{3.41}$$

The dissipative terms are dropped because $\partial\rho/\partial x$ appears only in the nonlinear term in Eq. (3.41). According to Eq. (3.41)

$$\frac{\partial\rho}{\partial x}=-\left(\frac{\gamma\, p_0}{\rho_0{}^{\gamma}}\rho^{(\gamma-2)}\right)^{-1}\left[\frac{\partial^2\varphi}{\partial x\partial t}+\frac{1}{2}\frac{\partial}{\partial x}\left(\frac{\partial\varphi}{\partial x}\right)^2+a(t)\right]. \tag{3.42}$$

By substituting Eq. (3.42) into Eq. (3.40), we obtain

$$\begin{aligned}\frac{\partial^2\varphi}{\partial t^2}+\frac{1}{2}\frac{\partial}{\partial t}\left(\frac{\partial\varphi}{\partial x}\right)^2&=\left[\frac{\partial^2\varphi}{\partial x\partial t}+\frac{1}{2}\frac{\partial}{\partial x}\left(\frac{\partial\varphi}{\partial x}\right)^2+a(t)\right]\frac{\partial\varphi}{\partial x}\\&+\frac{\gamma\, p_0}{\rho_0{}^{\gamma}r^2}\rho^{(\gamma-1)}\frac{\partial}{\partial x}\left(r^2\frac{\partial\varphi}{\partial x}\right)-\frac{da}{dt}x+\frac{\delta}{r^2}\frac{\partial^2}{\partial t\partial x}\left(r^2\frac{\partial\varphi}{\partial x}\right)-\sqrt{\frac{2\eta\omega}{r^2\rho}}\frac{\partial\varphi}{\partial t}.\end{aligned} \tag{3.43}$$

Using Eq. (3.36), Eq. (3.43) is presented in the form

$$\begin{aligned}\frac{\partial^2\varphi}{\partial t^2}+\frac{1}{2}\frac{\partial}{\partial t}\left(\frac{\partial\varphi}{\partial x}\right)^2&=\left[\frac{\partial^2\varphi}{\partial x\partial t}+\frac{1}{2}\frac{\partial}{\partial x}\left(\frac{\partial\varphi}{\partial x}\right)^2+a(t)\right]\frac{\partial\varphi}{\partial x}\\&+\frac{c^2}{r^2}\frac{\partial}{\partial x}\left(r^2\frac{\partial\varphi}{\partial x}\right)-\frac{da}{dt}x+\frac{\delta}{r^2}\frac{\partial^2}{\partial t\partial x}\left(r^2\frac{\partial\varphi}{\partial x}\right)-\sqrt{\frac{2\eta\omega}{r^2\rho}}\frac{\partial\varphi}{\partial t}.\end{aligned} \tag{3.44}$$

c^2 in Eq. (3.44) is replaced by

$$c^2=c_0{}^2-(\gamma-1)\left[\frac{\partial\varphi}{\partial t}+\frac{1}{2}\left(\frac{\partial\varphi}{\partial x}\right)^2+a(t)x\right], \tag{3.45}$$

which is obtained from Eq. (3.37) by dropping off the dissipation terms. After substituting Eq. (3.45) into Eq. (3.44), we obtain

$$\frac{c_0^2}{r^2}\frac{\partial}{\partial x}\left(r^2\frac{\partial\varphi}{\partial x}\right)-\frac{\partial^2\varphi}{\partial t^2}+\frac{\delta}{r^2}\frac{\partial^2}{\partial t\partial x}\left(r^2\frac{\partial\varphi}{\partial x}\right)-\sqrt{\frac{2\eta\omega}{r^2\rho}}\frac{\partial\varphi}{\partial t}=$$
$$\frac{da}{dt}x+a(t)\frac{\partial\varphi}{\partial x}+\frac{\gamma-1}{r^2}a(t)x\frac{\partial}{\partial x}\left(r^2\frac{\partial\varphi}{\partial x}\right)+2\frac{\partial^2\varphi}{\partial x\partial t}\frac{\partial\varphi}{\partial x}+ \tag{3.46}$$
$$\frac{\gamma-1}{r^2}\frac{\partial\varphi}{\partial t}\frac{\partial}{\partial x}\left(r^2\frac{\partial\varphi}{\partial x}\right)+\frac{1}{3}\frac{\partial}{\partial x}\left(\frac{\partial\varphi}{\partial x}\right)^3+\frac{\gamma-1}{2r^2}\left(\frac{\partial\varphi}{\partial x}\right)^2\frac{\partial}{\partial x}\left(r^2\frac{\partial\varphi}{\partial x}\right).$$

For the purpose of solving Eq. (3.46) numerically, it is better to write Eq. (3.46) in a dimensionless form. The dimensionless variables defined by Ilinskii *et al*. (1998) are used here

$$X=\frac{x}{l},\quad T=\omega t,\quad R=\frac{r}{l},\quad A=\frac{a}{l\omega_0{}^2},\quad \Phi=\frac{\varphi}{l^2\omega_0},\ \Omega=\frac{\omega}{\omega_0}, \tag{3.47}$$

where l is the length of the resonator, ω is the angular frequency of the periodic force that shakes the resonator. ω_0 is the frequency of the lowest mode of a cylindrical resonator of length l, which is calculated by

$$\omega_0=\frac{\pi c_0}{l}. \tag{3.48}$$

With the dimensionless variables, Eq. (3.46) takes the form

$$\frac{1}{\pi^2R^2}\frac{\partial}{\partial X}\left(R^2\frac{\partial\Phi}{\partial X}\right)-\Omega^2\frac{\partial^2\Phi}{\partial T^2}+\frac{G_B\Omega}{\pi^3R^2}\frac{\partial^2}{\partial T\partial X}\left(R^2\frac{\partial\Phi}{\partial X}\right)-\frac{G_S\Omega^{\frac{3}{2}}}{R}\frac{\partial\Phi}{\partial T}$$
$$=\Omega\frac{dA}{dT}X+A(T)\frac{\partial\Phi}{\partial X}+\frac{\gamma-1}{R^2}A(T)X\frac{\partial}{\partial X}\left(R^2\frac{\partial\Phi}{\partial X}\right)+2\Omega\frac{\partial^2\Phi}{\partial X\partial T}\frac{\partial\Phi}{\partial X}$$
$$+\frac{(\gamma-1)\Omega}{R^2}\frac{\partial\Phi}{\partial T}\frac{\partial}{\partial X}\left(R^2\frac{\partial\Phi}{\partial X}\right)+\frac{1}{3}\frac{\partial}{\partial X}\left(\frac{\partial\Phi}{\partial X}\right)^3+\frac{\gamma-1}{2R^2}\left(\frac{\partial\Phi}{\partial X}\right)^2\frac{\partial}{\partial X}\left(R^2\frac{\partial\Phi}{\partial X}\right).$$

(3.49)

Here the new notations, G_B and G_S, are introduced

$$G_B = \frac{\pi\delta\omega_0}{c_0^{\,2}}\ , \quad G_S = \sqrt{\frac{2\eta}{\rho_0\omega_0 l^2}}\ . \tag{3.50}$$

G_B is the same as G and D introduced by Ilinskii *et al.* (1998) and Erickson and Zinn (2003) respectively, G_S is a parameter associated with the shear viscosity. Eq. (3.50) shows that the coefficient of the shear viscosity term is inversely proportional to the dimensionless cross-section size, R, and the square root of the length, $\sqrt{l}$. By ignoring the third-order nonlinear terms, we get

$$\begin{aligned}
&\frac{\partial^2\Phi}{\partial T^2} - \frac{1}{\Omega^2\pi^2}\left\{\frac{1}{R^2}\frac{dR^2}{dX}\right\}\frac{\partial\Phi}{\partial X} - \frac{1}{\Omega^2\pi^2}\frac{\partial^2\Phi}{\partial X^2} \\
&= -\frac{2}{\Omega}\frac{\partial^2\Phi}{\partial X\partial T}\frac{\partial\Phi}{\partial X} - \frac{(\gamma-1)}{\Omega}\left\{\frac{1}{R^2}\frac{dR^2}{dX}\right\}\frac{\partial\Phi}{\partial T}\frac{\partial\Omega}{\partial X} - \frac{(\gamma-1)}{\Omega}\frac{\partial\Phi}{\partial T}\frac{\partial^2\Phi}{\partial X^2} \\
&- \frac{1}{\Omega^2}\left\{A\frac{\partial\Phi}{\partial X} + \Omega\frac{dA}{dT}X + (\gamma-1)\left\{\frac{1}{R^2}\frac{dR^2}{dX}\right\}\frac{\partial\Phi}{\partial X}AX + (\gamma-1)\frac{\partial^2\Phi}{\partial X^2}AX\right\} \\
&+ \frac{G_B}{\pi^3\Omega}\left\{\frac{1}{R^2}\frac{dR^2}{dX}\right\}\frac{\partial^2\Phi}{\partial T\partial X} + \frac{G_B}{\pi^3\Omega}\frac{\partial^3\Phi}{\partial T\partial X^2} - \frac{G_S}{\Omega^{1/2}R}\frac{\partial\Phi}{\partial T}.
\end{aligned} \tag{3.51}$$

Since both ends of the resonator are closed, the solution of the governing equation (3.51) should satisfy the following boundary conditions

$$\left.\frac{\partial\Phi}{\partial X}\right|_{X=0} = 0, \qquad \left.\frac{\partial\Phi}{\partial X}\right|_{X=1} = 0. \tag{3.52}$$

3.3.2 EQUATION FOR LOW ASPECT RATIO RECTANGULAR RESONATORS

Figure 3.5 shows a low aspect ratio rectangular resonator. The height of the duct is fixed at h and is assumed to be much smaller than the width $b(x)$, which is a function of x. The entire resonator is oscillated along the x-axis by an external body force. The Cartesian coordinate system is used for the duct. The governing equation is derived by manipulating three basic equations: (1) equation of state, (2) equation of mass conservation, and (3) equation of momentum conservation. The process is similar to the one used for the axisymmetric resonator in Section 3.3.1.

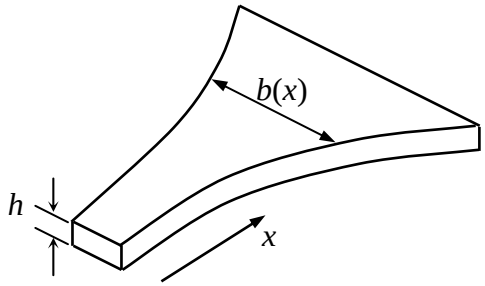

Figure 3.5 Low aspect ratio rectangular resonator, exponentially expanded.

The equation of state is the same as the one for the axisymmetric resonator. The equations of mass conservation and momentum conservation differ from those for the axisymmetric resonator due to different configuration. The mass conservation equation for the gas in the low aspect ratio rectangular resonator is of the form,

$$\frac{\partial \rho}{\partial t} + \frac{1}{hb}\frac{\partial}{\partial x}\left(hb\rho\bar{u}\right) = 0 . \tag{3.53}$$

Using shear viscous term of Eq. (3.21) and bulk viscous term of Eq. (3.22), which are derived in Section 3.2.2, the momentum equation for the low aspect ratio rectangular resonator is obtained as

$$\frac{\partial u}{\partial t}+\bar{u}\frac{\partial \bar{u}}{\partial x}=-\frac{1}{\rho}\frac{\partial p}{\partial x}-a(t)+\frac{(\zeta+4\eta/3)}{\rho}\frac{\partial}{\partial x}\left(\frac{1}{b}\frac{\partial}{\partial x}(bu)\right)-\frac{\sqrt{2\rho\eta\omega}}{h\rho}\bar{u}\,. \quad (3.54)$$

Following the same procedure in Section 3.3.1, the dimensionless wave equation for low aspect ratio rectangular resonator is of the following form,

$$\begin{aligned}
&\frac{\partial^2\Phi}{\partial T^2}-\frac{1}{\Omega^2\pi^2}\left\{\frac{1}{B}\frac{dB}{dX}\right\}\frac{\partial\Phi}{\partial X}-\frac{1}{\Omega^2\pi^2}\frac{\partial^2\Phi}{\partial X^2}\\
&=-\frac{2}{\Omega}\frac{\partial^2\Phi}{\partial X\partial T}\frac{\partial\Phi}{\partial X}-\frac{(\gamma-1)}{\Omega}\left\{\frac{1}{B}\frac{dB}{dX}\right\}\frac{\partial\Phi}{\partial T}\frac{\partial\Phi}{\partial X}-\frac{(\gamma-1)}{\Omega}\frac{\partial\Phi}{\partial T}\frac{\partial^2\Phi}{\partial X^2}\\
&-\frac{1}{\Omega^2}\left\{A\frac{\partial\Phi}{\partial X}+\Omega\frac{dA}{dT}X+(\gamma-1)\left\{\frac{1}{B}\frac{dB}{dX}\right\}\frac{\partial\Phi}{\partial X}AX+(\gamma-1)\frac{\partial^2\Phi}{\partial X^2}AX\right\}\\
&+\frac{G_B}{\pi^3\Omega}\left\{\frac{1}{B}\frac{dB}{dX}\right\}\frac{\partial^2\Phi}{\partial T\partial X}+\frac{G_B}{\pi^3\Omega}\frac{\partial^3\Phi}{\partial T\partial X^2}-\frac{G_S}{\Omega^{1/2}H}\frac{\partial\Phi}{\partial T},
\end{aligned} \quad (3.55)$$

where, $H=\frac{h}{l}$ and $B=\frac{b(x)}{l}$, and other parameters are the same as those in Eqs. (3.47) and (3.50).

3.3.3 PRESSURE EQUATIONS

When the dimensionless velocity potential Φ is obtained by solving Eqs. (3.51) and (3.55), acoustical parameters of interest may be calculated. For example, the gas velocity in the resonator can be calculated by Eq. (3.31). However, additional equations are needed for the pressures. The following are the derivation of pressure equation.

For axisymmetric resonators, by substituting Eq. (3.35) into Eq. (3.33), we obtain

$$\frac{\partial \varphi}{\partial t}+\frac{1}{2}\left(\frac{\partial \varphi}{\partial x}\right)^2=-\frac{\gamma p_0}{(\gamma-1)\rho_0}\left(\frac{\rho}{\rho_0}\right)^{(\gamma-1)}-a(t)x+\frac{\delta}{r^2}\frac{\partial}{\partial x}\left(r^2\frac{\partial \varphi}{\partial x}\right)-\sqrt{\frac{2\eta\omega}{r^2\rho}}\varphi+\frac{{c_0}^2}{\gamma-1}. \tag{3.56}$$

From Eq. (3.36) and (3.48) we have

$${c_0}^2=\frac{\gamma p_0}{\rho_0}=\left(\frac{\omega_0 l}{\pi}\right)^2. \tag{3.57}$$

Substitution of Eq. (3.57) into Eq. (3.56) yields

$$\frac{\partial \varphi}{\partial t}+\frac{1}{2}\left(\frac{\partial \varphi}{\partial x}\right)^2=\frac{{\omega_0}^2 l^2}{(\gamma-1)\pi^2}\left(1-\left(\frac{\rho}{\rho_0}\right)^{(\gamma-1)}\right)-a(t)x+\frac{\delta}{r^2}\frac{\partial}{\partial x}\left(r^2\frac{\partial \varphi}{\partial x}\right)-\sqrt{\frac{2\eta\omega}{r^2\rho}}\varphi. \tag{3.58}$$

By solving Eq. (3.58) we get the gas density for the axisymmetric resonator

$$\frac{\rho}{\rho_0}=\left(1-\frac{(\gamma-1)\pi^2}{{\omega_0}^2 l^2}\left(\frac{\partial \varphi}{\partial t}+\frac{1}{2}\left(\frac{\partial \varphi}{\partial x}\right)^2+a(t)x-\frac{\delta}{r^2}\frac{\partial}{\partial x}\left(r^2\frac{\partial \varphi}{\partial x}\right)+\sqrt{\frac{2\eta\omega}{r^2\rho}}\varphi\right)\right)^{1/(\gamma-1)}. \tag{3.59}$$

Using Eq (3.24), the pressure for the axisymmetric resonator is obtained as

$$\frac{p}{p_0}=\left(1-\frac{(\gamma-1)\pi^2}{{\omega_0}^2 l^2}\left(\frac{\partial \varphi}{\partial t}+\frac{1}{2}\left(\frac{\partial \varphi}{\partial x}\right)^2+a(t)x-\frac{\delta}{r^2}\frac{\partial}{\partial x}\left(r^2\frac{\partial \varphi}{\partial x}\right)+\sqrt{\frac{2\eta\omega}{r^2\rho}}\varphi\right)\right)^{\gamma/(\gamma-1)}. \tag{3.60}$$

In dimensionless forms, Eq. (3.59) and (3.60) become

$$\frac{\rho}{\rho_0}=\left[1-(\gamma-1)\pi^2\left(\Omega\frac{\partial\Phi}{\partial T}+\frac{1}{2}\left(\frac{\partial\Phi}{\partial X}\right)^2+AX-\frac{G_B}{\pi^3}\frac{1}{S}\frac{\partial}{\partial X}\left(S\frac{\partial\Phi}{\partial X}\right)+\frac{G_S\Omega^{1/2}\Phi}{R}\right)\right]^{\frac{1}{\gamma-1}}$$

(3.61)

$$\frac{P}{P_0}=\left[1-(\gamma-1)\pi^2\left(\Omega\frac{\partial\Phi}{\partial T}+\frac{1}{2}\left(\frac{\partial\Phi}{\partial X}\right)^2+AX-\frac{G_B}{\pi^3}\frac{1}{S}\frac{\partial}{\partial X}\left(S\frac{\partial\Phi}{\partial X}\right)+\frac{G_S\Omega^{1/2}\Phi}{R}\right)\right]^{\frac{\gamma}{\gamma-1}}.$$

(3.62)

With a similar procedure, the gas density for the low aspect ratio rectangular resonator is obtained as

$$\frac{\rho}{\rho_0}=\left[1-(\gamma-1)\pi^2\left(\Omega\frac{\partial\Phi}{\partial T}+\frac{1}{2}\left(\frac{\partial\Phi}{\partial X}\right)^2+AX-\frac{G_B}{\pi^3}\frac{1}{B}\frac{\partial}{\partial X}\left(B\frac{\partial\Phi}{\partial X}\right)+\frac{G_S\Omega^{1/2}\Phi}{H}\right)\right]^{\frac{1}{\gamma-1}},$$

(3.63)

and pressure expression for low aspect ratio rectangular resonator is

$$\frac{P}{P_0}=\left[1-(\gamma-1)\pi^2\left(\Omega\frac{\partial\Phi}{\partial T}+\frac{1}{2}\left(\frac{\partial\Phi}{\partial X}\right)^2+AX-\frac{G_B}{\pi^3}\frac{1}{B}\frac{\partial}{\partial X}\left(B\frac{\partial\Phi}{\partial X}\right)+\frac{G_S\Omega^{1/2}\Phi}{H}\right)\right]^{\frac{\gamma}{\gamma-1}}.$$

(3.64)

3.4 APPLICATION OF THE GALERKIN'S METHOD

3.4.1 THE GALERKIN'S METHOD

Equations (3.51) and (3.55) are solved by the Galerkin's method proposed by Erickson and Zinn (2003). This solution technique begins with an assumption that the velocity potential can be expressed by an infinite series expansion of the following form:

$$\Phi(X,T) = \sum_{n=1}^{\infty} \eta_n(T)\Psi_n(X), \tag{3.65}$$

where $\Psi_n(X)$, referred to as trial functions, describe the spatial dependence of the natural acoustic mode shape of a given duct geometry (to be discussed in detail later), and $\eta_n(T)$ are the unknown, time-dependent amplitudes of these acoustic modes. For the purpose of numerical calculation the infinite series in Eq. (3.65) is truncated to a finite number of modes.

Since the infinite series is truncated, the resulting solution for Φ is an approximation and does not satisfy Eqs. (3.51) and (3.55) exactly. When the truncated series for Φ is substituted into Eqs. (3.51) and (3.55), the resulting expression, called the residual $R(\Phi)$, is nonzero. The objective of the Galerkin method is to derive a set of equations for the time-dependent amplitudes, $\eta_n(T)$, and to solve those equations to minimize the residual $R(\Phi)$. It's known that a continuous function is zero if it is orthogonal (i.e., inner product equals to zero) to every member of a complete set. This orthogonality property leads to the formation of the following expression,

$$\int_0^1 R(\Phi(X,T))\cdot W_j(X)dX = 0, \qquad j = 1,2,\cdots, \tag{3.66}$$

where $W_j(X)$ are a complete set of weighting functions. Performing the integration over the duct length in Eq. (3.66) yields the following system of time-dependent coupled ordinary differential equations:

$$\begin{aligned}
&\sum_n G_{1n}\ddot{\eta}_1 + \sum_n H_{1n}\eta_n + \sum_n\sum_m Z_{1nm}\dot{\eta}_n\eta_m + \sum_n E^1_{1n}(T)\eta_n + \sum_n E^2_{1n}(T) + L^b_{1n}(T)\dot{\eta} + L^s_{1n}(T)\eta = 0\\
&\sum_n G_{2n}\ddot{\eta}_1 + \sum_n H_{2n}\eta_n + \sum_n\sum_m Z_{2nm}\dot{\eta}_n\eta_m + \sum_n E^1_{2n}(T)\eta_n + \sum_n E^2_{2n}(T) + L^b_{2n}(T)\dot{\eta} + L^s_{2n}(T)\eta = 0\\
&\vdots\\
&\sum_n G_{jn}\ddot{\eta}_1 + \sum_n H_{jn}\eta_n + \sum_n\sum_m Z_{jnm}\dot{\eta}_n\eta_m + \sum_n E^1_{jn}(T)\eta_n + \sum_n E^2_{jn}(T) + L^b_{jn}(T)\dot{\eta} + L^s_{jn}(T)\eta = 0\\
&\vdots\\
&\sum_n G_{(n-1)n}\ddot{\eta}_1 + \sum_n H_{(n-1)n}\eta_n + \sum_n\sum_m Z_{(n-1)nm}\dot{\eta}_n\eta_m + \sum_n E^1_{(n-1)n}(T)\eta_n + \sum_n E^2_{(n-1)n}(T) + L^b_{(n-1)n}(T)\dot{\eta}\\
&+L^s_{(n-1)n}(T)\eta = 0\\
&\sum_n G_{nn}\ddot{\eta}_1 + \sum_n H_{nn}\eta_n + \sum_n\sum_m Z_{nnm}\dot{\eta}_n\eta_m + \sum_n E^1_{nn}(T)\eta_n + \sum_n E^2_{nn}(T) + L^b_{nn}(T)\dot{\eta} + L^s_{nn}(T)\eta = 0
\end{aligned} \tag{3.67}$$

In Equation (3.67), the subscripts j, n and m all go from 1 to the specified number of included modes, N. G_{jn} and H_{jn} describe linear processes, Z_{jnm} describes nonlinear coupling, E^1_{jn} and E^2_{jn} describe the driving forces, and L^b_{jn} and L^s_{jn} describe viscous damping. These quantities are evaluated by the following expressions respectively,

$$G_{jn} = \int_0^1 W_j(X)\Psi_n(X)dX\,, \tag{3.68}$$

$$H_{jn} = -\frac{1}{\Omega^2\pi^2}\int_0^1 W_j(X)\left[\frac{d^2\Psi_n}{dX^2} + \left\{\frac{1}{S}\frac{dS}{dX}\right\}\frac{d\Psi_n}{dX}\right]dX\,, \tag{3.69}$$

$$Z_{jnm} = Z^1_{jnm} + Z^2_{jnm} + Z^3_{jnm}, \tag{3.70}$$

$$Z^1_{jnm} = \frac{2}{\Omega}\int_0^1 W_j(X)\frac{d\Psi_n}{dX}\frac{d\Psi_m}{dX}dX\ , \tag{3.71}$$

$$Z^2_{jnm} = \frac{\gamma\text{-}1}{\Omega}\int_0^1 W_j(X)\frac{1}{S}\frac{dS}{dX}\Psi_n\frac{d\Psi_m}{dX}dX\ , \tag{3.72}$$

$$Z^3_{jnm} = \frac{\gamma-1}{\Omega}\int_0^1 W_j(X)\Psi_n\frac{d^2\Psi_m}{dX^2}dX\ , \tag{3.73}$$

$$E^1_{jn}(T) = \frac{A}{\Omega^2}\left[\int_0^1 W_j(X)\frac{d\Psi_n}{dX}dX + \int_0^1 W_j(X)(\gamma-1)\left\{\frac{1}{S}\frac{dS}{dX}\right\}\frac{d\Psi_n}{dX}XdX + \int_0^1 W_j(X)(\gamma-1)\frac{d^2\Psi_n}{dX^2}XdX\right], \tag{3.74}$$

$$E^2_{jn}(T) = \frac{1}{\Omega}\int_0^1 W_j(X)\frac{dA}{dT}XdX\ , \tag{3.75}$$

$$L^b_{jn} = -\frac{G_B}{\pi^3\Omega}\int_0^1 W_j(X)\left[\left\{\frac{1}{S}\frac{dS}{dX}\right\}\frac{d\Psi_n}{dX} + \frac{\partial^2\Psi_n}{\partial X^2}\right]dX\ , \tag{3.76}$$

$$L^s_{jn} = \frac{G_S}{\Omega^{1/2}R}\int_0^1 W_j(X)\Psi_n dX\ . \tag{3.77}$$

Specification of initial conditions, trial functions $\Psi_n(X)$, and weighting functions $W_n(X)$ provides all the information needed to solve Eqs. (3.67), which are numerically integrated using the fourth-order Runge-Kutta method (Hoffman, 1993) to determine the amplitude function $\eta_j(T)$ from time zero to any desired time. It follows from Eq. (3.67) that the number of modes, N, included in the approximate solution directly determines the number of coupled differential equations which must

be solved. Additionally, the number of included modes also determines the accuracy of the solution. It is demonstrated by Erickson and Zinn (2003) that $N = 20$ can achieve both accuracy and efficiency in calculation. In this study N is set to be 20.

3.4.2 TRIAL FUNCTIONS

Erickson and Zinn (2003) suggested to choose the natural acoustic modes of the resonator duct as the trial functions $\Psi_n(X)$. These functions can be determined analytically by solving the following linear wave equation, corresponding to the left-hand side of Eq. (3.51) and (3.55):

$$\Omega^2 \frac{\partial^2 \Phi}{\partial T^2} - \frac{1}{\pi^2} \frac{1}{S} \frac{dS}{dX} \frac{\partial \Phi}{\partial X} - \frac{1}{\pi^2} \frac{\partial^2 \Phi}{\partial X^2} = 0, \tag{3.78}$$

where S is the cross-sectional area. In the present study, exponentially expanded cross-sectional area is used and S is a function of X in the following form

$$S = S_0 \exp(\alpha X), \tag{3.79}$$

$$\frac{1}{S} \frac{dS}{dX} = \alpha, \tag{3.80}$$

and α is referred to as the flare constant. So that, Eq. (3.78) becomes

$$(\pi \Omega)^2 \frac{\partial^2 \Phi}{\partial T^2} - \alpha \frac{\partial \Phi}{\partial X} - \frac{\partial^2 \Phi}{\partial X^2} = 0, \tag{3.81}$$

where Φ must satisfy the boundary conditions defined by Eq. (3.52).

Using the method of separation of variables to solve Eq. (3.81) subject to the boundary conditions described by Eq. (3.52), one obtains the following natural acoustic modes and resonance frequencies (please refer to Appendix A for more details)

$$\Psi_n(X) = \exp\left(\frac{-\alpha X}{2}\right)\left(\cos(n\pi X) + \frac{\alpha}{2n\pi}\sin(n\pi X)\right) \qquad n = 1, 2, 3, \ldots, \tag{3.82}$$

$$\Omega_n = \frac{\omega_n}{\omega_0} = \sqrt{n^2 + \frac{1}{4}\left(\frac{\alpha}{\pi}\right)^2}, \qquad n = 1, 2, 3, \ldots, \tag{3.83}$$

where $\Psi_n(X)$ forms a complete set and Ω_n is the corresponding natural resonance frequency. The first three natural acoustic modes for straight duct ($\alpha = 0$) and exponentially expanded duct ($\alpha = 5.75$) are illustrated in Figure 3.6 and Figure 3.7, respectively.

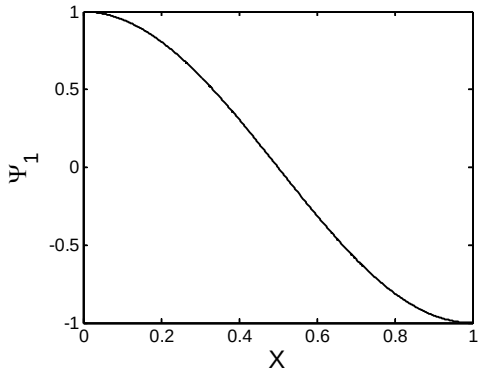

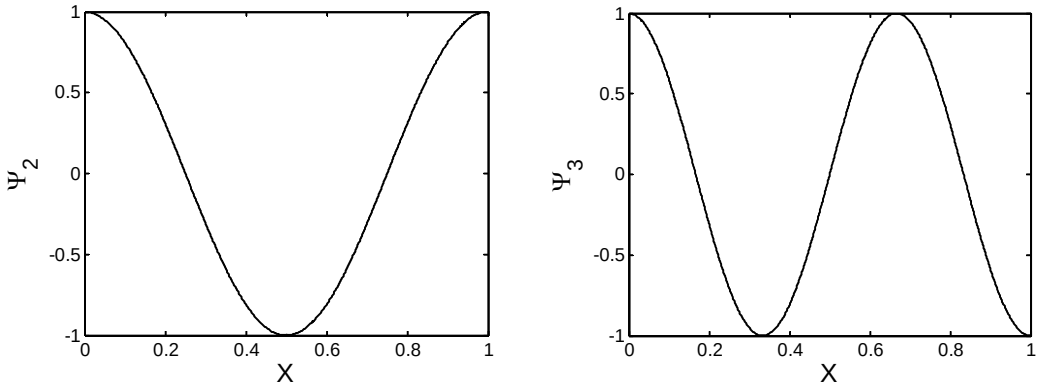

Figure 3.6 Natural acoustic modes for straight duct ($\alpha = 5.75$).

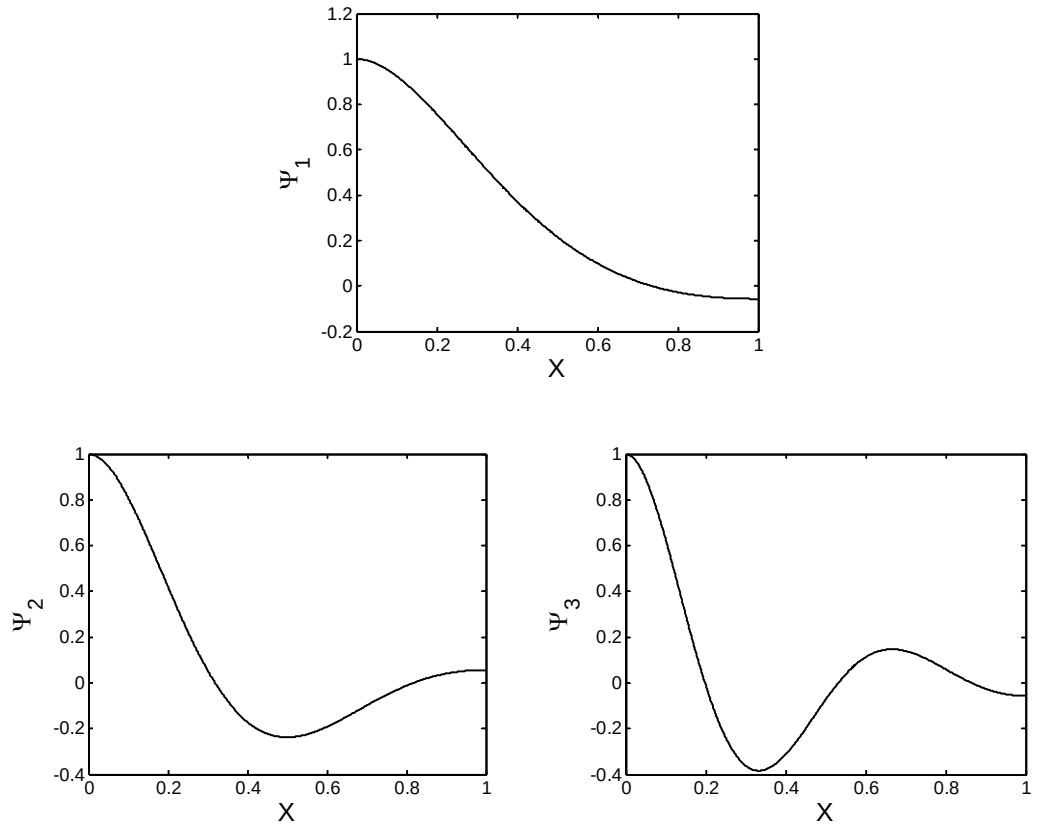

Figure 3.7 Natural acoustic modes for exponentially expanded duct ($\alpha = 5.75$).

The natural acoustic mode frequencies determined by Eq. (3.83) for the expanded resonators illustrate an important difference between straight and shaped ducts. Table 3.1 presents the first four natural acoustical mode frequencies for a straight duct ($\alpha = 0$) and two exponentially expanded resonators.

Table 3.1 Calculation of natural acoustical mode frequencies for straight and horn shaped ducts.

Natural acoustical mode	Straight duct $\alpha = 0$	Horn-shaped duct $\alpha = 3$	Horn-shaped duct $\alpha = 5.75$
Ω_1	1	1.108	1.356
Ω_2	2	2.056	2..199
Ω_3	3	3.038	3.137
Ω_4	4	4.028	4.103

3.4.3 WEIGHTING FUNCTIONS

The choice of weighting functions, $W_j(X)$, must satisfy the orthogonality condition of the Sturm Liouville equation governing the natural acoustic mode shapes expressed in Eq. (3.82), and is defined in this study following the study by Erickson and Zinn (2003),

$$\begin{aligned} W_n(X) &= S(X)\Psi_n(X) \\ &= \exp\left(\frac{\alpha X}{2}\right)\left(\cos(n\pi X) + \frac{\alpha}{2n\pi}\sin(n\pi X)\right). \end{aligned} \tag{3.84}$$

This form of weighting functions is chosen in order to simplify the first terms of Eq. (3.67) by reducing the summation to a single term where $n = m$.

3.5 RESULTS AND DISCUSSION

3.5.1 ACOUSTIC WAVES IN DIFFERENT RESONATORS

The one-dimensional wave equations (3.51) and (3.55) are solved by the Galerkin's method developed by Erickson and Zinn (2003). All parameters for the gas inside the resonators are assumed to have the same values as those used by Erickson and Zinn (2003). The coefficients of shear viscosity and bulk viscosity are of the same order, and for simplicity we set them to be equal to 1.7×10^{-5} Pa·s. The resonators are oscillated at an acceleration

$$A = \tilde{A}\cos(T), \tag{3.85}$$

where $\tilde{A}$ is the amplitude. The cross-sections of two classes resonators are exponentially expanded with an area:

$$S = S_0 e^{\alpha X} \text{ and } B = B_0 e^{\alpha X}, \tag{3.86}$$

where $S_0 = \pi r_0^2 / l^2$ for the axisymmetric resonator and $B_0 = b_0 / l$ for the low aspect ratio rectangular (LARR) resonator.

Cylindrical resonator (α =0)

The waveform in a cylindrical resonator ($\alpha = 0$) is tested first and the results will be used as reference for expanded resonators ($\alpha > 0$). The geometry of the resonator is $l = 0.02m$ and $r_0 / l = 0.02$. The resonator is oscillated at $\tilde{A} = 5\times10^{-4}$. Pressure waveforms are calculated and shown in Figure 3.8. These waveforms are calculated at $X = 0$. Figure 3.8 (a), (b), (c) display pressure wave shapes when the driving frequencies are below resonance, $\Omega < 1$. These waveforms are normally referred as u

wave (Lawrenson, 1998). It is seen that the shock waves start to form as the frequency approaches to $\Omega = 1$. Figure 3.8 (d) corresponds to the waveform at resonance frequency $\Omega = 1$. The saw-tooth waveform is always believed as the intrinsic limit for existing of high sound. Note that the peak-to-peak amplitude is about $0.18\,P_0$ in this case. Figure 3.8 (e), (f), (g) illustrate the waveforms at the driving frequencies above the resonance $\Omega > 1$. They are called *m* wave (Lawrenson, 1998). The variations of the pressure waveforms crossing the resonance frequency are well agreed with the results by Ilinskii *et al*. (1998).

The peak-to-peak pressure distribution along the cylindrical resonator axis is shown in Figure 3.9 (dotted line). It can be seen that the peak-to-peak pressure amplitude is about 0.2 at the end of the cylindrical resonator. The amplitude distribution of velocity (peak-to-peak value) in the cylindrical resonator is shown in Figure 3.10 (dotted line). The dimensionless velocity is defined by $U = \dfrac{\bar{u}}{l\omega_0}$. As the resonator is closed at both ends, the velocity is 0 at $X = 0$ and $X = 1$. The velocity amplitude distribution in a cylindrical resonator can be better viewed in Appendix B.

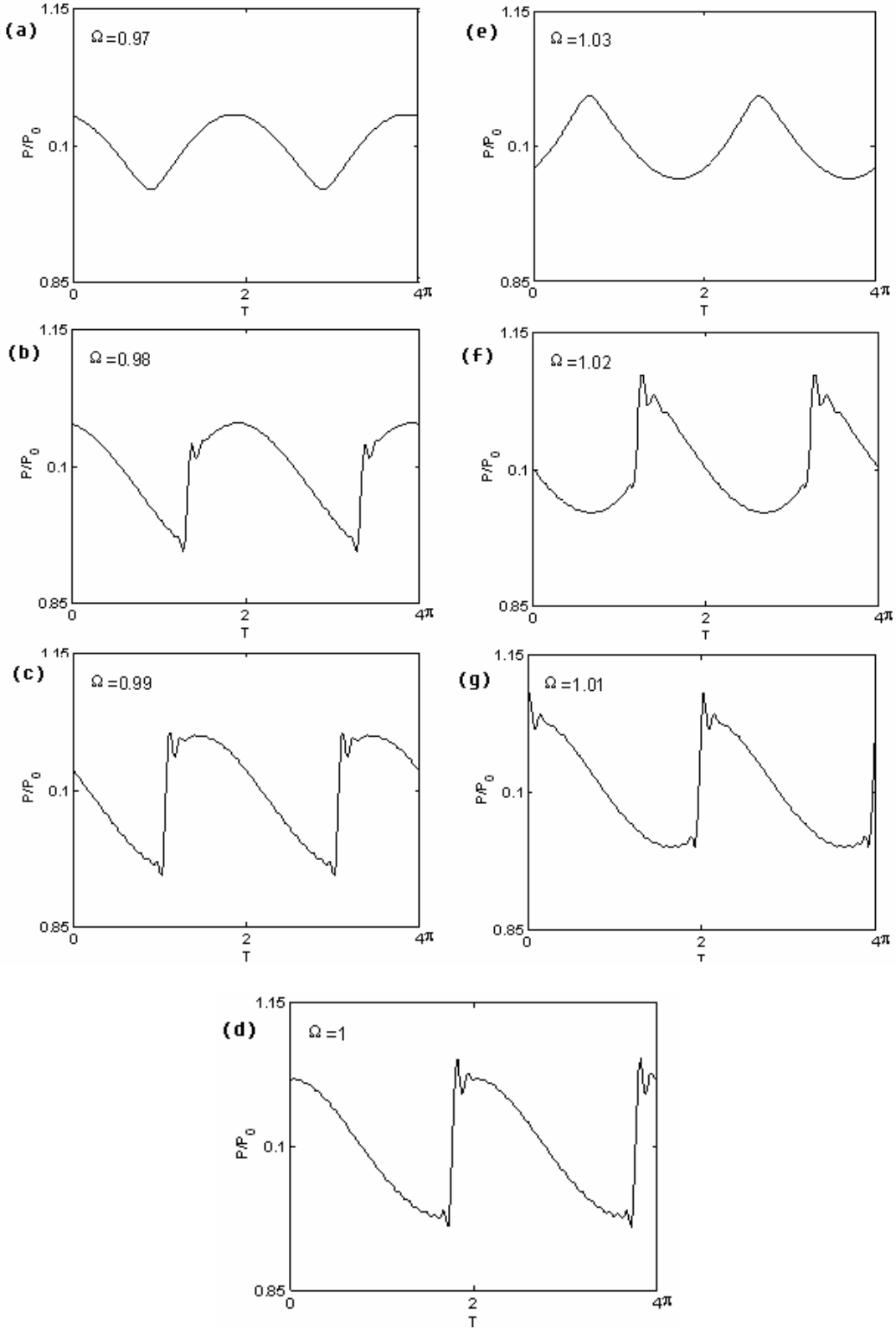

Figure 3.8 pressure waveforms near the resonance frequency (Ω=1) in the cylindrical resonator. The resonator is oscillated by a body force. (a) Ω=0.97, (b) Ω=1.03, (c) Ω=0.99, (d) Ω=1.02, (e) Ω=0.99, (f) Ω=1.01, (g) Ω=1 .

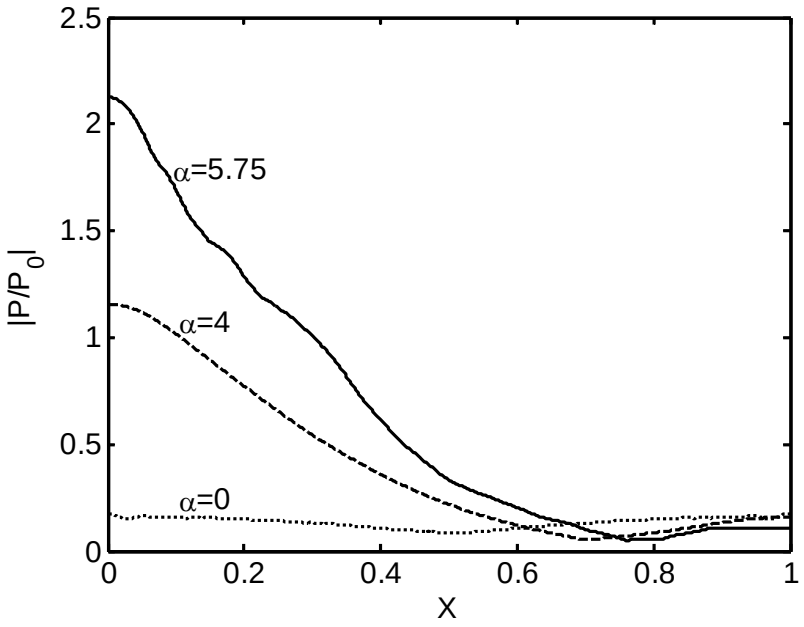

Figure 3.9 Amplitude distributions of peak-to-peak pressures in axisymmetric resonators along the axis. $S = \pi(r_0 / l)^2 e^{\alpha X}$ **,** $\alpha = 0, 4, 5.75$ **respectively,** $l = 0.2m$ **,** $r_0 / l = 0.02$ **.**

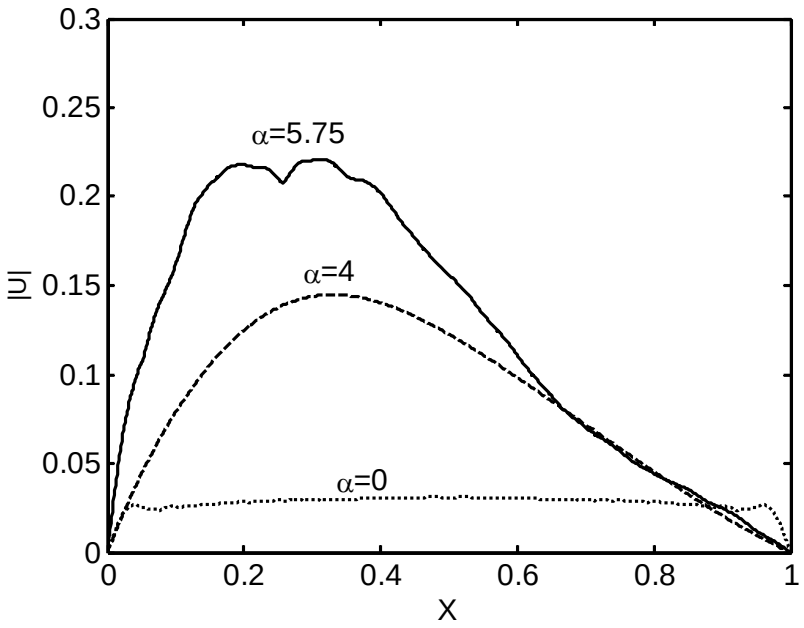

Figure 3.10 Amplitude distributions of velocities in axisymmetric resonators along the axis. $S = \pi(r_0 / l)^2 e^{\alpha X}$ **,** $\alpha = 0, 4, 5.75$ **respectively,** $l = 0.2m$ **,** $r_0 / l = 0.02$ **.**

Shaped resonator (α =4)

The resonance characteristics in a shaped axisymmetric resonator at $\alpha = 4$ are calculated. The geometry of the resonator is $l = 0.02m$ and $r_0 / l = 0.02$. For the same driving force ($\tilde{A} = 5 \times 10^{-4}$), the resonance in this shaped resonator ($\alpha = 4$) occurs at $\Omega = 1.195$. The distribution of the peak-to-peak pressure amplitude along the resonator is also shown in Figure 3.9 (dashed line), and the maximum value is found at the small end ($X = 0$). The maximum peak-to-peak pressure $|P|$ is 1.17 P_0 in this case, which is much higher than 0.18 P_0 in the cylindrical resonator. The lowest pressure amplitude is 0.05 P_0 at $X = 0.7$, which is different from 0 at $X = 0.5$ for a cylindrical resonator at weak driving (se Appendix B). The pressure waveforms at the small end are showed in Figure 3.11. It is very clear that the shock waves are disappeared and the pressure amplitudes are much higher than the pressures in the straight duct (Figure 3.8).

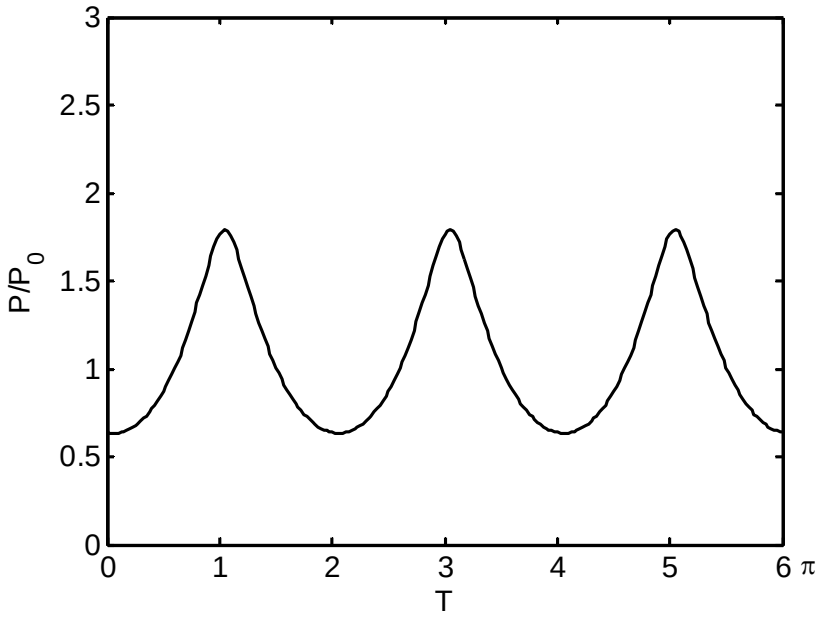

Figure 3.11 Pressure waveforms at the small end of the axisymmetric resonator.

$S = \pi (r_0 / l)^2 e^{\alpha X}$, $\alpha = 4$, $l = 0.2m$, $r_0 / l = 0.02$, $X = 0$.

The amplitude distribution of velocity (peak-to-peak value) in the shaped resonator ($\alpha = 4$) is shown in Figure 3.10 (dashed line). At both ends the velocity is 0 (closed boundary). The velocity amplitude distribution is not symmetric, and the maximum velocity is shifted to $X = 0.32$ inside the resonator.

Shaped resonator (α =5.75)

For a geometry of $l = 0.2m$ and $r_0 / l = 0.02$ at driving force $\tilde{A} = 5 \times 10^{-4}$, the resonance for the shaped axisymmetric resonator ($\alpha = 5.75$) occurs at a higher frequency of $\Omega = 1.359$. The distribution of the peak-to-peak pressure amplitude along the resonator is shown in Figure 3.9 (solid line). The peak-to-peak pressure amplitude distribution is not symmetric. The maximum value $|P|$=2.13 P_0 is found at the small end ($X = 0$), which is further increased. The pressure waveforms at the small end are shown in Figure 3.12. Comparing with Figure 3.11, the pressure is higher when flare constant α is increased from 4 to 5.75. The amplitude distribution of velocity (peak-to-peak value) in the shaped resonator ($\alpha = 5.75$) is shown in Figure 3.10 (solid line).

LARR resonator

For a shaped low aspect ratio rectangular (LARR) resonator ($\alpha = 5.75$, $l = 0.2m$, $h / l = 0.02$), it resonates at a frequency of $\Omega = 1.357$ when driving force $\tilde{A} = 5 \times 10^{-4}$. The pressure waveforms at the small end are shown in Figure 3.13. The peak-to-peak pressure is $0.95 P_0$, which is much lower comparing to the axisymmetric resonator with the same flare constant α. This is probably because the LARR resonator is more dissipative than the axisymmetric resonator.

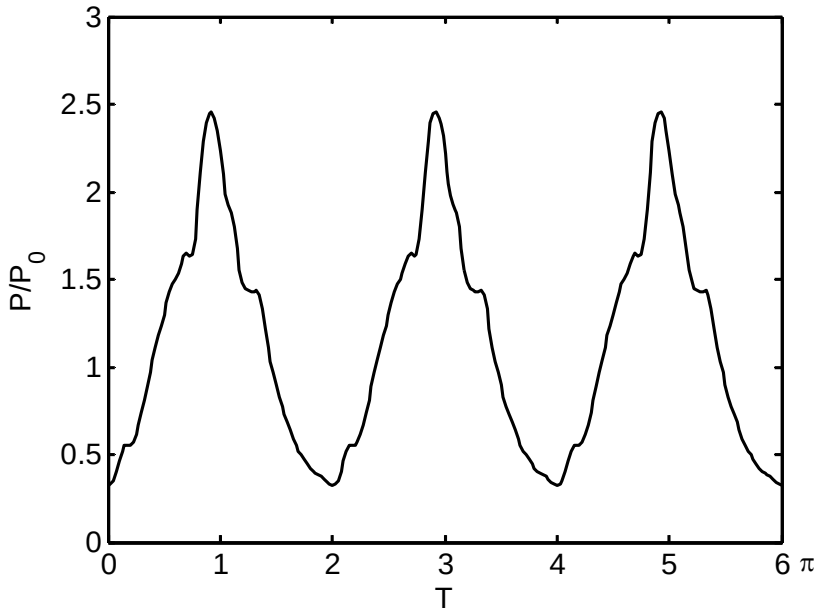

Figure 3.12 Pressure waveforms at the small end of the axisymmetric resonator.

$S = \pi(r_0 / l)^2 e^{\alpha X}$, $\alpha = 5.75$, $l = 0.2m$, $r_0 / l = 0.02$, $X = 0$.

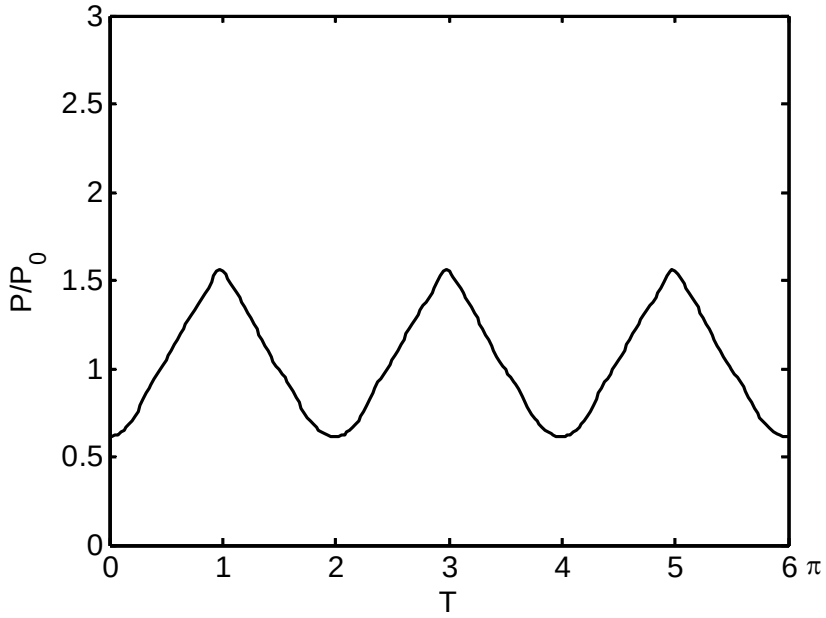

Figure 3.13 Pressure waveforms at the small end of the LARR resonator.

$S = b_0 h / l^2 e^{\alpha X}$, $\alpha = 5.75$, $l = 0.2m$, $h / l = 0.02$, $X = 0$.

Comparison with reported results

For the comparison purpose, the pressure waves obtained by Erickson and Zinn (2003) at the small end in the axisymmetric resonator are reproduced here with the same condition by setting $G_S = 0$ and assigning $G_B = 0.01$ in Eq. (3.51). The results are shown in Figure 3.14 by the dashed lines. In their results (the dashed line), the pressure waveforms were not dependent on the resonator dimensions, such as the resonator length l and the ratio r_0 / l, because there was no shear viscosity term in the wave equation. The solid lines in Figure 3.14 are the pressure waves calculated in the present study using Eqs. (3.51) and (3.62), in which G_B and G_S are evaluated according to Eq. (3.50) and the resonator length is $l = 0.2m$, $R_0 = r_0 / l = 0.02$.

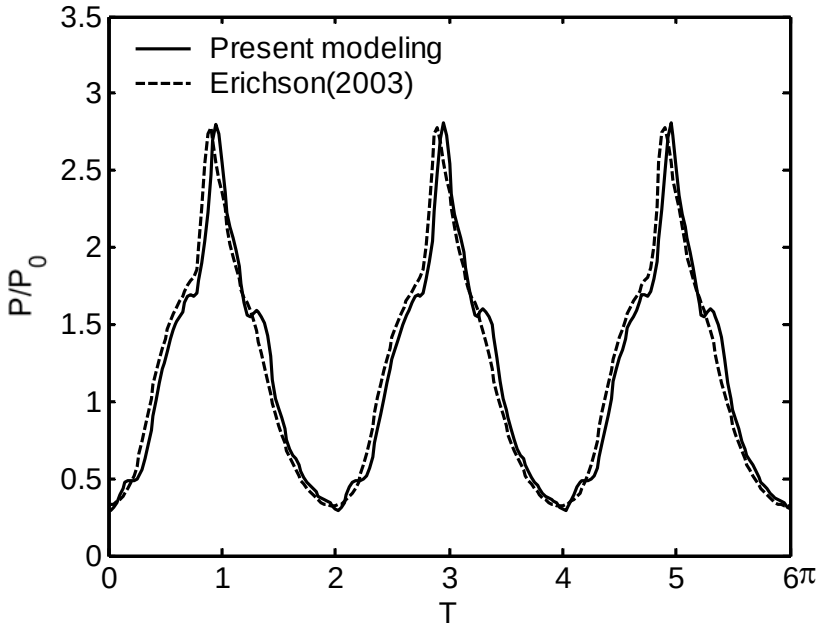

Figure 3.14 Pressure waveforms at the small end of the axisymmetric resonator. $S = \pi(r_0 / l)^2 e^{\alpha X}$, $\alpha = 5.75$**. Dashed line: reproduced for the results by Erickson and Zinn (2003). Solid line: Calculated from Eqs. (3.51) and (3.62),** $l = 0.2m$, $r_0 / l = 0.023$ **.**

It is seen that two waveforms are very similar in terms of amplitudes and shapes. The comparison is to validate the calculations in the present study. The results also indicate that the dimension effect is not significant in this case.

3.5.2 EFFECT OF RESONATOR DIMENSIONS ON RESONANCE CHARACTERISTICS

The study on effect of resonator dimensions is conducted through varying the dimension related parameters in the nonlinear dynamic equations, which are mainly associated with the shear viscosity dissipation terms. According to the dynamic equations and the resonator configurations, the parameters used in this study are r_0/l, h/l and l. These parameters are reduced from normal values to observe how the resonance characteristics change when the resonator dimensions are shrunken to miniature scales. The cross-section dimensions r_0/l and h/l also have effect on the nonlinear resonance, since they are important factor for dissipation. The study by Erickson and Zinn (2003) showed that the maximum pressures were obtained in the resonator with the flare constant $\alpha = 5.75$. In the following, most of our studies are conducted on this type of resonators. The studies are focused on (i) the dimension effect on the frequency response of pressures around the resonance frequencies, (ii) the dimension effect on the pressure waveforms and amplitudes, (iii) the dimension effect on the compression ratios, and (iv) the dimension effect on the resonance frequencies.

Dimension effect on the frequency response

Figure 3.15 shows the dimensionless frequency response at the small end of axisymmetric resonators ($\alpha = 5.75$ and $l = 0.2m$) with different cross-section

dimensions (r_0/l). As shown in Figure 3.15, the frequency response function is r_0/l dependent. With an increasing dimension (r_0/l), the response curve becomes more asymmetric and the resonance frequency leans towards higher frequencies. At the same time, pressure amplitudes also increase with a larger r_0/l .

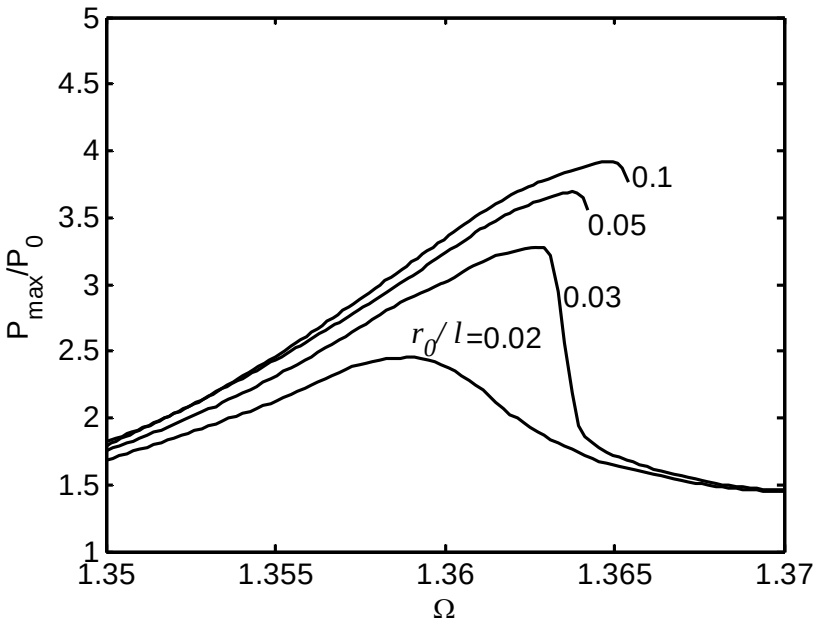

Figure 3.15 Dimensionless frequency response for axisymmetric resonator.

$S = \pi (r_0/l)^2 e^{\alpha X}$, $\alpha = 5.75$, $l = 0.2m$.

Dimension effect on the pressure waveforms and amplitudes

The pressure waveforms at the small end of axisymmetric resonators ($\alpha = 5.75$, $l = 0.2m$) with different r_0/l are plotted in Figure 3.16. When r_0/l is 0.05, the pressure amplitudes are large with sharp peaks (Figure 3.16(a)), indicating a strong resonance. When r_0/l is reduced to 0.02, the pressure amplitudes are reduced, as well as the sharp peaks (Figure 3.16(b)). When r_0/l is further reduced to 0.01 (Figure 3.16(c)), the pressure amplitudes are reduced further and there are no sharp peaks, indicating that the resonance has been weaken due to the energy dissipation. The

pressure waveforms in Figure 3.16 are calculated at resonance frequencies. Since r_0 / l is different, the resonance frequency Ω is therefore different.

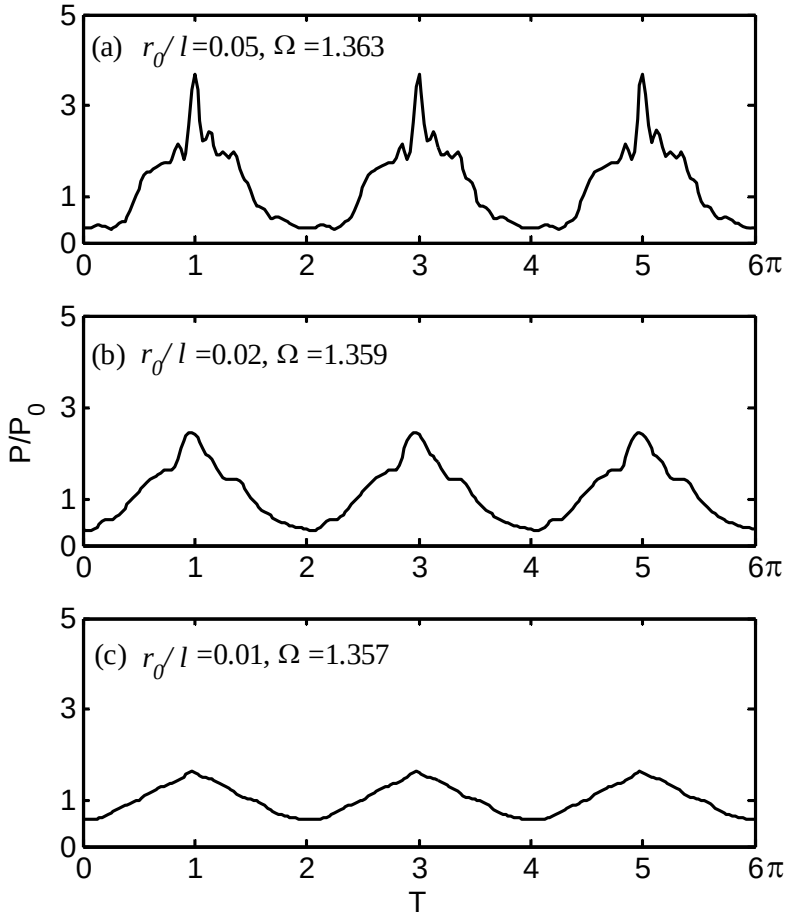

Figure 3.16 Pressure waveforms at the small end of the axisymmetric resonator. $S = \pi\left(r_0 / l\right)^2 e^{\alpha X}$**,** $\alpha = 5.75$**,** $l = 0.2m$**. (a)** $r_0 / l = 0.05$**, (b)** $r_0 / l = 0.02$**, and (c)** $r_0 / l = 0.01$**.**

The similar situation is also observed for the pressure waves in the LARR resonator ($\alpha = 5.75$ and $l = 0.2m$), which are plotted out in Figure 3.17. In this case, the waveforms have been smoothed down at $r_0 / l = 0.02$, because the LARR resonator is more dissipative than the axisymmetric resonator.

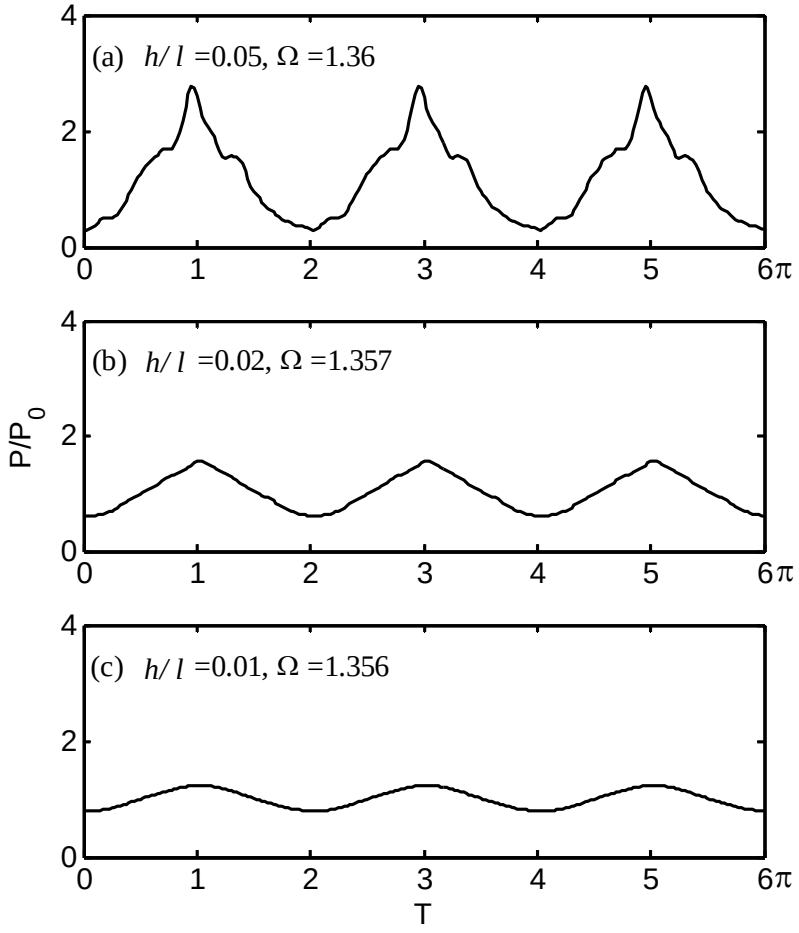

Figure 3.17 Pressure waveforms at the small end of the LARR resonator. $S = b_0 h / l^2 e^{\alpha X}$, $\alpha = 5.75, l = 0.2m$. **(a)** $h/l = 0.05$, **(b)** $h/l = 0.02$, **and (c)** $h/l = 0.01$.

Dimension effect on the compression ratios

The compression ratio is the ratio of the maximum pressure to the minimum pressure in one cycle. The higher compression ratio indicates a more useful dynamic pressure. The compression ratios are calculated based on the maximum and minimum pressures at the small end of the resonators. The solid lines in Figure 3.18 presents the compression ratio for the axisymmetric resonator ($\alpha = 5.75$) with different length ($l = 0.02m$ and $0.05m$). It is seen that the compression ratio can be greater than 10

when r_0/l is larger than 0.04 for the axisymmetric resonator with $l = 0.2\,\text{m}$, but drops to 2 when r_0/l is less than 0.01, showing that the cross-section dimension of the resonator has tremendous effect on the compression ratio, depending on r_0/l. On the other hand, when the overall length of the resonator, l, is reduced, the compression ratio is also reduced, as shown in Figure 3.18 by the results of $l = 0.05m$. This is because the shorter length will lead to a higher resonance frequency and therefore higher dissipation by the shear viscosity. The results presented in Figure 3.18 suggest that the resonator dimensions may be controlled by r_0/l and l for given driving strength and compression ratio.

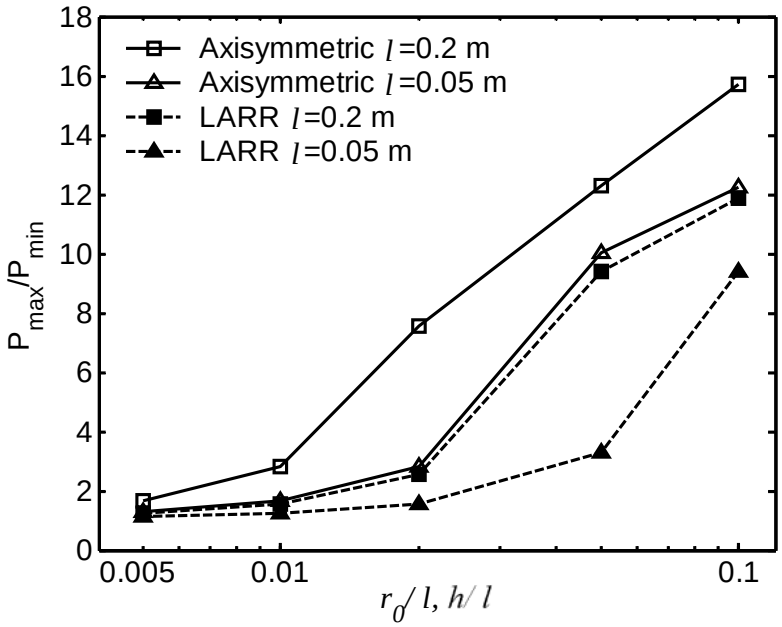

Figure 3.18 Compression ratios for axisymmetric and LARR resonators, $\alpha = 5.75$.

Similar results for the LARR resonator are also presented in Figure 3.18. The compression ratios for the LARR resonator are always lower than that of axisymmetric resonator. If one takes $l = 0.05m$ and $h/l = 0.05$, i.e., $l = 50mm$ and

$h = 2.5mm$, which is a small resonator, one may expect to have standing waves with a compression ratio 3, according to the results in Figure 3.18.

Dimension effect on the resonance frequencies

The cross-section dimensions of the resonators are found to have minor effect on the resonance frequencies, which are primarily determined by the resonator lengths and the axial-expansion shape. The calculated results for both axisymmetric and LARR resonators, plotted out in Figure 3.19, show that the variation of the dimensionless frequency (Ω) is less than 1% when the cross-section dimensions (r_0/l and h/l) change form 0.1 to 0.005.

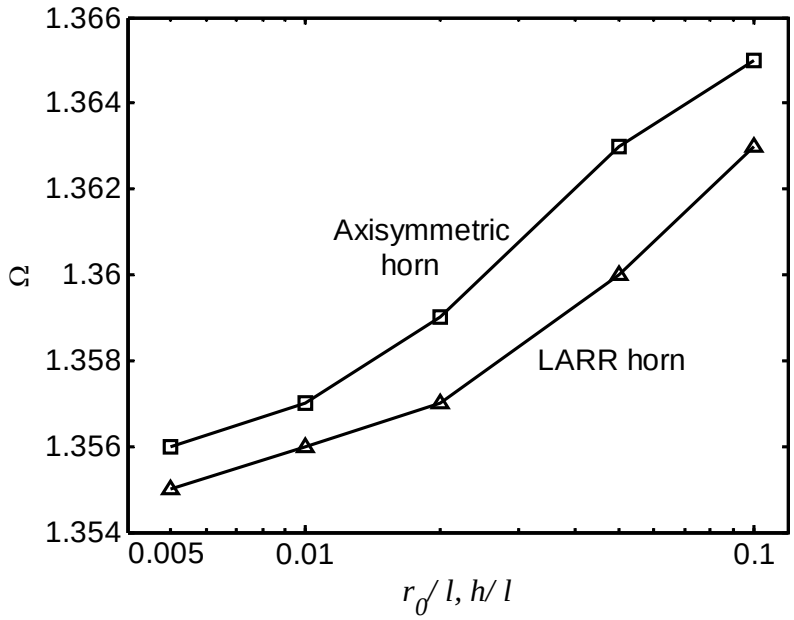

Figure 3.19 Dimensionless resonance frequency versus cross-section dimensions for both axisymmetric and LARR resonators, $\alpha = 5.75$, $l = 0.2m$.

3.6 SUMMARY

The effect of resonator dimensions on the nonlinear standing waves inside the shaped resonators has been studied. A shear viscosity term has been added to the one-dimensional momentum equation for the average axial velocity, and the wave equation has been solved by Galerkin's method for a 2D (axisymmetric) resonator and a 3D (low aspect ratio rectangular) resonator, whose cross sections are exponentially expanded. The following conclusions can be drawn: (i) the resonator configuration has great impact on the dissipation according to the shear and bulk vicious terms; (ii) shock waves are obtained in straight resonators at strong driving, and the pressure amplitude is only about 10% of ambient pressure; (iii) shock-free waves are obtained in shaped resonators at both weak and strong driving, and pressure amplitude may exceed $3P_0$, 3 times of the ambient pressure; (iv) shear viscosity dissipation plays a crucial role when the resonator sizes are reduced. The resonator length (l) and the ratio of cross-section dimension to the length (r_0/l and h/l) are two controlling parameters. When r_0/l and h/l are less than 0.01, the resonance becomes weak and the resonators are not functioning in these cases to generate large-amplitude pressures; (v) the dimension ratios control the frequency response curves in the same way as the excitation level does, following the hardening behavior of the shaped resonators.

CHAPTER 4

NONLINEAR RESONANCES GENERATED BY BOUNDARY DRIVING

4.1 INTRODUCTION

In Chapter Three, the high amplitude pressures in shaped resonators are generated by shaking the entire resonators. The entire shaking is believed to be more efficient in power delivery (Lawrenson *et al*., 1998) comparing to other methods, such as the piston driving. In order to broaden the potential of high amplitude pressures in shaped resonators in other engineering applications, such as miniature or micro fluidic devices, it is necessary to explore other driving mechanisms for various resonator configurations. The boundary driving in these applications may be a better way than shaking to generate useful dynamic pressures.

Following the discussions in Chapter 3 on nonlinear acoustic waves obtained by shaking resonators, this chapter presents a study of nonlinear resonance generated by the boundary driving. The theoretical modeling using the Galerkin's method is conducted on an axisymmetric resonator with one end connected to a piston. The resonance frequencies, pressures at two ends of the resonator and their ratios are calculated and compared with those obtained under shaking condition. Finally, some features and characteristics of two different driving methods are discussed.

4.2 NONLINEAR STANDING WAVES OBTAINED BY A PISTON

4.2.1 GOVERNING EQUATIONS

We consider an axisymmetric resonator shown in Figure 4.1. The resonator has length l and radius $r(x)$ which is a function of x. At $x=0$, the radius is r_0 and the cross-sectional area is $s_0=\pi r_0^2$. The cross-sectional area of the resonators is expanded exponentially along its axis, given by $s=s_0e^{\alpha l/x}$ (α is the flare constant indicating the rate of expansion). The resonator is sealed at the small end ($x=0$) and connected to a piston at the other end ($x=l$). The piston is oscillating at a velocity $u(t)=\tilde{u}\sin(\omega t)$ with the driving frequency ω.

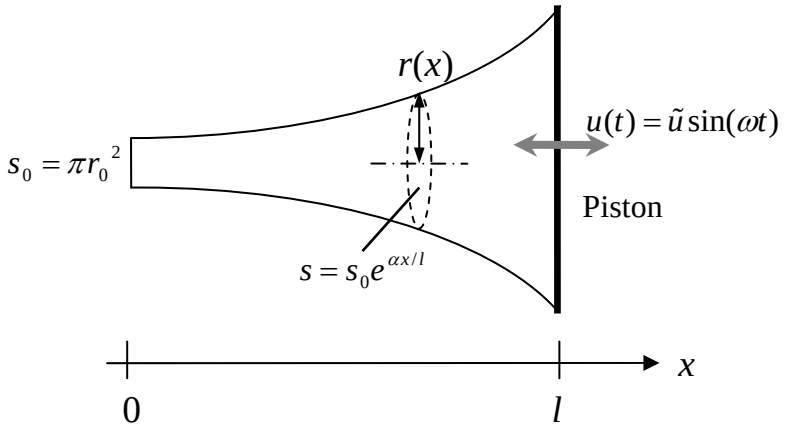

Figure 4.1 The exponentially expanded resonator with a piston driving at one end.

Three basic equations to describe the gas motion inside the resonator are: equation of state, equation of mass conservation and equation of momentum conservation, which are listed here

$$p=\left(\frac{\rho}{\rho_0}\right)^{\gamma}p_0, \tag{4.1}$$

$$\frac{\partial \rho}{\partial t}+\frac{1}{r^2}\frac{\partial}{\partial t}\left(r^2\rho\bar{u}\right)=0, \tag{4.2}$$

$$\frac{\partial u}{\partial t}+\bar{u}\frac{\partial \bar{u}}{\partial x}=-\frac{1}{\rho}\frac{\partial p}{\partial x}+\frac{(\zeta+4\eta/3)}{\rho}\frac{\partial}{\partial x}\left(\frac{1}{r^2}\frac{\partial}{\partial x}(r^2u)\right)-\frac{\sqrt{2\rho\eta\omega}}{r\rho}\bar{u}. \tag{4.3}$$

Equations (4.1) and (4.2) are the same as the fist two basic equations in the shaking driving (Eq. (3.24) and (3.29)) in Chapter 3. The momentum equation (4.3) is different from Eq. (3.30), as there is no acceleration term in the present case.

By letting the shaking acceleration be zero, i.e., setting $a=0$ and ignoring third-order terms in Eq. (3.46), we can get the one-dimensional governing equation in terms of velocity potential φ for piston driving,

$$\begin{aligned}&\frac{{c_0}^2}{r^2}\frac{\partial}{\partial x}\left(r^2\frac{\partial\varphi}{\partial x}\right)-\frac{\partial^2\varphi}{\partial t^2}+\frac{\delta}{r^2}\frac{\partial^2}{\partial t\partial x}\left(r^2\frac{\partial\varphi}{\partial x}\right)\\&\quad=\sqrt{\frac{2\eta\omega}{r^2\rho}}\frac{\partial\varphi}{\partial t}+2\frac{\partial^2\varphi}{\partial x\partial t}\frac{\partial\varphi}{\partial x}+\frac{\gamma-1}{r^2}\frac{\partial\varphi}{\partial t}\frac{\partial}{\partial x}\left(r^2\frac{\partial\varphi}{\partial x}\right).\end{aligned} \tag{4.4}$$

Using the dimensionless variables defined by Eq. (3.47) and (3.48), the dimensionless form of Eq. (4.4) is obtained as

$$\begin{aligned}&\frac{\partial^2\Phi}{\partial T^2}-\frac{1}{\Omega^2\pi^2}\left\{\frac{1}{R^2}\frac{dR^2}{dX}\right\}\frac{\partial\Phi}{\partial X}-\frac{1}{\Omega^2\pi^2}\frac{\partial^2\Phi}{\partial X^2}=\\&\quad-\frac{2}{\Omega}\frac{\partial^2\Phi}{\partial X\partial T}\frac{\partial\Phi}{\partial X}-\frac{(\gamma-1)}{\Omega}\left\{\frac{1}{R^2}\frac{dR^2}{dX}\right\}\frac{\partial\Phi}{\partial T}\frac{\partial\Omega}{\partial X}-\frac{(\gamma-1)}{\Omega}\frac{\partial\Phi}{\partial T}\frac{\partial^2\Phi}{\partial X^2}\\&\quad+\frac{G_B}{\pi^3\Omega}\left\{\frac{1}{R^2}\frac{dR^2}{dX}\right\}\frac{\partial^2\Phi}{\partial T\partial X}+\frac{G_B}{\pi^3\Omega}\frac{\partial^3\Phi}{\partial T\partial X^2}-\frac{G_S}{\Omega^{1/2}R}\frac{\partial\Phi}{\partial T}.\end{aligned} \tag{4.5}$$

4.2.2 BOUNDARY CONDITIONS

The resonator in Figure 4.1 is driven by a piston at $x = l$. The dimensional piston velocity is

$$u(t) = \tilde{u}\sin(\omega t), \tag{4.6}$$

where $\tilde{u}$ is velocity amplitude and ω is driving frequency. The dimensionless form is

$$U(T) = \tilde{U}\sin(T), \tag{4.7}$$

where $\tilde{U} = \dfrac{\tilde{u}}{l\omega_0}$ is the dimensionless velocity amplitude of the piston, indicating the driving strength. The boundary conditions in dimensionless forms are therefore

$$\left.\frac{\partial \Phi}{\partial X}\right|_{X=0} = 0, \qquad \left.\frac{\partial \Phi}{\partial X}\right|_{X=1} = \tilde{U}\sin(T). \tag{4.8}$$

From the discussion in Chapter 3.3, it is known that the trial functions depend only on X, and they satisfy homogenous boundary conditions. However, in the case of piston driving, the boundary conditions (Eq. (4.8)) are non-homogenous. In order to apply the Galerkin's method, the non-homogenous boundary conditions are converted to become homogenous by the following method.

Assuming that the solution Φ consists of two parts, i.e.,

$$\Phi = \Phi_A + \Phi_B, \tag{4.9}$$

where Φ_A is a new unknown function to be solved, which satisfies homogenous boundary conditions

$$\left.\frac{\partial \Phi_A}{\partial X}\right|_{X=0} = 0, \qquad \left.\frac{\partial \Phi_A}{\partial X}\right|_{X=1} = 0\,, \tag{4.10}$$

and Φ_B is a specified function, which satisfies non-homogenous boundary conditions

$$\left.\frac{\partial \Phi_B}{\partial X}\right|_{X=0} = 0, \quad \left.\frac{\partial \Phi_B}{\partial X}\right|_{X=1} = \tilde{U}\sin(T)\,. \tag{4.11}$$

By substitution of Eq. (4.9) into the governing equations, the boundary conditions (Eq. (4.8)) describing the piston oscillation can be converted to the homogenous boundary conditions. Thus the Galerkin's method can be applied to solve the unknown function Φ_A.

Substitution of Eq (4.9) into Eq (4.5), the modified governing equation for axisymmetric resonator by piston driving is obtained as

$$\begin{aligned}
&\frac{\partial^2 \Phi_A}{\partial T^2} - \frac{1}{\Omega^2\pi^2}\left\{\frac{1}{R^2}\frac{dR^2}{dX}\right\}\frac{\partial \Phi_A}{\partial X} - \frac{1}{\Omega^2\pi^2}\frac{\partial^2 \Phi_A}{\partial X^2} + \frac{2}{\Omega}\frac{\partial^2 \Phi_A}{\partial X \partial T}\frac{\partial \Phi_A}{\partial X} + \\
&\frac{(\gamma-1)}{\Omega}\left\{\frac{1}{R^2}\frac{dR^2}{dX}\right\}\frac{\partial \Phi_A}{\partial T}\frac{\partial \Phi_A}{\partial X} + \frac{(\gamma-1)}{\Omega}\frac{\partial \Phi_A}{\partial T}\frac{\partial^2 \Phi_A}{\partial X^2} \\
&-\frac{G_B}{\pi^3\Omega}\left\{\frac{1}{R^2}\frac{dR^2}{dX}\right\}\frac{\partial^2 \Phi_A}{\partial T \partial X} - \frac{G_B}{\pi^3\Omega}\frac{\partial^3 \Phi_A}{\partial T \partial X^2} + \frac{G_S}{R\Omega^{1/2}}\frac{\partial \Phi_A}{\partial T} = F_{piston},
\end{aligned} \tag{4.12}$$

where

$$F_{piston} = -\frac{\partial^2 \Phi_B}{\partial T^2} + \frac{1}{\Omega^2 \pi^2}\left\{\frac{1}{R^2}\frac{dR^2}{dX}\right\}\frac{\partial \Phi_B}{\partial X} + \frac{1}{\Omega^2 \pi^2}\frac{\partial^2 \Phi_B}{\partial X^2} - \frac{2}{\Omega}\frac{\partial^2 \Phi_A}{\partial X \partial T}\frac{\partial \Phi_B}{\partial X} - \frac{2}{\Omega}\frac{\partial^2 \Phi_B}{\partial X \partial T}\frac{\partial \Phi_A}{\partial X}$$
$$- \frac{2}{\Omega}\frac{\partial^2 \Phi_B}{\partial X \partial T}\frac{\partial \Phi_B}{\partial X} - \frac{(\gamma-1)}{\Omega}\left\{\frac{1}{R^2}\frac{dR^2}{dX}\right\}\frac{\partial \Phi_A}{\partial T}\frac{\partial \Phi_B}{\partial X} - \frac{(\gamma-1)}{\Omega}\left\{\frac{1}{R^2}\frac{dR^2}{dX}\right\}\frac{\partial \Phi_B}{\partial T}\frac{\partial \Phi_A}{\partial X}$$
$$- \frac{(\gamma-1)}{\Omega}\left\{\frac{1}{R^2}\frac{dR^2}{dX}\right\}\frac{\partial \Phi_B}{\partial T}\frac{\partial \Phi_B}{\partial X} - \frac{(\gamma-1)}{\Omega}\frac{\partial \Phi_A}{\partial T}\frac{\partial^2 \Phi_B}{\partial X^2} - \frac{(\gamma-1)}{\Omega}\frac{\partial \Phi_B}{\partial T}\frac{\partial^2 \Phi_A}{\partial X^2}$$
$$- \frac{(\gamma-1)}{\Omega}\frac{\partial \Phi_B}{\partial T}\frac{\partial^2 \Phi_B}{\partial X^2} - \frac{G_B}{\pi^3 \Omega}\left\{\frac{1}{R^2}\frac{dR^2}{dX}\right\}\frac{\partial^2 \Phi_B}{\partial T \partial X} - \frac{G_B}{\pi^3 \Omega}\frac{\partial^3 \Phi_B}{\partial T \partial X^2} + \frac{G_S}{R\Omega^{1/2}}\frac{\partial \Phi_B}{\partial T}. \tag{4.13}$$

F_{piston} consists all terms associated with Φ_B relating to the piston motion. There are many functions that satisfy the boundary conditions Eq. (4.11). A simple one is taken in the present study,

$$\Phi_B = \tilde{U}\frac{X^2}{2}\sin(T). \tag{4.14}$$

After solving the velocity potential $\Phi = \Phi_A + \Phi_B$, the density and pressure in the resonator driven by a piston can be evaluated by respectively,

$$\frac{\rho}{\rho_0} = \left[1-(\gamma-1)\pi^2\left(\Omega\frac{\partial \Phi_A}{\partial T} + \Omega\frac{\partial \Phi_B}{\partial T} + \frac{1}{2}\left(\frac{\partial \Phi_A}{\partial X} + \frac{\partial \Phi_B}{\partial X}\right)^2 \right.\right.$$
$$\left.\left. - \frac{G_B}{\pi^3}\frac{1}{S}\frac{\partial}{\partial X}\left(S\frac{\partial \Phi_A}{\partial X} + S\frac{\partial \Phi_B}{\partial X}\right) + \frac{G_S \Omega^{1/2}}{R}\left(\Phi_A + \Phi_B\right)\right)\right]^{\frac{1}{\gamma-1}}, \tag{4.15}$$

and

$$\frac{P}{P_0}=\left[1-(\gamma-1)\pi^2\left(\Omega\frac{\partial\Phi_A}{\partial T}+\Omega\frac{\partial\Phi_B}{\partial T}+\frac{1}{2}\left(\frac{\partial\Phi_A}{\partial X}+\frac{\partial\Phi_B}{\partial X}\right)^2\right.\right.$$
$$\left.\left.-\frac{G_B}{\pi^3}\frac{1}{S}\frac{\partial}{\partial X}\left(S\frac{\partial\Phi_A}{\partial X}+S\frac{\partial\Phi_B}{\partial X}\right)+\frac{G_S\Omega^{1/2}}{R}\left(\Phi_A+\Phi_B\right)\right)\right]^{\frac{\gamma}{\gamma-1}}. \tag{4.16}$$

4.2.3 DRIVING STRENGTH $\tilde{U}$

As the piston oscillates harmonically, it is of an acceleration

$$a(t)=\tilde{a}\cos(\omega t), \tag{4.17}$$

where $\tilde{a}$ is the acceleration amplitude of the harmonic piston motion and ω is the driving frequency. The piston acceleration can be evaluated from the velocity,

$$a(t)=\frac{d}{dt}u(t)=\frac{d}{dt}\left(\tilde{u}\sin(\omega t)\right)=\tilde{u}\omega\cos(\omega t). \tag{4.18}$$

Comparing the right hand sides of Eqs. (4.17) and (4.18), the amplitude relation between the acceleration and velocity of the piston motion is

$$\tilde{a}=\tilde{u}\omega. \tag{4.19}$$

In dimensionless forms, we have the acceleration

$$A(T)=\tilde{A}\cos(T), \tag{4.20}$$

the velocity,

$$U(T)=\tilde{U}\sin(T), \tag{4.21}$$

and

$$\tilde{A} = \tilde{U}\Omega . \tag{4.22}$$

The dimensionless variables are defined by

$$T = \omega t , \ \tilde{U} = \frac{\tilde{u}}{l\omega_0} , \ \tilde{A} = \frac{\tilde{a}}{l\omega_0^{\,2}} . \tag{4.23}$$

Using Eq. (4.22), the piston driving strength $\tilde{U}$ can be converted to an acceleration strength $\tilde{A}$. This will be used in the following discussion when the piston driving is compared with the shaking driving.

4.3 RESULTS AND DISSCUSIONS

The cross-sectional area of the resonator is given by

$$S = S_0 e^{\alpha X}, \tag{4.24}$$

where $S_0 = \pi\left(r_0 / l\right)^2$ is the dimensionless cross-sectional area at the small end ($X = 0$). $\alpha = 0$ represents a straight resonator without expansion and $\alpha > 0$ represents exponentially expanded resonator. The gas inside the resonators is air.

4.3.1 ACOUSTIC CHARACTERISTICS FOR DIFFERENT VALUES OF α

Pressure waveforms

It is known that high amplitude pressures will be located at the small end in a shaped resonator. Figure 4.2 illustrates the resonance pressure waveforms at the small end ($X = 0$) of exponentially expanded resonators with various flare constants. The resonator geometries are $\alpha = 0$, 2, 4, $l = 0.02m$ and $r_0 / l = 0.02$. The piston driving strength in this case is $\tilde{U} = 5 \times 10^{-4}$ (according to Eq. (4.22), its acceleration amplitude is of the same order as those in shaking case, considering $\Omega < 1.5$ in these resonators). It shows saw-tooth waveforms with low pressure amplitudes for the straight ($\alpha = 0$) and little expanded ($\alpha = 2$) resonators, and shock-free waveforms with high pressure amplitudes for highly expanded ($\alpha = 4$) resonator. These are typical characteristics in shaped resonators under shaking conditions.

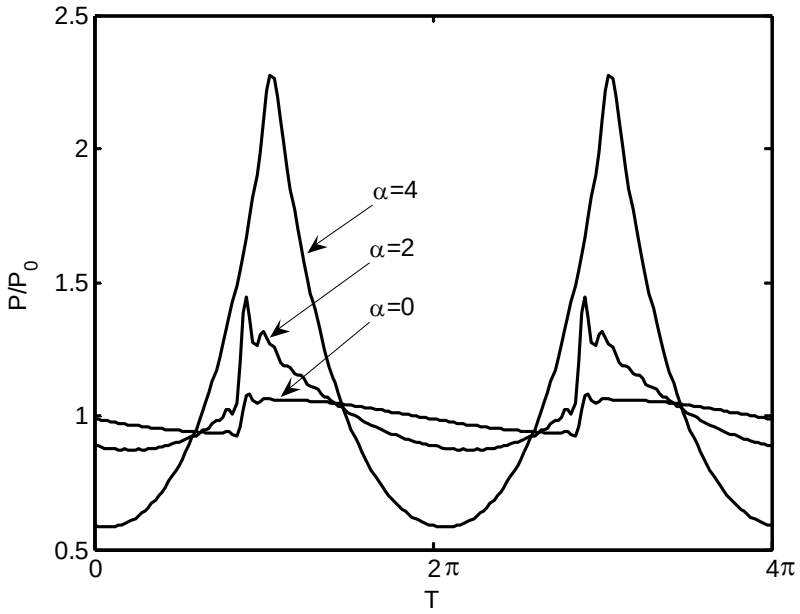

Figure 4.2 The waveforms at $X = 0$ in exponentially expanded resonators with different flare constant ($\alpha = 0, 2, 4$, $l = 0.2m$, $r_0 / l = 0.02$, $\tilde{U} = 5\times10^{-4}$).

Resonance frequencies

The resonance frequencies of the resonators ($l = 0.2m$, $r_0 / l = 0.02$) with different expansion rate α are identified based on the driving frequencies which produce maximum pressure amplitudes. The results are shown in Figure 4.3, together with the frequencies calculated by Eq. (3.83). Two driving strengths are calculated here, $\tilde{U} = 5\times10^{-4}$ and $\tilde{U} = 5\times10^{-6}$. It is seen that the resonance frequency basically follows Eq. (3.83) to increase with the expansion rate. For a straight resonator ($\alpha = 0$), the resonance frequency is $\Omega = 1$. When the flare constant increases to 6, the resonance frequency raises to about 1.39. It also can be seen that the strong driving ($\tilde{U} = 5\times10^{-4}$) increases the resonance frequencies comparing to the weak driving ($\tilde{U} = 5\times10^{-6}$), showing the hardening behavior. The calculated results for $\alpha = 5.6$ is also depicted in Figure 4.3, because the exponentially expanded resonator with this

flare constant is used in the experiment study (see details in Chapter 6). The calculated resonance frequency for $\alpha = 5.6$ is about 1.35.

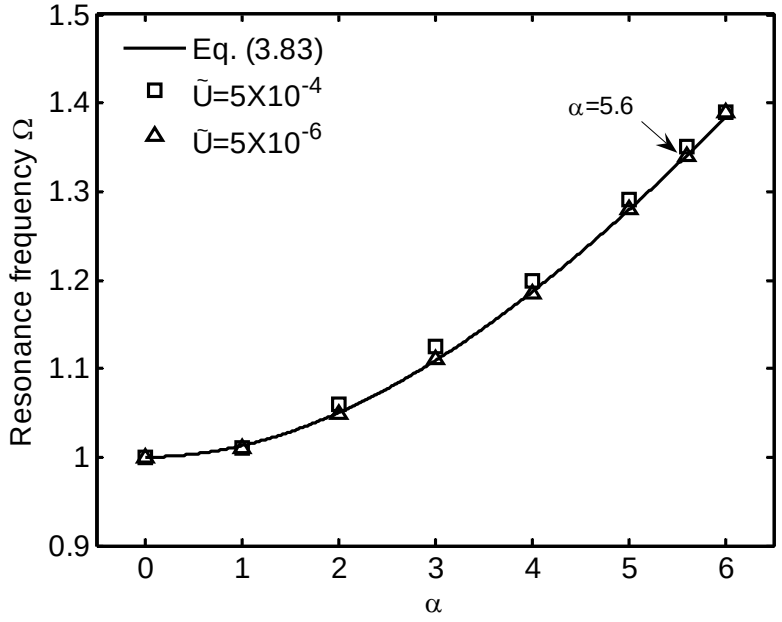

Figure 4.3 The dimensionless resonance frequency of exponentially expanded resonators ($l = 0.2m$, $r_0 / l = 0.02$) with different flare constant. The open squares and triangles are the results at strong and weak driving strengths respectively. The solid line shows the predicted results by Eq. (3.83).

Ratios of pressure amplitudes from two ends

The ratios of the pressure amplitude at the small end to the pressure amplitude at the big end are calculated for resonators ($l = 0.2m$, $r_0 / l = 0.02$) under different expansion rates and driving strengths. The results are plotted in Figure 4.4. For a straight resonator ($\alpha = 0$), the pressure ratio is 1, indicating that both ends have equal pressure amplitudes. The pressure ratio increases slowly with the expansion rate in the lower range where the flare constant $\alpha < 5$, and it goes up much faster after $\alpha > 5$, especially under higher strength driving. With $\alpha = 6$ the compression ratio reaches to 25 at the strong driving. Here the results for $\alpha = 5.6$ is also plotted. The pressure ratio

for $\alpha = 5.6$ is 18.6 at strong driving ($\tilde{U} = 5\times10^{-4}$) and 16.5 at weak driving ($\tilde{U} = 5\times10^{-6}$). These values will be used as references in the experimental studies.

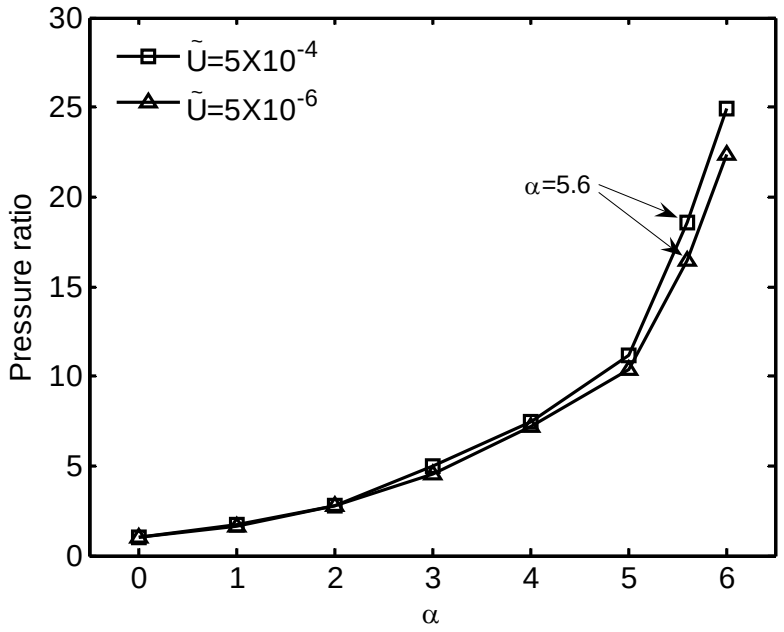

Figure 4.4 The ratio of pressure amplitudes at the small end to the big end in exponentially expanded resonators ($l = 0.2m$, $r_0 / l = 0.02$) with different flare constants.

4.3.2 DISCUSSION ON THE SELECTION OF FUNCTION Φ_B

Since the selection of Φ_B is arbitrary, as long as it satisfies the boundary conditions Eq. (4.11), it is necessary to check if the results would be different for the different types of Φ_B. Two different forms of Φ_B are used to examine their effects on the calculations. One is $\Phi_B = \tilde{U}\frac{X^2}{2}\sin(T)$, which is given in Eq. (4.14) and used in the present study. The other one is $\Phi_B = -\tilde{U}\frac{\cos(\pi X/2)}{\pi/2}\sin(T)$. Using the two functions as Φ_B, the pressure waves in a shaped resonator ($\alpha = 5.75$, $l = 0.2m$, $r_0 / l = 0.05$) at a driving strength of $\tilde{U} = 2.2\times10^{-4}$ are calculated respectively. The results are shown

in Figure 4.5. In order to see both waveforms clearly, the pressure waveforms are shifted a little (otherwise the waveforms will overlap completely). It can be seen that by using $\Phi_B = \tilde{U}\frac{X^2}{2}\sin(T)$ and $\Phi_B = -\tilde{U}\frac{\cos(\pi X/2)}{\pi/2}\sin(T)$, the calculated pressure waveforms are quite similar. It can be concluded that the selection of Φ_B has no effect on the calculation.

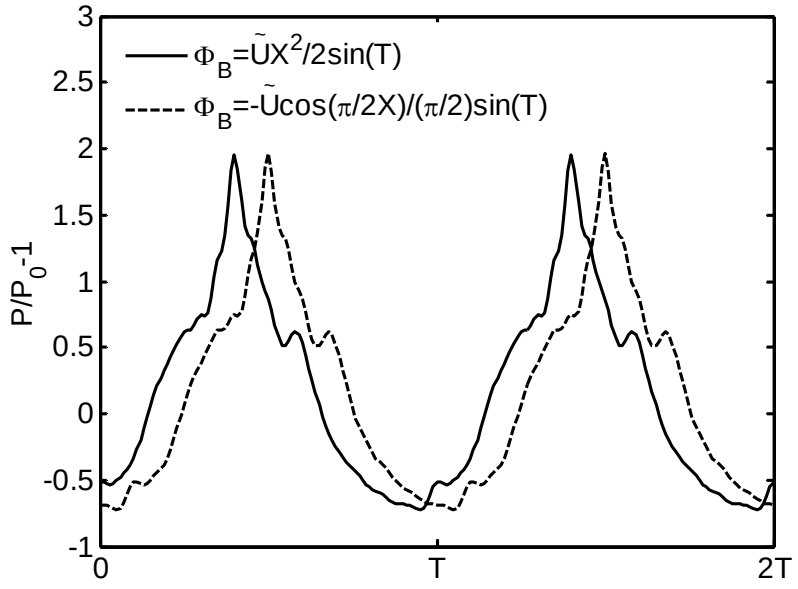

Figure 4.5 The waveforms are produced by piston driving ($\tilde{U} = 2.2\times10^{-4}$) in a shaped resonator ($\alpha = 5.75$, $l = 0.2m$ and $r_0/l = 0.05$).

4.3.3 COMPARISON OF PISTON DRIVING WITH SHAKING METHOD

The piston driving is compared with the shaking driving on the same resonator in terms of resonance characteristics. In order to provide a base for the comparison, the strengths in two driving methods must be related. It is assumed that the piston is of the same acceleration as that produced by the shaking on the resonator, i.e., $\tilde{A} = \tilde{U}\Omega$. The comparison is qualitative because the piston delivery the power to the resonator

through the air contacting to its surface, while the shaking provides excitation to the whole inner surface of the resonator.

Pressure waveforms

Figure 4.6 illustrates the pressure waveforms at the small end of resonators with the flare constant $\alpha = 4$ and 5.75 respectively. Other geometry parameters of the resonators are kept the same as $l = 0.02m$ and $r_0 / l = 0.02$. The dashed lines are the pressures generated by shaking and the solid lines are produced by piston driving. The driving strengths are $\tilde{A} = 1 \times 10^{-4}$ in shaking for both resonators. The corresponding piston driving strength are $\tilde{U} = 8.42 \times 10^{-5}$ and $\tilde{U} = 7.37 \times 10^{-5}$ for $\alpha = 4$ and 5.75 resonators respectively. The piston driving strengths are determined according to $\tilde{U} = \tilde{A} / \Omega$. The results in Figure 4.6 show that the piston driving generates similar pressures to that generated by the shaking, in terms of the waveforms and amplitudes.

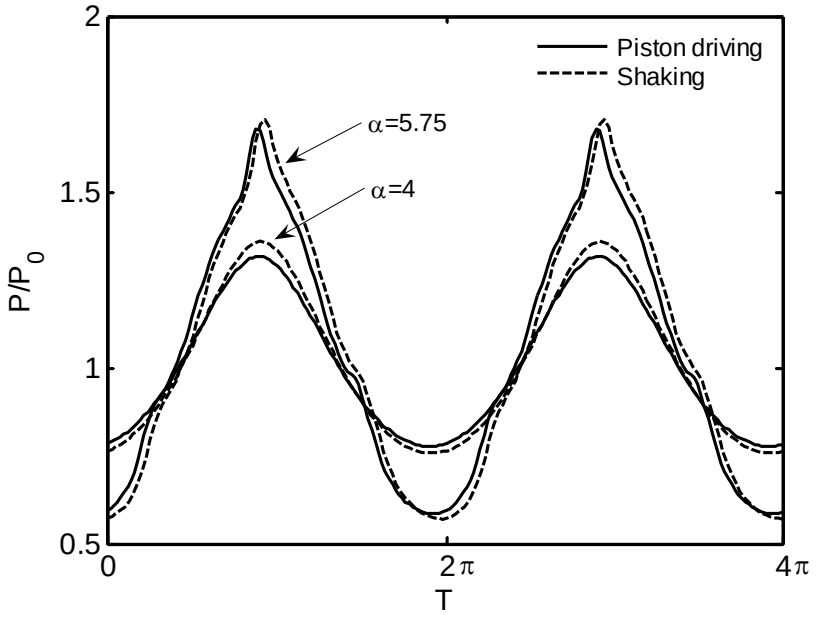

Figure 4.6 The small end pressure waveforms in two exponentially expanded resonators ($\alpha = 4$ and 5.75), obtained by the piston driving and shaking respectively.

Resonance frequencies

The resonance frequencies obtained by the shaking and piston driving are examined to view if the driving mechanism would affect the resonance frequency. This is conducted on a shaped resonator ($\alpha = 5.75$, $l = 0.2m$, $r_0 / l = 0.05$), and the results are listed in Table 4.1. A set of the shaking acceleration $\tilde{A}$ and the corresponding $\tilde{U}$ are denoted as a force set, and five force sets are listed in Table 4.1. For a given shaking driving strength, a resonance frequency corresponding to maximum pressure response can be obtained, which is shown in the second column. For comparison purpose, the piston driving strength is determined by $\tilde{U} = \tilde{A}/\Omega$, where Ω is the resonance frequency for shaking condition. For example, the shaped resonator resonates at Ω=1.357 when the driving strength is $\tilde{A} = 1\times10^{-4}$. When this shaped resonator is driven by the piston, the driving strength is set as $\tilde{U} = 1\times10^{-4}/1.357 = 7.37\times10^{-5}$. It is seen from the Table 4.1 that the effect of the driving method on the resonance frequency is negligible.

Table 4.1 Different driving for a shaped resonator ($\alpha = 5.75, l = 0.2m, r_0 / l = 0.05$).

Force set	Shaking		Piston driving	
	$\tilde{A}$	Resonance frequency Ω	$\tilde{U}$	Resonance frequency Ω
1	1×10^{-4}	1.357	7.37×10^{-5}	1.357
2	2×10^{-4}	1.361	1.47×10^{-4}	1.3605
3	3×10^{-4}	1.3635	2.20×10^{-4}	1.363
4	4×10^{-4}	1.3655	2.93×10^{-4}	1.365
5	5×10^{-4}	1.367	3.66×10^{-4}	1.367

Pressures at X=0 and 1

Figure 4.7 shows the pressure amplitudes at two ends of the shaped resonator ($\alpha = 5.75$, $l = 0.2m$, $r_0 / l = 0.05$). The resonator is driven by shaking and piston respectively with different strength, in terms of force sets which are listed in Table 4.1. When the driving becomes stronger, the pressure amplitude at $X = 0$ increases and the pressure amplitude at $X = 1$ decreases in both driving conditions. For each driving force set, the results obtained from two driving methods are very close. The results presented in Figure 4.7 show that the piston driving has the same effect as the shaking in generating high amplitude pressures.

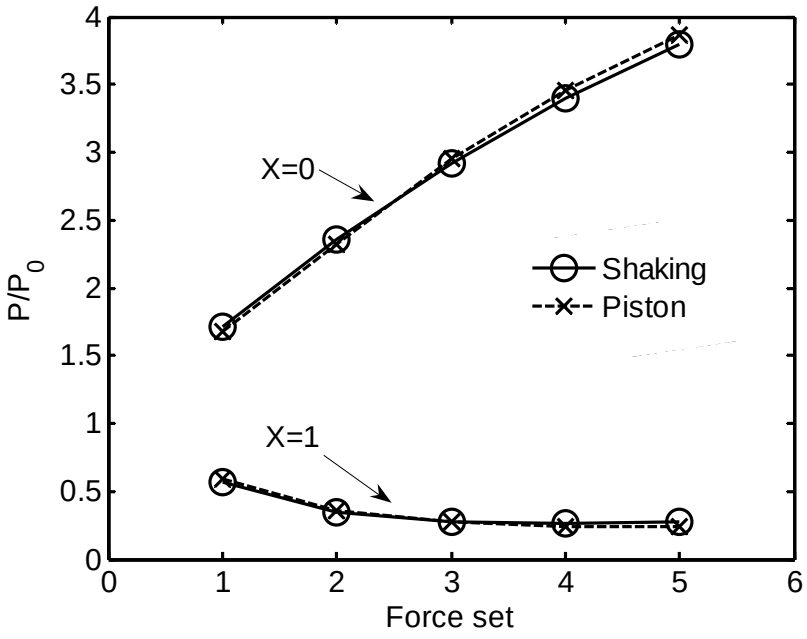

Figure 4.7 Comparison of maximum and minimum pressures produced by shaking and piston driving.

Pressure amplitude ratios between the small end to big end

In another comparison, the pressure amplitude ratios between the small end to big end for the shaped resonator ($\alpha = 5.75$, $l = 0.2m$, $r_0 / l = 0.05$) are calculated, as shown in

Figure 4.8. The pressure amplitude ratios for shaking and piston driving agree well for force set 1, 2 and 3, but become different when the driving strength is increased. The maximum difference is about 2.3 at force set 5, as shown in Figure 4.8.

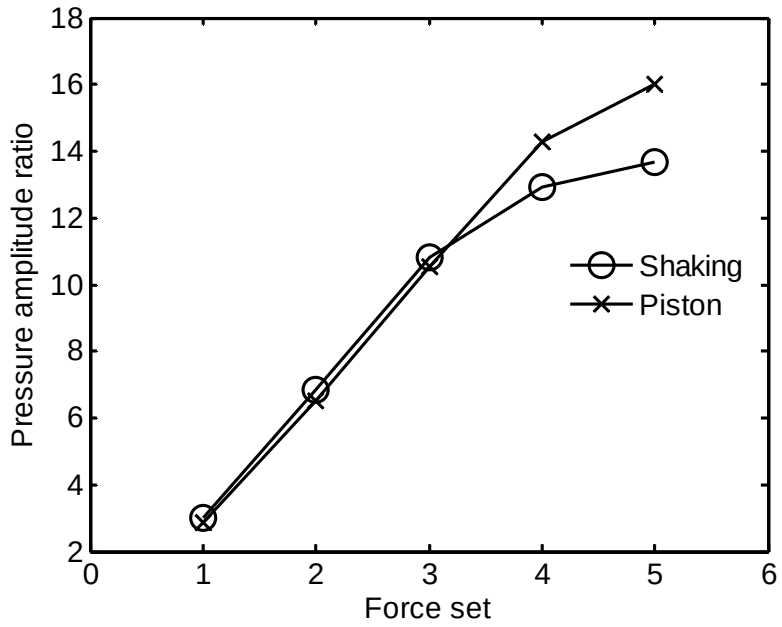

Figure 4.8 Comparison of pressure amplitude ratios between the small end to big end produced by shaking and piston driving.

It should be pointed out that the comparisons conducted here are still qualitative although the results produced by the two driving methods agree well. This is because the shaking will apply an acceleration uniformly on the gas inside the resonator, while the piston driving only gives the same acceleration to the gas immediately contacting to the piston at $X = 1$.

4.4 DRIVING TERMS $F_{shaking}$ AND F_{piston}

Similar acoustic characteristics obtained by shaking and piston driving have been demonstrated in Section 4.3.3. In this section, the driving mechanism associated with shaking and piston driving will be examined through their driving terms.

For comparison purpose, the governing equations under shaking and piston driving conditions are rearranged in a similar form:

$$\mathbb{F}(\Phi) = F_{shaking}(A, \Phi), \tag{4.25}$$

$$\mathbb{F}(\Phi_A) = F_{psiton}(\Phi_B, \Phi_A), \tag{4.26}$$

where $\mathbb{F}$ is an operator for unknown functions Φ and Φ_A. It consists of all the terms which are not related to driving A or Φ_B. The definition of $\mathbb{F}(\Phi)$ is given by

$$\begin{aligned}\mathbb{F}(\Phi) = {} & \frac{\partial^2\Phi}{\partial T^2} - \frac{1}{\Omega^2\pi^2}\left\{\frac{1}{R^2}\frac{dR^2}{dX}\right\}\frac{\partial\Phi}{\partial X} - \frac{1}{\Omega^2\pi^2}\frac{\partial^2\Phi}{\partial X^2} + \frac{2}{\Omega}\frac{\partial^2\Phi}{\partial X\partial T}\frac{\partial\Phi}{\partial X} \\ & + \frac{(\gamma-1)}{\Omega}\left\{\frac{1}{R^2}\frac{dR^2}{dX}\right\}\frac{\partial\Phi}{\partial T}\frac{\partial\Omega}{\partial X} + \frac{(\gamma-1)}{\Omega}\frac{\partial\Phi}{\partial T}\frac{\partial^2\Phi}{\partial X^2} \\ & - \frac{G_B}{\pi^3\Omega}\left\{\frac{1}{R^2}\frac{dR^2}{dX}\right\}\frac{\partial^2\Phi}{\partial T\partial X} - \frac{G_B}{\pi^3\Omega}\frac{\partial^3\Phi}{\partial T\partial X^2} + \frac{G_S}{\Omega^{1/2}R}\frac{\partial\Phi}{\partial T},\end{aligned} \tag{4.27}$$

$F_{shaking}$ is the driving term of shaking condition. It is a combination of all the terms related to the acceleration A. $F_{shaking}$, as a function of A and Φ, is defined by

$$\begin{aligned}F_{shaking} = {} & -\frac{1}{\Omega^2}\left\{A\frac{\partial\Phi}{\partial X} + \Omega\frac{dA}{dT}X\right. \\ & \left. + (\gamma-1)\left\{\frac{1}{R^2}\frac{dR^2}{dX}\right\}\frac{\partial\Phi}{\partial X}AX + (\gamma-1)\frac{\partial^2\Phi}{\partial X^2}AX\right\}.\end{aligned} \tag{4.28}$$

F_{piston} is the driving term of piston driving condition. It is a combination of all the terms related to the piston driving Φ_B. F_{piston}, as a function of Φ_B and , Φ_A is defined by

$$
\begin{aligned}
F_{piston} = & -\frac{\partial^2 \Phi_B}{\partial T^2} + \frac{1}{\Omega^2 \pi^2}\left\{\frac{1}{R^2}\frac{dR^2}{dX}\right\}\frac{\partial \Phi_B}{\partial X} + \frac{1}{\Omega^2 \pi^2}\frac{\partial^2 \Phi_B}{\partial X^2} - \frac{2}{\Omega}\frac{\partial^2 \Phi_B}{\partial X \partial T}\frac{\partial \Phi_B}{\partial X} \\
& -\frac{(\gamma-1)}{\Omega}\left\{\frac{1}{R^2}\frac{dR^2}{dX}\right\}\frac{\partial \Phi_B}{\partial T}\frac{\partial \Phi_B}{\partial X} - \frac{(\gamma-1)}{\Omega}\frac{\partial \Phi_B}{\partial T}\frac{\partial^2 \Phi_B}{\partial X^2} \\
& -\frac{G_B}{\pi^3 \Omega}\left\{\frac{1}{R^2}\frac{dR^2}{dX}\right\}\frac{\partial^2 \Phi_B}{\partial T \partial X} - \frac{G_B}{\pi^3 \Omega}\frac{\partial^3 \Phi_B}{\partial T \partial X^2} + \frac{G_S}{D\Omega^{1/2}}\frac{\partial \Phi_B}{\partial T} \\
& -\frac{2}{\Omega}\frac{\partial^2 \Phi_A}{\partial X \partial T}\frac{\partial \Phi_B}{\partial X} - \frac{2}{\Omega}\frac{\partial^2 \Phi_B}{\partial X \partial T}\frac{\partial \Phi_A}{\partial X} - \frac{(\gamma-1)}{\Omega}\left\{\frac{1}{R^2}\frac{dR^2}{dX}\right\}\frac{\partial \Phi_A}{\partial T}\frac{\partial \Phi_B}{\partial X} \\
& -\frac{(\gamma-1)}{\Omega}\left\{\frac{1}{R^2}\frac{dR^2}{dX}\right\}\frac{\partial \Phi_B}{\partial T}\frac{\partial \Phi_A}{\partial X} - \frac{(\gamma-1)}{\Omega}\frac{\partial \Phi_A}{\partial T}\frac{\partial^2 \Phi_B}{\partial X^2} - \frac{(\gamma-1)}{\Omega}\frac{\partial \Phi_B}{\partial T}\frac{\partial^2 \Phi_A}{\partial X^2}.
\end{aligned}
\tag{4.29}
$$

Equations (4.25) and (4.26) show the governing equations for shaking and piston driving have an identical left hand side. The only difference is in the driving terms $F_{shaking}$ and F_{piston}. By examining these two driving terms, we can get better understanding of the similar resonance behavior under shaking and piston driving conditions. However, $F_{shaking}$ and F_{piston} can not be evaluated directly from their driving force A and Φ_B, as solution Φ and Φ_A are also involved in the driving terms. Only after Φ and Φ_A are solved, can $F_{shaking}$ and F_{piston} be calculated. For the convenience of discussion, the driving terms $F_{shaking}$ and F_{piston} need to be simplified. Following are the analysis and simplification of the driving terms.

4.4.1 THE DRIVING TERMS OF SHAKING CONDITION

Once solution Φ for Eq. (4.25) is obtained, every term in $F_{shaking}$ can be evaluated. Here, we examine an axisymmetric resonator ($\alpha = 5.75$, $l = 0.2m$, $r_0 / l = 0.05$) under shaking condition ($\tilde{A} = 1\times10^{-4}$). According to the calculation, Φ is in the order of 10^{-2}, $\frac{\partial \Phi}{\partial X}$ is in the order of 10^{-4} and $\frac{\partial^2 \Phi}{\partial X^2}$ is in the order of 10^{-6}. Therefore the first, third and last term in Eq. (4.28), which are associated with $\frac{\partial \Phi}{\partial X}$ and $\frac{\partial^2 \Phi}{\partial X^2}$, are very small comparing to the second term. By dropping the three small terms, $F_{shaking}$ can be approximated by

$$F_{shaking} \simeq -\frac{1}{\Omega}\frac{\partial A}{\partial T} X \ . \tag{4.30}$$

$F_{shaking}$ is simplified as a function of only the driving force A. This will be helpful in the following discussion.

The simplified driving term $F_{shaking}$ (Eq. (4.30)) for the shaped resonator ($\alpha = 5.75$, $l = 0.2m$, $r_0 / l = 0.05$) under driving strength $\tilde{A} = 1\times10^{-4}$ is plotted in Figure 4.9. From this plot we can see that $F_{shaking}$ is sinusoidal with respect to time. The driving amplitude is large at the small end ($X = 0$) and it is zero at the large end ($X = 1$).

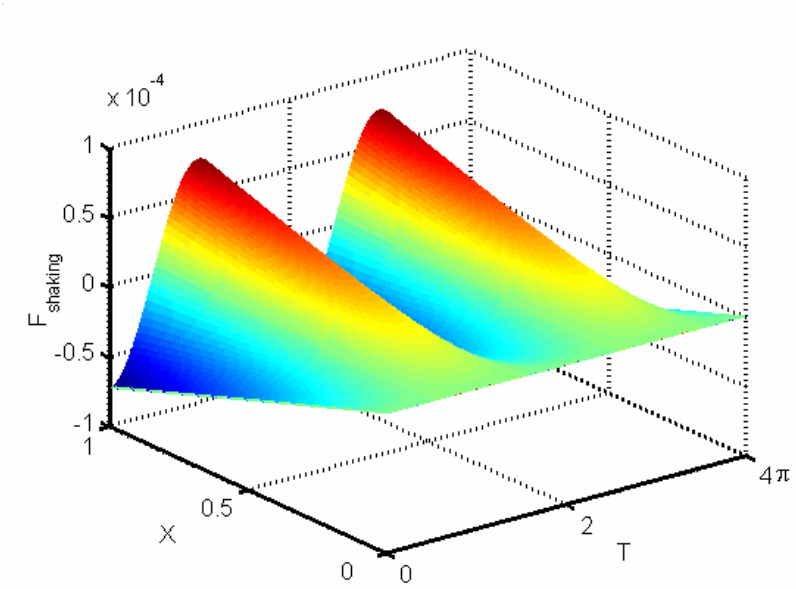

Figure 4.9 Simplified driving term $F_{shaking}$ (4.30) as a function of T and X.

4.4.2 THE DRIVING TERMS OF PISTON DRIVING CONDITION

For comparison purpose, same resonator profile ($\alpha = 5.75$, $l = 0.2m$, $r_0 / l = 0.05$) is used for piston driving condition ($\tilde{U} = 7.37 \times 10^{-5}$). Once solution Φ_A is obtained, the orders of Φ_A, Φ_B and their derivatives can be evaluated, which are listed in Table 4.2.

Table 4.2 Orders of Φ_A, Φ_B and their derivatives.

Φ_A	0.01	Φ_B	10^{-5}
$\frac{\partial \Phi_A}{\partial X}$	10^{-5}	$\frac{\partial \Phi_B}{\partial X}$	10^{-4}
$\frac{\partial \Phi_A}{\partial T}$	10^{-3}	$\frac{\partial \Phi_B}{\partial T}$	10^{-5}
$\frac{\partial^2 \Phi_A}{\partial X^2}$	10^{-6}	$\frac{\partial^2 \Phi_B}{\partial X^2}$	10^{-4}
$\frac{\partial^2 \Phi_A}{\partial T^2}$	10^{-4}	$\frac{\partial^2 \Phi_B}{\partial T^2}$	10^{-5}

It can be seen that Φ_A for piston driving is also in the order of 10^{-2}. It is much larger than Φ_B. This is quite reasonable, since the acoustic waves can be much stronger than the driving at the resonance. By keeping terms in order of 10^{-5} and dropping off all smaller terms in Eq. (4.29), the driving term F_{piston} is simplified as

$$F_{piston} = -\frac{\partial^2 \Phi_B}{\partial T^2} + \frac{1}{\Omega^2 \pi^2}\left\{\frac{1}{R^2}\frac{dR^2}{dX}\right\}\frac{\partial \Phi_B}{\partial X} + \frac{1}{\Omega^2 \pi^2}\frac{\partial^2 \Phi_B}{\partial X^2}, \tag{4.31}$$

which consists of only first-order terms of Φ_B. When Φ_B is defined by Eq. (4.14), the driving terms can be estimated by

$$F_{piston} \simeq \tilde{U}\sin(T)\left(\frac{1}{\Omega^2 \pi^2} + \frac{1}{\Omega^2 \pi^2}\left\{\frac{1}{R^2}\frac{dR^2}{dX}\right\}X + \frac{X^2}{2}\right). \tag{4.32}$$

The driving term F_{piston} for shaped resonator ($\alpha = 5.75$, $l = 0.2m$, $r_0 / l = 0.05$) under driving strength $\tilde{U} = 7.37 \times 10^{-5}$ is plotted in Figure 4.10. It is seen that the driving is very large at the small end ($X = 0$) and it is very small at the large end ($X = 1$). Figure 4.9 and Figure 4.10 show that $F_{shaking}$ and F_{piston} have similar distribution in time and space.

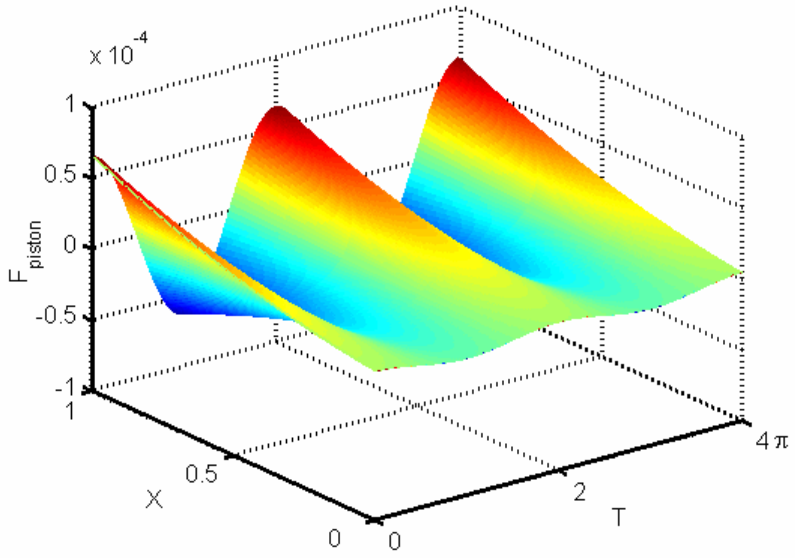

Figure 4.10 Driving term F_{piston} as a function of T and X.

From above discussion, we find that the driving terms $F_{shaking}$ and F_{piston} can be approximated by functions of A and U respectively. This makes it possible for following discussion.

4.4.3 THE EQUIVALENT ACCELERATION FORCE

In order to compare the piston driving to shaking, an equivalent acceleration force is introduced here. According to Eq. (4.30), the magnitude of acceleration A can be estimated as

$$\left|A_{eq-shaking}\right| = \left|\Omega \frac{\partial F_{shaking}}{\partial X}\right|, \tag{4.33}$$

where $A_{eq-shaking}$ is an approximate acceleration derived from the driving term for shaking condition and is defined as the equivalent acceleration. Following Eq. (4.33), an equivalent acceleration for piston driving can be defined by

$$\left|A_{eq-piston}\right| = \left|\Omega \frac{\partial F_{piston}}{\partial X}\right|. \tag{4.34}$$

By substituting Eq. (4.31) into Eq. (4.34), the equivalent acceleration for piston driving can be estimated by

$$\left|A_{eq-piston}\right| = \left|\Omega \frac{\partial}{\partial X}\left(\frac{\partial^2 \Phi_B}{\partial T^2} - \frac{1}{\Omega^2 \pi^2}\left\{\frac{1}{R^2}\frac{dR^2}{dX}\right\}\frac{\partial \Phi_B}{\partial X} - \frac{1}{\Omega^2 \pi^2}\frac{\partial^2 \Phi_B}{\partial X^2}\right)\right|. \tag{4.35}$$

By using Φ_B defined in Eq. (4.14), the equivalent acceleration becomes

$$\left|A_{eq-piston}\right| = \left|\Omega \tilde{U} \cos(T)\left(\frac{1}{\Omega^2 \pi^2}\left\{\frac{1}{R^2}\frac{dR^2}{dX}\right\} + X\right)\right|. \tag{4.36}$$

Two driving forces in terms of equivalent acceleration are compared in Figure 4.11. For the comparison purpose, $A_{eq-shaking}$ is normalized by $\tilde{A}$ and $A_{eq-piston}$ is normalized by $\Omega\tilde{U}$. Here, $\tilde{A} = \tilde{U}\Omega$ is assumed. It can be seen that the equivalent acceleration force of shaking have a uniform value of 1. It presents a uniform acceleration force along resonator. While the equivalent acceleration force of piston is not uniform along the axis. Since the piston drives at the large end ($X = 1$), it provides a larger equivalent acceleration at $X = 1$ and a smaller one at $X = 0$.

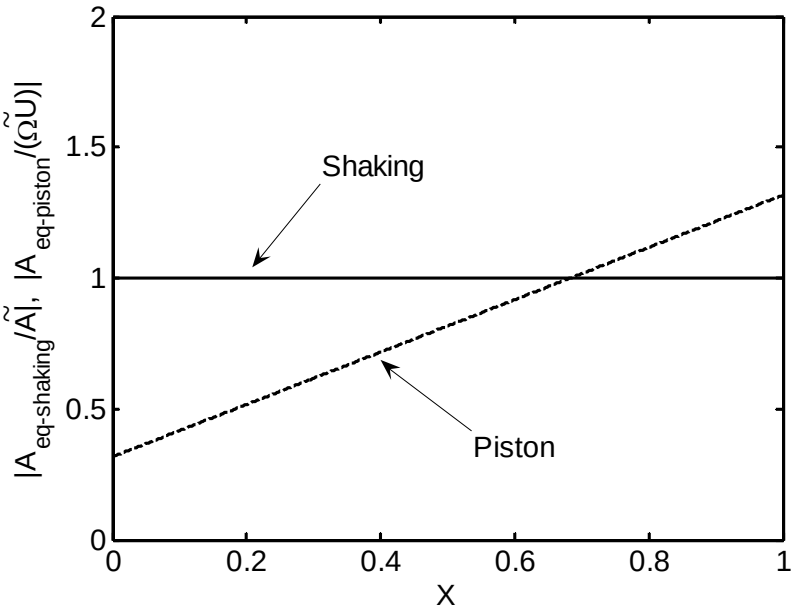

Figure 4.11 The equivalent acceleration force of shaking condition (solid line) and piston driving condition (dashed line). $\tilde{A} = \tilde{U}\Omega$ **is assumed here. The piston is located at** $X = 1$**.**

4.5 SUMMARY

The acoustic resonances in cylindrical and shaped resonators generated by piston driving have been studied. The non-homogenous boundary condition associated with the piston driving is converted to homogenous boundary condition by introducing a new function to the solution which satisfies the velocity boundary condition, so that the Galerkin's method is applied. From the calculations following conclusions can be drawn: (i) shock waves are generated in a cylindrical resonator driven by a piston when the driving is strong; (ii) shock-free waves can be obtained in shaped resonators by piston driving at strong driving; (iii) when the shaking and piston driving satisfies $\tilde{A} = \tilde{U}\Omega$, similar acoustic characteristics can be obtained in the same resonator. Finally, the driving terms $F_{shaking}$ and F_{piston} for shaking and piston driving conditions are discussed. Two drivings are related and compared by the equivalent acceleration force. The piston driving provides a non-uniform equivalent acceleration force along the resonator axis, which is large at the driving end and small at the other end.

CHAPTER 5

ENERGY LOSS

5.1 INTRODUCTION

When a resonator is driven by a shaking force or a piston, standing waves are built up inside the resonator. The standing waves at the resonance frequency can be very strong and nonlinear if the driving is powerful enough, which has been discussed in previous chapters. In the meanwhile, part of the input power is dissipated in the resonator due to viscosity and heat conduction in the fluid. Viscosity is the internal friction of gas produced by the movement of its molecules against each other. Because of viscosity, the wall of resonator exerts a frictional shear force on the overlying gas. At the same time, thermal conduction allows heat transfer to take place between the gas and the wall. The two processes tend to transform energy associated with the organized motion of sound waves into heat. Therefore, the energy content of the acoustic wave decreases. Energy loss also depends on resonator size. When the resonator size is reduced, the fraction of energy loss becomes more significant. Energy loss due to viscosity and heat conduction in various resonators are investigated in this chapter.

5.2 ENERGY LOSS MECHANISM

5.2.1 ACOUSTIC BOUNDARY LAYER

Viscous dissipation

Consider the propagation of a time-harmonic sound wave (angular frequency ω) in a resonator. Although fluid particles in the mainstream (i.e. away from the resonator wall) oscillate back and forth, the layer of particles adjacent to the wall adheres to the wall. A transition therefore takes place where the particle oscillation amplitude decreases from its nominal value in the mainstream to zero at the wall, as shown in Figure 5.1. The transition region is called the acoustic viscous boundary layer. If the fluid were inviscid, it could "slip" past the wall perfectly, i.e., the flow could be frictionless and the boundary layer thickness would be zero. The presence of viscosity causes the boundary layer to be finite though nevertheless quite thin. As the boundary layer thickness is much thinner than the acoustic wave length (about 2 times of the resonator length), sound appears to traverse the boundary layer almost instantaneously.

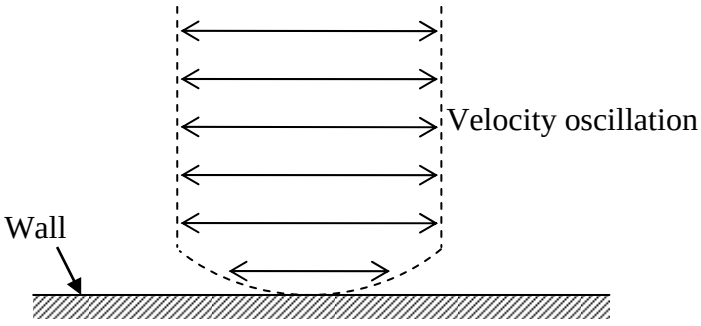

Figure 5.1 Viscous boundary layer for oscillation flow.

The acoustic viscous boundary layer thickness is given by (Blackstock, 2000)

$$\theta_{visc}^{BL} = \sqrt{\frac{2\eta}{\omega\rho}} = \sqrt{\frac{2\nu}{\omega}}, \tag{5.1}$$

where $\nu = \eta / \rho$ is the kinematic viscosity and ω is angular frequency. At 1000 Hz in air, for example, the thickness is about 0.07 mm. Therefore, the viscous boundary layer takes up very little of the cross section of resonator. The acoustic viscous boundary layer cannot grow very much because the fluid never flows in one direction for more than half a period.

Thermal dissipation

Co-existing with the viscous boundary layer is a thermal boundary layer associated with heat conduction. In the mainstream the compressions and expansions take place adiabatically. Because the wall is effectively an infinite heat source or sink, adjacent fluid particles stay at the wall temperature (any temperature change in the adjacent fluid would immediately be quenched by heat flow into or out of the wall). The region near the wall where the flow changes character from adiabatic to isothermal is called thermal boundary layer. The thermal boundary layer is comparable to that of the viscous boundary layer and is given by (Blackstock, 2000):

$$\theta_{therm}^{BL} = \sqrt{\frac{2\kappa}{\rho\omega C_p}} = \sqrt{\frac{2\eta}{\omega\rho\,\mathrm{Pr}}} = \frac{\theta_{visc}^{BL}}{\sqrt{\mathrm{Pr}}}. \tag{5.2}$$

Here Pr is the Prandtl's number and is given as

$$\mathrm{Pr} = \frac{C_p \eta}{K}, \tag{5.3}$$

where C_p is specific heat capacity at constant pressure and K is thermal conductivity.

Thermoviscous dissipation

The losses associated with the viscous and thermal boundary layers give rise to absorption and dissipation of sound. Their effects on sound waves in the mainstream may be modeled in one-dimensional fashion by letting the control volume contain just the fluid in the mainstream, that is, outside the boundary layer. The effect of the viscous boundary layer is to exert a shear force on the side of the control volume. Similarly, the effect of the thermal boundary layer is to transfer heat to the control volume though the side surface. It's suggested by Blackstock (2000) and Ilinskii (2001) that to replace the factor $\sqrt{\eta}$ in governing equation by $\sqrt{\eta}\left(1+\frac{\gamma-1}{\sqrt{\mathrm{Pr}}}\right)$ to include the heat transfer at the wall.

The absorption coefficient for the thermoviscous acoustic boundary layer for an axisymmetric duct with radius r is given as (Blackstock, 2000)

$$\alpha^{BL}=\frac{1}{r}\sqrt{\frac{\omega\eta}{2\rho_0 {c_0}^2}}\left(1+\frac{\gamma-1}{\mathrm{Pr}}\right). \tag{5.4}$$

5.2.2 EFFECT OF ACOUSTIC BOUNDARY LAYERS

Variation of temperature and G_S

The thermoviscous dissipation converts the energy associated with wave motion into heat, which leads to the increasing of gas temperature. Since the temperature change may result in the variation of gas parameters, such as the viscosity coefficient η, thermoviscous dissipation affects the acoustic boundary layer characteristics in return. It is necessary to study the temperature effect on the air parameters first in order to fully consider the acoustic boundary layer effect. The parameters used in present

study for different temperatures are listed in Table 5.1. It is seen that the coefficient of viscosity of gases increases with increasing temperature. It is because that intermolecular forces in gases are not as important in viscosity as collisions between the molecules. An increase in temperature increases the number of collisions, thus increasing the coefficient of viscosity. A result of the kinetic theory of gases is that the viscosity of a gas is independent of the density of a gas. The physical mechanism for most, if not all, of its effect is related to the time required to establish thermodynamic equilibrium between the translational and the rotation-vibration motions of the gas molecules (Morse, 1968).

Table 5.1 Air properties between 0^0C and 100^0C

Temperature (^0C)	Density (kg/m^3)	Dynamic viscosity ($N\bullet s/m^2)\times10^{-5}$	Kinematic viscosity ($m^2/s)\times10^{-5}$	Speed of sound (m/s)	Prandtl's number
0	1.296	1.71	1.32	331.4	0.715
10	1.248	1.76	1.41	337.4	0.714
20	1.205	1.82	1.51	343.4	0.713
30	1.162	1.86	1.60	349.1	0.712
40	1.127	1.87	1.66	354.7	0.711
50	1.108	1.95	1.76	360.3	0.710
60	1.059	1.97	1.86	365.7	0.709
70	1.031	2.03	1.97	371.2	0.708
80	1.000	2.07	2.07	376.6	0.708
90	0.973	2.14	2.20	381.7	0.706
100	0.948	2.17	2.29	386.9	0.703

In our previous chapters, it is shown that viscosity affects the resonance pressures through the dimensionless parameters G_B and G_S governing equation. The variation

of G_S against temperature is shown in Figure 5.2. Since G_B is not as important as G_S in terms of viscosity (will be discussed later), it is not shown in Figure 5.2. The solid line shows the variation of G_S against temperature without consideration of thermal dissipation. The rising of temperature increases the viscosity coefficient η, so does G_S.

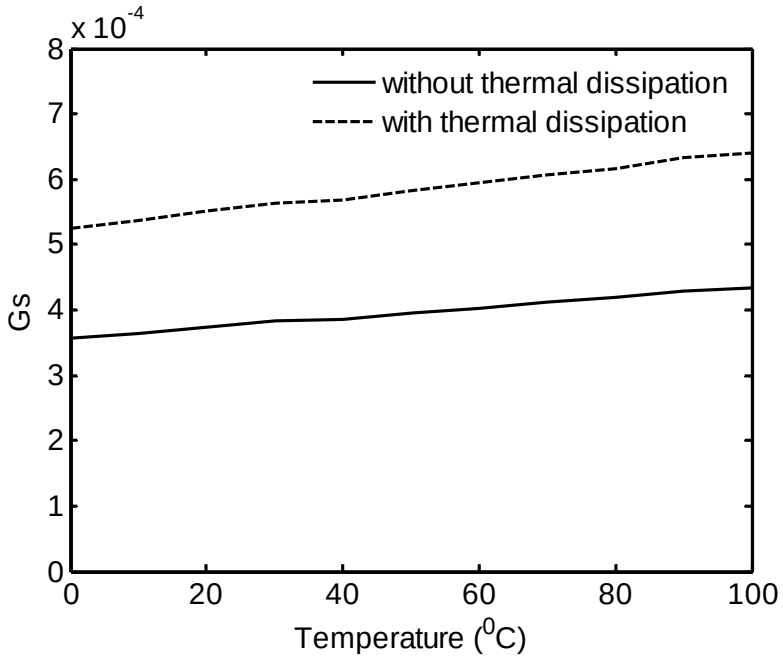

Figure 5.2 The dependence of G_S on temperature and thermal condition.

When the thermal dissipation is considered, G_S becomes

$$G_{S(tv)} = \sqrt{\frac{2\eta}{\pi\rho_0 c_0 l}}\left(1+\frac{\gamma-1}{\sqrt{\mathrm{Pr}}}\right). \tag{5.5}$$

where (tv) denotes thermoviscous flow to distinguish G_S which is for viscosity only. The dashed line in Figure 5.2 shows the variation of $G_{S(tv)}$ against temperature with consideration of thermal dissipation. With consideration of thermal dissipation, $G_{S(tv)}$ always has a higher value.

Effect of thermal dissipation

By modifying the parameter G_S to include to thermal dissipation, the governing equation (3.51) in Chapter 3 is solved to examine the thermal boundary effect on the resonance pressures. Figure 5.3 shows the pressure waves in a resonator ($\alpha = 5.75$, $l = 0.2m$, $r_0 / l = 0.02$) with and without consideration of thermal dissipation. The driving strength is $\tilde{A} = 3 \times 10^{-4}$. The solid line presents the waveforms without thermal dissipation at $20\,^0C$ and the maximum overpressure is $0.89P_0$. The dashed line presents the waveform with thermal dissipation. In this condition the maximum overpressure is $0.55P_0$, which is about 38% less than if thermal dissipation is not included. It shows the thermal condition may affect the pressure wave substantially. The pressure amplitude distribution along the resonator is also calculated and is shown in Figure 5.4. The allocations of maximum and minimum value in two cases are very close.

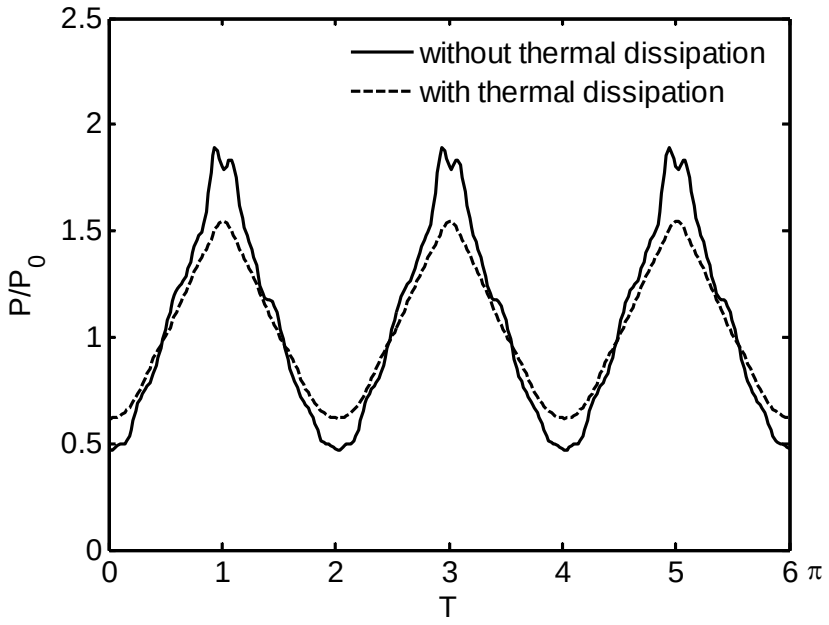

Figure 5.3 Effect of thermal condition on pressure waveform.

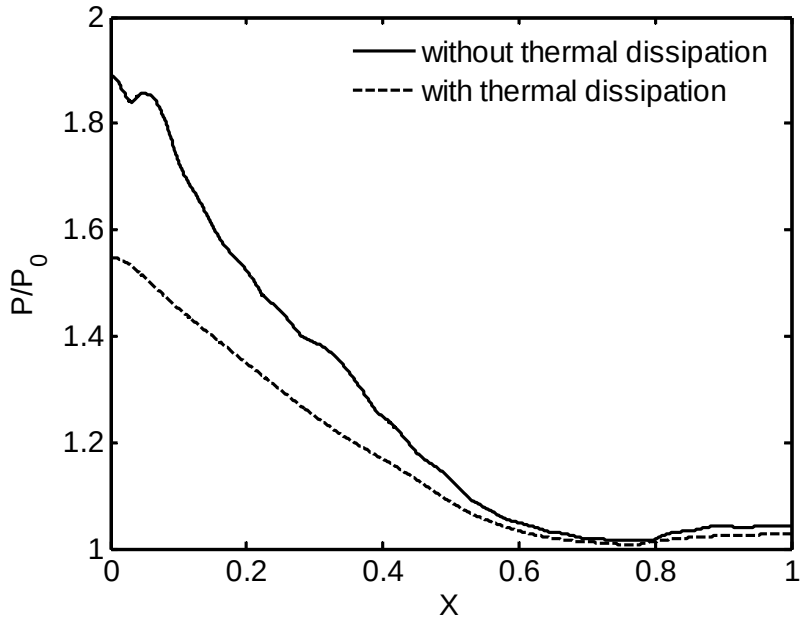

Figure 5.4 Effect of thermal condition on pressure distribution.

Figure 5.5 presents the temperature effect on the compression ratio. When temperature increases, the dimensionless shear viscosity coefficient G_S also increases, as shown in Figure 5.2, therefore the compression ratio decreases, as viscosity and thermal dissipation take away more energy.

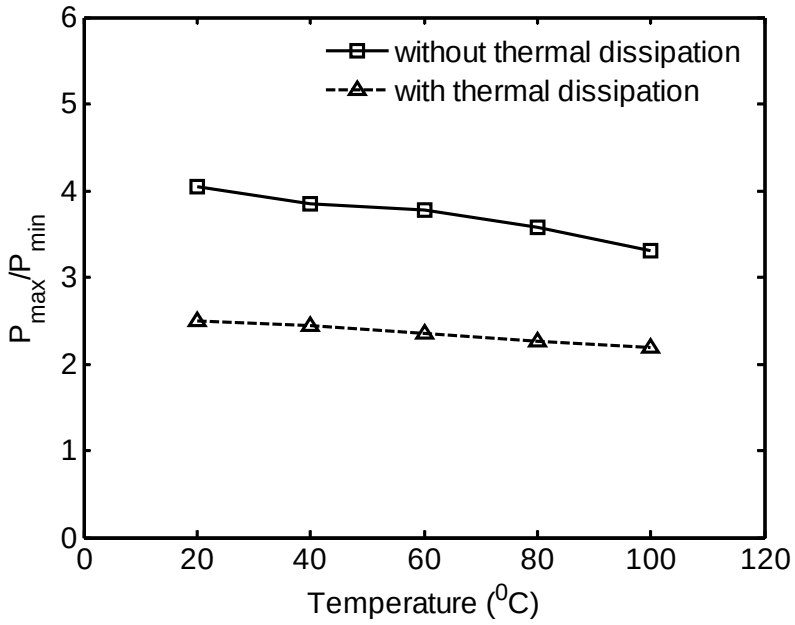

Figure 5.5 Influence of temperature and thermal condition on compression ratio.

From above discussion, it can be seen that the thermal dissipation in a resonator could be an important factor for resonance characteristics. Further study on this issue may be necessary, especially an experiment needs to be conducted to verify the effect of the thermal boundary dissipation.

5.3 ENERGY DISSIPATION IN RESONATORS

It is shown in Chapter 3 that the bulk viscosity in axisymmetric resonator is $(\zeta + 4\eta/3)\frac{\partial}{\partial x}\left(\frac{1}{r^2}\frac{\partial}{\partial x}(r^2 u)\right)$, and the shear viscosity is $\frac{\sqrt{2\rho\eta\omega}}{r}u$. The ratio of two viscosities is estimated by

$$\frac{\text{bulk viscosity}}{\text{shear viscosity}} = \frac{(\zeta + 4\eta/3)\frac{\partial}{\partial x}\left(\frac{1}{r^2}\frac{\partial}{\partial x}\left(r^2 u\right)\right)}{\frac{\sqrt{2\rho_0\eta\omega}}{r}u} \simeq \frac{r(\zeta + 4\eta/3)}{l^2\sqrt{2\rho_0\eta\omega}}. \tag{5.6}$$

Viscosity coefficients ζ and η are in order of 10^{-5} for air. The oscillation frequency ω is in order of 10^4 (taking the length of 0.2 m). Hence, the ratio of bulk viscosity to shear viscosity is in order of 10^{-4}, that is, the bulk viscosity is much smaller than the shear viscosity. Therefore, the bulk viscosity can be neglected in the viscous dissipation analysis, and only the shear viscosity is considered for the viscous dissipation. The average work done by the shear viscosity in a period is given by

$$e_{dis} = \left\langle \int \frac{\sqrt{2\rho\eta\omega}}{r} u^2 dv \right\rangle, \tag{5.7}$$

where $\langle\ \rangle$ denotes an average value and e_{dis} is the average dissipated power in one period.

Using the following dimensionless variables

$$U = \frac{u}{\omega_0 l} \text{ and } \Omega = \frac{\omega}{\omega_0},$$

Eq. (5.7) can be rewritten as

$$e_{dis} = l^4 \omega_0^{\,2} \sqrt{2\eta\rho_0\omega_0}\,\Omega^{\frac{1}{2}} \left\langle \int_V \sqrt{\frac{\rho}{\rho_0}} \frac{U^2}{R} dV \right\rangle. \tag{5.8}$$

Recall the definition of non-dimensional shear viscosity parameter $G_s = \sqrt{\dfrac{2\eta}{\rho_0\omega_0 l^2}}$, Eq. (5.8) becomes

$$e_{dis} = l^5 \omega_0^{\,3} \rho_0 G_S \Omega^{\frac{1}{2}} \left\langle \int_V \sqrt{\frac{\rho}{\rho_0}} \frac{U^2}{R} dV \right\rangle, \tag{5.9}$$

where $l^5\omega_0^{\,3}\rho_0$ has a dimension of power. By using $l^5\omega_0^{\,3}\rho_0$ to normalize Eq. (5.9), the dimensionless dissipation is obtained as

$$D = \frac{e_{dis}}{l^5\omega_0^{\,3}\rho_0} = G_S \Omega^{\frac{1}{2}} \left\langle \int_0^1 \sqrt{\frac{\rho}{\rho_0}} \frac{U^2}{R} dV \right\rangle. \tag{5.10}$$

Since pressure, velocity and density vary with location and time, a local dissipation density, $\hat{D}$, is introduced,

$$\hat{D} = G_S \Omega^{\frac{1}{2}} \sqrt{\frac{\rho}{\rho_0}} \frac{U^2}{R}, \tag{5.11}$$

which denotes to the dissipation power per unit volume. Eq. (5.10) becomes

$$D = \left\langle \int_V \hat{D} dV \right\rangle = \left\langle \int_0^1 \hat{D} S dX \right\rangle. \tag{5.12}$$

The dimensionless period is 2π and the average dissipation can be calculated by

$$D = \frac{1}{2\pi}\int_{T}^{T+2\pi}\left(\int_{0}^{1}\hat{D}SdX\right)dT\,. \tag{5.13}$$

An accumulative dissipation is also introduced here,

$$D_{acc}(X) = \int_{0}^{X}\hat{D}(\xi)S(\xi)d\xi\,. \tag{5.14}$$

and Eq. (5.12) can therefore be written as

$$D = \left\langle D_{acc}(X=1)\right\rangle. \tag{5.15}$$

The distribution of the dissipation density in an exponentially expanded resonator ($\alpha = 5.75$, $l = 0.2m$, $r_0/l = 0.01$) driven by a shaking force $A = 5\times10^{-4}\cos(T)$ is shown Figure 5.6. At $X = 0$ the dissipation density is zero because the velocity here is zero. With the increase of X the dissipation density increases rapidly, and reaches its peak value at around $X = 0.2$. After it the dissipation density decreases and becomes zero at $X = 1$. The ratio of accumulative dissipation to total dissipation in the axisymmetric resonator is shown in Figure 5.7. It shows that most of energy (about 70%) is lost within the left half resonator. The results (Figure 5.6 and Figure 5.7) show that most of energy is lost at small end as the effect of viscosity is strong there.

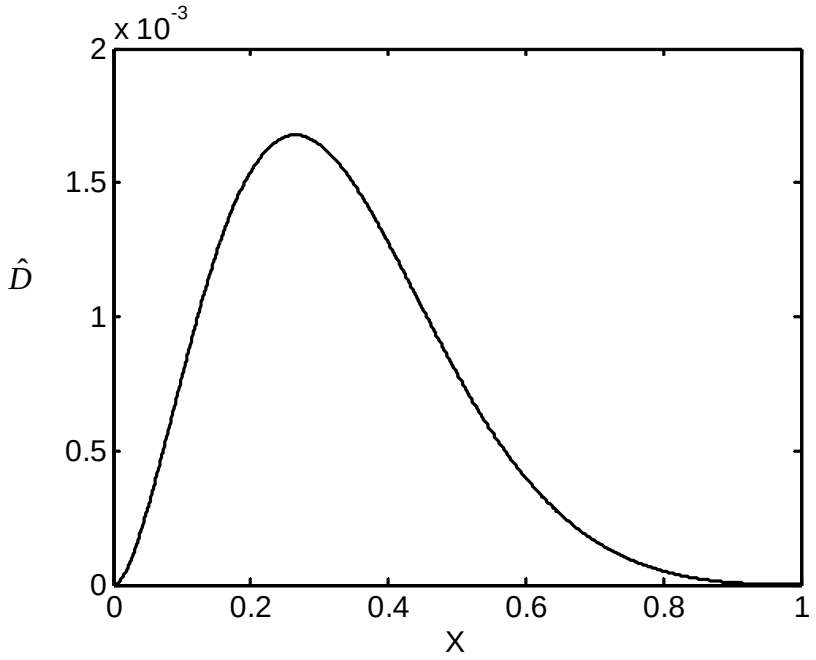

Figure 5.6 Dissipation density in an exponentially expanded resonator

($\alpha = 5.75,\ l = 0.2m,\ r_0 / l = 0.01,\ \tilde{A} = 5\times10^{-4}$).

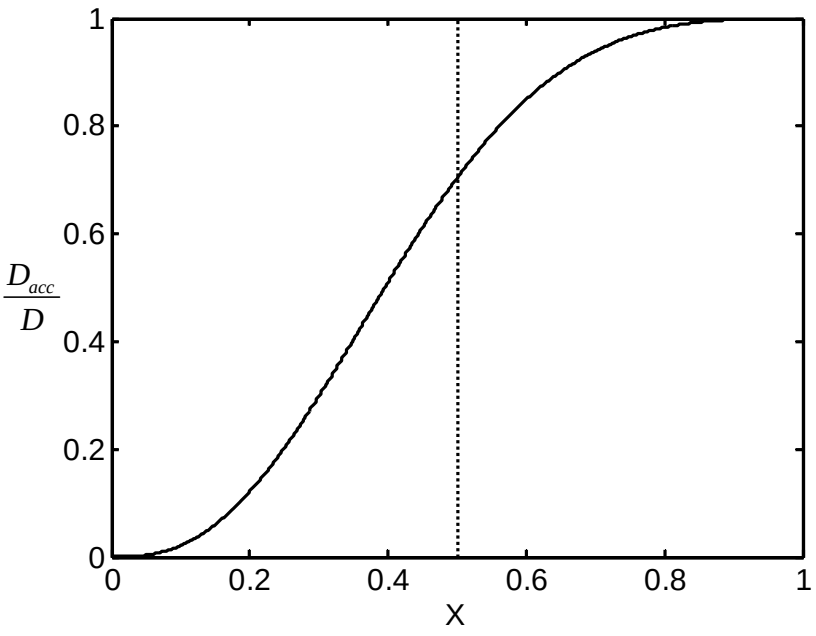

Figure 5.7 Accumulative dissipation in an exponentially expanded resonator

($\alpha = 5.75,\ l = 0.2m,\ r_0 / l = 0.01,\ \tilde{A} = 5\times10^{-4}$).

5.4 QUALITY FACTORS OF RESONATORS

5.4.1 QUALITY FACTOR BASED ON LINEAR APPROXIMATION

The energy loss in a dynamic system may be measured by quality factor which is the ratio of total energy stored in the system to the energy dissipated in one cycle. There are many ways to calculate the quality factor and one of them is to use the decay factor κ from the time factor $e^{-\kappa t}$ (Morse and Ingard, 1968),

$$Q = \frac{\pi f_0}{\kappa}, \tag{5.16}$$

where, f_0 is the fundamental frequency of the system. Eq. (3.51) in Chapter 3 can be reduced to a linear equation by dropping all quadratic terms, together with the driving force A:

$$\frac{\partial^2 \Phi}{\partial T^2} - \frac{1}{\Omega^2 \pi^2}\frac{\partial^2 \Phi}{\partial X^2} = \frac{G_B}{\Omega \pi^3}\frac{\partial^3 \Phi}{\partial T \partial X^2} - \frac{G_S}{\Omega^{1/2} R}\frac{\partial \Phi}{\partial T}. \tag{5.17}$$

By substituting the fundamental mode $\Phi = C\cos(\pi X)e^{(i-\sigma)T} = C\cos(\pi X)e^{(i-\sigma)\omega t}$ into Eq. (5.17), where $\sigma = \kappa/\omega_0$, is the dimensionless decay factor, setting $\Omega = 1$ ($\omega = \omega_0$), at which the energy losses are the maximum (Ilinskii *et al*. 2001), and keeping terms of the first order of σ, one obtains

$$\sigma = \frac{1}{2}\left(\frac{G_B}{\pi} + \frac{G_S}{R}\right). \tag{5.18}$$

In Eq. (5.18), R follows the resonator expansion profile $R(X) = (r_0/l) f(X)$. By denoting

$$I = \int_0^1 \frac{dX}{f(X)}, \tag{5.19}$$

the average of σ over the resonator length can be calculated as

$$\bar{\sigma} = \frac{1}{2}\left(\frac{G_B}{\pi} + \frac{G_S}{r_0/l}\int_0^1 \frac{dX}{f(X)}\right) = \frac{1}{2}\left(\frac{G_B}{\pi} + \frac{IG_S}{r_0/l}\right). \tag{5.20}$$

The quality factor is calculated by

$$Q = \frac{\pi f_0}{k} = \frac{\pi f_0}{\bar{\sigma}\omega_0} = \left(\frac{G_B}{\pi} + \frac{IG_S}{r_0/l}\right)^{-1} = \left(\frac{1}{Q_B} + \frac{1}{Q_s}\right)^{-1}, \tag{5.21}$$

where,

$$Q_B = \frac{\pi}{G_B} = \frac{c_0\rho_0 l}{\pi\left(\zeta + 4\eta/3\right)}, \tag{5.22}$$

is the quality factor due to the dissipation associated with the volume change (Ilinskii *et al*., 1998).

$$Q_S = \frac{r_0/l}{IG_S} = \frac{r_0}{l}\frac{1}{I}\sqrt{\frac{\pi l c_0\rho_0}{2\eta}}, \tag{5.23}$$

which is the quality factor due to the dissipation associated with the shear motion in tubes. Since the viscosity coefficients ζ and η are in order of 10^{-5} and Q_s/Q_B are in order of $\sqrt{\eta} < 10^{-2}$, the overall quality factor can be approximated by Q_s, i.e.,

$$Q \simeq Q_S = \frac{r_0}{l}\frac{1}{I}\sqrt{\frac{\pi l c_0\rho_0}{2\eta}}. \tag{5.24}$$

Eq. (5.24) shows that the quality factor is proportional to ratio r_0 / l and $1/G_S$.

The quality factors are calculated based on Eq. (5.24), for three resonators used in experiments by Lawrenson *et al*. (1998). The parameters of these resonators are listed below:

Cylinder ($l = 0.10m$), $r(x) = 0.0222m$,

Cone ($l = 0.17m$), $r(x) = 0.0056 + 0.2680x \quad m$,

Horn-corn ($l = 0.24m$), $r(x) = \begin{cases} r_{th}\cosh(gx), & 0 \le x \le 0.06m; \\ r_c + \alpha x, & 0.06 \le x \le 0.24m, \end{cases}$

$$r_{th} = 0.0068m,\ r_c = r_{th}\cosh(gx)\big|_{x=0.06},$$
$$\alpha = r_{th}\sinh(gx)\big|_{x=0.06},\ g = 23.86m^{-1}$$

The results are given in Table 5.2 for both refrigerant (R-134a) (Japanese Association of Refrigeration, 1991) and air. It can be seen that the values are in order of 500, which was measured in the experiment (Lawrenson *et al.*, 1998). The results are also close to the values reported by Ilinskii *et al*. (2001).

Table 5.2 Quality factors of resonators.

Quality Factors calculated by Eq. (3.95)			Lawrenson	Ilinskii
	R-134a	Air		
Cylinder	1047	440	~500	300~580
Cone	745	313		
Horn-cone	740	311		
Bulb	574	241		

For the resonator shown in Figure 3.4 in Chapter 3, the radius expansion function is

$$f(X) = e^{\alpha X/2}, \tag{5.25}$$

where α is the flare constant indicating the expansion rate. The quality factors are computed for different α and the results are presented in Figure 5.8. The quality factor for the LARR and straight resonators, shown in Figure 5.8, can be obtained by simply replacing r_0/l with d/l and setting $I=1$ in Eq. (5.24). It is seen that the axisymmetric resonator with larger flare number has higher quality factors, and the axisymmetric resonators have higher quality factors than the LARR resonator. This is because the energy dissipation due to the shear viscosity is reduced along the axisymmetric resonators when the cross-sections are expanded, whereas the energy dissipation in the LARR resonator is increased from the small end to the big end, as the height h between the upper/lower walls is fixed and wall areas are increased.

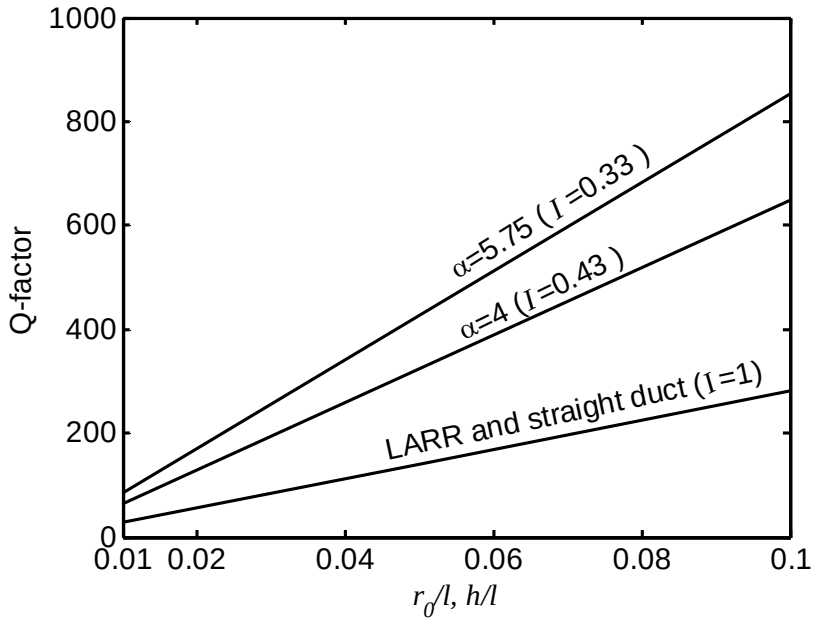

Figure 5.8 The quality factor versus r_0/l and h/l for the axisymmetric resonators and LARR resonators.

5.4.2 QUALITY FACTOR BASED ON ENERGY LOSS

The quality factor Q of an oscillator provides information about energy dissipation and may be defined as (Chow, 1995):

$$Q = \frac{\omega \times (\text{stored energy})}{\text{power} \quad \text{dissipated}}. \tag{5.26}$$

A high Q means that energy dissipation is low, while low Q factor implies large damping of energy.

The energy stored in the resonator can be calculated by (Ilinskii *et al*., 2001)

$$e = \left\langle \int \rho u^2 dv \right\rangle, \tag{5.27}$$

where dv is a volume element. In dimensionless form the total energy of the gas is

$$E = \frac{e}{l^5 \omega_0{}^2 \rho_0} = \left\langle \int_0^1 \frac{\rho}{\rho_0} U^2 S dX \right\rangle, \tag{5.28}$$

where $l^5 \omega_0{}^2 \rho_0$ has a dimension of energy. Similar to the local dissipation density defined in Eq. (5.11), we define a local energy density $\hat{E}$,

$$\hat{E} = \frac{\rho}{\rho_0} U^2, \tag{5.29}$$

and Eq. (5.28) can be rewritten as

$$E = \left\langle \int_0^1 \hat{E} S dX \right\rangle. \tag{5.30}$$

Figure 5.9 shows the stored energy density distribution along an axisymmetric resonator($\alpha = 5.75,\ l = 0.2m,\ r_0 / l = 0.01$). The distribution of stored energy density is similar to that for dissipation (Figure 5.6). The ratio of dissipation density to stored energy density is shown in Figure 5.10 for different values of r_0 / l. It is seen that most of energy are lost at the small end. This is very reasonable, as the viscosity effect at the small end is greater than that at large end. The smaller r_0 / l is, the more energy is lost, which agrees well with the pressure amplitude drop against resonator dimension showing in Chapter 3.

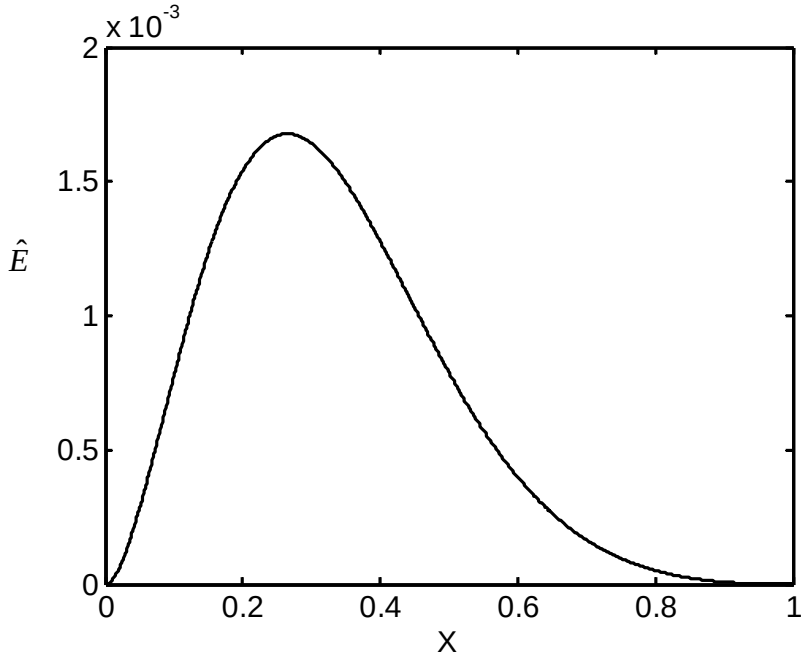

Figure 5.9 The kinetic energy density of gas inside an axisymmetric resonator ($\alpha = 5.75, l = 0.2m, r_0 / l = 0.01,\ \tilde{A} = 5 \times 10^{-4}$).

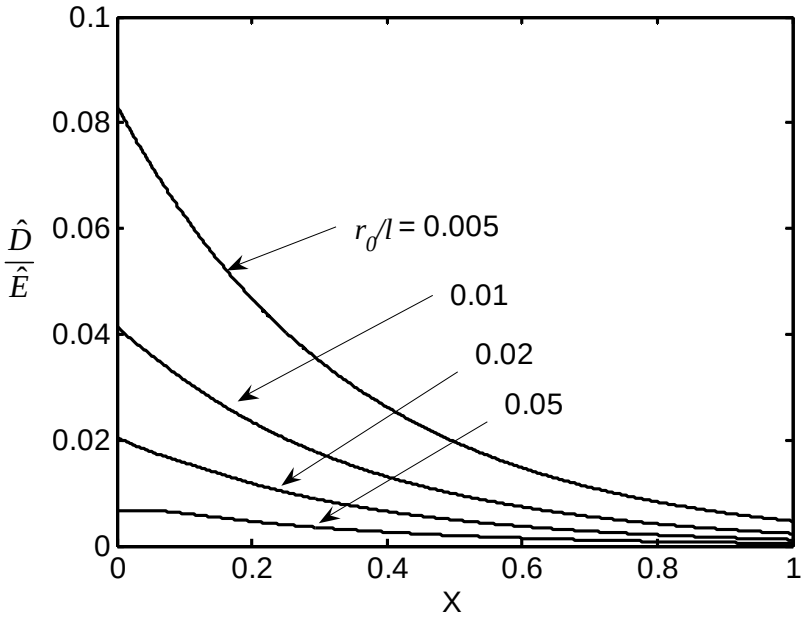

Figure 5.10 Density ratio of dissipation to stored energy of different across sectional area size.

With the dimensionless energy E and dissipation D in a resonator, we can calculate the quality factor based on energy loss

$$Q = \frac{\omega e}{e_{dis}} = \frac{\Omega E}{D}, \tag{5.31}$$

where stored energy E can be estimated by Eq. (5.28), the energy dissipation rate D can be obtained from Eq. (5.10), and Ω is the resonance frequency.

Table 5.3 presents the quality factors of some resonators driven by a shaking force ($\tilde{A} = 5\times10^{-4}$). These axisymmetric resonators have flare constant $\alpha = 5.75$ and length $l = 0.2m$. From Table 5.3, it is seen that the dimension of the resonator across section has great effect on the total energy and dissipation. When r_0/l is very small, e.g.,

0.005, the resonator has a small quality factor and the energy dissipation is relatively high comparing to the total energy.

Table 5.3 Quality factors from nonlinear analytical results.

r_0 / l	Ω	Total energy (E)	Dissipation (D)	Q
0.005	1.356	1.43×10^{-7}	3.22×10^{-9}	60
0.01	1.356	2.22×10^{-6}	2.50×10^{-8}	121
0.02	1.359	3.00×10^{-5}	1.67×10^{-7}	244
0.05	1.364	3.00×10^{-4}	6.53×10^{-7}	621

The Q factors based on energy loss are calculated from nonlinear resonance pressures and velocities (shown in Table 5.3), which have taken into account of the resonator shapes and frequency shift. They are different from the Q factors obtained from the linear approximation presented in 5.4.1. The nonlinear Q-factors and linear Q-factors are list in the second and third column in Table 5.4. The different is probably because the Q factor in linear approximation does not account for the frequency shift due to the resonator cross section expansion. If we correct the linear Q factor by Ω, the results are agreeable, shown in Table 5.4.

Table 5.4 Comparison of the Q-factors.

r_0 / l	Q (linear)	Corrected Q (linear)		Q (nonlinear)
		Ω	$Q\Omega$	
0.005	43	1.356	58	60
0.01	85	1.356	115	121
0.02	171	1.359	232	244
0.05	427	1.364	582	621

5.5 SUMMARY

The acoustical boundary layer as a combination of viscous boundary layer and thermal boundary layer has been discussed. The effect of the viscous boundary layer is to exert a shear force on the side of the control volume. The effect of the thermal boundary layer is to transfer heat to the control volume though the side surface. In order to consider thermal dissipation, $\sqrt{\eta}$ should be replaced by $\sqrt{\eta}\left(1+\frac{\gamma-1}{\sqrt{\mathrm{Pr}}}\right)$ in the governing equations. Simulation results show that thermal boundary layer has significant effect on acoustic waves. Pressure amplitude reduces greatly when thermal dissipation is considered. However the temperature change has less impact on the pressure waves. Further more, the total energy and dissipated energy in resonator have been calculated. Shear viscosity is found to be the main reason of dissipation. It is also found that the smaller r_0/l is, the more energy is lost, which agrees well with the pressure amplitude drop against resonator dimension showing in Chapter 3. In the region of near small end, most of the energy is dissipated and most of the kinetic energy is also stored in the meanwhile. The quality factor is estimated based on linear approximation. It is found that the axisymmetric resonator with larger flare number and r_0/l value has higher quality factors, and the axisymmetric resonators have higher quality factors than the LARR resonator. Q-factors are also calculated based on the dissipated and stored energy, which are obtained from the solution of nonlinear governing equations. Good agreement is obtained by the two methods.

CHAPTER 6

EXPERIMENT

6.1 INTRODUCTION

Experimental studies have been carried out and the details are presented in this chapter. The main purposes of the experiments are: (1) to verify some of the results calculated in previous chapters for resonators driven by a piston, such as resonance frequencies and pressure ratios; and (2) to explore the possibility of generating resonance pressure in miniature low-aspect-ratio rectangular (LARR) resonators. Firstly, an exponentially expanded axisymmetric resonator is tested for the piston driving. A loudspeaker, functioning as the piston, is used to drive the resonator at its big end. Resonance pressures at both end of the resonator are recorded and the experimental measurements are compared with the simulation results. The experimental study is then extended to small LARR resonators. These resonators are driven by a loudspeaker at their side walls. Finally, a miniature LARR resonator is proposed and tested, which is driven by a piezoelectric disk at one side of the resonance cavity.

6.2 RESONATORS AND DRIVING UNITS

Four acoustical resonators were used in the experiment, including a horn-shaped axisymmetric resonator (Type-1) and three LARR resonators (Type-2, 3, 4). There were 3 driving units, made from 2 loudspeakers and 1 piezoelectric disk, to drive these resonators. Type 2 and 3 resonators shared the same driving unit.

6.2.1 TYPE-1 RESONATOR

Figure 6.1 shows the Type-1 resonator and its driving unit. Type-1 resonator was a horn-shaped resonator with exponentially expanded across sectional areas. It was made of aluminum alloy. The Type-1 resonator was driven by a 5-inch 40W loudspeaker, which was installed in a speaker box.

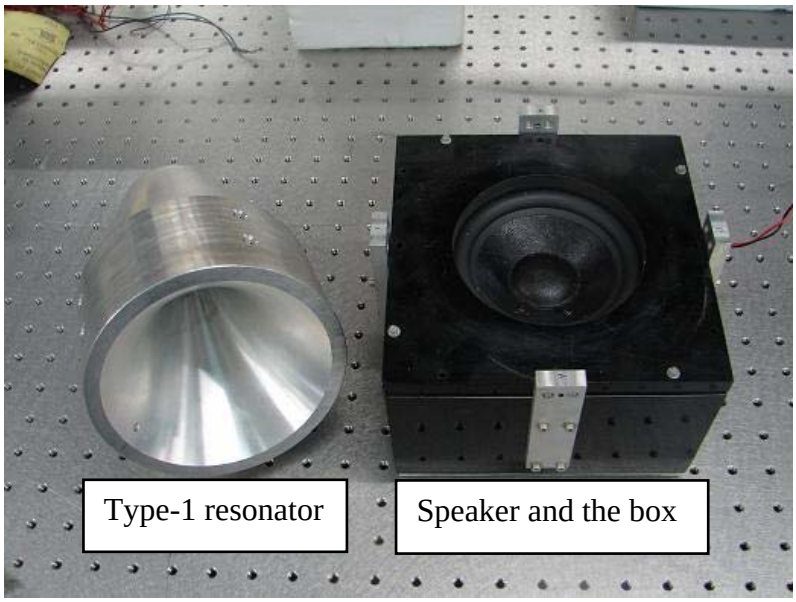

Figure 6.1 Type-1 resonator and driving unit.

The internal profile of the exponentially expanded resonator is shown in Figure 6.2. The length of the resonator is $l = 200\text{mm}$. Taking speed of sound $c_0 = 343\text{m/s}$, the nature fundamental resonance frequency of a straight duct with the same length (200mm) is calculated by

$$f_0 = \frac{c_0}{2l} = 857.5 \text{ Hz.} \tag{6.1}$$

The cross sectional area of this shaped resonator was expanded exponentially with the flare constant $\alpha = 5.6$. The radius at the small end was 4mm and the radius at the big end was 65.8mm. The equation of the internal profile of Type-1 resonator is given by

$$r = r_0 e^{2.8x/l}, \qquad 0 \le x \le 200, \quad r_0 = 4, \; l = 200, \text{ Unit: mm.} \tag{6.2}$$

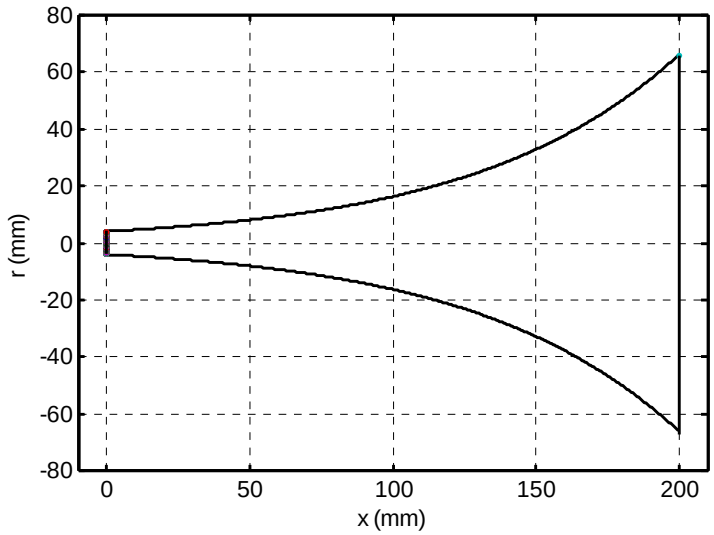

Figure 6.2 The profile of Type-1 resonator.

Figure 6.3 shows the Type-1 resonator assembly. The small end of the resonator was sealed and the large end was connected to a speaker box through a 110mm diameter hole. The box was made with 12mm thick plastic to ensure strength so that it was able to support the resonator resting on it. The plastic were glued together and sealant was applied to the joints to prevent leakage. Behind the hole to the resonator, there was a Eurotech 5-inch 40W loudspeaker (as shown in Figure 6.1) functioning as the piston. Factors were considered to select the speaker, including the power and the physical

size. There was a ¼ inch microphone behind the speaker to measure the sound pressure levels inside the speaker box. Since the back space of the box was isolated from the resonator by the speaker diaphragm, the sound pressure level measured there was not directly related to the resonance pressures inside the resonator but served as an indicator for the piston driving strength. Two pressure transducers were fixed at the two ends of the resonator to measure dynamic pressures inside the resonator, as shown in Figure 6.3. The pressure transducer at the small end was denoted as A and the pressures measured from it were denoted as P_A accordingly. Similarly, the pressures measured at the big end were denoted as P_B.

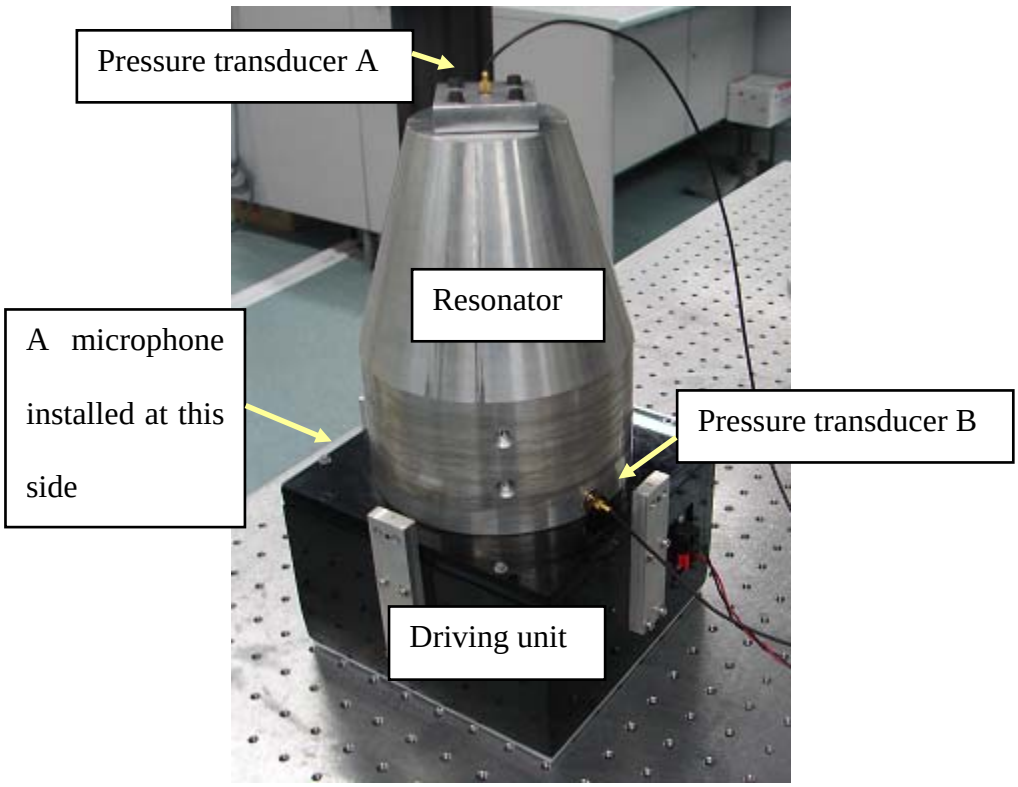

Figure 6.3 Type-1 resonator assembly.

6.2.2 TYPE-2 RESONATOR

The Type-2 resonator was a LARR resonator with rectangular across sectional area. Figure 6.4 schematically shows the Type-2 resonator and its driving unit. The resonator was formed between a cavity plate and a cover plate. The cavity was machined on a brass plate and the depth of the cavity was 5mm (Figure 6.5). A 3-inch 20W loudspeaker was mounted on the cover plate to function as a piston (Figure 6.5). The Type-2 resonator had an exponentially expanded section between the cavity and the small end.

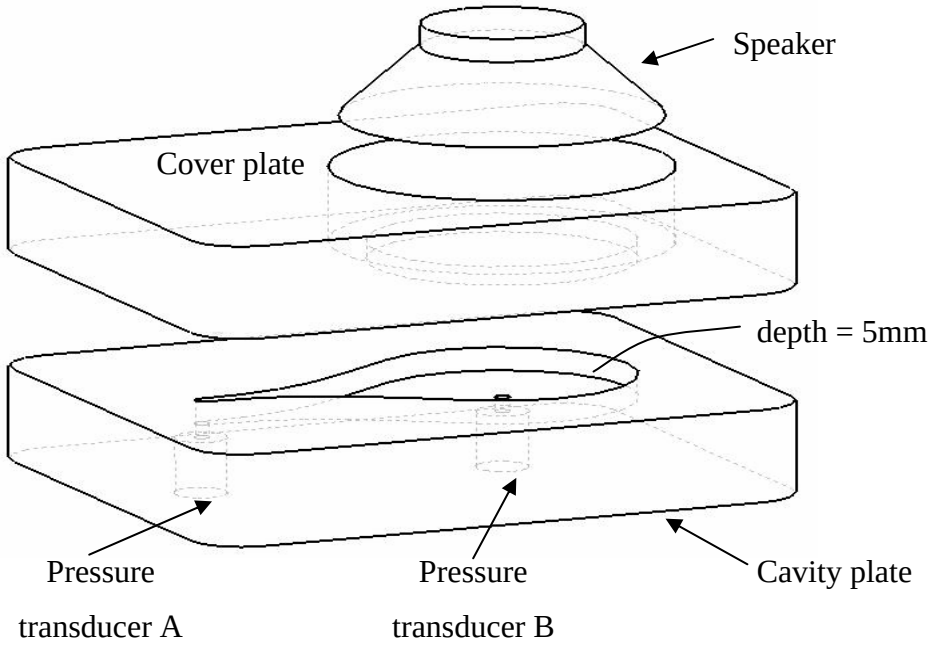

Figure 6.4 Schematic illustration of Type-2 resonator driven by a loudspeaker.

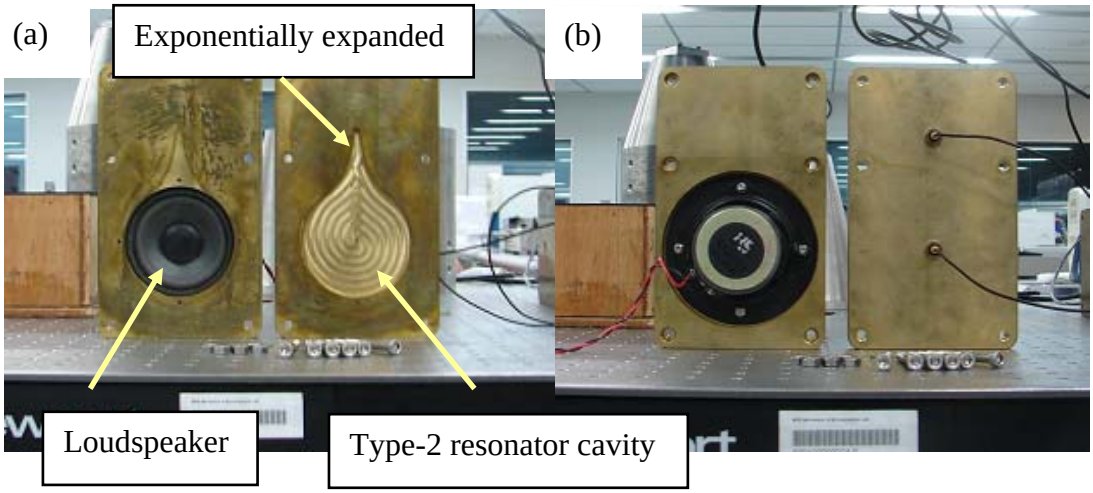

Figure 6.5 Type-2 resonator and loudspeaker.

Figure 6.6 shows the profile of Type-2 resonator. The total internal length of this flat resonator is 121.5mm. The profile of the cavity consists of a 3mm diameter semi-circle at the small end, an 80mm diameter semi-circle at the big end, and an exponentially expanded section between two ends. The natural fundamental frequency corresponding to a straight cylindrical resonator can be calculated based on either the total length or the distance from the small end to the centre of the cavity at the big end, which 80mm in this case. They are listed below:

$$f_0 = \frac{c_0}{2l} = \begin{cases} 2143.8 \text{ Hz}, \ l = 80 \text{ mm}; \\ 1411.5 \text{ Hz}, \ l = 121.5 \text{ mm}, \end{cases} \tag{6.3}$$

where the speed of sound $c_0 = 343 m/s$. These resonance frequencies will be used to evaluate the frequency shift. The profile of Type-2 resonator is given by

$$\begin{cases} y = \sqrt{1.5^2 - x^2} & -1.5 \le x \le 0 \\ y = 1.5e^{0.0578x} & 0 < x \le 47.7 \\ y = \sqrt{40^2 - (x-80)^2} & 47.7 < x \le 120 \end{cases} \quad \text{unit: mm} \tag{6.4}$$

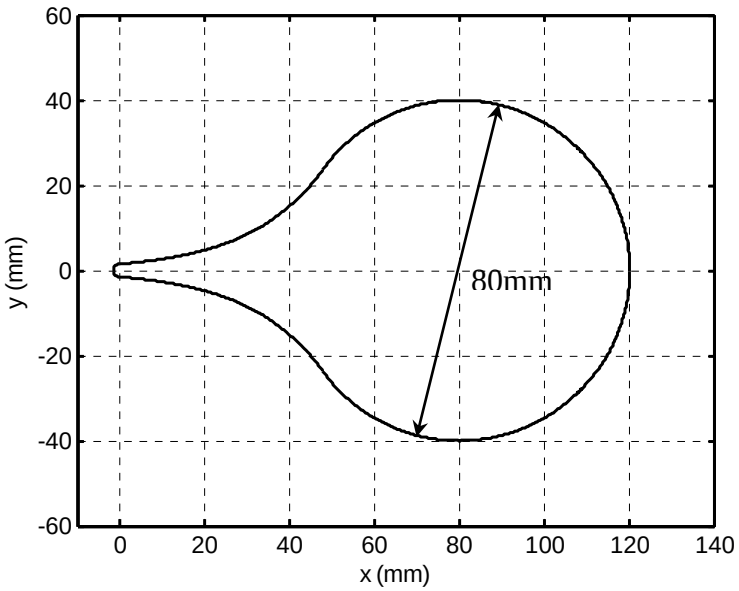

Figure 6.6 The profile of Type-2 resonator.

Figure 6.7 shows the Type-2 resonator assembly. The cover plate was fixed onto the cavity plate by six screws, and it had two pressure transducers mounted on it. The pressure transducers were the same as that used for Type-1 resonator, one was located at the small end to give pressure P_A and another was located at the centre of the semi-circle at the big end to give P_B. The resonator was supported by the speaker box and the driving strength was measured by a microphone inside the speaker box.

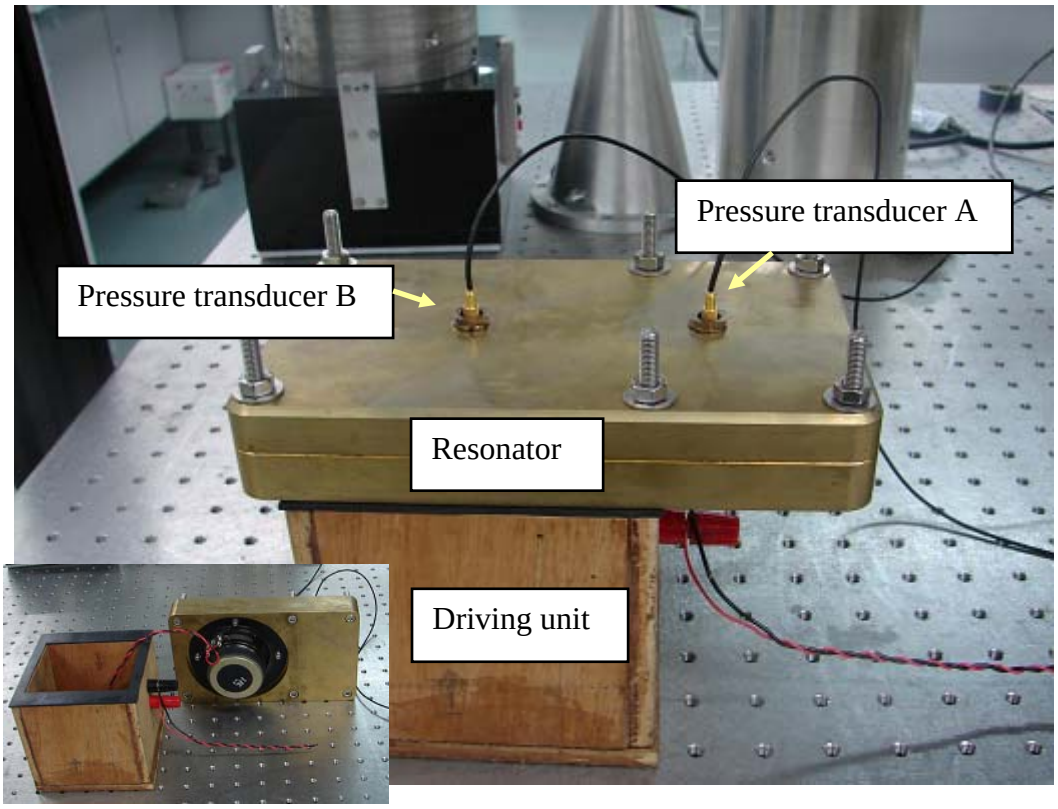

Figure 6.7 Type-2 resonator assembly.

6.2.3 TYPE-3 RESONATOR

The Type-3 resonator had a similar configuration of Type-2 resonator, except the cavity profile. The parts and driving unit for the Type-3 resonator are shown in Figure 6.8. Type-3 resonator was also a LARR resonator with rectangular across sectional area. The resonator was formed between a cavity plate and a cover plate (refer to Figure 6.4). The cavity was machined on a brass plate and the depth of the cavity was 5mm (Figure 6.8). The 3-inch 20W loudspeaker was mounted on the cover plate to drive the resonator (Figure 6.8). The Type-3 resonator had a linearly expanded section between the cavity and the small end.

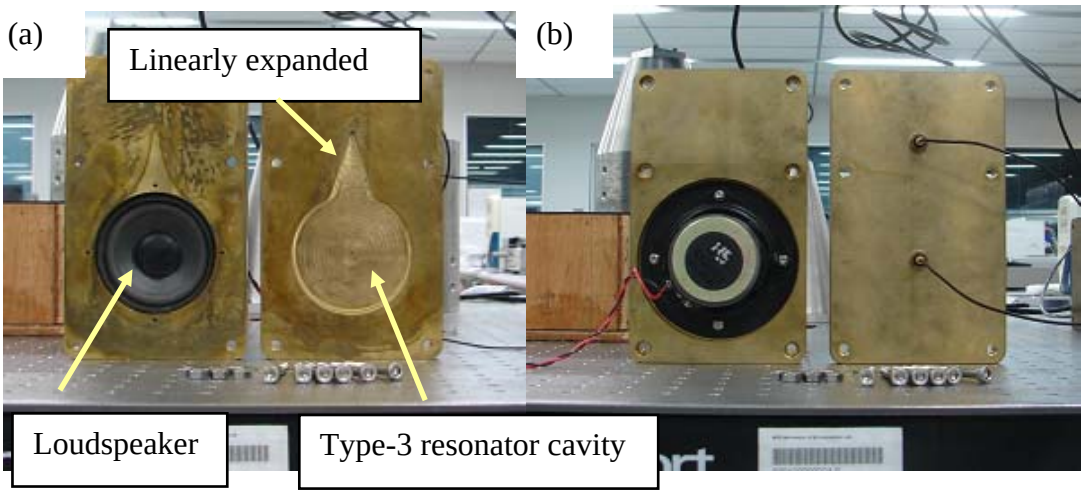

Figure 6.8 Type-3 resonator and loudspeaker.

Figure 6.9 shows the Type-3 resonator profile. The total internal length of this flat resonator is 121.5mm. The profile of the cavity consists of a 3mm diameter semi-circle at the small end, an 80mm diameter semi-circle at the big end, and a linearly expanded section between two ends. The distance from the small end to the centre of the semi-circle at the big end is 80mm, the natural fundamental frequency corresponding to the straight cylindrical resonator is therefore the same as that for Type-2 resonator listed in Equation (6.3). The profile of Type-3 resonator is given by

$$\begin{cases} y = \sqrt{1.5^2 - x^2} & -1.5 \le x \le -0.388 \\ y = 0.268x + 1.553 & -0.388 < x \le 37.309 \\ y = 21.209 - \sqrt{10^2 - (x - 34.721)^2} & 37.309 < x \le 43.777 \\ y = \sqrt{40^2 - (x - 80)^2} & 43.777 < x \le 120 \end{cases} \quad \text{unit: mm} \qquad (6.5)$$

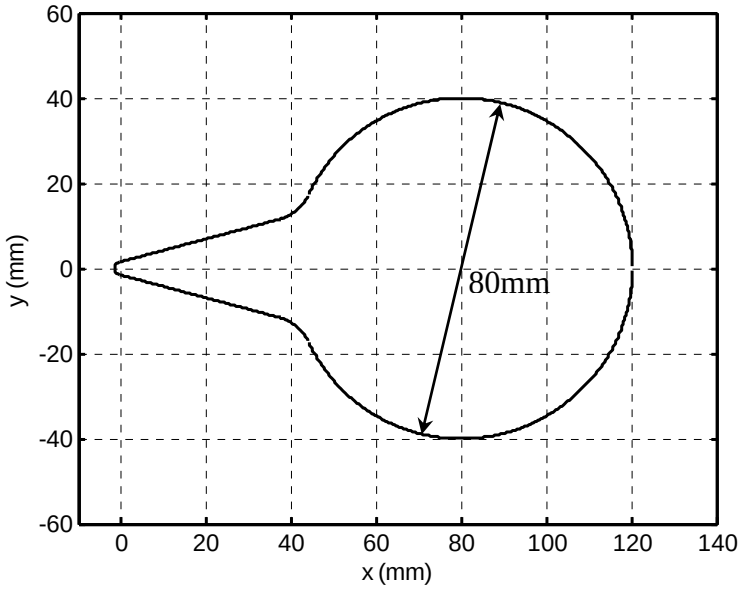

Figure 6.9 The profile ofType-3 resonator.

The Type-3 resonator assembly can be referred to Figure 6.7. Except for the cavity plate, others are the same as the Type-2 resonator assembly. Similarly, two pressure transducers were used. One was located above the small end to give pressure P_A and another was located above the centre of the semi-circle at the big end to give P_B.

6.2.4 TYPE-4 RESONATOR

The Type-4 resonator was also a LARR resonator with rectangular across sectional area, but much smaller than Type-2 and Type-3. The resonator was formed between a cavity plate and a cover plate, as shown in Figure 6.10. The cavity was machined on a brass plate. The depth of the cavity was 3mm, which was less than those in Type-2 and Type-3. A piezoelectric disk was flatly mounted on the cover plate as a boundary driving actuator. Type-4 resonator had an exponentially expanded section between the cavity and the small end. Figure 6.11 shows Type-4 resonator, its parts and its driving unit.

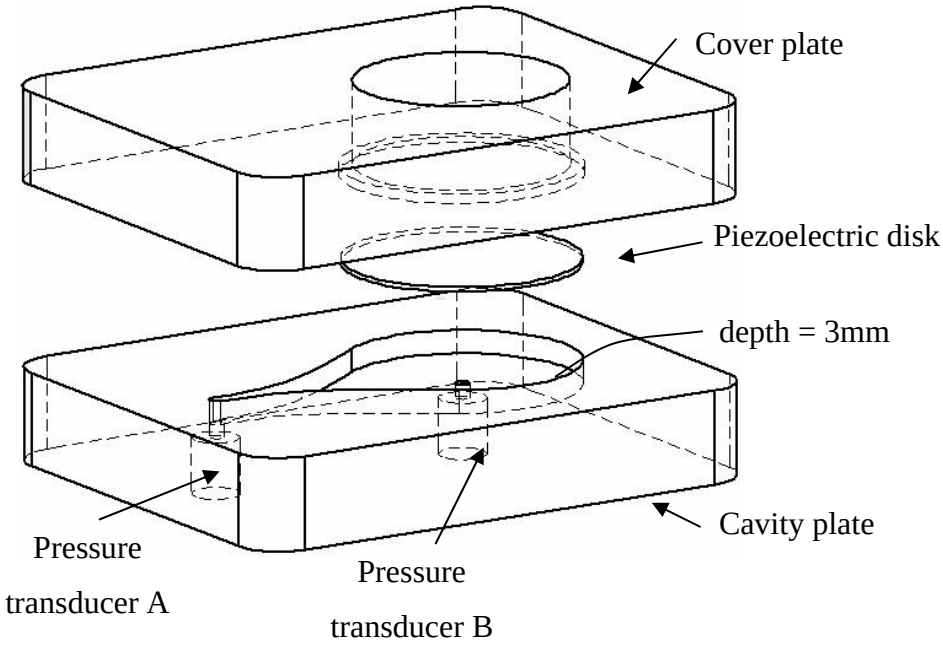

Figure 6.10 Schematic illustration of Type-4 resonator driven by a piezoelectric disk.

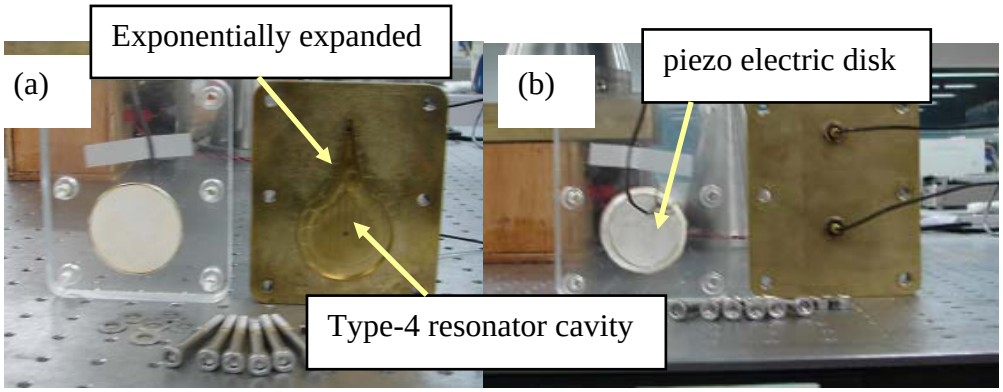

Figure 6.11 Type-4 resonator and piezoelectric disk.

Figure 6.12 shows the Type-4 resonator profile. The total internal length of this flat resonator is 86.5mm. The profile of the cavity consists of a 3mm diameter semi-circle at the small end, a 50mm diameter semi-circle at the big end, and a section between two ends. By taking the distance from the small end to the centre of the semi-circle at the big end as the characteristic length, which is 60mm, the natural fundamental frequency is

$$f_0 = \frac{c_0}{2l} = 2858.3\,\text{Hz}, \tag{6.6}$$

where the speed of sound c_0 = 343m/s and $l = 60$mm. The profile of Type-4 resonator is given by

$$\begin{cases} y = \sqrt{1.5^2 - x^2} & -1.5 \le x \le 0 \\ y = 1.5e^{0.0583x} & 0 < x \le 42.1 \quad \text{unit: mm} \\ y = \sqrt{25^2 - (x-60)^2} & 42.1 < x \le 85 \end{cases} \tag{6.7}$$

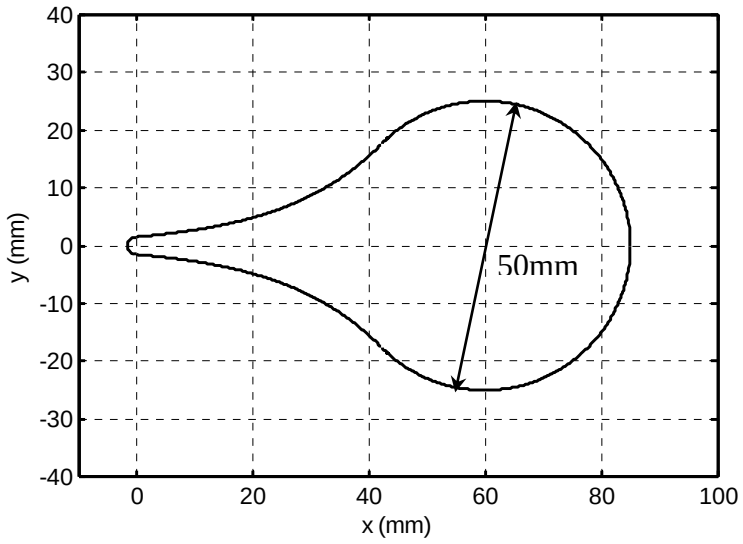

Figure 6.12 The profile of Type-4 resonator.

Type-4 resonator assembly is shown in Figure 6.13. A piezoelectric disk was mounted, as part of the surface, on the cover plate. The diameter of the disk was 50mm and thickness was 0.5mm. The cover plate was fixed onto the cavity plate, and the resonator was formed with the piezoelectric disk being one sidewall of the resonator cavity. The resonator was under the boundary driving when driving voltages were applied on the piezoelectric disk. The pressure transducers were the same as that used

for the axisymmetric resonator, one was located at the small end to give pressure P_A and another was located at the centre of the semi-circle at the big end to give P_B.

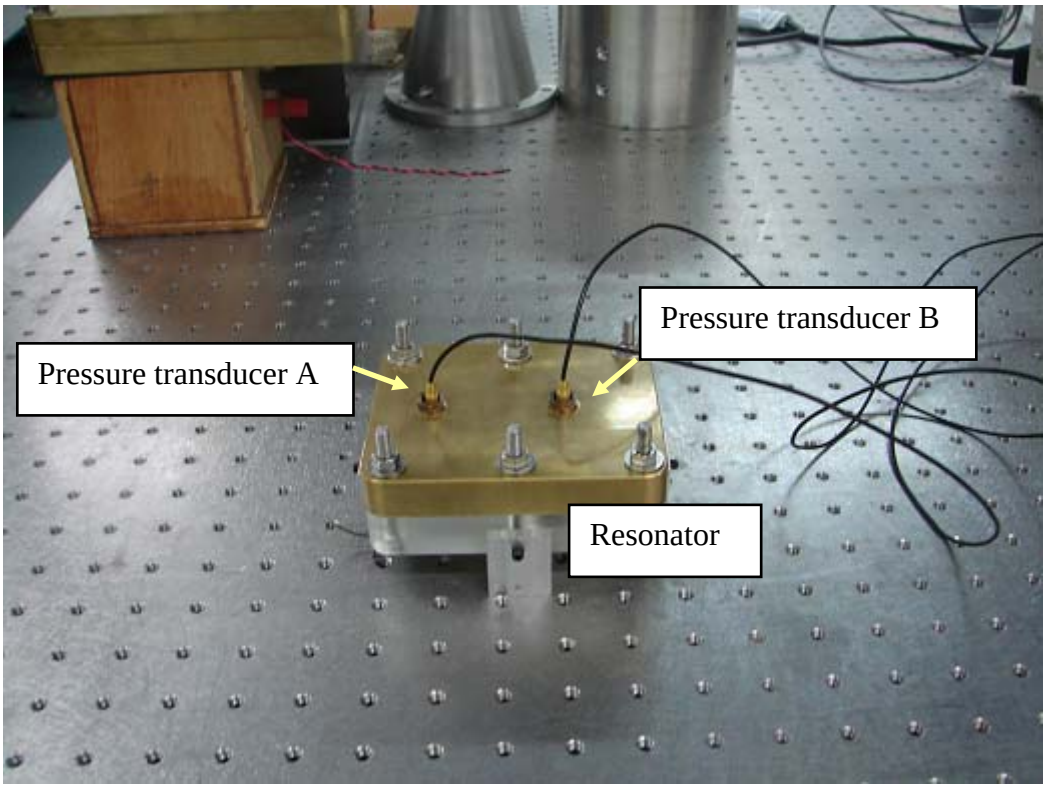

Figure 6.13 Type-4 resonator assembly.

6.3 EXPERIMENTAL SETUP AND INSTRUMENTATION

Figure 6.14 shows the schematic diagram of the experiment, including the resonator, driving unit, two pressure transducers and other supporting equipments. Totally four resonators were used in this experimental study, and each resonator had its own driving unit. Figure 6.14 only shows the setup for Type-1 resonator and its driving unit. The voltage input to the driving unit was supplied by an HP 33120A function generator and a power amplifier. The waveform and frequency of the input were modified by the function generator, while the amplitude was controlled by the function generator and the amplifier. Two pressure transducers (PCB Piezotronics Inc. Model 103B12) were used to measure dynamic pressure in the resonator. The signals from the pressure transducers were received by a signal conditioner (PCB Model 483A) and analyzed by a FFT analyzer (ONO SOKKI CF-5220Z).

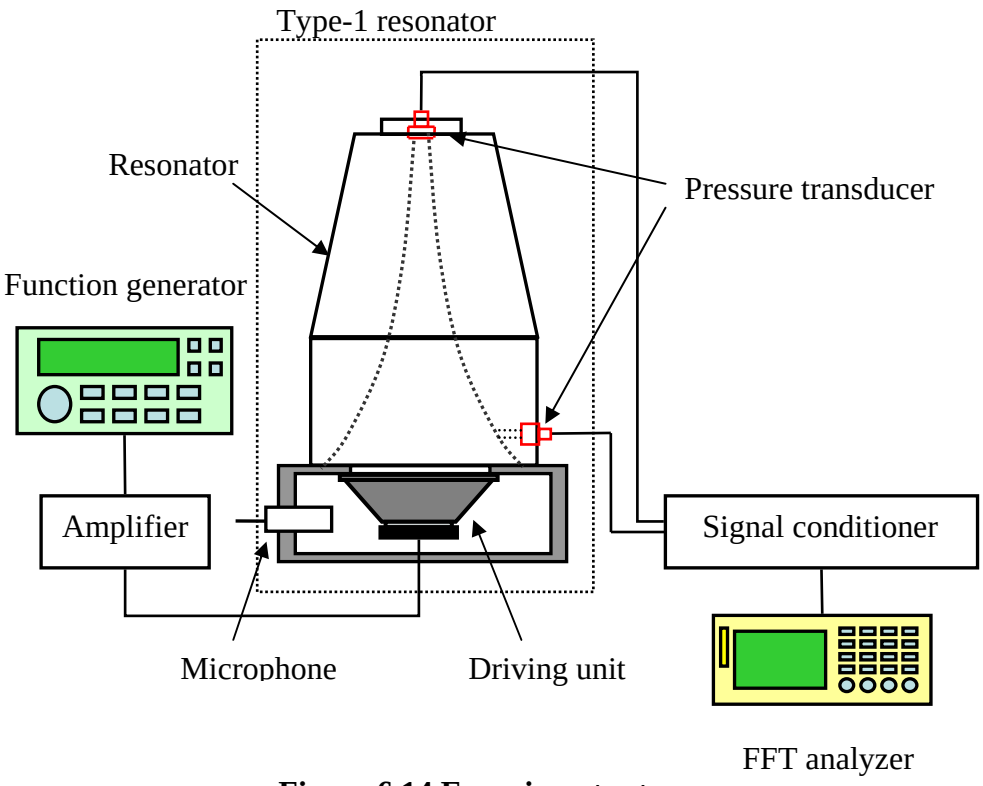

Figure 6.14 Experiment setup.

6.2.1 PRESSURE TRANSDUCER

Two PCB Piezotronics Inc. pressure transducers (Model 103B12), as shown in Figure 6.15, were used to measure dynamic pressure inside the resonators. The specifications of Model 103B12 at the room temperature are listed in Appendix C. The pressure transducers were installed in resonators and clamped by a nut. O-ring was used for protection and sealing. Signals received by pressure transducer were sent to the signal conditioner, which will be introduced later. The calibration details for the pressure transducers are presented in Appendix C2. The two pressure transducers had sensitivities 65.4 mV/kPa and 68.3 mV/kPa respectively.

Figure 6.15 PCB Piezotronics Inc. pressure transducer (Model 103B12).

6.2.2 FUNCTION GENERATOR

Figure 6.16 shows the HP33120A function generator used in the experimental study. Waveforms generated by the function generator can be adjusted through the front panel controls for frequency, amplitude and DC offset voltage.

Figure 6.16 HP/Agilent 33120A Function generator.

In the present experiment only sine waveforms were used, which is described by the following equation,

$$v(t) = V_A \sin(2\pi f) + V_{OFF} \tag{6.8}$$

where f is the frequency, V_A the amplitude, and V_{OFF} the offset voltage.

6.2.3 POWER AMPLIFIER

Two power amplifiers were used in the experiment. One was a Crown D75 two-channel power amplifier to drive the 40W speaker for Type-1 resonator and the 20W speaker for Type-2/3 resonators. Another was a PCB 790 series amplifier to drive the piezoelectric disk for Type-4 resonator. The amplifiers are shown in Figure 6.17.

Figure 6.17 Crown D75 amplifier (left) and PCB 790 series amplifier (right).

6.2.4 CONDITIONER

Figure 6.18 shows PCB 483A signal conditioner used in the experiments. The signal conditioner received signals from pressure transducers and converted them into outputs in voltages. The outputs of the signal conditioner were received and analyzed by a FFT analyzer.

Figure 6.18 Signal conditioner.

6.2.5 FFT ANALYZER

ONO SOKKI Multi-Purpose FFT analyzer CF-5220Z (shown in Figure 6.19) was used in the experiment to record and analyze the signals from the pressure transducers. CF-5220Z was 2-channel FFT analyzer mainly for analyzing sound and vibration at high speed and with high accuracy. Its specifications are listed in Appendix C.

Figure 6.19 ONO SOKKI Multi-Purpose FFT analyzer (CF-5220Z).

6.5 AXISYMMETRIC RESONATOR (TYPE-1) RESULTS AND DISCUSSIONS

6.5.1 RESONANCE FREQUENCY AND PRESSURES

The frequency response for the Type-1 resonator is shown in Figure 6.20. The vertical axis is the dynamic pressure received from pressure transducer A (located in the small end), under 5 different driving strengths. The microphone (work as an input indicator) indicated that the sound pressure levels (SPL) inside the speaker box was 80dB, 90dB, 100dB, 110dB, 120dB respectively. It can be seen from Figure 6.20 that the frequency response is nearly symmetrical and the resonance frequency is 1100Hz for all the driving strengths. According to Eq. (3.47) in Chapter 3, the nonlinear resonance frequency is calculated as

$$\Omega = \frac{\omega}{\omega_0} = \frac{f}{f_0} = 1.28, \tag{6.9}$$

where f_0 for Type-1 resonator is 857.5Hz. At a weak driving (80dB) the resonance pressure at the small end was 117.3Pa (135.4dB). When the driving strength is increased to 120dB, the resonance pressure is raised up to 1.15×10^4 Pa (175.2dB). The pressure waveforms at small end corresponding to the driving strength 120dB are shown in Figure 6.21, which are of sinusoidal forms without distortions. Compared with the high amplitude pressures at the small end, the pressure amplitude at the big end (near the speaker) is found much lower. The pressure amplitude ratio $\left|P_A / P_B\right|$ between the two ends of the resonator is about 17.6.

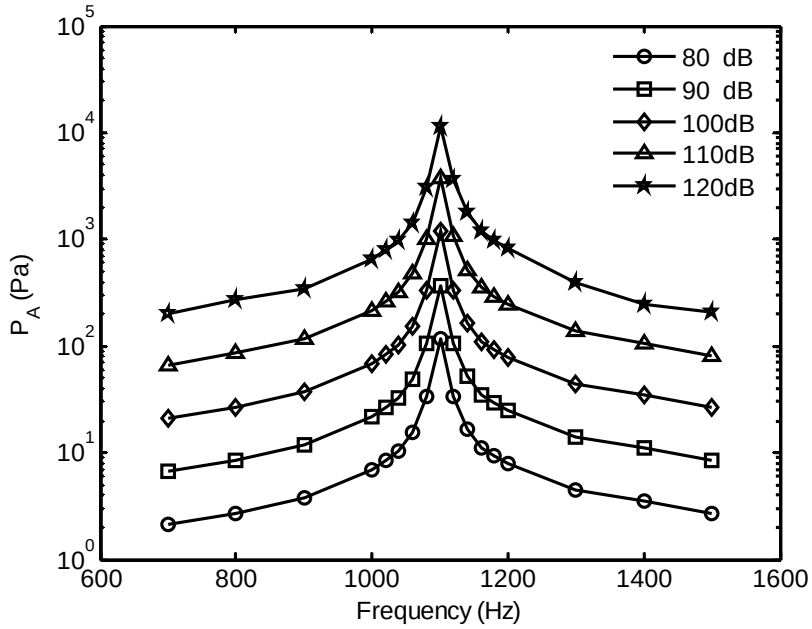

Figure 6.20. The frequency responses in the horn-shaped resonator at different driving strengths. The speaker power indicator is 80dB, 90 dB, 100dB, 110dB, and 120dB respectively.

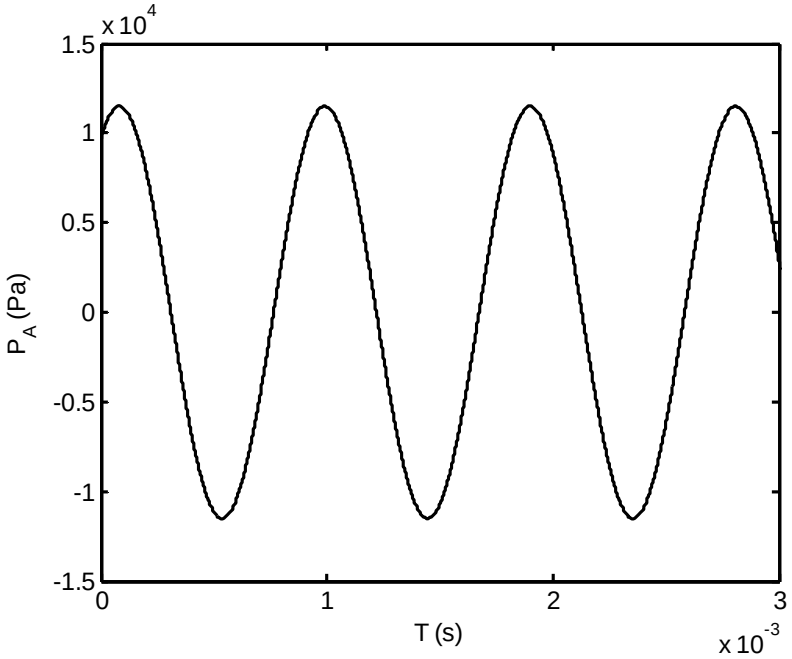

Figure 6.21. Pressure waveform at the small end of Type-1 resonator (driving strength SPL=120dB).

6.5.2 ESTIMATION OF THE DRIVING FORCE U^*

In order to compare the pressures measured at two ends of the resonator with the calculated values from the modeling in Chapter 4, the piston velocity U^* corresponding to the sound pressure level inside the speaker box needs to be obtained. Figure 6.22 shows the simplified version of the speaker box.

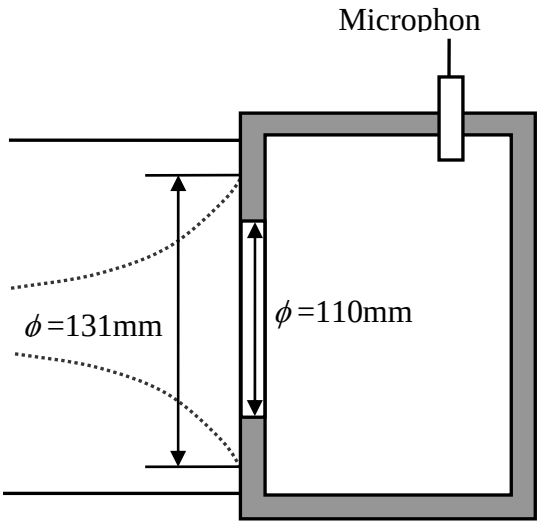

Figure 6.22. The simplified version of the speaker box for the horn-shaped resonator.

The sound box is assumed to be perfectly sealed, so that there is no net mass change in the box and

$$\frac{d(\rho V)}{dt} = V\frac{d\rho}{dt} + \rho\frac{dV}{dt} = 0. \tag{6.10}$$

Here, ρ is the density and V is the volume of the air in the speaker box. Since the volume change of the box is caused by the vibration of piston, so that,

$$\frac{dV}{dt} = s_{piston}u, \tag{6.11}$$

where s_{piston} is piston surface area and u is piston velocity. Substituting Eq. (6.9) into Eq. (6.8), one obtains

$$V\frac{d\rho}{dt}+\rho s_{piston}u=0. \tag{6.12}$$

Since the speed of sound is

$$c_0{}^2=\frac{dp}{d\rho}=\frac{dp}{dt}\Big/\frac{d\rho}{dt}, \tag{6.13}$$

so that

$$\frac{d\rho}{dt}=\frac{1}{c_0{}^2}\frac{dp}{dt}. \tag{6.14}$$

By combining Eq. (6.12) and Eq. (6.14), the piston velocity is obtained as

$$u=-\frac{V}{\rho c_0{}^2 s_{piston}}\frac{dp}{dt}, \tag{6.15}$$

and the velocity amplitude is

$$u^*=\frac{V}{\rho c_0{}^2 s_{piston}}\left|\frac{dp}{dt}\right|. \tag{6.16}$$

$\frac{dp}{dt}$ can be further approximated as

$$\left|\frac{dp}{dt}\right|=\omega\Delta p, \tag{6.17}$$

where ω is the speaker frequency and Δp is the dynamic pressure of air inside the box, which can be calculated from the measured SPL by the microphone, i.e.,

$$\Delta p = 10^{SPL/20} \times 2 \times 10^{-5}. \tag{6.18}$$

Using Eq. (6.17) and (6.18), Eq. (6.16) becomes

$$u^* = \frac{V\omega}{\rho c_0^{\,2} s_{piston}} 10^{SPL/20} \times 2 \times 10^{-5}. \tag{6.19}$$

In the dimensionless form,

$$U^* = \frac{u^*}{\pi c_0} = \frac{V\omega}{\pi \rho c_0^{\,3} s_{piston}} 10^{SPL/20} \times 2 \times 10^{-5}. \tag{6.20}$$

Since V and s_{piston} are difficult to evaluate and the big end of the resonator is partly driven by the speaker, a factor k is used here to simplify Eq. (6.20), i.e.,

$$U^* = k 10^{SPL/20}. \tag{6.21}$$

The factor k was calibrated by comparing the measured pressure amplitude at the small end with the calculated value, adjusting U^* until they were the same. At SPL=80dB, k was found to be 2.4×10^{-11}, and this k factor was used for other driving SPL values to determine the corresponding U^*.

6.5.3 COMPARISON WITH SIMULATION RESULTS

Resonance frequency

The calculated pressures under 5 piston driving strengths (U^*) were calculated and compared with the experimental data from the Type-1 resonator ($\alpha = 5.6$, $l = 0.2m$,

$r_0 / l = 0.02$). According to Eq. (3.83) in Chapter 3, the dimensionless fundamental resonance frequency for the Type-1 resonator is

$$\Omega_1 = \sqrt{1 + \frac{1}{4}\left(\frac{5.6}{\pi}\right)} = 1.34 . \tag{6.22}$$

The dimensional resonance frequency, taking f_0 = 857.5 Hz in Eq. (6.1), is therefore

$$f = f_0 \Omega_1 = 1149 \text{ Hz}. \tag{6.23}$$

Comparing with the measured resonance frequency, 1100Hz, the predicted resonance frequency is about 4.5% higher than the experimental result. Considering that the loudspeaker used in the experiment is not the flat piston assumed in the modeling, the agreement between the predicted resonance frequency difference and the measured value is quite good.

Resonance pressure amplitudes

The results on the pressure amplitudes are shown in Figure 6.23, in which the predicted pressures at the small end ($X = 0$) are compared to the measured values P_A from the experiment, and the predicted pressures at the big end ($X = 1$) are compared to P_B measured in the experiment. A good agreement is seen in this comparison.

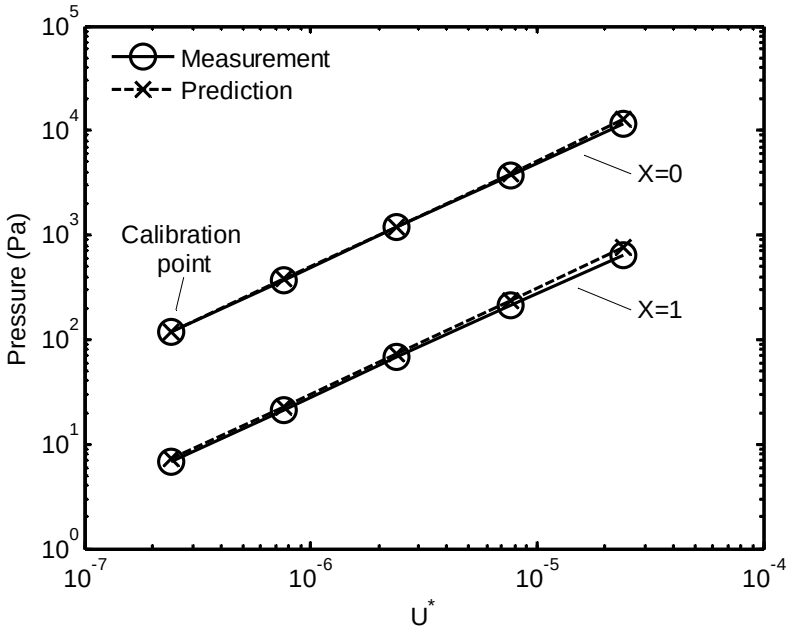

Figure 6.23. The small end and big end pressure in the Type-1 resonator obtained in the experiment (solid lines) and by the simulation (dashed line).

Pressure amplitude ratios

The pressure ratio $|P_A / P_B|$ obtained from the experiment is shown in Figure 6.24. The open triangle indicates the experimental data. With increasing the driving strength, $|P_A / P_B|$ increases slightly and the average value is 17.6, which is shown in the dashed line. This is close to the simulation result 16.5 which is indicated Figure 4.4 in Chapter 4.

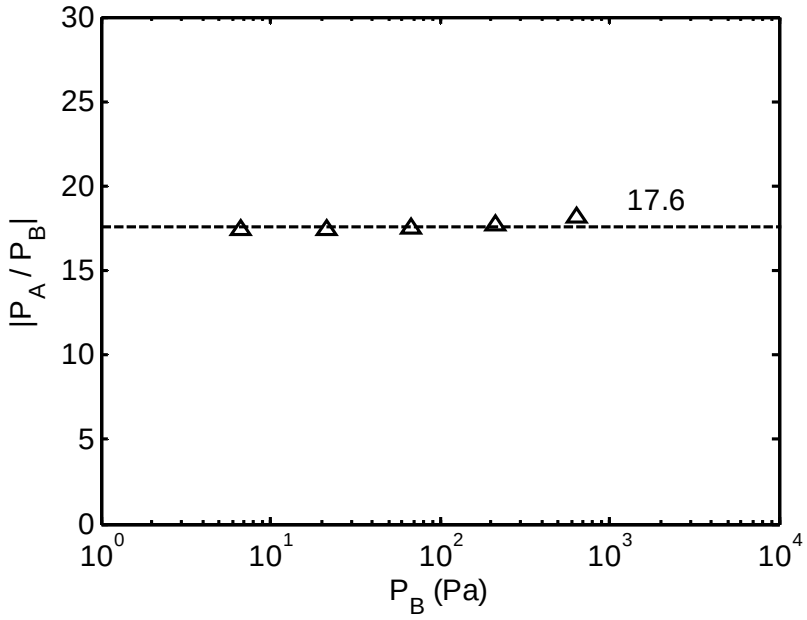

Figure 6.24. The ratio of pressure amplitudes at the small end to the big end for Type-1 resonator measured from the experiment, indicated by open triangles. The dashed line is the mean value ($\left|P_A / P_B\right| = 17.6$).

6.6 LARR RESONATOR (TYPE-2/3/4) RESULTS AND DISCUSSIONS

In this section, the experimental results on three low-aspect-ratio resonators are presented and discussed. Although there are no simulations on the performance of these resonators, the experimental results are evaluated according to the typical resonance characteristics established in shaped resonators, such as resonance frequency shift and pressure amplitude ratios between two ends.

6.6.1 RESONATOR DRIVEN BY A SPEAKER AT SIDE WALL

Exponentially expanded LARR resonator (Type-2)

Figure 6.25 shows the frequency response in Type-2 resonator driven by a 20W-loudspeaker. The vertical axis is the dynamic pressure received from pressure transducer A at the small end. Three different driving strengths were used, indicated by the microphone measured SPL inside the speaker box as 80dB, 90dB, and 100dB respectively. As the loudspeaker was less powerful, the driving strength was limited at SPL = 100dB in this experiment. It can be seen from Figure 6.25 that the response is not symmetrical and the pressure drops faster at high frequency side. The resonance frequency was found to be 2280Hz for all the driving strengths and the dimensionless resonance frequency can be calculated as $\Omega = \frac{2280}{f_0} = 1.06$ for f_0 = 2143.8 based on l = 80mm, and $\Omega = 1.61$ for f_0 = 1411.5 based on l = 121.5mm. The resonance frequency shift, one of the characteristics for shaped resonators, has been confirmed.

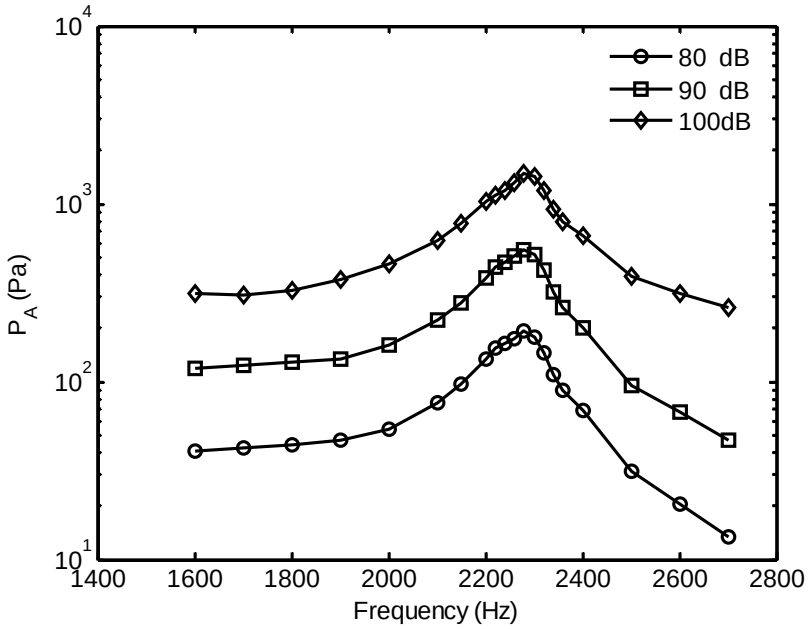

Figure 6.25. The frequency responses in the Type-2 resonator at the driving strength 80dB, 90 dB and 100dB respectively.

Figure 6.26 shows the resonance pressure at the small end from pressure transducer A and the resonance pressure near the speaker from pressure transducer B. For the lower strength driving (80dB), the pressure at the small end is 192.4Pa (139.7dB in SPL). When the driving strength is increased to 100dB, the resonance pressure reaches to 1476 Pa (157.4dB in SPL). The pressures obtained from pressure transducer B are much lower than that from the transducer A and the pressure amplitude ratio $|P_A / P_B|$ is about 20.8, shown in Figure 6.27. This is comparable to 17.6 obtained in the Type-1 resonator. The pressure waveforms at the small end with the driving strength SPL=100dB is plotted in Figure 6.28, showing that there is no distortions in pressure waveforms.

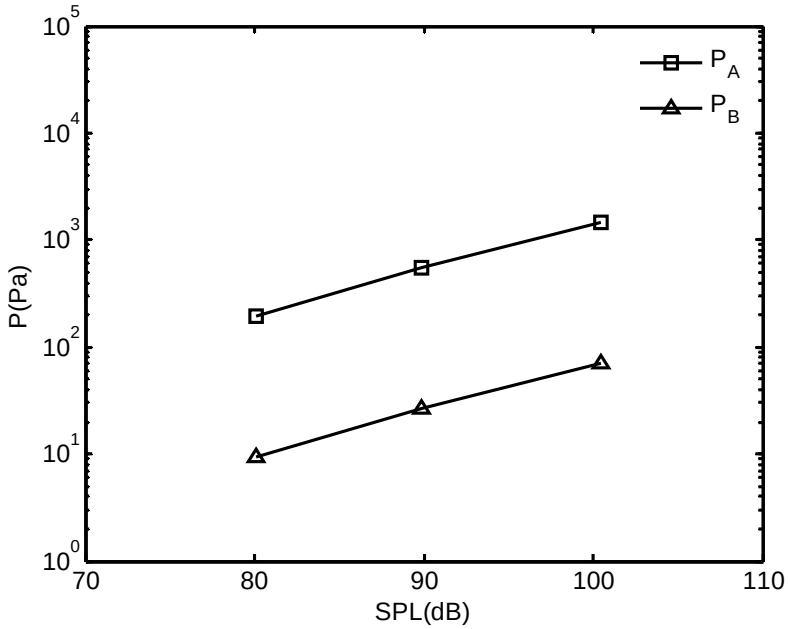

Figure 6.26. Resonance pressures obtained from sensors A and B in the Type-2 resonator against driving strength SPL inside the speaker box.

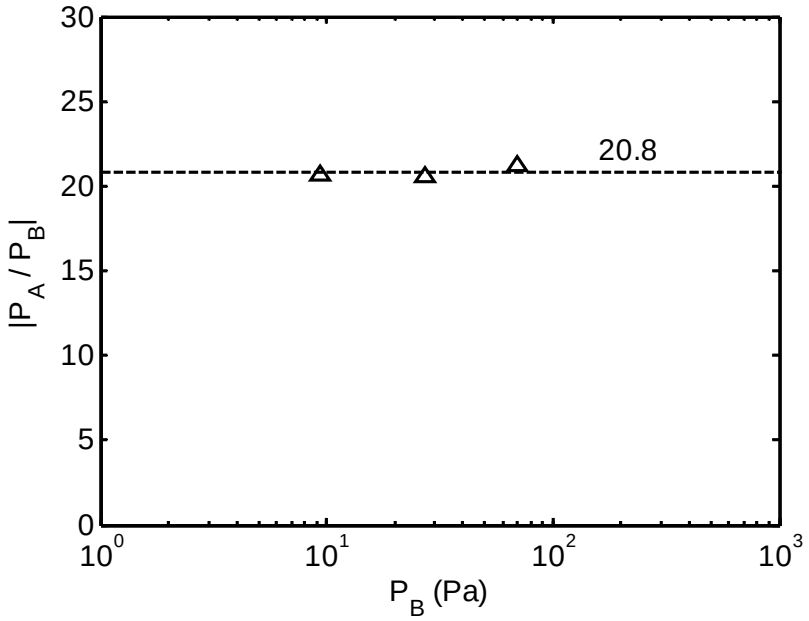

Figure 6.27. The ratio of pressure amplitudes at the small end to the big end for Type-2 resonator measured in the experiment, indicated by open triangles. The dashed line is the mean value ($|P_A / P_B| = 20.8$).

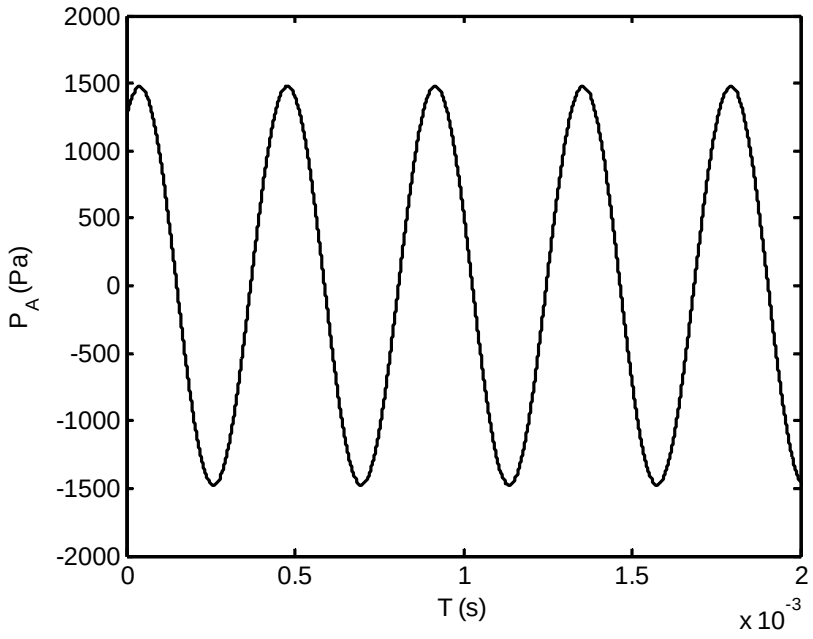

Figure 6.28. Pressure waveform at the small end of Type-2 resonator (driving strength SPL=100dB).

Linearly expanded flat resonator (Type-3)

The frequency response in Type-3 resonator is shown in Figure 6.29. The vertical-axis is the dynamic pressure received from pressure transducer A at the small end. Again, three different input strengths were used here, indicated by the microphone SPL inside the speaker as 80dB, 90dB, and 100dB respectively. The frequency response in the linearly expanded Type-3 resonator is similar to the response obtained in the exponentially expanded Type-2 resonator, which is not symmetrical and drops faster at high frequency side. The resonance frequency was found at 2150Hz for all driving strengths, which is close to the natural fundamental frequency $f_0 = 2143.8$ Hz based on $l = 80$mm from the small end to the cavity centre. However, if the total length $l = 121.5$mm is used as the characteristic length, the natural fundamental frequency will be $f_0 = 1411.5$ Hz and the dimensionless resonance frequency becomes

$$\Omega = 2150/1411.5 = 1.52 . \quad (6.24)$$

The resonance frequency shift is observed.

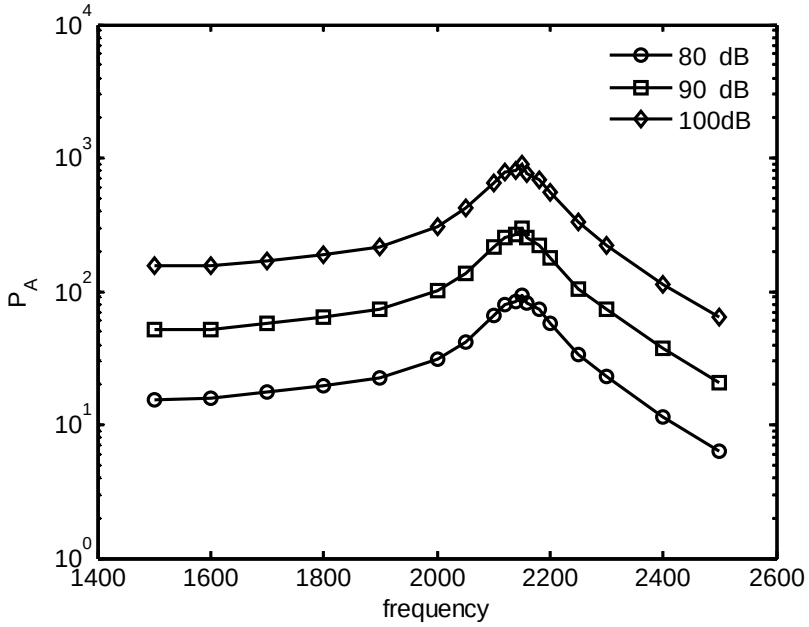

Figure 6.29. The frequency responses in the linearly expanded flat resonator at different input power. The speaker power indicator is 80dB, 90 dB and 100dB respectively.

Figure 6.30 shows the resonance pressure at the small end from pressure transducer A and the resonance pressure near the speaker from pressure transducer B. For a lower driving strength with SPL = 80dB, the pressure at the small end is 94Pa (133.4dB in SPL). When the driving strength is increased from 80dB to 100dB, the resonance pressure reaches to 892.8Pa (153dB in SPL). The resonance pressures obtained in the Type-3 resonator (linearly expanded) are lower than the resonance pressures in the Type-2 resonator (exponentially expand) for the same driving. The pressure amplitude ratio $|P_A / P_B|$ is about 20.2 showing in Figure 6.31, which is similar to the ratio in Type-2 resonator and also comparable to 17.6 obtained in the Type-1 resonator.

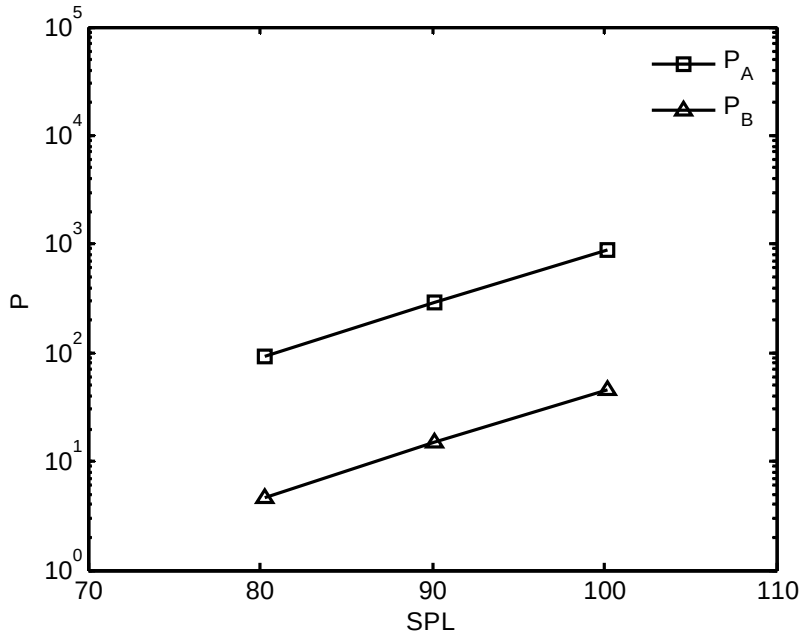

Figure 6.30. Dynamic pressures obtained from sensors A and B in Type-3 resonator against driving strength SPL inside the speaker box.

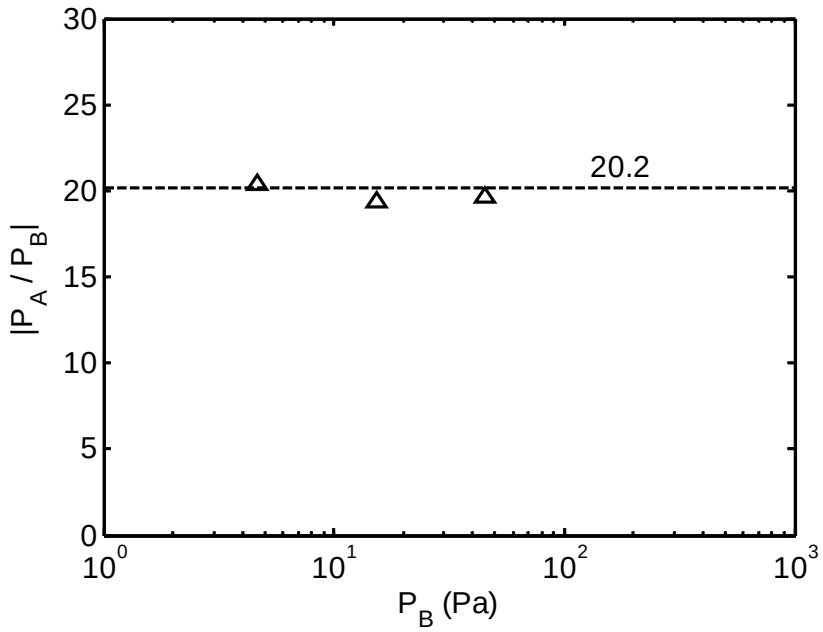

Figure 6.31. The ratio of pressure amplitudes at the small end to the big end of Type-3 resonator measured from the experiment, indicated by open triangles. The dashed line is the mean value ($\left|P_A / P_B\right| = 20.2$).

The experimental results of the two LARR resonators driven by a speaker are summarized in Table 6.1. It can be seen that the Type-2 with an exponentially expanded section performs better in terms of resonance pressure amplitudes.

Table 6.1 Comparison of the two flat resonators

	Resonance frequency shift based on f_0 = 1411.5 Hz, Ω	Pressure ratio $\lvert P_A / P_B \rvert$	Resonance pressures (Pa)at the small end under various driving strengths		
Type-2 (with an exponentially expanded section)	1.61	20.8	192.4	555.4	1476
Type-3 (with a linearly expanded section)	1.52	20.2	94	294.7	892.8

6.6.2 MINIATURE LARR RESONATOR DRIVEN BY A PIEZOELECTRIC DISK AT SIDE WALL (TPYE-4)

In above discussion, it shows that the exponentially expanded profile for low aspect ratio rectangular resonator can generate higher pressure waves than linearly expanded profile, so that the exponentially expanded profile was used when the resonator size was further reduced. The type-4 LARR resonator was called miniature because the channels height was only 3mm. The boundary driving in this case was produced by a flat piezoelectric disk which formed one side wall of the resonance cavity. When the driving signals from the PCB amplifier were applied on the piezoelectric disk in voltages, the piezoelectric disk would vibrate to excite the resonator. The driving

strength is this case was determined by the voltages applied on the piezoelectric disk. The resonance frequency for this miniature resonator was measured in the experiment to be 4020Hz. By taking the fundamental resonance frequency, f_0 = 2858.3 Hz, corresponding to distance (60 mm) from the small end to the centre of the semi-circle at the big end as the characteristic length, dimensionless resonance frequency can be calculated by

$$\Omega = \frac{f}{f_0} = \frac{4020}{2858.3} = 1.41, \tag{6.25}$$

which is comparable to $\Omega = 1.28$, 1.6 and 1.5 for the Type-1, Type-2 and Type-3 resonators respectively. The resonance frequency shift, as one of the characteristics, is similar to other shaped resonators.

The resonance pressures P_A (at the small end) and P_B (at the centre of the cavity) under different driving voltages, from 2V to 23V, are plotted out in Figure 6.32. It shows that the pressures at both ends are linearly increased with the driving voltages applied on the boundary disk, and the pressures at the small end are much higher than that at the big end, which is a typical characteristics observed in other shaped resonators. The ratio of P_A to P_B is calculated based on the data is shown in Figure 6.33, and an average value is found to be 20.2, which is similar to the ratios obtained in Type-2 and Type-3 resonators.

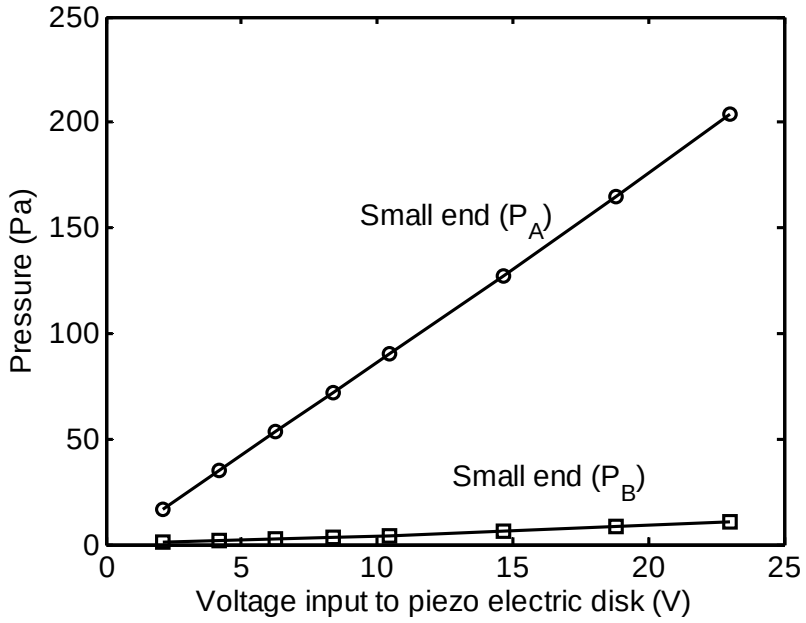

Figure 6.32 The pressure obtained from sensor A and B in Type-4 resonator at different driving voltages.

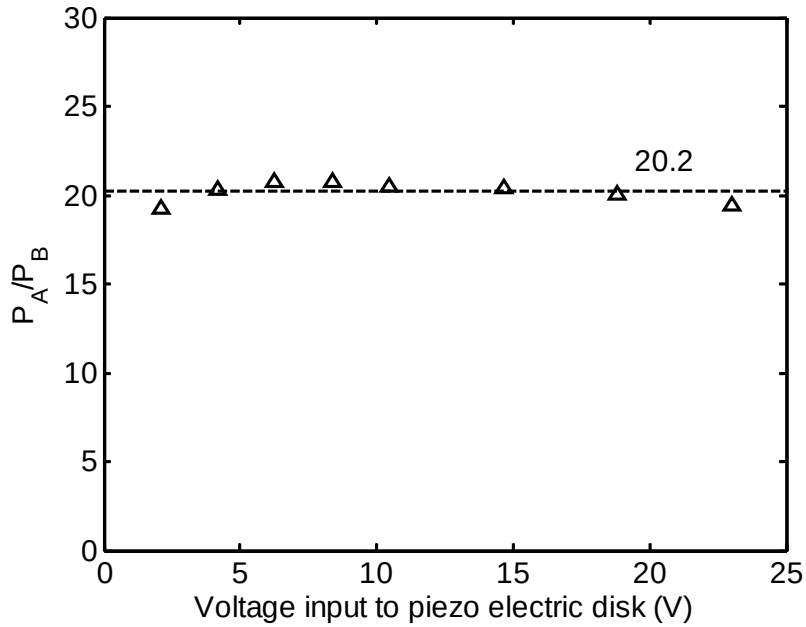

Figure 6.33. The ratio of pressure amplitudes at the small end to the big end of Type-4 resonator measured from the experiment, indicated by open triangles. The dashed line is the mean value ($P_A / P_B = 20.2$).

6.7 SUMMARY

A series of experiments have been conducted in this chapter. In the experiment on an exponentially expanded axisymmetric resonator (Type-1 resonator), the resonance frequency shift was found to be Ω =1.28. The maximum resonance pressure of 1.15×10^4 Pa (175.2dB) was found at the small end and the pressure ratio between the two ends was about 17.6. The experimental results have good agreement with simulation results in terms of resonance frequency, pressure amplitudes and pressure ratios. These resonance characteristics were further observed and confirmed in low-aspect-ratio rectangular (LARR) resonators, where the driving was generated at the resonator cavity side-walls. The pressure amplitude ratios and resonance frequency shifts obtained in LARR resonators demonstrate that the low aspect ratio rectangular resonator driven by the sidewall has the resonance characteristics similar to that for axisymmetric resonators. The experimental results suggest that the boundary driving, incorporated with properly designed resonators, could be a promising method to provide useful dynamic pressures for various applications, especially in small scale devices.

CHAPTER 7

CONCLUSIONS AND RECOMMENDATIONS

7.1 CONCLUSIONS

The nonlinear resonance characteristics of gas oscillations in shaped resonator, including pressure waveforms, resonance frequency, pressure amplitude, pressure ratio and quality factor, have been studied in this project. It consists two parts of work: theoretical modeling and experimental investigation. In the theoretical part, acoustical characteristics of nonlinear standing waves in exponentially expanded resonators, driven by shaking or an oscillating piston, have been studied. In the experimental part, the resonance characteristics are measured and analyzed for one axisymmetric resonator and three low-aspect-ratio rectangular resonators. From the results of both theoretical and experimental studies, the following conclusions can be drawn.

1. The effect of resonator dimensions on the characteristics of nonlinear standing waves has been studied. A shear viscosity term has been added to the one-dimensional momentum equation, and the wave equation has been solved by the Galerkin's method for axisymmetric resonators and low aspect ratio rectangular (LARR) resonators, whose cross sections are exponentially expanded. By examining the nonlinear resonance characteristics in resonators with different sizes, it is found that shear viscosity dissipation plays a crucial role in altering the resonance pressures when the resonator sizes are reduced. The resonator length (l) and the ratio of cross-section dimension to the length (r_0/l and h/l) are two controlling parameters. When r_0/l and h/l are less than 0.01, the resonance becomes weak and the resonators are

not functioning in these cases to generate large-amplitude pressures. The LARR resonators proposed in the present study have been found to have similar performance in nonlinear resonance to the axisymmetric ones, although they are more dissipative. The frequency responses for different dimension ratios (r_0/l and h/l) show that the dimension ratios control the frequency response curves in the same way as the excitation level does, following the hardening behavior of the shaped resonators.

2. The acoustic resonances in cylindrical and exponentially expanded resonators generated by piston driving have been studied. The non-homogenous boundary condition associated with the piston driving is converted to the homogenous boundary condition by introducing a new function to the solution which satisfies the velocity boundary condition, so that the Galerkin's method can be applied. Similar to the shaking driving, shock waves are obtained in a cylindrical resonator driven by the piston when the driving is strong, and shock-free waves are generated when the same driving is applied to the exponentially expanded resonators. The results show that, driven either by shaking or the piston, similar resonance characteristics can be obtained in the same resonator as long as the driving strengths satisfy $\tilde{A} = \tilde{U}\Omega$.

3. Energy dissipation in resonators has been studied by calculating the quality factors and examining the acoustic boundary layers. The quality factor is computed in two ways. One is based on decay factors for linear systems, and another is according to the ratio of dissipated energy to the total stored energy during the nonlinear resonance, so that the nonlinear effect is included. The results confirm that the smaller resonators, in terms of the dimension ratio r_0/l and h/l, are of lower quality factors and more dissipative, which are consistent to the weaker resonances observed in size-reduced

resonators, especially in the LARR resonators. The energy is mainly dissipated in the acoustic boundary layers associated with viscosity and thermal diffusions in the fluid. The thermal diffusion effect can be included in the simulation by replacing the viscosity term $\sqrt{\eta}$ with $\sqrt{\eta}\left(1+\frac{\gamma-1}{\sqrt{\mathrm{Pr}}}\right)$, and the results show that the effect of thermal diffusion on the resonance pressures is substantially high, which has not been reported in open literatures.

4. The experimental measurements carried out on an exponentially expanded axisymmetric resonator have been directly compared with simulations for the case of piston driving. The piston in the experiment was a speaker box at the big end of the resonator. Good agreement between the experimental results and the simulated ones has been obtained, in terms of resonance frequencies, pressure amplitudes and ratios of pressure amplitudes at the ends of resonators, indicating that the modeling method developed in the present study is valid and can be applied to other similar cases.

5. The piston driving has been extended to a general boundary driving method and applied to LARR resonators. The experimental studies have been conducted on prototypes of small and miniature LARR resonators. The driving in these LARR resonators is generated at the cavity sidewalls, rather than from the ends. The pressure amplitude ratios and resonance frequency shifts observed in the LARR resonators demonstrate that the low aspect ratio rectangular resonators driven by the sidewalls have the resonance characteristics similar to that generated in axisymmetric resonators. The results from this study suggest that the boundary driving, incorporated with

properly designed resonators, could be a promising method to provide useful dynamic pressures for various applications, especially in small scale devices.

7.2 RECOMMENDATIONS FOR FUTURE WORKS

In order to develop miniature acoustic resonators, many issues related to configurations and driving mechanisms need to be further investigated. The author would like to highlight some works for further studies.

1. The present one-dimensional model has successfully predicted the acoustic resonances in shaped resonators, but in most of cases, it is limited to axisymmetric resonators. In the future, it would be of interest to extend the one-dimensional model to three-dimensional cases to study the resonance characteristics for configurations other than axisymmetric resonators, such as the low-aspect-ratio rectangular resonators with boundary driving from sidewalls. This probably requires techniques of computational fluid dynamics (CFD). Since the CFD approach obtains the result from basic equations and uses discrete cells to describe computational domain, it can handle complicated resonator configuration and driving method.

2. It has shown that the performance of the shaped resonators depends highly on the expanded shapes. An optimization study may be necessary to look into the resonator shapes in order to generate high amplitude resonance pressures. The optimization study should take into account the resonator configurations and also the driving methods.

3. Acoustic boundary layers in resonators, consisted of viscosity boundary layer and thermal diffusion boundary layer, have been discussed in the present study. It is generally understood that the viscosity is the dominate fact associated with the energy dissipation. However, the simulation results obtained in the present study show that

thermal diffusion may also be an important fact. This needs to be further investigated by both experimental and theoretical studies.

4. Shock-free pressure waves have been observed in horn-shaped resonator and low-aspect-ratio rectangular resonators experimentally. Although the pressure amplitude ratios from the resonator ends have been found to be about 20, the dynamic pressures are not high enough, especially in the LARR resonators. This is probably due to the weaker driving strengths in these cases. A future study focusing on the power delivery through the boundary driving will be necessary in order to generate useful dynamic pressures in small scale resonators.

REFERENCE

Abramowitz M. and Stegun I., *Handbook of Mathematical Functions with Formulas, Graphs and Mathematical Tables*, United States of America, Department of Commerce, 355-434 (1972).

Bash C. E., Patel C. D. and Beitelmal A., *Acoustic compression for thermal management of multi-load electronic system*, Inter Society Conference on Thermal Phenomena, 395-402 (2002).

Baz A., *Proposal for a piezoelectric acoustic compressor*, unpublished work, University of Maryland, USA, (2000).

Betchov B., *Non-linear oscillations of the column of a gas*, Phys. Fluids. 1, 205-212 (1958).

Bishop R., Standing wave pump, U.S Patent Number 6-079-214, (2000).

Biwa T., Ueda Y., Nomura H., Mizutani U. and Yazaki T., *Measurement of the Q value of an acoustic resonator*, Phys. Rev. E72, 026601, 1-6 (2005).

Breidenthal R. E., Elements of entrainment, in *Turbulencia*, ABCM, Rio de Janeiro, 5(2), 205-211, (2006).

Breidenthal R. E., *The vortex as a clock*, DFD03 meeting of The American Physical Society, November 23-25, (2003).

Chester W., *Nonlinear resonant oscillations of a gas in a tube of varying cross-section*, Proc. R. Soc. London, Ser. A 444, 591-604 (1994).

Chester W., *Resonant oscillations in closed tubes*, J. Fluid Mech. 18, 44-64 (1964).

Chun Y. D. and Kim Y. H., *Numerical analysis for nonlinear resonant oscillations of gas in axisymmetric closed tubes*, J. Acoust. Soc. Am. 108, 2766-2774 (2000).

Coppens A. B. and Sanders J. V., *Finite-amplitude standing waves within real cavities*, J. Acoust. Soc. Am. 58, 1133-1140 (1975).

Coppens A. B. and Sanders J. V., *Finite-amplitude standing waves in rigid-walled tubes*, J. Acoust. Soc. Am. 43, 516-529 (1968).

Cruikshank D. B., *Experimental investigation of finite-amplitude acoustic oscillations in a closed tube*, J. Acoust. Soc. Am. 52, 1024-1036 (1972).

Dickens R. A., *Optimization of a piezoelectric acoustical compressor*, thesis, University of Maryland, USA, (2004).

Eisner E., *Complete solution of the Webster horn equation*, J. Acoust.Soc. Am., 41, 1126-1146 (1967).

Erickon R. R., and Zinn B. T., *Modeling of finite amplitude acoustic wave in closed cavities using the Galerkin method*, J. Acoust. Soc. Am., 103, 1863-1870 (2003).

Gad-et-Hak M., *The fluid mechanics of microdevices – the freeman scholar lecture*, Journal of Fluids Engineering, 121, 5-32 (1999).

Gaitan D. F. and Atchley A. A., *Finite amplitude standing waves in harmonic and anharmonic tubes*, J. Acoust. Soc. Am. 93, 2489–2495 (1993).

Goldstein S. and McLachlan N. W., *Sound waves of finite amplitude in an exponential horn*, J. Acoust. Soc. Am. 6, 275-278 (1935).

Hamilton M. F., Ilinskii Y. A., and Zabolotskaya E. A., *Linear and nonlinear frequency shifts in acoustical resonators with varying cross sections*, J. Acoust. Soc. Am. 110, 109–119 (2001).

Hoffman J. D., *Numerical methods for engineers and scientists*, McGraw-Hill, Singapore, 279-282 (1993).

Holland K. R., Fahy F. J. and Morfey C. L., *Prediction and measurement of the one-parameter behaviour of horns*, J. Audio Eng. Soc., 39(5), 315-337 (1991).

Huang P. T. and Brisson J. G., *Active control of finite amplitude acoustic waves in a confined geometry*, J. Acoust. Soc. Am. 102, 3256-3268 (1997).

Ilinskii Y. A., Lipkens B. and Zabolotskaya E. A., *Energy losses in an acoustical resonator*, J. Acoust. Soc. Am. 109, 1859–1870 (2001).

Ilinskii Y. A., Lipkens B., Lucas T. S., Van Doren T. W. and Zabolotskaya E. A., *Nonlinear standing waves in an acoustical resonator*, J. Acoust. Soc. Am. 104, 2664-2674 (1998).

Japanese Association of Refrigeration, *Thermophysical Properties of Environmentally Acceptable Fluorocarbons*, HFC-134a and HCFC-123 (1991).

Landau L. D. and Lishitz E. M., *Fluid Mechanics*, Pergamon, Oxford, 44-94 (1987)

Lawrenson C., Lipkens B., Lucas T. S., Perkins D. K. and Van Doren T. W., *Measurements of macrosonic standing waves in oscillating closed cavities*, J.

Acoust. Soc. Am., 104, 623–636 (1998).

Lee C. P. and Wang T. G., *Nonlinear resonance and viscous dissipation in an acoustic chamber*, J. Acoust. Soc. Am. 92, 2195-2206 (1992).

Lucas T. S. and Van Doren T. W., Resonant macrosonic synthesis, U.S Patent Number 5-515-684, (1996).

Lucas T. S., Compression-evaporation cooling system having standing wave compressor, U.S Patent Number 5-357-757, (1994).

Masuda M. and Sugimoto N., *Experiments of high-amplitude and shock-free oscillation of air column in a tube with array of Helmholtz resonators*, J. Acoust. Soc. Am. 118, 113-123 (2005).

Moloney J. M. and Hatten D. L., *Acoustic quality factor and energy loss in cylindrical pipes*, Am. J. Phys. 69 (3), (2001).

Morse P. M. and Ingard K. U., *Theoretical Acoustics*, Mcgraw-Hill, New York, (1968).

Nguyen N. T., Meng A. H., Black J. and White R. M., *Integrated Flow Sensor for In Situ Measurement and Control of Acoustic Streaming in Flexural Plate Wave Micro Pumps*, Sens. Actuators A, 79, 115–121 (2000).

Post J. T. and Hixson E. L., *A modeling and measurement study of acoustic horns*, Report of the Electroacoustics Research Laboratory, Department of Electrical and Computer Engineering, The University of Texas, Austin (1994).

Sabbagh A. E. and Baz A., *A coupled nonlinear model for axisymmetric acoustic*

resonators driven by piezoelectric bimorphs, Mechanics of Advanced Materials and Structures, 13, 205-217 (2006).

Saenger R. and Hudson G., *Periodic hock waves in resonating gas columns*, J. Acoust. Soc. Am. 32, 961–970 (1960).

Sugimoto N., Masuda M. and Hashiguchi T., *Frequency response of nonlinear oscillations of air column in a tube with an array of Helmholz resonators*, J. Acoust. Soc. Am. 114, 1772-1784 (2003).

Taleyarkhan R. P. and Lahey R. T., *Bubble power*, IEEE Spectrum, 42, 38-43, May (2005).

Temkin, *Propagating and standing sawtooth waves*, J. Acoust. Soc. Am. 45, 224-227 (1969).

Vanhille C. and Campos-Pozuelo C., *A high-order finite-difference algorithm for the analysis of standing acoustic waves of finite but moderate amplitude*, Journal of Computational Physics 165, 334–353 (2000).

Webster A. G., *Acoustical impedance, and the theory of horns and of the phonograph*, Proc. Natl. Acad. Sci. USA 5, 275-282 (1919).

Weiner S., *Standing sound waves of finite amplitude*, J. Acoust. Soc. Am. 40, 240-243 (1966).

Zettl A., *Sturm-Liouville Theory*, American Mathematical Society, (2005).

APPENDIX A

LINEAR ACOUSTIC MODE FUNCTIONS

The linear acoustic modes of an exponentially expanded resonator can be obtained by solving the linear wave equation Eq. (3.80),

$$(\pi\Omega)^2 \frac{\partial^2 \Phi}{\partial T^2} - \alpha \frac{\partial \Phi}{\partial X} - \frac{\partial^2 \Phi}{\partial X^2} = 0. \tag{A.1}$$

The dimensional form of Eq. (A.1) is

$$\frac{1}{c_0^2}\frac{\partial^2 \varphi}{\partial t^2} - \frac{\alpha}{l}\frac{\partial \varphi}{\partial x} - \frac{\partial^2 \varphi}{\partial x^2} = 0, \tag{A.2}$$

where c_0 is the speed of sound and l is resonator length. The solution of Eq. (A.2) can be written in a form

$$\varphi(x,t) = \tau(t)\psi(x). \tag{A.3}$$

Substitution of Eq. (A.3) into the governing partial differential equation Eq. (A.2) yields

$$\frac{1}{c_0^2}\tau''\psi - \frac{\alpha}{l}\tau\psi' - \tau\psi'' = 0. \tag{A.4}$$

After dividing Eq. (A.4) by $\tau\psi$ and rearrangement, Eq. (A.4) becomes

$$\frac{1}{c_0^{\,2}}\frac{\tau''}{\tau}=\frac{\alpha}{l}\frac{\psi'}{\psi}+\frac{\psi''}{\psi}. \tag{A.5}$$

The left hand side is a function only of t, and the right hand side is a function only of x, so that they must be equal to a constant. Let the constant be $-k^2$, two ordinary differential equation are obtained,

$$\tau''+\left(kc_0\right)^2\tau=0, \tag{A.6}$$

and

$$\psi''+\frac{\alpha}{l}\psi'+k^2\psi=0. \tag{A.7}$$

Assume a solution form

$$\psi=e^{\lambda x}, \tag{A.8}$$

and substituting Eq. (A.8) into Eq. (A.7), one obtains

$$e^{\lambda x}\left(\lambda^2+\frac{\alpha}{l}\lambda+k^2\right)=0, \tag{A.9}$$

of which the unknown λ is found

$$\lambda=\frac{-\alpha\pm\sqrt{\alpha^2-4k^2l^2}}{2l}=-\frac{\alpha}{2l}\pm i\sqrt{k^2-\left(\frac{\alpha}{2l}\right)^2}, \tag{A.10}$$

where $\left(kl\right)^2>\frac{\alpha}{4}^2$. The general solution for Eq.(A.7) is

$$\psi = \exp\left(\frac{-\alpha x}{2l}\right)\left[C_1 \cos\left(\sqrt{k^2 - \left(\frac{\alpha}{2l}\right)^2}\, x\right) + C_2 \sin\left(\sqrt{k^2 - \left(\frac{\alpha}{2l}\right)^2}\, x\right)\right], \qquad \text{(A.11)}$$

where C_1 and C_2 are two arbitrary constants. Since both ends of the resonator are closed, Eq. (A.7) subjects to the following boundary conditions

$$\psi'\big|_{x=0} = 0, \qquad \psi'\big|_{x=l} = 0\,. \qquad \text{(A.12)}$$

Using Eq. (A.11), the boundary condition in at $x = 0$ gives

$$\psi'\big|_{x=0} = \left(\frac{-\alpha}{2l} C_1 + C_2 \sqrt{k^2 - \left(\frac{\alpha}{2l}\right)^2}\right) = 0\,, \qquad \text{(A.13)}$$

i.e.,

$$C_2 = C_1 \frac{\alpha}{2l} \Big/ \sqrt{k^2 - \left(\frac{\alpha}{2l}\right)^2}\,. \qquad \text{(A.14)}$$

Using Eq. (A.14), the boundary condition at $x = l$ gives

$$\psi'_n\big|_{x=l} = \exp\left(\frac{-\alpha}{2}\right)\left(-k^2 C_1\right) \Big/ \sqrt{k^2 - \left(\frac{\alpha}{2l}\right)^2} \sin\left(\sqrt{(kl)^2 - \frac{\alpha^2}{4}}\right) = 0\,. \qquad \text{(A.15)}$$

For non-zero k and C_1, $\exp\left(\frac{-\alpha}{2}\right)\left(-k^2 C_1\right) \Big/ \sqrt{k^2 - \left(\frac{\alpha}{2l}\right)^2} \neq 0$. Then

$$\sin\left(\sqrt{(kl)^2 - \frac{\alpha^2}{4}}\right) = 0\,, \qquad \text{(A.16)}$$

So that

$$\sqrt{(kl)^2 - \frac{\alpha}{4}^2} = n\pi, \qquad n = 1, 2, 3\cdots, \tag{A.17}$$

therefore,

$$k_n = \sqrt{\left(\frac{n\pi}{l}\right)^2 + \frac{1}{4}\left(\frac{\alpha}{l}\right)^2}, \qquad n = 1, 2, 3\cdots. \tag{A.18}$$

Using Eqs. (A.18), Eq. (A.14) becomes

$$C_2 = \frac{\alpha}{2n\pi} C_1 . \tag{A.19}$$

By substitution Eqs. (A.17) and (A.19) into Eq. (A.11), the natural acoustic modes are obtained as

$$\psi_n(x) = \exp\left(\frac{-\alpha x}{2l}\right)\left[\cos\left(\frac{n\pi x}{l}\right) + \frac{\alpha}{2n\pi}\sin\left(\frac{n\pi x}{l}\right)\right], \tag{A.20}$$

in which, the arbitrary C_1 is set to be a unit. In the dimensionless form

$$\Psi_n(x) = \exp\left(-\frac{\alpha}{2} X\right)\left[\cos\left(n\pi X\right) + \frac{\alpha}{2n\pi}\sin\left(n\pi X\right)\right]. \tag{A.21}$$

The solution of Eq. (A.6) is of a form, for each k_n,

$$\tau_n = C_3 \cos(k_n c_0 t) + C_4 \sin(k_n c_0 t). \tag{A.22}$$

where C_3 and C_4 are arbitrary constants. The nth mode frequency is

$$\omega_n = k_n c_0 \,. \tag{A.23}$$

Using Eq. (A.18) and $\omega_0 = \dfrac{\pi c_0}{l}$, dimensionless form of the mode frequency is obtained as

$$\Omega_n = \frac{\omega_n}{\omega_0} = \sqrt{n^2 + \frac{1}{4}\left(\frac{\alpha}{\pi}\right)^2} \,. \tag{A.24}$$

The fundamental mode frequency is

$$\Omega_1 = \sqrt{1 + \frac{1}{4}\left(\frac{\alpha}{\pi}\right)^2} \,. \tag{A.25}$$

For a cylindrical resonator ($\alpha = 0$), the fundamental natural frequency is $\Omega_1 = 1$.

APPENDIX B

ACOUSTIC WAVES IN CYLINDRICAL RESONATOR

Acoustic characteristics in a cylindrical resonator ($S = \pi(r_0 / l)^2 e^{\alpha X}$, $\alpha = 0$, $l = 0.2m$ and $r_0 / l = 0.02$) are illustrated as following. The cylindrical resonator is driven by a shaking force at different strengths.

1. Weak driving ($A = 5 \times 10^{-6} \cos(T)$)

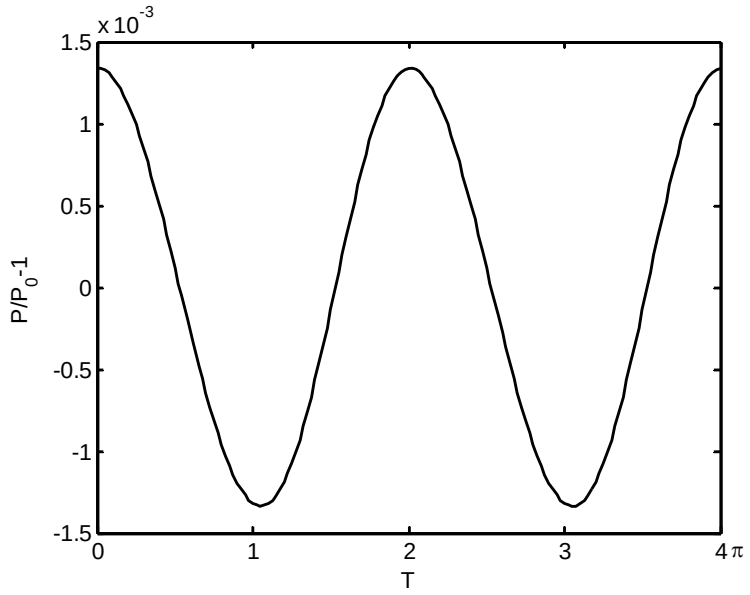

Figure B.1 Pressure waveforms at one end ($X = 0$) of the cylindrical resonator. $S = \pi(r_0 / l)^2 e^{\alpha X}$, $\alpha = 0$, $l = 0.2m$, $r_0 / l = 0.02$ and $A = 5 \times 10^{-6} \cos(T)$.

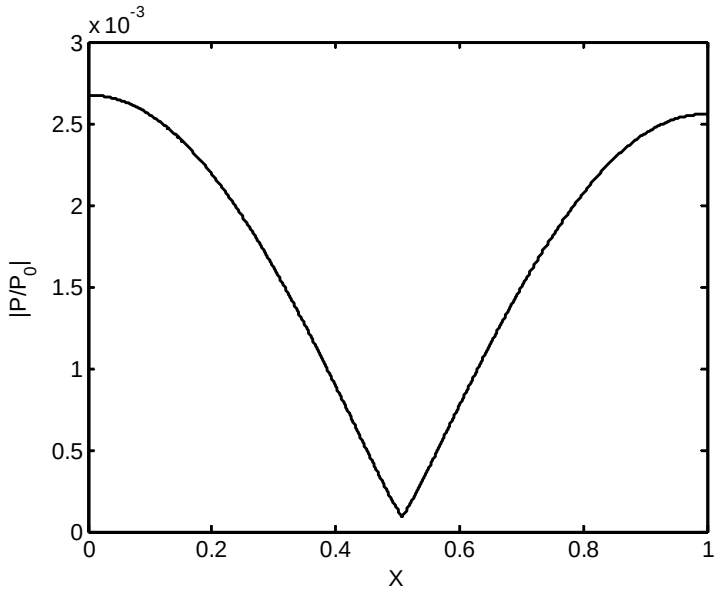

Figure B.2 Peak-to-peak pressure distribution in the cylindrical resonator along the axis. $S = \pi(r_0 / l)^2 e^{\alpha X}$, $\alpha = 0$, $l = 0.2m$, $r_0 / l = 0.02$ **and** $A = 5\times10^{-6}\cos(T)$.

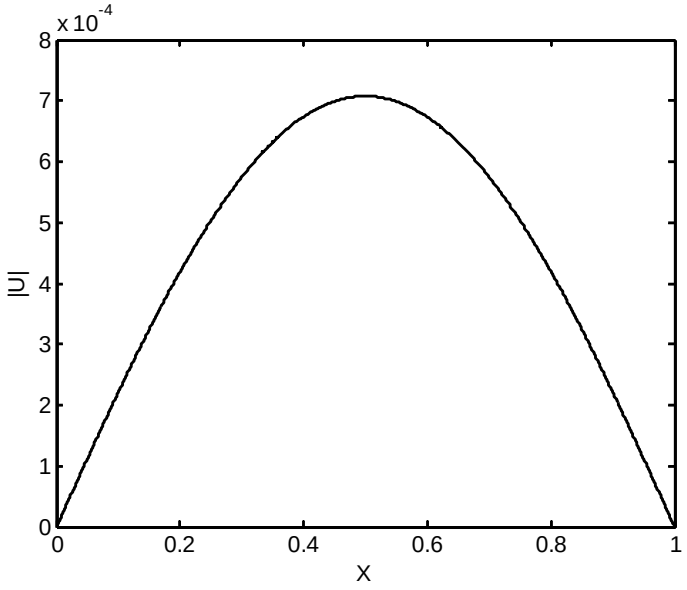

Figure B.3 Velocity amplitude distribution in the cylindrical resonator along the axis. $S = \pi(r_0 / l)^2 e^{\alpha X}$, $\alpha = 0$, $l = 0.2m$, $r_0 / l = 0.02$ **and** $A = 5\times10^{-6}\cos(T)$.

2. Moderate driving ($A = 5\times10^{-5}\cos(T)$)

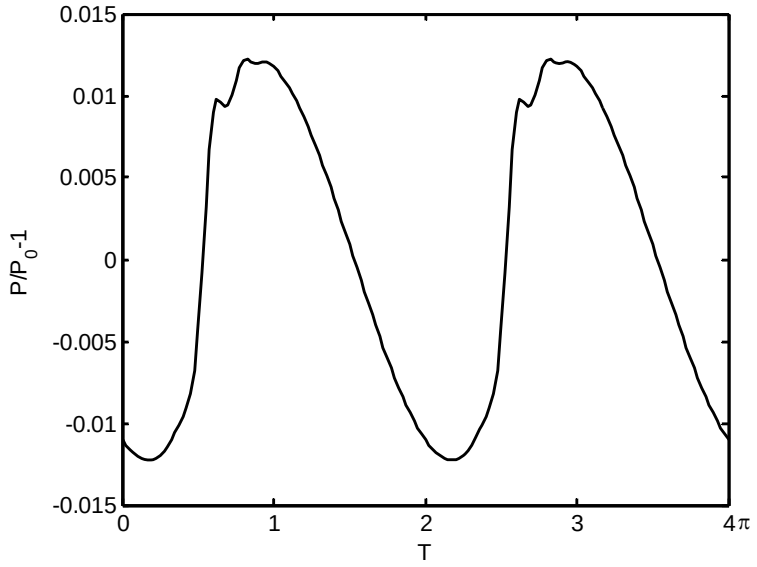

Figure B.4 Pressure waveforms at one end ($X = 0$) of the cylindrical resonator. $S = \pi(r_0/l)^2 e^{\alpha X}$, $\alpha = 0$, $l = 0.2m$, $r_0/l = 0.02$ **and** $A = 5\times10^{-5}\cos(T)$.

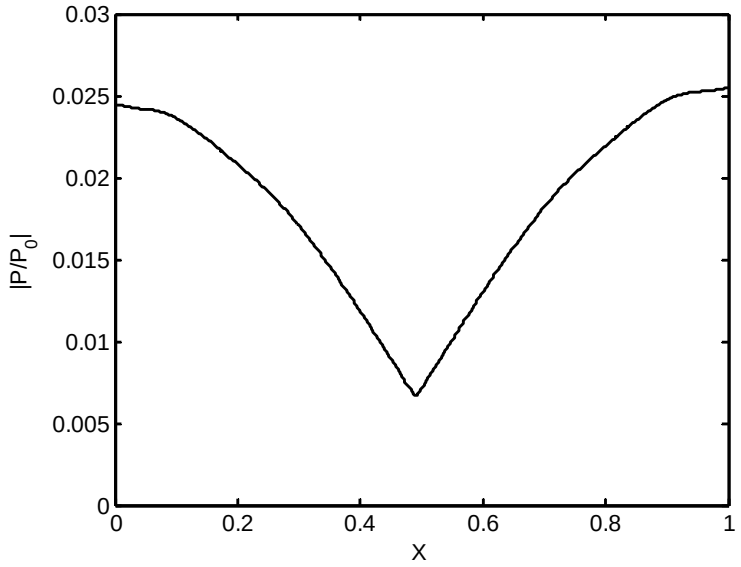

Figure B.5 Peak-to-peak pressure distribution in the cylindrical resonator along the axis. $S = \pi(r_0/l)^2 e^{\alpha X}$, $\alpha = 0$, $l = 0.2m$, $r_0/l = 0.02$ **and** $A = 5\times10^{-5}\cos(T)$.

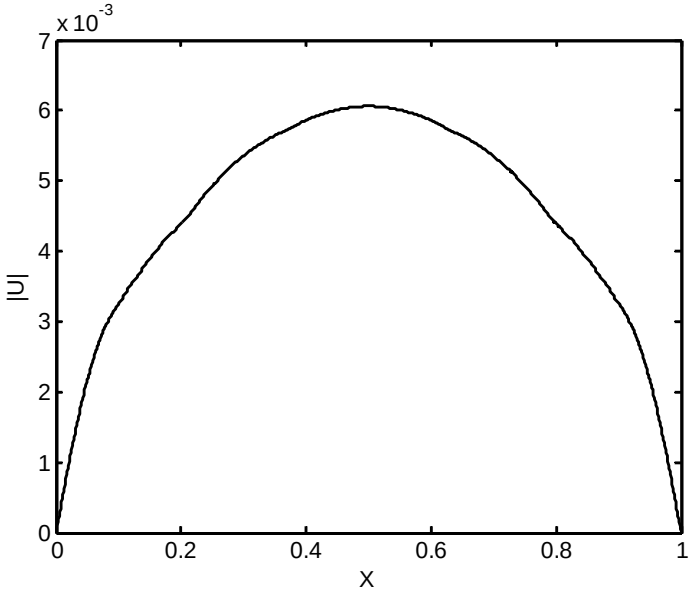

Figure B.6 Velocity amplitude distribution in the cylindrical resonator along the axis. $S=\pi(r_0/l)^2 e^{\alpha X}$, $\alpha=0$, $l=0.2m$, $r_0/l=0.02$ **and** $A=5\times10^{-5}\cos(T)$.

3. Strong driving ($A=5\times10^{-4}\cos(T)$ **)**

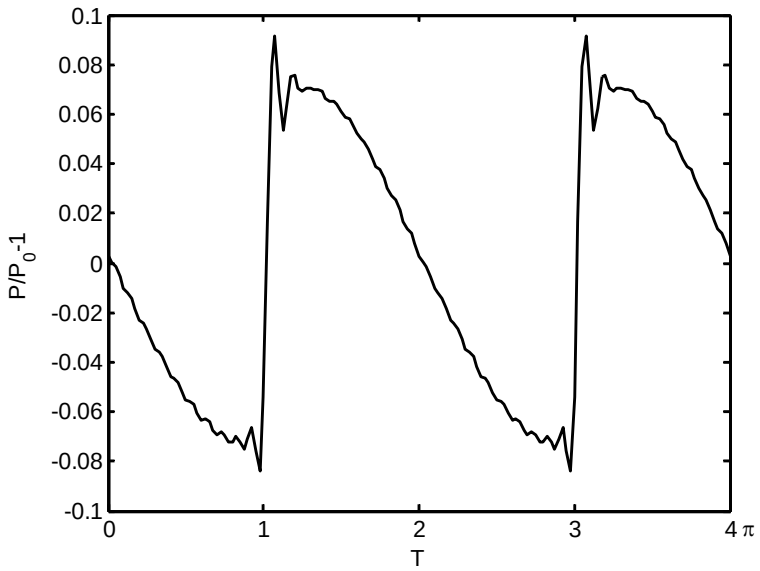

Figure B.7 Pressure waveforms at one end ($X=0$ **) of the cylindrical resonator.** $S=\pi(r_0/l)^2 e^{\alpha X}$, $\alpha=0$, $l=0.2m$, $r_0/l=0.02$ **and** $A=5\times10^{-4}\cos(T)$.

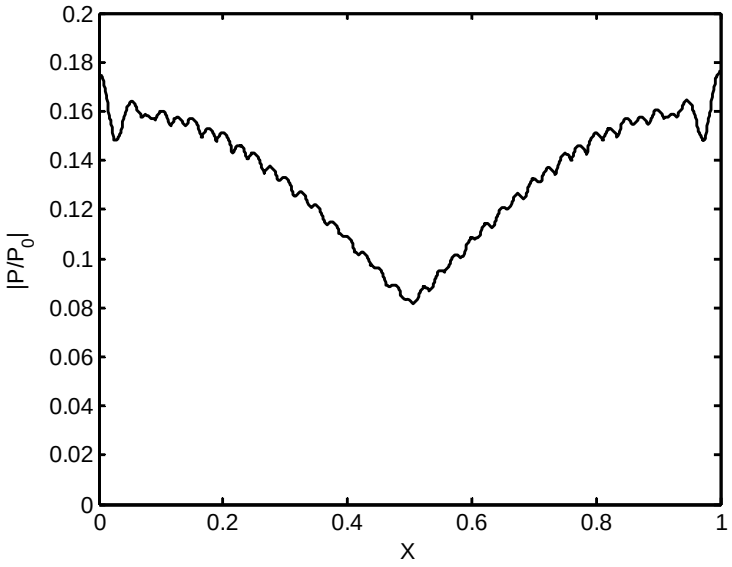

Figure B.8 Peak-to-peak pressure distribution in the cylindrical resonator along the axis. $S=\pi(r_0/l)^2 e^{\alpha X}$, $\alpha=0$, $l=0.2m$, $r_0/l=0.02$ **and** $A=5\times10^{-4}\cos(T)$.

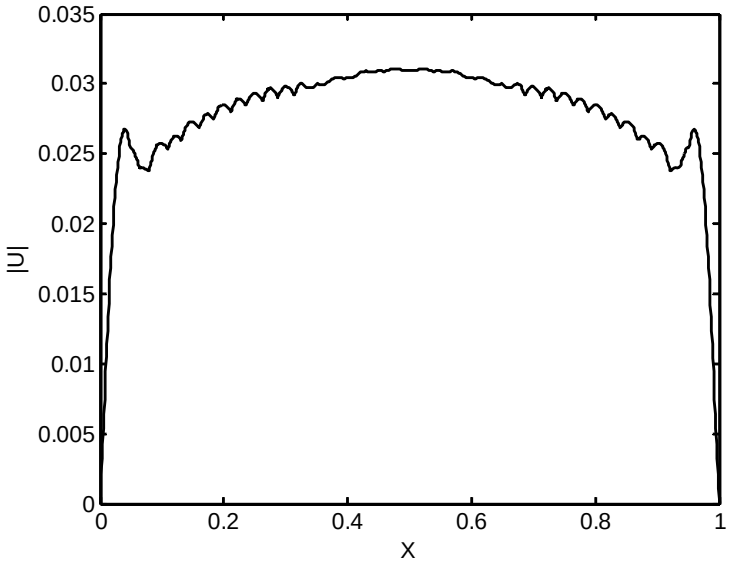

Figure B.9 Velocity amplitude distribution in the cylindrical resonator along the axis. $S=\pi(r_0/l)^2 e^{\alpha X}$, $\alpha=0$, $l=0.2m$, $r_0/l=0.02$ **and** $A=5\times10^{-4}\cos(T)$.

For a weak driving $A=5\times10^{-6}\cos(T)$, the acoustic waves in the cylindrical resonator present a linear behavior. The pressure waveform (Figure B.1) is nearly sinusoidal. As

the resonator has a uniform cross section, the distributions of peak-to-peak pressure and velocity amplitude are symmetric about $X = 0.5$. The maximum peak-to-peak pressure is found at two ends of the resonator ($X = 0$ and $X = 1$), and the minimum value is at $X = 0.5$, which is close to 0. While the velocity amplitude distribution (Figure B.3) behaves in an opposite way. At a moderate driving $A = 5 \times 10^{-5} \cos(T)$, the pressure amplitude is increased and distortion is also observed at the same time (Figure B.4). As acoustic waves become nonlinear, higher order harmonics are included. So that the peak-to-peak pressure at $X = 0.5$ becomes larger than 0. When the driving is strong ($A = 5 \times 10^{-4} \cos(T)$), the acoustic waves shock completely, as shown in Figure B.7. The distributions of peak-to-peak pressure and velocity amplitude present strong nonlinearity.

APPENDIX C

EXPERIMENT INSTRUMENTS AND PROCEDURES

C1. EXMPERIMENT INSTRUMENT SPECIFICATIONS

1. Pressure transducer (Model 103B12)

PERFORMANCE	ENGLISH	SI
Measurement Range (± 5 V output)	10 psi	190.7 dB
Useful Overrange (± 10 V output)	20 psi	196.7 dB [1]
Sensitivity (± 15 %)	500 mV/psi	72.5 mV/kPa
Maximum Pressure	250 psi	1724 kPa
Resolution	0.06 mpsi	86.3 dB
Resonant Frequency	≥ 13 kHz	≥ 13 kHz
Rise Time	≤ 25 µ sec	≤ 25 µ sec
Low Frequency Response (-5 %)	5 Hz	5 Hz
Non-Linearity	≤ 2.0 % FS	≤ 2.0 % FS [2]
ENVIRONMENTAL		
Acceleration Sensitivity	≤ 0.0005 psi/g	≤ 0.0035 kPa/(m/s^2)
Temperature Range (Operating)	-100 to 250 °F	-73 to 121 °C
Temperature Coefficient of Sensitivity	≤ 0.2 %/°F	≤ 0.36 %/°C
Maximum Flash Temperature	1000 °F	538 °C
Maximum Shock	1000 g pk	9807 m/s^2 pk
ELECTRICAL		
Output Polarity (Positive Pressure)	Positive	Positive
Discharge Time Constant (at room temp)	≥ 0.1 sec	≥ 0.1 sec
Excitation Voltage	20 to 30 VDC	20 to 30 VDC
Constant Current Excitation	2 to 20 mA	2 to 20 mA
Output Impedance	≤ 100 ohm	≤ 100 ohm
Output Bias Voltage	7 to 13 VDC	7 to 13 VDC
PHYSICAL		

Sensing Element	Ceramic	Ceramic
Housing Material	Stainless Steel	Stainless Steel
Diaphragm	316L Stainless Steel	316L Stainless Steel
Sealing	Welded Hermetic	Welded Hermetic
Electrical Connector	10-32 Coaxial Jack	10-32 Coaxial Jack
Weight	0.11 oz	3.15 gm

ACCESSORIES:

Model 060A10 Clamp nut 1/2-20-2A thd 7/16" hex (1)

Model 065A66 Adhesive Mounting Ring (3)

Model 160-0242-00 O-ring .250x.375(2-0100) (3)

NOTES:

[1] For +10 volt output, minimum 24 VDC supply voltage required. Negative 10 volt output may be limited by output bias.

[2] Zero-based, least-squares, straight line method.

2. Crown D75 amplifier

Signal/Noise : 106dB.

Damping factor : >400 from DC to 400Hz.

Controlled slew rate : (Slew rates are limited to useful levels for ultrasonic/Rf protection) >6V/ms.

MD : <0.01% at rated output.

HD : <0.001% from 20Hz to 400 Hz. Increasing linearly to 0.05% at 20 kHz.

Frequency response : ±0.1dB from 20 Hz to 20 kHz at 1 watt.

Phase response : $+10^0$ to -15^0 from 20 Hz to 20 kHz at 1 watt.

Input impedance : Nominally 20 kOhm balanced, and 10kOhm unbalanced.

Output impedance : <15mOhm in series with <3mH.

3. ONO SOKKI Multi-Purpose FFT analyzer CF-5220Z

Processing Functions	Time domain	Time waveform, absolute-value waveform, auto/cross-correlation function, impulse response, lissajous pattern, Hilbert transform, cepstrum, inverse FFT
	Frequency domain	Power spectrum, Fourier spectrum, cross-spectrum, phase spectrum, frequency response function, coherence function, coherent output power, 1/1 & 1/3 octave analysis, liftered spectrum, group delay, rpm order ratio analysis, rpm tracking analysis
	Amplitude domain	Amplitude probability density/distribution function
Input Section	Number of input channels	2
	Input configuration	Isolated single-ended
	Voltage range	1 mVr to 31.6 Vr
	Dynamic range	90 dB (TYP) or better
	A/D conversion	16 bits
	Amplitude flatness	±0.1 dB or better
	Cross-talk	-120 dB or better
Analysis Section	Frequency range	10 mHz to 100 kHz
	Frequency accuracy	±0.005% of reading
	Sampling frequency	2.56 times of the selected frequency range, external sampling clock
	Frequency resolution	25 / 50 / 100 / 200 / 400 / 800 / 1600 lines
	Window function	Rectangular Hanning flat-top force

		exponential, and use-defined windows
	Averaging	number of averaging : 1 to 65535 averaging time : 1s to 999s (in 1s-step)
	FFT processing	32-bit floating point (IEEE single precision format)
Memory Function Section	Record memory	512k word x 2-ch
	Block memory	200 blocks (4k bytes/block)
	CMOS memory	expanded to 2 M byte
	Panel condition memory	10 kinds
	Auto-sequence memory	7 programs
	Floppy disc drive	3.5 inch FDD × 1 drive (MS-DOS format compatible)
Output Section	Data bus	GP-IB interface
	Built-in printer	Thermal line dot type, paper width 112mm
	Keyboard interface	Serial
	Video output	for external VGA monitor
	Signal output	Sine, impulse, swept sine, pseudorandom, random, periodic random, pink random, linear/log sine sweep, arbitrary waveform
General	Power supply	100 to 240 VAC (47 to 440 Hz), 150VA max.
	Operating temperature	0 to +40°C
	Outer dimensions	420 (W) × 200 (H) × 300 (D) mm
	Weight	Approx. 11 kg

C2. PRESSURE TRANSDUCER CALIBRATION

The pressure inputs were received and converted to electrical signals by pressure transducers. Before the measurement of pressure waves, sensitivities of two pressure transducers need be calibrated. The schematic layout of calibration setup is shown in Figure C3.1. A conical duct with two holes at the bottom was made for calibration purpose. Two holes formed an angle of 90^0; one was connected with a microphone and the other with a pressure transducer. The small end of the duct was sealed and the big end was driven by the 5-inch 40W loudspeaker. As this was an axisymmetric duct, the pressure amplitudes obtained by the pressure transducer and microphone must be the same. Based on this principle, the calibration was conducted.

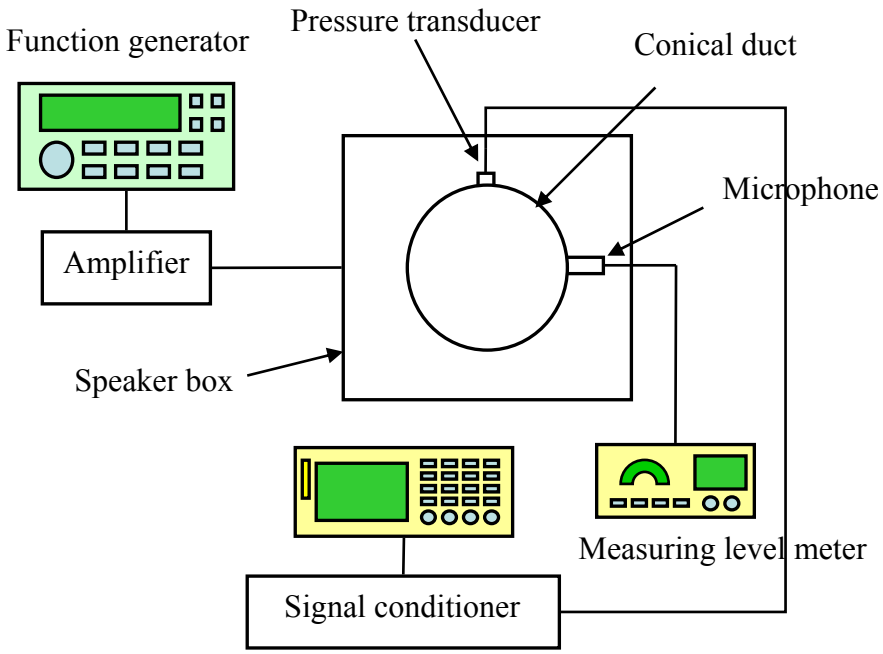

Figure C3.1 Pressure transducer calibration setup.

The input to loudspeaker was supplied by HP 33120A function generator and Crown D75 power amplifier. The output electrical signal obtained by the pressure transducer was recorded by the ONO SOKKI CF-5220Z FFT analyzer through the signal

conditioner, and the output pressure obtained by the microphone was received by the measuring level meter.

In order to minimize the error due to the difference of the two holes of the conical duct, the conical duct was placed in 4 different positions for each driving setting. At first, put the duct on the sound box placing microphone at position 1 and pressure transducer at position 2 as show in Figure C3.2. Next, turn the duct anticlockwise by 90^0, so that microphone is at position 2 and pressure transducer is at position 3. After that, put the microphone in position 3 and 4 for the third and forth round.

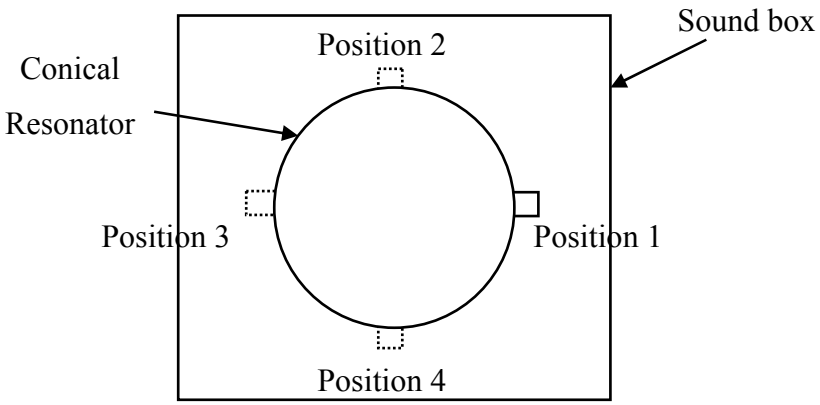

Figure C3.2 Definition of calibration position point.

The calibration procedure is as following:

STEP 1: Calibrate the measuring level meter. Connect the precision microphone to the pre-amplifier. Then link the pre-amplifier with the measuring level meter. Turn on measuring level meter. Plug the microphone into the calibrator and read the pressure value (in dB) on the measuring level meter. If the reading is 94 dB, the microphone is accurate. Otherwise, adjust the pressure pointer of the measuring level meter to 94 dB.

STEP 2: Connect all the devices as shown in Figure C3.1 correctly. Adjust the amplifier at minimum amplify level. Turn on function generator and amplifier, and the speaker works immediately; turn on signal conditioner and FFT analyzer.

STEP3: Set the function generator. Choose the sin-wave in the wave selection group. Press the FREQ button and set the frequency 200 Hz by rotating the knob on the upper-right corner of the control panel. Next Press the AMPL button and set a proper amplitude value. Observe the sound pressure level (SPL) on the measuring level meter, and adjust the amplifier so that SPL is 94dB. Record the digital dB value on the upper-right corner of the control panel. Convert SPL to Pascal using following equation

$$P_{mic} = 2 \times 10^{-5} \times 10^{\frac{SPL}{20}} . \tag{0.1}$$

STEP 4: Select the spectrum domain on FFT Analyzer by press down the SPECTR key. Set proper x-axis and y-axis range to observe the spectrum obtained by the sensor. Record the first harmonic amplitude V_{sen}.

STEP 5: Calculate pressure transducer sensitivity.

$$\text{Sensitivity} = V_{sen} / P_{mic} . \tag{0.2}$$

STEP 6: Place the conical duct in position 2, 3 and 4, and repeat STEP 3-5. Take the average sensitivity. The above process is repeated at 400Hz, 600Hz and 800 Hz.

The calibration results are listed in Table C.1. Sensitivity of pressure transducer S/N 3956 was 65.4 mV/kPa; sensitivity of pressure transducer S/N 3955 was 68.3 mV/kpa.

Table C.1 Pressure transducer calibration data (S/N: 3956) (Channel A)

Frequency	Position	Voltage	Pressure		Sensitivity
Hz		μVr	dB	Pa	mV/kPa
	1	65.167	94.0	1.0024	65.0126
	2	65.293	93.9	0.9909	65.8926
200	3	65.512	93.9	0.9909	66.1136
	4	65.201	93.9	0.9909	65.7998
			Average		65.7046
	1	65.901	94.0	1.0024	65.7449
	2	66.705	94.0	1.0024	66.5470
400	3	66.829	94.0	1.0024	66.6707
	4	66.167	94.0	1.0024	66.0103
			Average		66.2432
	1	65.418	94.0	1.0024	65.2630
	2	66.300	94.1	1.0140	65.3858
600	3	66.865	94.2	1.0257	65.1882
	4	66.234	94.1	1.0140	65.3207
			Average		65.2894
	1	64.488	94.0	1.0024	64.3352
	2	64.446	93.9	0.9909	65.0378
800	3	64.298	94.0	1.0024	64.1457
	4	63.745	93.9	0.9909	64.3304
			Average		64.4623
			Average		65.4249

Table C.2 Pressure transducer calibration data (S/N: 3955) (Channel B)

Frequency	Position	Voltage	Pressure		Sensitivity
Hz		μVr	dB	Pa	mV/kPa
	1	70.124	94.0	1.0024	69.9579
	2	69.565	93.9	0.9909	70.2038
200	3	70.091	93.9	0.9909	70.7347
	4	70.460	93.9	0.9909	71.1070
		Average			70.5009
	1	69.383	94.0	1.0024	69.2186
	2	68.693	94.0	1.0024	68.5303
400	3	69.074	94.1	1.0140	68.1216
	4	69.282	94.0	1.0024	69.1179
		Average			68.7471
	1	67.257	94.0	1.0024	67.0977
	2	67.247	93.8	0.9796	68.6504
600	3	67.299	94.0	1.0024	67.1396
	4	67.030	93.9	0.9909	67.6455
		Average			67.6333
	1	66.481	94.0	1.0024	66.3235
	2	66.310	94.0	1.0024	66.1529
800	3	67.528	94.1	1.0140	66.5969
	4	65.783	94.0	1.0024	65.6272
		Average			66.1751
		Average			68.2541

C3. PORCEDURE FOR DATA COLLECTION FROM FFT ANALYZER

1. Initializing a floppy disk

Insert a new floppy disk into the floppy disk drive. The floppy disk drive must be write-enabled. Make the following soft key setting:

Memory & Disk → DISK UTILITY → INITIALIZE → START

Select the format using the UP and DOWN switch of the CURSOR group and then press the ENTER switch. The formatting operation begins and message “formatting” appears; the LED on the floppy disk drive comes on and remains lit during the operation. When the formatting operation is completed, the LED on the floppy disk drive goes off and message “complete” appears. When formatting a floppy disk with format—2HD type with a capacity of 1.44 MB, the following procedure is required.

Memory & Disk → DISK UTILITY → DISK FORMAT → 1.44 MB

2. Saving analysis data to a floppy disk

The analyzer is provided with the following two methods for saving analysis data to a floppy disk.

Saving the display screen directly to a floppy disk

DISPLAY Operates the display screen and saves it in a floppy disk.

AUTO Save the display screen automatically each time the screen is updated after analysis or averaging.

Saving the block memory data to a floppy disk

BLOCK Saves the block memory data to a floppy disk on a screen basis.

BLOCKALL Automatically saves all block memory data to a floppy disk.

The name of files for saving analysis data consists of a filename and a three-digit number (data number) following the filename. The data number is used only when data sets are managed under the same file name. In multi-frame display modes, the data number stars from the data displayed in the top frame and is then incremented. The starting number can be set to a number from 001 to 999. The default value is 001.)

2.1. Saving display data on a screen basis

Make the following soft key settings

Memory & Disk → DISK LD/ST → STORE DISPLAY → DISPLAY

The following window appears

FILE NAME ? No.1

Enter a filename of up to five characters using the panel switches. The character type can be changed by pressing the following soft key.

A-Z 1-9: Uppercase letters and numbers

a-z etc. : Lowercase letters and special characters

To clear all characters, press the ESC switch. To delete the last character, press the BACK switch. To change the data number (001 to 999), turn the rotary knob. When a filename has been entered, press the ENTER switch. The message “WRITING” is displayed and data is saved to a floppy disk under the specified filename. If a file with the same filename already exists on the disk, the following message appears.

DELETE OLD? Y or N

To overwrite the file, enter Y (or press the SENSOR-Y switch). To change the filename enter N (or press the NYQ/ORB-N switch) and then press ENTER switch.

2.2. Saving display data in succession

Put the analyzer in the pause condition. Make the following soft key settings

Memory & Disk → DISK LD/ST → STORE DISPLAY → AUTO

The following window appears

FILE NAME ? No.1

Enter a filename of up to five characters using the panel switches. The character type can be changed by pressing the following soft key.

A-Z 1-9: Uppercase letters and numbers

a-z etc. : Lowercase letters and special characters

To clear all characters, press the ESC switch. To delete the last character, press the BACK switch. To change the data number (001 to 999), turn the rotary knob. When a filename has been entered, press the ENTER switch. Press the START switch of the COMMAND group to start the save operation. The message “WRITING” is displayed and data is saved to a floppy disk under the specified filename. To cancel the save operation, press the PAUSE key and the AUTO soft key. If a file with the same filename already exists on the disk, the following message appears.

DELETE OLD? Y or N

To overwrite the file, enter Y (or press the SENSOR-Y switch). To change the filename enter N (or press the NYQ/ORB-N switch) and then press ENTER switch.